Applications of Statistical Shape Modelling in Orthopaedics

by

Mehrdad Palizi

A thesis submitted in partial fulfillment of the requirements for the degree of

Doctor of Philosophy

in

STRUCTURAL ENGINEERING

Department of Civil and Environmental Engineering
University of Alberta

ABSTRACT

Statistical Shape Models (SSMs) describe the shape variation in a family of similar objects in a computational format. An example of a shape family is the periphery of a specific bone for different individuals. SSMs have diverse applications in computer vision and medicine. In orthopaedics, SSMs are used to study the morphology of bones, automate image segmentation, and restore the healthy shape of injured bones. To build an SSM, an invertible mapping should be identified between the objects, referred to as correspondence. Point-set registration methods are used to establish correspondence between the objects which are represented by a dense set of points. This doctoral thesis explores a range of applications of statistical shape modelling in orthopaedics.

Firstly, this research implements hypoelastic constitutive equations into the finite element software Abaqus. Abaqus is a computational platform that could be used for the biomechanical simulation of anatomical structures with various types of nonlinearity; the software allows the user to implement advanced constitutive models through the user-material subroutine. However, the implementation of a constitutive model into Abaqus is not straightforward, and the constitutive model should be expressed in a special hypoelastic form. This thesis provides such reformulation for several hypoelastic models and describes the algorithms behind many variables in the UMAT subroutine.

Second, the thesis employs SSMs to study the geometry of the pelvic bone, focusing on variation within individuals, asymmetry, and sexual dimorphism (sex-based differences). Using computational methods in shape analysis and statistical tests, the significant patterns of variation, as well as the areas of significant variation, are identified on the pelvic bone. Anatomical

measurements and interpretation are then provided. Previous studies have been solely focused on a single type of variation on the pelvic bone or studied men and women collectively. However, the pelvic bone shows noticeable differences between men and women and its variation within a population arises from the differences in the shape, size, position, and orientation of its components. This research provides a sex-specific assessment of pelvic geometry at multiple levels of variation, including the shape of the hemipelvis, the shape-size of the hemipelvis, and the shape-size of the left-right hemipelvis in the pelvic structure. In addition, the thesis characterizes and evaluates the ability of SSMs to simulate training samples as well as predict unseen samples, for two bones, the hemipelvis, and talus.

Lastly, the thesis addresses a limitation of a probabilistic point-set registration method; the Coherent Point Drift (CPD) is a probabilistic registration method that matches complex objects such as anatomical structures. However, the method might struggle to match the intricate local features of the objects. To address this limitation, this thesis investigates the effect of geometry-aware sampling on the performance of the CPD method in matching objects with local features. In geometry-aware sampling, a higher density of points is sampled on local features, which could improve the perception of point sets in the registration process. To investigate the effectiveness of the approach, a set of two- and three-dimensional synthetic experiments, as well as a set of examples of aligning femur cartilages are performed.

PREFACE

This thesis is an original work by Mehrdad Palizi. Four papers have been published/in preparation for publication on the basis of this thesis. The details of the corresponding chapters are summarized below:

A version of Chapter 2 has been published as ***Palizi, M., Federico, S., & Adeeb, S. (2020). Consistent numerical implementation of hypoelastic constitutive models. Zeitschrift für angewandte Mathematik und Physik, 71, 1-23.*** For the consistency and coherence of this thesis, contents have been modified, removed, or added to the submitted paper. Mehrdad Palizi was responsible for conceptualization, methodology development, numerical model development, analysis implementation, and paper composition. Samer Adeeb and Salvatore Federico were in charge of conceptualization, supervision, funding acquisition, and paper revision. All other authors provided extensive and resourceful technical input for methodology formulation and result validation.

A version of Chapter 3 is to be submitted as ***Palizi, M., Ead, M.S., Jaremko J.L., Westover, L., & Adeeb, S. (2023). Quantitative assessment of pelvic morphology using statistical shape modelling***. For the consistency and coherence of this thesis, contents have been modified, removed, or added to the submitted paper. Mehrdad Palizi was responsible for conceptualization, methodology development, numerical model development, analysis implementation, and paper composition. Maha Ead was responsible for the numerical model development (image segmentation) and commenting on the article. Jakob Jaremko was in charge of the critical revision of the article. Lindsey Westover was in charge of data collection and commenting on the article.

Samer Adeeb was in charge of conceptualization, supervision, funding acquisition, and paper revision.

A version of Chapter 4 is to be submitted as ***Palizi, M. & Adeeb, S. (2023). Quality measurement of anatomical shape models in simulation of training shapes and unseen shapes (hemipelvis and talus).*** For the consistency and coherence of this thesis, contents have been modified, removed, or added to the submitted paper. Mehrdad Palizi was responsible for conceptualization, methodology development, numerical model development, analysis implementation, and paper composition. Samer Adeeb was in charge of conceptualization, supervision, funding acquisition, and paper revision.

A version of Chapter 5 is to be submitted as ***Palizi, M. & Adeeb, S. (2023). Effect of geometry-aware sampling on the performance of the coherent point drift registration method.*** For the consistency and coherence of this thesis, contents have been modified, removed, or added to the submitted paper. Mehrdad Palizi was responsible for conceptualization, methodology development, numerical model development, analysis implementation, and paper composition. Samer Adeeb was in charge of conceptualization, supervision, funding acquisition, and paper revision.

DEDICATION

To my loving family

ACKNOWLEDGMENTS

Foremost, I would like to express my deepest gratitude to my supervisor, Dr. Samer Adeeb, for his invaluable guidance and encouragement throughout my Ph.D. studies, from inception to completion. His brilliant insight guided me through my research and trained me to be an independent researcher. This dissertation would not have been possible without their overwhelming support and mentorship.

My sincere appreciation also goes to every member of my examination committee, Dr. Yong Li, Dr. Chun I1 Kim, Dr. Qipei (Gavin) Mei, and Dr. Abdolhamid Akbarzadeh Shafaroudi for their intelligent direction towards producing a better version of this research work. I am also grateful to the chair of my defense exam, Dr. Yuxiang Chen. Furthermore, I want to sincerely thank Dr. Salvatore Federico, Dr. Lindsey Westover, and Dr. Amin Komeili for their incredible guidance and help through different phases of this work.

And last but not least, I want to thank my family members and my friends, for all their endless support and encouragement in the special journey of my life.

TABLE OF CONTENTS

LIST OF TABLES

LIST OF FIGURES

GLOSSARY OF TERMS

CPD	=	Coherent Point Drift
CT	=	Computed Tomography
DVF	=	Displacement Vector Field
FE-HBM	=	Finite Element Human Body Model
GM	=	Geometric Morphometrics
GMM	=	Gaussian Mixture Model
ICP	=	Iterative Closest Point
KC	=	Kernel Correlation
MRI	=	Magnetic Resonance Imaging
PC	=	Principal Component
PCA	=	Principal Component Analysis
SD	=	Standard Deviation
SSM	=	Statistical Shape Model
TPS		Thin-Plate Spline Transformation
UMAT	=	User-Material

CHAPTER 1: INTRODUCTION

1.1 Background

1.1.1 Rebirth of shape analysis in biology

Biological shape analysis, referred to as morphometrics, is an old topic that studies the size and shape of biological structures [1]. A biologist traditionally measured some specific angles, distances, and distance ratios between biologically meaningful points, referred to as landmarks, and performed statistical analyses on them to quantify the shape or size variances of a biological structure within a population or across populations, an approach that is called multivariate morphometrics [1]. This approach suffers from two issues: (1) angles, distances, and distance ratios cannot capture the entire geometry of biological structures, and (2) it is not possible to reconstruct the geometry of a biological structure using discrete measurements, while the reverse process is easy to perform [2].

A key notion in morphometrics was to retain all of the geometric information contained in the data and directly use the coordinates of landmarks, rather than relying on distances and angles [2]. This approach is called geometric morphometrics and was started by D'Arcy Thompson's substantial work in 1927, titled "On Growth and Form". In this work, Thompson studied the size and shape variance between species by drawing a regular square grid pattern on one object and deforming the grid to lie on the second object (Figure 1-1) [1, 3]. By comparing the original and deformed grids, the differences in size and shape among the species were examined [1].

Bookstein categorized the landmarks used in geometric morphometrics into three types: (1) points located at the intersection of tissues, (2) points of maximum curvature, and (3) external points such as the endpoints of maximum length or breadth [4]. During the initial stages of geometric morphometrics, studies involve statistical analysis of Cartesian coordinates of these landmarks, which anatomists manually marked on two-dimensional digital images of comparable specimens [5]. Despite its robustness, this approach was challenging in terms of repeatability, and inter-observer and intra-observer errors were introduced in the process [6].

The advent of three-dimensional scanning devices, alongside the theoretical and computational developments in shape analysis, led to the rebirth of biological shape analysis and its fast growth in many domains [2]. In orthopaedics, three-dimensional scanning modalities such as Computed Tomography (CT) and Magnetic Resonance Imaging (MRI) describe the shape of skeletal elements with dense volumetric representation [6] and computational tools such as statistical shape modelling provide a rich and concise model for the shape variability of skeletal elements within a population or across populations [6].

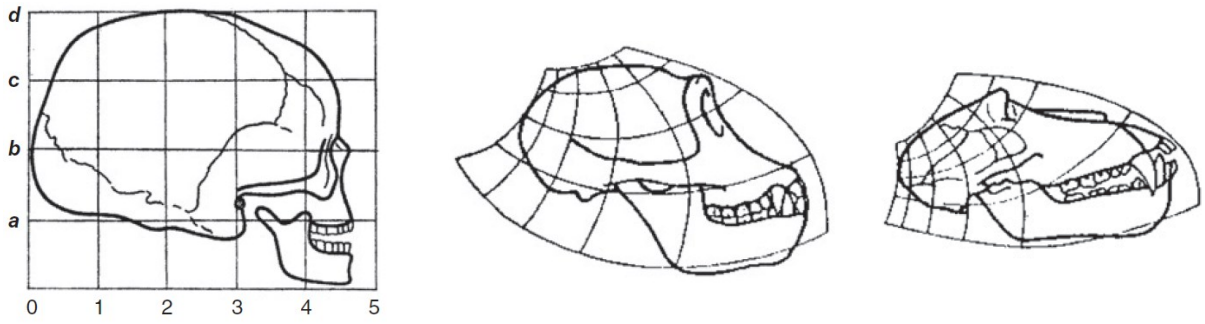

(a) (b) (c)

Figure 1-1: Regular square grid pattern placed on a human skull (a), and the deformed grid patterns matched on a chimpanzee's skull (b) and a baboon's skull (c) [1, 3]

1.1.2 Applications of statistical shape modelling in orthopaedics

Statistical shape modelling is a powerful computational approach for analyzing the shape variability of biological structures [7]. A Statistical Shape Model (SSM) of a biological entity comprises two components: (1) the average shape of the samples, typically represented by a dense set of points, and (2) the modes of variation within the samples, represented by Displacement Vector Fields (DVFs) defined on the average shape.

In the last two decades, researchers have employed SSMs to investigate the morphology of anatomical structures. The majority of the studies have been focused on the variation of the anatomical elements within individuals, referred to as anatomical variation, which proved to be highly beneficial in orthopaedics [8-12]. For example, Ahrend et. al. used SSM to study the anatomical variation of the pelvis in the Asian population and manufactured generic Asian pelvic ABMs (Artificial Bone Models) for educational and research purposes (Figure 1-2 (a)) [8]. In

addition to the anatomical variation, studies have investigated the sexual dimorphism of the anatomical elements using SSM-based approaches, especially for the pelvis and skull [9, 10, 12, 13]. As an example, Shui et al. constructed two SSMs for the skull and face using 140 samples of 3D heads (70 male and 70 female), determined the craniofacial relationship (correlation between the skull and face SSMs), and determine sex based on developed SSMs, with the highest sex classification rate of 91.43% [13]. Statistical shape modelling has also been used to study the asymmetry [14, 15], allometry (the relationship between the shape and size) [16, 17], as well as clustering the shape of bones as healthy and pathological [7].

A great advantage of SSMs is their generative power. An SSM of an anatomical structure could generate numerous plausible shape instances for the structure [18]. Some studies have leveraged SSMs as a deformable template to convert the dense three-dimensional images (CT and MRI) and sparse two-dimensional images (X-rays) of bone specimens into meshes and point sets [19]. Previously, medical image segmentation was performed semi-automatically by anatomists who draw contours on 2D slices of the images in modelling software, and then the software converted the contours into a mesh. However, such a process was labor-intensive. A novel idea was to generate shape instances from an SSM and fit shape instances on the image data of a specimen. As an example, Dworzak et al. constructed an SSM for the rib cage using CT scans of 29 individuals, generated artificial binary projection for the instances of the SSM (from two views), and by minimizing distance measures between the silhouettes of (artificial) SSM-based projection and real images, reconstructed the 3D geometry and pose (position and orientation) of the individual's rib cage (Figure 1-2 (c)) [20]. Similarly, virtual bone reconstruction has employed

SSMs to fit shape instances onto meshes of injured bones, with significant portions of the bone being distorted due to degenerative conditions [21-24]. SSM-based virtual bone reconstruction provides a plausible model for the native shape of injured bone which could be highly beneficial in decision-making over the size and shape of the implant components used to restore the bone.

SSMs have also shown great potential to incorporate with the Finite Element Human Body Models (FE-HBMs) with huge benefits in assessing the risk of injury in scenarios such as motor vehicle crashes [25, 26]. The main idea of SSM-based FEM models is to expand the limited number of specimens available for the evaluation of injury risk in FM-HBMs to an enlarged set of shape instances generated by the SSM. For the mechanical simulation of a shape instance, the instance is deformed on the samples of FM-HBMs, and through the computed mapping, the boundary conditions and volumetric mesh of the FM-HBMs samples are transformed to the SSM instances. Some studies have considered the relationship between the morphology of bones and their biomechanics, by applying various types of loading to the modes of variation of anatomical SSMs [27-29].

Lastly, SSMs could provide more realistic biomechanical simulation for the human bones and soft tissues during growth. Nonlinear continuum mechanics is the standard approach to modeling biological tissue growth [30]. A promising framework for simulating growth is the multiplicative decomposition of the deformation gradient into (1) an elastic component that reflects the mechanical response, and (2) a time-dependent biological component (e.g. [30] for bulk growth and [31] for surface growth simulation). However, in this framework, identifying an appropriate deformation gradient for the time-dependent component is nontrivial [31]. In recent

years, SSMs have been combined with multiple linear regression methods to correlate the bone geometry with anthropometric variables including age, offering age-specific models for various bones (see [11] for the pelvis, [25] for the femur and tibia, and [32] for the ribcage). The age-related pattern of morphometric SSM could be used as the biological deformation field in the constitutive growth laws, enabling more realistic simulations. In addition, the spatiotemporal SSMs could be constructed based on the longitudinal datasets of a bone to describe (1) the subject-specific morphological changes at the unobserved time and (2) the average and main morphological changes at a specific time [7].

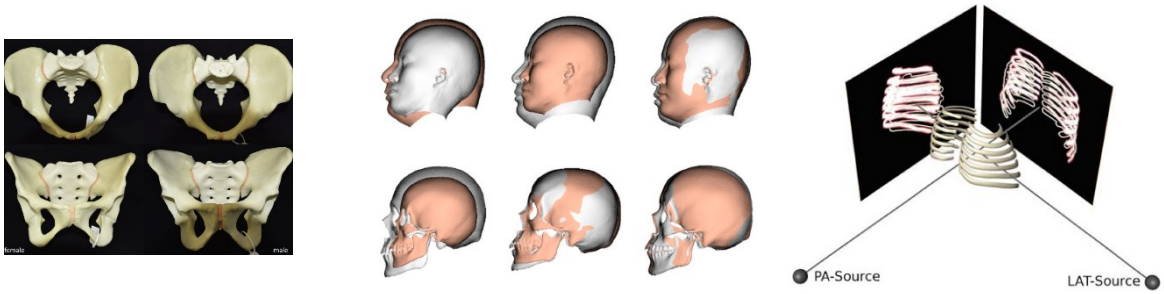

(a) (b) (c)

Figure 1-2: Examples of anatomical SSMs being employed in orthopaedics: (a) Manufactured artificial bone models for the average male and female models for a pelvic SSM constructed for 100 Asian adults (left: female, right: male) [8], (b) the comparison of the extreme instances of the first three modes of variation (±3SD) for the models built for the face and skull (mode1 to mode3 are shown from left to right) [13], (c) Generation of two orthogonal images for a shape instance of rib-cage SSM from specific views and the silhouettes of the virtual image (beige) and the reference image (red) [20].

1.1.3 Point-set registration methods

To build an SSM for an anatomical structure, the most challenging step is to establish correspondence between the specimens. The establishment of "unfavorable" correspondence between the shape samples results in models with artifacts (Figure 1-3) [7]. In the past, the correspondence was constructed manually between the samples, during the process of specifying the landmarks by anatomists [6]. However, the manual marking process is not feasible for the dense representation of shapes. Point-set registration is a computational approach to automatically detect the correspondence between two point sets.

There are various classifications for point-set registration, in which, a single aspect of the techniques is considered [33]. For instance, based on the applied transformation, the point set registrations are classified into rigid and non-rigid algorithms [33]. For a rigid point set registration, the transformation, which deforms the "source" point set to align it on the "target" point set, preserves the distance between each two points on the source [33]. Rigid transformation includes rotation, reflection, translation, and scaling [33]. It should be noted that, for scaling, the ratios of distances, rather than distances, are preserved.

By comparison, in non-rigid registrations, the relative distances on the source point set are not preserved during registration and the point set undergoes stretching and bending. Affine transformation is a simple non-rigid transformation in which the point set is allowed to undergo anisotropic scaling and skewness [33]. Thin-plate spline transformation (TPS) is a well-known non-rigid transformation in which, the source point set is deformed and matched on the target point

set while an energy of the Euclidean space, called the bending energy, is preserved at its minimum [34].

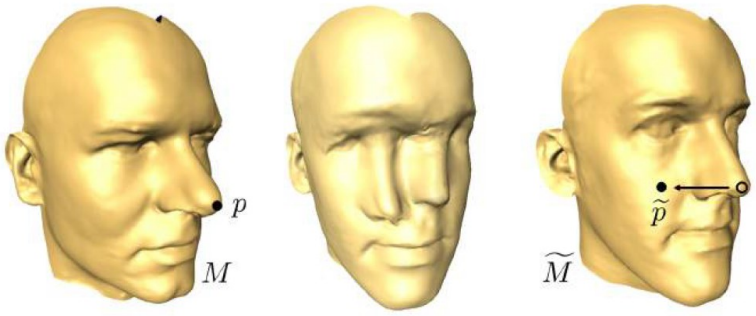

Figure 1-3: Establishment of unfavorable correspondence between two head samples (the noise of the left head is aligned with a point on the cheek of the right head), and the average of two heads with artifacts (middle head with two noses) [7].

The iterative closest point (ICP) algorithm is the classical point set registration [35]. The ICP is an iterative algorithm with two steps: (1) for each point on the source point set, the point with minimum Euclidean distance on the target point set is found and the points become a corresponding pair, and (2) the source point set is parameterized by a rigid transformation and, by minimizing the mean squared distance of the corresponding pairs, the transformation parameters are calculated. The second step of the ICP algorithm has a direct solution, and therefore, the algorithm has low computational complexity. However, the first part of the algorithm, i.e. estimation of correspondence pairs, is sensitive to the initial pose of the source and target point sets. An unfavorable estimation of correspondence pairs can lead to a situation in which the transformed source points would be trapped in a local minimum.

The kernel correlation (KC) algorithm, introduced in [36], was the starting point of an important class of point set registrations called probabilistic algorithms. Unlike one-to-one correspondence in the ICP method, the probabilistic approaches establish soft correspondence between the points which allows for partial assignments of points, indicating the likelihood or confidence of a match between two points. The correlation techniques are originally used to align intensity (gray-level) images. KC algorithm introduces three levels of kernel correlations: (1) kernel correlation between two points: for an isotropic Gaussian kernel, the correlation is the density at the first point when a Gaussian kernel is centered at the second point (or vice versa); (2) kernel correlation between a point set and a single point inside the point set: for Gaussian kernels, the correlation is the density at the single point when Gaussian kernels are centered at the rest of the points in the point set. This correlation is also referred to as leave-one-out kernel correlation and (3) kernel correlation of a whole point set which is the summation of all of the leave-one-out kernel correlations. Using the Gaussian kernels, (1) the correlation between two points is maximized when the points are located on each other, and (2) the correlation of a whole point set is high when the points inside the point set are close to each other and the point set is "compact". KC algorithm treats the registration problem as maximizing the kernel correlation of a point set which is the union of the target point set and the parameterized version of the source point set. When the source point set is aligned with the target point set, the compactness of the collective point set is at its highest level and the kernel correlation of the collective point set is maximum.

Jian and Vemuri [37] utilized the Gaussian Mixture Model (GMM) version of the KC algorithm with TPS transformation in a non-rigid registration method called GMMReg. In

GMMReg, the point sets are represented by GMMs, and the distance between the point sets is defined as the L2 divergence of the associated GMMs. L2 divergence is a similarity measurement between two GMMs. GMMReg treats the registration problem as minimizing the L2 divergence between the GMM of the target point set and the GMM of the parameterized source point set. To preserve the coherence of the source point set during registration, a regularization term that contains the coefficients of the TPS transformation is introduced in the objective function.

The Coherent Point Drift (CPD) algorithm is a state-of-the-art non-rigid registration technique [38]. The CPD algorithm treats the registration problem as a probability estimation problem. In this algorithm, the source point set is represented by a GMM, and the target point set is considered the dataset. The centroids of the GMM are parameterized by a rigid or non-rigid transformation, and by maximizing the likelihood of the GMM given the dataset, the source point set is matched on the target point set. The non-rigid transformation of the CPD method is based on motion coherence in which, the close points exhibit cohesion, and as the distance between two points increases, the cohesion diminishes. To ensure the smoothness of the motion, the CPD method uses high-content energy of the displacement field in the Fourier space as a regularization term. The CPD method has been widely used in recent years to establish correspondence between complex objects such as anatomical elements.

1.2 Problem statements

1.2.1 Consistent Implementation of Hypoelastic Constitutive Equations into Finite Element Software Abaqus

Abaqus allows the user to implement finite-strain constitutive models for biomechanical phenomena using the user-material (UMAT) subroutine. However, the implementation of advanced constitutive models into Abaqus is challenging. Hypoelasticity plays a central role in the structure of the UMAT subroutine. In a hypoelastic constitutive model, an objective stress rate such as the Jaumann rate of Cauchy or Kirchhoff stress is related to the rate of deformation by an elasticity tensor. The Jacobian matrix (DDSDDE) is a UMAT variable that must be updated at each increment. The incorrect update of this variable gives rise to early divergence or slow convergence of the model. To correctly update the Jacobian matrix, the constitutive model should be expressed as a relationship between the Jaumann rate of the Kirchhoff stress and the rate of deformation, i.e. the format of a hypoelastic constitutive model, and the components of the elasticity tensor which connects the Jaumann rate of the Kirchhoff stress to the rate of deformation, should be used to update the Jacobian matrix. This thesis provides the consistent implementation for six hypoelastic constitutive equations and describes the algorithms used for multiple variables in the UMAT subroutine. To validate the implementation, the numerical responses for a simple 8-node brick element (C3D8) under uniaxial extension and simple shear loading conditions are compared with the available analytical solutions, and the consequences of using an inconsistent Jacobian matrix are illustrated.

1.2.2 Morphological study of the pelvic bone using statistical shape modelling

The pelvis is a complex anatomical structure with multiple components and noticeable differences between men and women. Pelvic morphology has been studied in traditional and modern morphometrics in terms of anatomical variation (inter-individual), matching asymmetry (intra-individual), allometry, and sexual dimorphism [8-12, 39-41]. However, the knowledge about the sex-specific inter- and intra-individual variation, especially bilateral asymmetry, remained limited. Furthermore, the SSM-based studies have focused on a single type of variation in the pelvis, such as the shape-size variation of the hemipelvis [9, 12], or the shape-size variation of the entire pelvic structure [8, 10, 11]; By starting with the shape of the hemipelvis and systematically incorporating the variations due to the size and then position and orientation of the hemipelvis, the current study provides a sex-specific investigation of the left-right hemipelves in the pelvic structure at multiple levels.

1.2.3 Quality measures of statistical shape models

Anatomical SSMs have been characterized in terms of their ability to simulate in-training samples and predict unseen samples, respectively called accuracy and generalizability [18]. Previous studies have measured the SSM qualities based on comparing the model-derived shape instances with a representation of samples that were used in the models [12, 42]. However, the

representation of samples in the model is a deformed version of a template being matched on the sample and does not "perfectly" match the original representation of a specimen (due to the smooth transformation of the registration process). This thesis characterizes and evaluates the quality of SSMs for the hemipelvis and talus; the SSM instances are compared with the original meshes of the samples, which provides a more realistic evaluation of the models.

1.2.4 Effect of geometry-aware point set sampling on the performance of CPD registration method in matching local features

The CPD method is commonly used to match the point sets of anatomical elements. In addition, refinements and extensions have been proposed to improve various aspects of the CPD registration method, e.g. estimation of correspondence by adding features [43, 44] or higher robustness against noise [45]. Despite the accurate performance of the CPD method in matching the global structure of anatomical entities, the CPD method might struggle to match the delicate local features of shapes. To address this limitation, this thesis investigates the effect of geometry-aware sampling on the performance of the CPD method in matching shapes with local features. A set of 2D and 3D synthetic experiments are designed which involve aligning simple shapes with discernable local features. Using uniform and geometry-aware distribution of points, the performance of the CPD registration method is assessed in terms of aligning these local features. Furthermore, the effectiveness of the approach is assessed on a set of real examples which involve

matching the samples of femur cartilage which is a thin layer with complex geometry on the femur bone surface.

1.3 Research objectives and methodologies

The ultimate goal of this study is: (1) to provide consistent implementation of hypoplastic constitutive equations in the finite element software Abaqus, (2) to provide a sex-specific assessment of pelvic morphology using statistical shape models, (3) to measure the qualities of statistical shape models in modelling the in-training samples and unknown samples for the hemipelvis and talus, (4) to investigate the effect of geometry-aware point set sampling on the performance of coherent point drift in matching shapes with local features. To accomplish each section, the following steps are taken:

Objective 1: Consistent numerical implementation of hypoplastic constitutive equations into finite element software Abaqus.

a) Identification of algorithms behind the stress and strain variables of the UMAT subroutine in Abaqus.
b) Reformulation of various hypoplastic constitutive equations as a relation between the Jaumann rate of the Kirchhoff stress and the rate of deformation.

c) Validation of the implementations by comparing the results for a simple eight-node brick element C3D8 under simple shear and uniaxial extension with the available analytical solutions

Objective 2: Morphological study of the pelvic bone using statistical shape analysis.

a) Development of a computational pipeline to convert the CT image dataset of 40 pelves (20 male and 20 female) into refined triangle meshes and point sets in correspondence.
b) Computation of sex-specific DVFs related to anatomical variation and asymmetry, as well as the DVF related to sexual dimorphism.
c) Identification of patterns of anatomical variation and asymmetry using principal component analysis.
d) Local measurement of anatomical variation and asymmetry and identification of areas showing high local anatomical variation and local asymmetry.
e) Assessment of the significance of identified patterns and areas by non-parametric and permutation-based statistical tests.
f) Visualization of significant patterns and areas as color-map animations and plots.
g) Anatomical interpretation of the significant patterns and areas.

Objective 3: Quality measurement of anatomical shape models in simulation of training shapes and unseen shapes for the hemipelvis and talus.

a) Development of a computational workflow to convert the CT images of 40 hemipelvis (20 female and 20 male) and 96 talus samples (41 female and 55 male) into golden-standard refined triangle meshes and point sets in correspondence.
b) Construction of sex-specific and overall models for the shape and shape-size of the bones.
c) Characterization of the ability of a model in simulating the in-training samples and predicting unknown samples (based on goldern-standard meshes).
d) Evaluation of the qualities of the SSMs constructed for the hemipelvis and talus.

Objective 4: Investigation of the effect of geometry-aware point-set sampling on the performance of the CPD point-set registration in matching shapes with local features.

a) Construction of synthetic objects with local features in two- and three-dimensions.
b) Investigation of the effect of geometry-aware and uniform point-set sampling on the accuracy of coherent point drift registration algorithm in aligning 2D synthetic objects with different local features.
c) Preprocessing of the femur cartilages (10 subjects with unknown sex).
d) Repeating step (c) for three-dimensional synthetic objects.
e) Development of geometry-aware and uniform sampling algorithms for automated point-set sampling from 3D shapes (real and synthetic).
f) Investigation of the effect of geometry-aware and uniform point-set sampling on the accuracy of the CPD method in matching the femur cartilage samples.

1.4 Organization of thesis

The remainder of the thesis is organized as follows:

Chapter 2 describes the theoretical and computational aspects of the consistent implementation of six hypoplastic constitutive models into finite element software Abaqus.

Chapter 3 presents the morphological study of the pelvic bone using statistical shape modelling, including anatomical variation, asymmetry, and sexual dimorphism.

Chapter 4 presents the quality measurement of statistical shape models for the hemipelvis and talus.

Chapter 5 investigates the effect of geometry-aware point-set sampling on the performance of the CPD registration method in matching synthetic and real shapes with local features.

Chapter 6 summarizes the contribution of the research work, draws conclusions, and presents ideas for future work. The limitations of the current work are provided as well.

References

[1] Dryden, I. L., & Mardia, K. V. (2016). Statistical shape analysis: with applications in R (Vol. 995). John Wiley & Sons.

[2] Slice, D. E. (2007). Geometric morphometrics. Annu. Rev. Anthropol., 36, 261-281.

[3] Thompson, D. A. W. (1942). On Growth and Form, Cambridge Univ. Press1942.

[4] Bookstein, F. L. (1991). Morphometric tools for landmark data Cambridge University Press. New York.

[5] Slice, D. E. (Ed.). (2006). Modern morphometrics in physical anthropology. Springer Science & Business Media.

[6] Sarkalkan, N., Weinans, H., & Zadpoor, A. A. (2014). Statistical shape and appearance models of bones. Bone, 60, 129-140.

[7] Ambellan, F., Lamecker, H., von Tycowicz, C., & Zachow, S. (2019). Statistical shape models: understanding and mastering variation in anatomy (pp. 67-84). Springer International Publishing.

[8] Ahrend, M. D., Noser, H., Shanmugam, R., Burr, F., Kamer, L., Kamarul, T., ... & Gueorguiev-Rüegg, B. (2020). Development of generic Asian pelvic bone models using CT-based 3D statistical modelling. Journal of orthopaedic translation, 20, 100-106.

[9] van Veldhuizen, W. A., van der Wel, H., Kuipers, H. Y., Kraeima, J., Ten Duis, K., Wolterink, J. M., ... & IJpma, F. F. (2023). Development of a Statistical Shape Model and Assessment of Anatomical Shape Variations in the Hemipelvis. Journal of Clinical Medicine, 12(11), 3767.

[10] Arand, C., Wagner, D., Richards, R. G., Noser, H., Kamer, L., Sawaguchi, T., & Rommens, P. M. (2019). 3D statistical model of the pelvic ring–a CT-based statistical evaluation of anatomical variation. Journal of Anatomy, 234(3), 376-383.

[11] Brynskog, E., Iraeus, J., Reed, M. P., & Davidsson, J. (2021). Predicting pelvis geometry using a morphometric model with overall anthropometric variables. Journal of biomechanics, 126, 110633.

[12] Audenaert, E. A., Pattyn, C., Steenackers, G., De Roeck, J., Vandermeulen, D., & Claes, P. (2019). Statistical shape modelling of skeletal anatomy for sex discrimination: their training size, sexual dimorphism, and asymmetry. Frontiers in bioengineering and biotechnology, 7, 302.

[13] Shui, W., Zhou, M., Maddock, S., He, T., Wang, X., & Deng, Q. (2017). A PCA-Based method for determining craniofacial relationship and sexual dimorphism of facial shapes. Computers in biology and medicine, 90, 33-49.

[14] Handrich, K., Kamer, L., Mayo, K., Sawaguchi, T., Noser, H., Arand, C., ... & Rommens, P. M. (2021). Asymmetry of the pelvic ring evaluated by CT-based 3D statistical modelling. Journal of anatomy, 238(5), 1225-1232.

[15] Hierl, T., Doerfler, H. M., Huempfner-Hierl, H., & Kruber, D. (2021). Evaluation of the midface by statistical shape modelling. Journal of Oral and Maxillofacial Surgery, 79(1), 202-e1.

[16] Fischer, B., & Mitteroecker, P. (2015). Covariation between human pelvis shape, stature, and head size alleviates the obstetric dilemma. Proceedings of the National Academy of Sciences, 112(18), 5655-5660.

[17] Fischer, B., & Mitteroecker, P. (2017). Allometry and sexual dimorphism in the human pelvis. The Anatomical Record, 300(4), 698-705.

[18] Davies, Rhodri H., Carole J. Twining, Timothy F. Cootes, John C. Waterton, and Christopher J. Taylor. "A minimum description length approach to statistical shape modelling." IEEE transactions on medical imaging 21, no. 5 (2002): 525-537.

[19] Heimann, T., & Meinzer, H. P. (2009). Statistical shape models for 3D medical image segmentation: a review. Medical image analysis, 13(4), 543-563.

[20] Dworzak, J., Lamecker, H., von Berg, J., Klinder, T., Lorenz, C., Kainmüller, D., ... & Zachow, S. (2010). 3D reconstruction of the human rib cage from 2D projection images using a statistical shape model. International journal of computer assisted radiology and surgery, 5, 111-124.

[21] Paprosky, W. G., Perona, P. G., & Lawrence, J. M. (1994). Acetabular defect classification and surgical reconstruction in revision arthroplasty: a 6-year follow-up evaluation. The Journal of arthroplasty, 9(1), 33-44.

[22] Zachow, S., Lamecker, H., Elsholtz, B., & Stiller, M. (2005, May). Reconstruction of mandibular dysplasia using a statistical 3D shape model. In International congress series (Vol. 1281, pp. 1238-1243). Elsevier.

[23] Meynen, A., Matthews, H., Nauwelaers, N., Claes, P., Mulier, M., & Scheys, L. (2020). Accurate reconstructions of pelvic defects and discontinuities using statistical shape models. Computer methods in biomechanics and biomedical engineering, 23(13), 1026-1033.

[24] Plessers, K., Berghe, P. V., Van Dijck, C., Wirix-Speetjens, R., Debeer, P., Jonkers, I., & Vander Sloten, J. (2018). Virtual reconstruction of glenoid bone defects using a statistical shape model. Journal of shoulder and elbow surgery, 27(1), 160-166.

[25] Klein, K. F. (2015). Use of parametric finite element models to investigate effects of occupant characteristics on lower-extremity injuries in frontal crashes (Doctoral dissertation, University of Michigan).

[26] Zhang, K., Cao, L., Fanta, A., Reed, M. P., Neal, M., Wang, J. T., ... & Hu, J. (2017). An automated method to morph finite element whole-body human models with a wide range of stature and body shape for both men and women. Journal of biomechanics, 60, 253-260.

[27] Fitzpatrick, C. K., Baldwin, M. A., Laz, P. J., FitzPatrick, D. P., Lerner, A. L., & Rullkoetter, P. J. (2011). Development of a statistical shape model of the patellofemoral joint for investigating relationships between shape and function. Journal of biomechanics, 44(13), 2446-2452.

[28] Baldwin, M. A., Langenderfer, J. E., Rullkoetter, P. J., & Laz, P. J. (2010). Development of subject-specific and statistical shape models of the knee using an efficient segmentation and mesh-morphing approach. Computer methods and programs in biomedicine, 97(3), 232-240.

[29] Campbell, J. Q., & Petrella, A. J. (2016). Automated finite element modelling of the lumbar spine: using a statistical shape model to generate a virtual population of models. Journal of biomechanics, 49(13), 2593-2599.

[30] Adeeb, S., & Herzog, W. (2009). Simulation of biological growth. Computer Methods in Biomechanics and Biomedical Engineering, 12(6), 617-626.

[31] Kida, N., & Morishita, Y. (2018). Continuum mechanical modeling of developing epithelial tissues with anisotropic surface growth. Finite Elements in Analysis and Design, 144, 49-60

[32] Wang, Y., Cao, L., Bai, Z., Reed, M. P., Rupp, J. D., Hoff, C. N., & Hu, J. (2016). A parametric ribcage geometry model accounting for variations among the adult population. Journal of biomechanics, 49(13), 2791-2798.

[33] Laga, H., Guo, Y., Tabia, H., Fisher, R. B., & Bennamoun, M. (2018). 3D Shape analysis: fundamentals, theory, and applications. John Wiley & Sons.

[34] Bookstein, F. L., & Green, W. D. (1993, June). Thin-plate spline for deformations with specified derivatives. In Mathematical Methods in Medical Imaging II (Vol. 2035, pp. 14-28). SPIE.

[35] Besl, P. J., & McKay, N. D. (1992, April). Method for registration of 3-D shapes. In Sensor fusion IV: control paradigms and data structures (Vol. 1611, pp. 586-606). Spie.

[36] Tsin, Y., & Kanade, T. (2004). A correlation-based approach to robust point set registration. In Computer Vision-ECCV 2004: 8th European Conference on Computer Vision, Prague, Czech Republic, May 11-14, 2004. Proceedings, Part III 8 (pp. 558-569). Springer Berlin Heidelberg.

[37] Jian, B., & Vemuri, B. C. (2005, October). A robust algorithm for point set registration using mixture of Gaussians. In Tenth IEEE International Conference on Computer Vision (ICCV'05) Volume 1 (Vol. 2, pp. 1246-1251). IEEE.

[38] Myronenko, A., & Song, X. (2010). Point set registration: Coherent point drift. IEEE transactions on pattern analysis and machine intelligence, 32(12), 2262-2275.

[39] Kurki, H. K. (2017). Bilateral asymmetry in the human pelvis. The Anatomical Record, 300(4), 653-665.

[40] Tobolsky, V. A., Kurki, H. K., & Stock, J. T. (2016). Patterns of directional asymmetry in the pelvis and pelvic canal. American Journal of Human Biology, 28(6), 804-810.

[41] Bruzek, J. (2002). A method for visual determination of sex, using the human hip bone. American Journal of Physical Anthropology: The Official Publication of the American Association of Physical Anthropologists, 117(2), 157-168.

[42] Marzola, A., Robilotta, C., Volpe, Y., Governi, L., & Furferi, R. (2021). Statistical Shape Model: comparison between ICP and CPD algorithms on medical applications. International Journal on Interactive Design and Manufacturing (IJIDeM), 15, 85-89.

[43] Saval-Calvo, M., Azorin-Lopez, J., Fuster-Guillo, A., Villena-Martinez, V., & Fisher, R. B. (2018). 3D non-rigid registration using color: color coherent point drift. Computer Vision and Image Understanding, 169, 119-135.

[44] Peng, L., Li, G., Xiao, M., & Xie, L. (2016). Robust CPD algorithm for non-rigid point set registration based on structure information. PloS one, 11(2), e0148483.

[45] Wang, Peng, Ping Wang, ZhiGuo Qu, YingHui Gao, and ZhenKang Shen. "A refined coherent point drift (CPD) algorithm for point set registration." Science China Information Sciences 54 (2011): 2639-2646.

CHAPTER 2: CONSISTENT NUMERICAL IMPLEMENTATION OF HYPOELASTIC CONSTITUTIVE MODELS

This chapter is derived from the published paper:

Palizi, M., Federico, S., & Adeeb, S. (2020). Consistent numerical implementation of hypoelastic constitutive models. Zeitschrift für angewandte Mathematik und Physik, 71, 1-23.

Abstract

In hypoelastic constitutive models, an objective stress rate is related to the rate of deformation through an elasticity tensor. The Truesdell, Jaumann, and Green–Naghdi rates of the Cauchy and Kirchhoff stress tensors are examples of the objective stress rates. The finite element analysis software ABAQUS uses a co-rotational frame which is based on the Jaumann rate for solid elements and on the Green–Naghdi rate for shell and membrane elements. The user subroutine UMAT is the platform to implement a general constitutive model into ABAQUS, but, in order to update the Jacobian matrix DDSDDE in UMAT, the model must be expressed in terms of the Jaumann rate of the Kirchhoff stress tensor. This study aims to formulate and implement various hypoelastic constitutive models into the ABAQUS UMAT subroutine. The developed UMAT subroutine codes are validated using available solutions, and the consequence of using wrong Jacobian matrices is elucidated.

Keywords: hypoelastic constitutive equations; ABAQUS UMAT subroutine; stress array update; Jacobian matrix update

2.1 Introduction

Hypoelasticity is a rate form of elastic material model [1], in which an objective stress rate is linearly related to the rate of deformation by means of a fourth-order elasticity tensor which, in general, is not obtainable from a strain energy density. Originally, Dienes [2] showed that the zero-graded hypoelastic model, i.e. a hypoelastic model with constant isotropic elasticity tensor, exhibits oscillation in simple shear, if it is constructed based on the Jaumann rate of the Cauchy stress. However, zero-graded hypoelastic models which are based on the Truesdell or Green–Naghdi rates do not suffer this problem [3]. We remark that the definition of elements in ABAQUS is based on the Jaumann rate for solid elements [4] and on the Green–Naghdi rate for structural elements (shells, membranes, beams, trusses) [5, 6], as mentioned in the ABAQUS Theory Manual (Section 1.5.3 in [7]).

This study aims to formulate and implement various hypoelastic constitutive models into the ABAQUS UMAT (user material) subroutine. To attain this, it is essential to express the elasticity tensor of the hypoelastic model in terms of the elasticity tensor which relates the Jaumann rate of the Kirchhoff stress tensor to the rate of deformation. According to Pinsky et al. [8], such relations seemed difficult to be constructed for models associated with the Green–Naghdi stress rates;

however, the kinematical relations provided in Mehrabadi and Nemat-Nasser [9] enable us to establish such connections.

The study starts with a review of some basic definitions, the concept of objective rate and the structure of hypoelastic constitutive models. Next, the relations between the elasticity tensors of various hypoelastic models and the elasticity tensor relating the Jaumann rate of the Kirchhoff stress to the rate of deformation are constructed. Next, the formulation behind such UMAT-subroutine variables as the consistent Jacobian (DDSDDE), stress array (STRESS), incremental strain array (DSTRAN), and incremental rotation matrix (DROT) is discussed. The understanding of the formulation is required to properly update the consistent Jacobian and the Cauchy stress in various hypoelastic constitutive models. Various simulations, including simple shear and uniaxial extension, are considered in ABAQUS, and the numerical solutions of the hypoelastic models are validated through the available solutions.

The models considered in this study are zero-graded models based on the Jaumann, Truesdell, and Green–Naghdi rates of the Cauchy and Kirchhoff stress tensors. However, development of UMAT subroutine codes for advanced hypoelastic constitutive equations follows the same steps. As an example of such advanced hypoelastic models, we refer the Reader to the hypoelasticity theory established by Freed [10], later refined in [11], for modelling the passive response of soft biological tissues.

2.2 Theoretical background

The notation follows essentially that traced by Truesdell and Noll [1] and Marsden and Hughes [12], but a simplified treatment in Cartesian coordinates is adopted throughout, following that by Bonet and Wood [13] or Bonet et al. [14], to which we refer the Reader for detailed definitions and proofs.

2.2.1 Basic definitions

The three-dimensional Euclidean space is denoted $\mathcal{S}$ and a material body is identified with a reference configuration $\mathcal{B}$, which is regarded as an open subset of $\mathcal{S}$ [12, 15]. The motion of the body $\mathcal{B}$ is described by the configuration map, which is defined, at each time t, by

$$\phi(.,t): \mathcal{B} \to \mathcal{S}: \boldsymbol{X} \to \boldsymbol{x} = \phi(\boldsymbol{X}, t) \tag{2-1}$$

Where the material point $\boldsymbol{X}$ denotes the position of a particle in the reference configuration $\mathcal{B}$ and the spatial point $\boldsymbol{x} = \phi(\boldsymbol{X}, t)$ is the current placement of point $\boldsymbol{X}$ at time t. The placement or configuration of the body at time t is denoted

$$\mathcal{B}_t \equiv \phi(\mathcal{B}, t) \tag{2-2}$$

The codomain restriction to $\mathcal{B}_t \equiv \phi(\mathcal{B}, t)$ of the configuration map $\phi(.,t)$ is required to be invertible, continuous, and differentiable along with its inverse, i.e. a *diffeomorphism*.

The deformation gradient $\boldsymbol{F}$ is a two-point tensor [12], mapping material vectors $\boldsymbol{M}$ attached at point $\boldsymbol{X}$ into spatial vectors $\boldsymbol{m} = \boldsymbol{FM}$ attached at the spatial point $\boldsymbol{x}$ and is defined, in components, as

$$F_{iJ} = \frac{\partial \phi_i}{\partial X_J} = \phi_{i,J} \tag{2-3}$$

The determinant $J = \det \boldsymbol{F}$ of the deformation gradient $\boldsymbol{F}$ describes the local change of volume and, due to the requirement of invertibility and regularity of ϕ, it must be strictly positive. Cauchy's polar decomposition theorem allows to express the deformation gradient $\boldsymbol{F}$ as

$$\boldsymbol{F} = \boldsymbol{RU} = \boldsymbol{VR} \tag{2-4}$$

Where $\boldsymbol{U}$ and $\boldsymbol{V}$ are symmetric and positive definite tensors and $\boldsymbol{R}$ is a proper orthogonal tensor. Moreover, the right stretch tensor $\boldsymbol{U}$ is completely material, the left stretch tensor $\boldsymbol{V}$ is completely spatial and the rotation tensor $\boldsymbol{R}$ is, like $\boldsymbol{F}$, a two-point tensor. The right and left Cauchy–Green deformation tensors are completely material and completely spatial, respectively, and are defined as

$$\boldsymbol{C} = \boldsymbol{F}^T\boldsymbol{F} = \boldsymbol{U}^2, \boldsymbol{b} = \boldsymbol{F}\boldsymbol{F}^T = \boldsymbol{V}^2 \tag{2-5}$$

The *Eulerian* spatial velocity $\boldsymbol{v}$ is defined as the vector field such that

$$\boldsymbol{v}(\boldsymbol{x}, t) = \boldsymbol{v}(\phi(\boldsymbol{X}, t), t) = \dot{\phi}(\boldsymbol{X}, t) \tag{2-6}$$

where $\dot{\phi}(\boldsymbol{X}, t)$ is the *Lagrangian* spatial velocity at $\boldsymbol{x} = \phi(\boldsymbol{X}, t)$. The gradient of the spatial velocity field $\boldsymbol{v}$ w.r.t. the spatial coordinates x_i, i.e.

$$\boldsymbol{l} = \text{grad}\boldsymbol{v} = \nabla v \tag{2-7}$$

is called the velocity gradient and has components $l_{ij} = v_{i,j}$. The symmetric and skew-symmetric parts of the velocity gradient are the rate of deformation $\boldsymbol{d}$ and the spin or vorticity tensor $\boldsymbol{w}$, respectively:

$$\boldsymbol{d} = \frac{1}{2}(\boldsymbol{l} + \boldsymbol{l}^T), \;\; \boldsymbol{w} = \frac{1}{2}(\boldsymbol{l} - \boldsymbol{l}^T) \tag{2-8}$$

The skew-symmetric tensor

$$\boldsymbol{\Omega} = \dot{\boldsymbol{R}}\boldsymbol{R}^T \tag{2-9}$$

where $\boldsymbol{R}$ is the two-point rotation tensor of the polar decomposition in Eq. (2-4) of $\boldsymbol{F}$, is called *rigid spin* [6]. Its skew-symmetry can be easily shown by taking the time derivative of $\boldsymbol{R}\boldsymbol{R}^T = \boldsymbol{i}$, where $\boldsymbol{i}$ is the spatial identity tensor. It can also be shown that the spin tensor $\boldsymbol{w}$ and the rigid spin tensor $\boldsymbol{\Omega}$ are related by (see, e.g. [13] or [14])

$$\boldsymbol{w} = \boldsymbol{\Omega} + \frac{1}{2}\boldsymbol{R}\left(\dot{\boldsymbol{U}}\boldsymbol{U}^{-1} - \boldsymbol{U}^{-1}\dot{\boldsymbol{U}}\right)\boldsymbol{R}^T \tag{2-10}$$

There are two cases for which $\boldsymbol{w}$ and $\boldsymbol{\Omega}$ coincide. The first case is when the motion is rigid and $\boldsymbol{F} = \boldsymbol{R},\ \boldsymbol{U} = \boldsymbol{I}, \dot{\boldsymbol{U}} = \boldsymbol{0}$ and $\boldsymbol{l} = \boldsymbol{w}$ (or, equivalently, $\boldsymbol{d} = \boldsymbol{0}$). The second case is when the (normalized) eigenvectors of $\boldsymbol{U}$ remain constant during the motion, which implies that $\dot{\boldsymbol{U}}$ has the same eigenvectors and thus *commutes* with $\boldsymbol{U}$.

The fundamental measure of stress in continuum mechanics is the Cauchy stress $\boldsymbol{\sigma}$, which *linearly* relates the unit normal vector $\boldsymbol{n}$ at a point on the boundary $\partial\mathcal{R}_t$ of an arbitrary region

$\mathcal{R}_t \equiv \phi(\mathcal{R}, t)$, subset of the current configuration $\mathcal{B}_t \equiv \phi(\mathcal{B}, t)$, to the corresponding surface traction vector $\boldsymbol{t}_n$, i.e.

$$\boldsymbol{t}_n = \boldsymbol{\sigma n} \tag{2-11}$$

The Cauchy stress $\boldsymbol{\sigma}$ is power-conjugated to the rate of deformation $\boldsymbol{d}$ (or, equivalently, to the velocity gradient $\boldsymbol{l}$), in the sense that the internal power (or deformation power) in an arbitrary region $\mathcal{R}_t$ is given by

$$\mathcal{P}_{int} = \int_{\mathcal{R}_t} \boldsymbol{\sigma}: \boldsymbol{d}\, dv \tag{2-12}$$

Another measure of stress, often employed in numerical applications, is the Kirchhoff stress $\boldsymbol{\tau}$, which is obtained by pulling the integral in Eq. (2-12) on $\mathcal{R}_t$ back to the referential region $\mathcal{R}$, subset of $\mathcal{B}$ by means of the theorem of the change of variables, i.e.

$$\mathcal{P}_{int} = \int_{\mathcal{R}} J\boldsymbol{\sigma}: \boldsymbol{d} dv = \int_{\mathcal{R}} \boldsymbol{\tau}: \boldsymbol{d} dV \tag{2-13}$$

From which we obtain the relation

$$\boldsymbol{\tau} = J\boldsymbol{\sigma} \tag{2-14}$$

2.2.2 Objective stress rates

The principle of material frame indifference states that the constitutive equations must be form-invariant under changes of the frame of reference, i.e. under arbitrary rototranslations [1, 16]. The regular substantial time derivative of a spatial measure of stress, such as the Cauchy stress, is *not* frame-indifferent, as we shall briefly show now. Let us denote the substantial time derivative by a superposed dot, i.e.

$$\dot{\boldsymbol{\sigma}} = \mathrm{D}_t\boldsymbol{\sigma}, \quad \dot{\boldsymbol{\sigma}}_{ij} \equiv \mathrm{D}_t\sigma_{ij} = \sigma_{ij,k}v_k + \partial_t\sigma_{ij} \tag{2-15}$$

Under a spatial rotation $\boldsymbol{Q}$, the stress transforms as

$$\tilde{\boldsymbol{\sigma}} = \boldsymbol{Q}\boldsymbol{\sigma}\boldsymbol{Q}^T \tag{2-16}$$

Therefore, the rate $\dot{\boldsymbol{\sigma}}$ transforms as (see, e.g. [13, 14])

$$\dot{\tilde{\boldsymbol{\sigma}}} = \dot{\boldsymbol{Q}}\boldsymbol{\sigma}\boldsymbol{Q}^T + \boldsymbol{Q}\dot{\boldsymbol{\sigma}}\boldsymbol{Q}^T + \boldsymbol{Q}\boldsymbol{\sigma}\dot{\boldsymbol{Q}}^T \tag{2-17}$$

Which does *not* preserve the form of the transformation in Eq. (2-16). In contrast, it can be shown [13, 14] that the rate of deformation $\boldsymbol{d}$ is frame-indifferent.

Objective stress rates have been introduced precisely to overcome the problem suffered by stress rates and are all essentially based on the use of *Lie derivatives*, as elegantly shown by Marsden and Hughes [12]: the Oldroyd rate is precisely a Lie derivative, the Jaumann rate is a linear combination of Lie derivatives, the Green–Naghdi rate is modelled after a linear combination of Lie derivatives, and finally, the Truesdell rate (of the Cauchy stress) is a Lie

derivative involving the volume form (or volume element). In this work, we use the objective rates below, in the notation of Bonet and Wood [13].

Truesdell Rate of the Cauchy Stress:

$$\boldsymbol{\sigma}^{\circ} = \dot{\boldsymbol{\sigma}} - \boldsymbol{\sigma}\boldsymbol{\ell}^{T} - \boldsymbol{\ell}\boldsymbol{\sigma} + (\mathrm{tr}\boldsymbol{d})\boldsymbol{\sigma} \tag{2-18}$$

Truesdell Rate of the Kirchhoff Stress (also called *Oldroyd rate* [17] and coincident with the Lie derivative of the Kirchhoff stress [13]):

$$\boldsymbol{\tau}^{\circ} = \dot{\boldsymbol{\tau}} - \boldsymbol{\tau}\boldsymbol{\ell}^{T} - \boldsymbol{\ell}\boldsymbol{\tau} \tag{2-19}$$

Jaumann Rate of the Cauchy Stress:

$$\boldsymbol{\sigma}^{\nabla} = \dot{\boldsymbol{\sigma}} + \boldsymbol{\sigma}\boldsymbol{w} - \boldsymbol{w}\boldsymbol{\sigma} \tag{2-20}$$

Jaumann Rate of the Kirchhoff Stress:

$$\boldsymbol{\tau}^{\nabla} = \dot{\boldsymbol{\tau}} + \boldsymbol{\tau}\boldsymbol{w} - \boldsymbol{w}\boldsymbol{\tau} \tag{2-21}$$

Green–Naghdi Rate of the Cauchy Stress:

$$\boldsymbol{\sigma}^{\Delta} = \dot{\boldsymbol{\sigma}} + \boldsymbol{\sigma}\boldsymbol{\Omega} - \boldsymbol{\Omega}\boldsymbol{\sigma} \tag{2-22}$$

Green–Naghdi Rate of the Kirchhoff Stress:

$$\boldsymbol{\tau}^{\Delta} = \dot{\boldsymbol{\tau}} + \boldsymbol{\tau}\boldsymbol{\Omega} - \boldsymbol{\Omega}\boldsymbol{\tau} \tag{2-23}$$

The proof of objectivity and non-objectivity of various kinematic and stress variables can be found in Sections 4.15 and 5.6 of Bonet and Wood [13] or Bonet et al. [14]. A more extensive discussion is provided in Chapter 1, Box 6.1 of the book by Marsden and Hughes [12], who also

make the distinction between objectivity with respect to isometries (i.e. rototranslations), which coincides with frame indifference, and objectivity with respect to diffeomorphisms, which coincides with the condition of *covariance*.

2.2.3 Co-rotational frames

As discussed in Section 2.2.2, the definition of objective rates such as Truesdell, Jaumann, and Green–Naghdi is based on the notion of Lie derivative. Here, we show that, in an appropriate *co-rotational frame*, the components of the Jaumann and Green–Naghdi stress rates can be expressed as the time rate of the components of the stress (see also Section 1.5.3 of ABAQUS Theory Manual [7]).

A time-dependent basis $\{\boldsymbol{e}_\alpha\}_{\alpha=1}^3$ is co-rotational with respect to the spin tensor $\boldsymbol{w}$ if it transforms following Poisson's Theorem locally, i.e. according to the value of the spin tensor $\boldsymbol{w}$ at the point considered:

$$\dot{\boldsymbol{e}}_\alpha = \boldsymbol{w}\boldsymbol{e}_\alpha = \boldsymbol{e}_\alpha \boldsymbol{w}^T = -\boldsymbol{e}_\alpha \boldsymbol{w} \tag{2-24}$$

Considering that $\boldsymbol{w} = w_{\mu\nu}\boldsymbol{e}_\mu \otimes \boldsymbol{e}_\nu$ and using the properties of the tensor product, Eq. (2-24) reads

$$\dot{\boldsymbol{e}}_\alpha = w_{\mu\nu}\big(\boldsymbol{e}_\mu \otimes \boldsymbol{e}_\nu\big)\boldsymbol{e}_\alpha = w_{\mu\alpha}\boldsymbol{e}_\mu = -w_{\alpha\mu}\boldsymbol{e}_\mu \tag{2-25}$$

In this $\boldsymbol{w}$-co-rotational frame, the Cauchy stress $\boldsymbol{\sigma}$ (exactly the same considerations can be made for the Kirchhoff stress $\boldsymbol{\tau}$) reads

$$\boldsymbol{\sigma} = \sigma_{\alpha\beta}\boldsymbol{e}_\alpha \otimes \boldsymbol{e}_\beta \tag{2-26}$$

And thus its substantial time derivative is

$$\begin{aligned}\dot{\boldsymbol{\sigma}} &\equiv \left(\sigma_{\alpha\beta}\boldsymbol{e}_\alpha \otimes \boldsymbol{e}_\beta\right)^{\cdot} \\ &= \dot{\sigma}_{\alpha\beta}\boldsymbol{e}_\alpha \otimes \boldsymbol{e}_\beta + \sigma_{\alpha\beta}\dot{\boldsymbol{e}}_\alpha \otimes \boldsymbol{e}_\beta + \sigma_{\alpha\beta}\boldsymbol{e}_\alpha \otimes \dot{\boldsymbol{e}}_\beta \\ &= \dot{\sigma}_{\alpha\beta}\boldsymbol{e}_\alpha \otimes \boldsymbol{e}_\beta + \sigma_{\alpha\beta}\left(w_{\mu\alpha}\boldsymbol{e}_\mu\right) \otimes \boldsymbol{e}_\beta + \sigma_{\alpha\beta}\boldsymbol{e}_\alpha \otimes \left(-w_{\beta\nu}\boldsymbol{e}_\nu\right) \\ &= \dot{\sigma}_{\alpha\beta}\boldsymbol{e}_\alpha \otimes \boldsymbol{e}_\beta + w_{\mu\alpha}\sigma_{\alpha\beta}\boldsymbol{e}_\mu \otimes \boldsymbol{e}_\beta - \sigma_{\alpha\beta}w_{\beta\nu}\boldsymbol{e}_\alpha \otimes \boldsymbol{e}_\nu\end{aligned} \tag{2-27}$$

where we used Eq. (2-25). Switching indices μ and α in the second term and ν and β in the third term, we have

$$\left(\sigma_{\alpha\beta}\boldsymbol{e}_\alpha \otimes \boldsymbol{e}_\beta\right)^{\cdot} = \dot{\sigma}_{\alpha\beta}\boldsymbol{e}_\alpha \otimes \boldsymbol{e}_\beta + w_{\alpha\mu}\sigma_{\mu\beta}\boldsymbol{e}_\alpha \otimes \boldsymbol{e}_\beta - \sigma_{\alpha\nu}w_{\nu\beta}\boldsymbol{e}_\alpha \otimes \boldsymbol{e}_\beta \tag{2-28}$$

And, solving for $\dot{\sigma}_{\alpha\beta}\boldsymbol{e}_\alpha \otimes \boldsymbol{e}_\beta$, we obtain

$$\dot{\sigma}_{\alpha\beta}\boldsymbol{e}_\alpha \otimes \boldsymbol{e}_\beta = \left(\sigma_{\alpha\beta}\boldsymbol{e}_\alpha \otimes \boldsymbol{e}_\beta\right)^{\cdot} + \sigma_{\alpha\nu}w_{\nu\beta}\boldsymbol{e}_\alpha \otimes \boldsymbol{e}_\beta - w_{\alpha\mu}\sigma_{\mu\beta}\boldsymbol{e}_\alpha \otimes \boldsymbol{e}_\beta \tag{2-29}$$

On the right-hand side of Eq. (2-29), we recognize the Jaumann rate of the Cauchy stress, i.e.

$$\begin{aligned}\boldsymbol{\sigma}^{\nabla} &= \left(\boldsymbol{\sigma}^{\nabla}\right)_{\alpha\beta}\boldsymbol{e}_\alpha \otimes \boldsymbol{e}_\beta \\ &= \left(\sigma_{\alpha\beta}\boldsymbol{e}_\alpha \otimes \boldsymbol{e}_\beta\right)^{\cdot} + \sigma_{\alpha\nu}w_{\nu\beta}\boldsymbol{e}_\alpha \otimes \boldsymbol{e}_\beta - w_{\alpha\mu}\sigma_{\mu\beta}\boldsymbol{e}_\alpha \otimes \boldsymbol{e}_\beta\end{aligned} \tag{2-30}$$

Therefore, comparing Eq. (2-29) and Eq. (2-30), we finally obtain that, in this $\boldsymbol{w}$-co-rotational basis, the components of the Jaumann rate are equal to the (substantial) time derivatives of the components of the stress, i.e.

$$(\boldsymbol{\sigma}^{\nabla})_{\alpha\beta} = \dot{\sigma}_{\alpha\beta} \tag{2-31}$$

Analogously, if we define a basis $\{\boldsymbol{e}_\alpha\}_{\alpha=1}^{3}$ that is co-rotational with respect to the rigid spin tensor $\boldsymbol{\Omega}$, in the sense that

$$\dot{\boldsymbol{e}}_\alpha = \boldsymbol{\Omega}\boldsymbol{e}_\alpha = \boldsymbol{e}_\alpha\boldsymbol{\Omega}^T = -\boldsymbol{e}_\alpha\boldsymbol{\Omega} \tag{2-32}$$

We can show that, in this $\boldsymbol{\Omega}$-co-rotational basis, the components of the Green–Naghdi rate equal the (substantial) time derivatives of the components of the stress, i.e.

$$(\boldsymbol{\sigma}^{\Delta})_{\alpha\beta} = \dot{\sigma}_{\alpha\beta} \tag{2-33}$$

2.2.4 Linearization of the deformation

Linearization is essential in finite element formulations [13]. The linearization of the deformation about a specific configuration map $\boldsymbol{\phi}$ entails the evaluation of the deformation gradient $\boldsymbol{F}$ and of all derived quantities, after a *perturbation* is applied to $\boldsymbol{\phi}$. We call this perturbation an *infinitesimal displacement*, which we denote $\delta\boldsymbol{u}$ when seen as a function of the material point $\boldsymbol{X}$ and $\delta\boldsymbol{u}$ when seen as a function of the spatial point $\boldsymbol{x}$, i.e.

$$(\delta\boldsymbol{u})(\boldsymbol{X}, t) = (\delta\boldsymbol{u})(\boldsymbol{x}, t) \tag{2-34}$$

The perturbed configuration map is thus

$$\breve{\phi}(\boldsymbol{X},t) = \phi(\boldsymbol{X},t) + (\delta\boldsymbol{u})(\boldsymbol{X},t) \tag{2-35}$$

The deformation gradient of the perturbed configuration map $\breve{\phi}$ is given by (see Section 4.2 in the book by Marsden and Hughes [12])

$$\breve{\boldsymbol{F}}(\boldsymbol{X},t) = \boldsymbol{F}(\boldsymbol{X},t) + \nabla(\delta\boldsymbol{u})(\boldsymbol{X},t) \tag{2-36}$$

Where $\boldsymbol{F}$ is the deformation gradient of the unperturbed ϕ and we recall that the large nabla, ∇ denotes the gradient performed with respect to the referential coordinates X_I. It is helpful to express in Eq. (2-36) as a multiplicative decomposition [19]. Indeed, by definition of inverse, we have

$$\breve{\boldsymbol{F}}(\boldsymbol{X},t) = [\boldsymbol{i} + \overline{\nabla}(\delta\boldsymbol{u})(\boldsymbol{X},t)\boldsymbol{F}^{-1}(\boldsymbol{x},t)]\boldsymbol{F}(\boldsymbol{X},t) \tag{2-37}$$

Then, the transformation rule for the gradient states that

$$\overline{\nabla}(\delta\boldsymbol{u})(x,t) = \nabla(\delta\boldsymbol{u})(\boldsymbol{X},t)\boldsymbol{F}^{-1}(\boldsymbol{x},t) \tag{2-38}$$

Where we recall that the small nabla, $\overline{\nabla}$ denotes the gradient with respect to the spatial coordinates x_i. Therefore, we can write Eq. (2-37) as

$$\breve{\boldsymbol{F}}(\boldsymbol{X},t) = [\boldsymbol{i} + \overline{\nabla}(\delta\boldsymbol{u})(x,t)]\boldsymbol{F}(\boldsymbol{X},t) \tag{2-39}$$

where

$$(\delta\boldsymbol{F})(\boldsymbol{x},t) = \boldsymbol{i} + \overline{\nabla}(\delta\boldsymbol{u})(x,t) \tag{2-40}$$

is the deformation gradient mapping from the configuration $\mathcal{B}_t = \phi(\mathcal{B}, t)$ to the perturbed configuration $\breve{\mathcal{B}}_t = \breve{\phi}(\mathcal{B}, t)$. Finally, the multiplicative decomposition equivalent to Eq. (2-36) is given by Eq. (2-39) and Eq. (2-40) as

$$\breve{\boldsymbol{F}}(\boldsymbol{X}, t) = (\delta \boldsymbol{F})(\boldsymbol{x}, t)\boldsymbol{F}(\boldsymbol{X}, t) \tag{2-41}$$

In the following, we shall need to perform the linearization *in time*, i.e. considering the *relative infinitesimal displacement* between the configuration $\mathcal{B}_t = \phi(\mathcal{B}, t)$ at time t and the configuration $\mathcal{B}_s = \phi(\mathcal{B}, s)$ at time $s > t$. In this case, the perturbed configuration map $\breve{\phi}$ and the perturbed deformation gradient $\breve{\boldsymbol{F}}$ are replaced by the configuration map $\phi(., s)$ and deformation gradient $\boldsymbol{F}(., s)$ at time $s > t$. Thus, we have

$$\phi(\boldsymbol{X}, s) = \phi(\boldsymbol{X}, t) + (\delta \boldsymbol{u})_s(\boldsymbol{X}, t) \tag{2-42}$$

and

$$\boldsymbol{F}(\boldsymbol{X}, s) = \boldsymbol{F}(\boldsymbol{X}, t) + \nabla(\delta \boldsymbol{u})_s(\boldsymbol{X}, t) \tag{2-43}$$

where the subscript s emphasizes that the relative displacement $(\delta \boldsymbol{u})_s(\boldsymbol{X}, t) = \phi(X, s) - \phi(X, t)$ points to $\phi(X, s)$. Passages analogous to those seen above yield

$$\boldsymbol{F}(\boldsymbol{X}, s) = (\delta \boldsymbol{F})_s(\boldsymbol{x}, t)\boldsymbol{F}(\boldsymbol{X}, t) \tag{2-44}$$

where the *relative deformation gradient* $(\delta \boldsymbol{F})_s(\boldsymbol{x}, t)$ is given by

$$(\delta \boldsymbol{F})_s(\boldsymbol{x}, t) = \boldsymbol{i} + \overline{\nabla}(\delta \boldsymbol{u})_s(\boldsymbol{x}, t) \tag{2-45}$$

We note that this treatment is based on the concept of *relative deformation*, for which we refer the Reader to the treatise by Eringen [20].

2.2.5 Hypoelasticity

Hypoelasticity describes a class of elastic materials defined in rate-form. Truesdell and Noll [1] proved that the general forms of hypoelastic constitutive equations must be given by

$$\boldsymbol{s}^{\blacksquare} = \mathbb{c}\colon \boldsymbol{d} \tag{2-46}$$

where $\boldsymbol{s}^{\blacksquare}$ is an objective rate of a stress tensor $\boldsymbol{s}$, which could be either the Cauchy stress $\boldsymbol{\sigma}$ or the Kirchhoff stress $\boldsymbol{\tau}$, $\boldsymbol{d}$ is the rate of deformation and $\mathbb{c}$ is the fourth-order elasticity tensor, which, in general, depends on the stress $\boldsymbol{s}$, i.e. $\mathbb{c} = \hat{\mathbb{c}}(\boldsymbol{s})$.

As mentioned in section 2.1, in this study, the hypoelastic constitutive equations are assumed to be zero-graded, which means that the fourth-order elasticity tensor $\mathbb{c}$ is isotropic and independent of the stress, i.e. can be expressed as

$$\mathbb{c} = \mathbb{c}^0 = \lambda \boldsymbol{i} \otimes \boldsymbol{i} + 2\mu \boldsymbol{i} \,\underline{\overline{\otimes}}\, \boldsymbol{i} \tag{2-47}$$

where the superscript zero stands for zero-graded material, λ and μ are Lame's constants, $\boldsymbol{i}$ is the spatial identity tensor with components δ_{ij} (the Kronecker delta), and the special tensor product $\underline{\overline{\otimes}}$ is defined by Curnier et al. [21] and is such that the component representation of Eq. (2-47) is

$$c_{ijkl} = c^0_{ijkl} = \lambda \delta_{ij}\delta_{kl} + 2\mu \left[\frac{1}{2}\left(\delta_{ik}\delta_{jl} + \delta_{il}\delta_{jk}\right)\right] \tag{2-48}$$

Given the Young's modulus E and the Poisson's ratio ν, the Lame's constants can be calculated via the well-known relations

$$\lambda = \frac{E\nu}{(1+\nu)(1-2\nu)}, \quad \mu = \frac{E}{2(1+\nu)} \tag{2-49}$$

2.3 Hypoelasticity in ABAQUS user subroutine UMAT

A clear understanding of variables provided by the UMAT subroutine is essential to properly implement constitutive models into ABAQUS. In this section, we shall discuss the essential theoretical and numerical aspects of the UMAT-subroutine variables. It should be noted that, also for the case of a *hyperelastic* material, which is described by a strain energy density, the Jacobian matrix of the UMAT subroutine DDSDDE should be updated based on a particular rate-form equation. In this sense, the treatment below holds for both hyperelastic and hypoelastic models.

2.3.1 UMAT-subroutine variable DDSDDE

Based on Section 1.1.44 of ABAQUS User Subroutines Reference Guide [7], in order to implement a hyperelastic material, for which the Cauchy stress tensor is explicitly expressed in terms of the deformation gradient and other kinematic variables, it is necessary to evaluate the *consistent Jacobian matrix* DDSDDE. This is defined as the matrix representing the fourth-order tensor $\mathbb{D}$ featuring in the expression

$$\dot{\boldsymbol{\tau}} = J(\mathbb{D}:\boldsymbol{d} - \boldsymbol{\sigma w} + \boldsymbol{w\sigma}) \tag{2-50}$$

Eq. (2-50) can be promptly justified by using the definition (14) of Kirchhoff stress $\boldsymbol{\tau}$ to eliminate the Cauchy stress $\boldsymbol{\sigma}$ and the definition in Eq. (2-21) of Jaumann rate $\boldsymbol{\tau}^{\nabla}$of the Kirchhoff stress, i.e.

$$\boldsymbol{\tau}^{\nabla} = J\mathbb{D}\colon \boldsymbol{d} \tag{2-51}$$

If we define $\mathbb{c}^{\boldsymbol{\tau}^{\nabla}}$ as the fourth-order tensor relating $\boldsymbol{\tau}^{\nabla}$ to $\boldsymbol{d}$, i.e.

$$\boldsymbol{\tau}^{\nabla} = \mathbb{c}^{\boldsymbol{\tau}^{\nabla}}\colon \boldsymbol{d} \tag{2-52}$$

Comparison of Eq. (2-51) and Eq. (2-52) yields

$$\mathbb{D} = J^{-1}\mathbb{c}^{\boldsymbol{\tau}^{\nabla}} \tag{2-53}$$

A similar formulation is employed for the Jacobian matrix in hypoelastic materials, i.e. for rate-form constitutive models. As we shall show later in Section 2.4, the employment of the consistent Jacobian matrix DDSDDE based on Eq. (2-53) results in convergence, while other Jacobian matrices may give rise to slow convergence [6, 22] or even divergence. In order to implement a hypoelastic model into UMAT subroutine, it is essential to relate the elasticity tensor of the hypoelastic model to the fourth-order tensor $\mathbb{D}$ of Eq. (2-53), represented by the consistent Jacobian matrix DDSDDE. Below, we report the tensor $\mathbb{D}$ that must be used for each choice of hypoelastic formulation (proofs and UMAT implementations are provided in Appendix A).

Truesdell Rate of the Cauchy Stress:

$$\mathbb{D}_{ijkl} = \mathbb{c}^{\sigma^{\circ}}_{ijkl} + \sigma_{ik}\delta_{jl} + \sigma_{jl}\delta_{ik} \tag{2-54}$$

Truesdell Rate of the Kirchhoff Stress:

$$\mathbb{D}_{ijkl} = J^{-1}\mathbb{c}^{\tau^{\circ}}_{ijkl} + \sigma_{ik}\delta_{jl} + \sigma_{jl}\delta_{ik} \tag{2-55}$$

Jaumann Rate of the Cauchy Stress:

$$\mathbb{D}_{ijkl} = \mathbb{c}^{\sigma^{\nabla}}_{ijkl} + \sigma_{ij}\delta_{kl} \tag{2-56}$$

Jaumann Rate of the Kirchhoff Stress, i.e. the point of departure, Eq. (2-53):

$$\mathbb{D}_{ijkl} = J^{-1}\mathbb{c}^{\tau^{\nabla}}_{ijkl} \tag{2-57}$$

Green–Naghdi Rate of the Cauchy Stress:

$$\mathbb{D}_{ijkl} = \mathbb{c}^{\sigma^{\Delta}}_{ijkl} - B_{mjkl}\sigma_{im} + B_{imkl}\sigma_{jm} + \sigma_{ij}\delta_{kl} \tag{2-58}$$

Green–Naghdi Rate of the Kirchhoff Stress:

$$\mathbb{D}_{ijkl} = J^{-1}\mathbb{c}^{\tau^{\Delta}}_{ijkl} - B_{mjkl}\sigma_{im} + B_{imkl}\sigma_{jm} \tag{2-59}$$

In the expressions above, we used

$$B_{ijkl} = \sum_{\alpha,\beta=1}^{3} \frac{\lambda_\beta - \lambda_\alpha}{\lambda_\beta + \lambda_\alpha} (\boldsymbol{b}_\alpha)_{ik} (\boldsymbol{b}_\alpha)_{jl} \tag{2-60}$$

where λ_α are the principal stretches (eigenvalues of the left-stretch tensor $\boldsymbol{V}$, so that λ_α^2 are the eigenvalues of the left Cauchy–Green deformation $\boldsymbol{b}$), and

$$\boldsymbol{b}_\alpha = \prod_{\beta=1,\beta\neq\alpha}^{3} \frac{\boldsymbol{b} - \lambda_\beta^2 \boldsymbol{i}}{\lambda_\alpha^2 - \lambda_\beta^2} \tag{2-61}$$

Are the eigenprojections of the left Cauchy–Green deformation $\boldsymbol{b}$, with $\boldsymbol{i}$ being the spatial second-order identity tensor, as seen earlier. The proof of Eq. (2-54), Eq. (2-55), and Eq. (2-56)

can also be found in Wooseok et al. [23] and the proof of Eq. (2-58) and Eq. (2-59) is based on the relation.

$$\boldsymbol{\Omega} = \boldsymbol{w} + \sum_{\alpha,\beta=1}^{3} \frac{\lambda_\beta - \lambda_\alpha}{\lambda_\beta + \lambda_\alpha} \boldsymbol{b}_\alpha \boldsymbol{d}\boldsymbol{b}_\beta \tag{2-62}$$

The derivation of which can be found in Mehrabadi and Nemat-Nasser [9], and also Zhou and Tamma [24].

2.3.2 UMAT-subroutine variables DSTRAN and DROT

The UMAT-subroutine variables DSTRAN and DROT contain the components of the incremental strain and incremental rotation, respectively, between the configuration $\mathcal{B}_n = \phi(\mathcal{B}, t_n)$ at time t_n and the configuration $\mathcal{B}_{n+\frac{1}{2}} = \phi\left(\mathcal{B} + t_{n+\frac{1}{2}}\right)$ at time t_{n+1}.

The incremental deformation is evaluated following the procedure outlined in Section 2.2.4 and employs a midpoint formula [25] considering the configuration $\mathcal{B}_{n+\frac{1}{2}} = \phi\left(\mathcal{B}, t_{n+\frac{1}{2}}\right)$ at time.

$$t_{n+\frac{1}{2}} = t_n + \frac{1}{2}(\delta t)_n = t_n + \frac{1}{2}(t_{n+1} - t_n) \tag{2-63}$$

where t_n is the time at the beginning of the increment and $(\delta t)_n = t_{n+1} - t_n$ is the increment from t_n to t_{n+1}. Our goal here is to determine the relative displacement gradient, the midpoint displacement gradient, the midpoint velocity, and the midpoint velocity gradient. From the

midpoint deformation rate, symmetric part of the midpoint velocity gradient, we shall derive the incremental strain DSTRAN.

The deformation gradient at time t_{n+1} is obtained as a function of the relative deformation gradient and of the deformation gradient at time t_n, following Eq. (2-44), as

$$\boldsymbol{F}(\boldsymbol{X}, t_{n+1}) = (\delta \boldsymbol{F})_{n+1}(\boldsymbol{x}, t_n)\boldsymbol{F}(\boldsymbol{X}, t_n) \tag{2-64}$$

With the relative deformation gradient as in Eq. (2-45), i.e.

$$(\delta \boldsymbol{F})_{n+1}(\boldsymbol{x}, t_n) = \boldsymbol{i} + \nabla(\delta \boldsymbol{u})_{n+1}(x, t_n) \tag{2-65}$$

where we use the subscript $n+1$ in place of t_{n+1} in $(\delta \boldsymbol{F})_{n+1}(\boldsymbol{x}, t_n)$ and $(\delta \boldsymbol{u})_{n+1}(\boldsymbol{x}, t_n)$.

Now, we approximate the displacement between t_n and $t_{n+\frac{1}{2}}$ as *half* the displacement between t_n and t_{n+1}:

$$\begin{aligned}(\delta \boldsymbol{u})_{n+\frac{1}{2}}(\boldsymbol{x}, t_n) &= \phi\left(\boldsymbol{X}, t_{n+\frac{1}{2}}\right) - \phi(\boldsymbol{X}, t_n) \\ &\simeq \frac{1}{2}(\delta \boldsymbol{u})_{n+1}(\boldsymbol{x}, t_n) = \frac{1}{2}[\phi(\boldsymbol{X}, t_{n+1}) - \phi(\boldsymbol{X}, t_n)].\end{aligned} \tag{2-66}$$

Using again Eq. (2-45) for the relative deformation gradient between t_n to $t_{n+\frac{1}{2}}$ with the displacement in Eq. (2-66), we have

$$(\delta \boldsymbol{F})_{n+\frac{1}{2}}(\boldsymbol{x}, t_n) = \boldsymbol{i} + \frac{1}{2}\overline{\nabla}(\delta \boldsymbol{u})_{n+1}(\boldsymbol{x}, t_n) \tag{2-67}$$

Which, together with Eq. (2-65), yields the alternative expression

$$(\delta \boldsymbol{F})_{n+\frac{1}{2}}(\boldsymbol{x}, t_n) = \frac{1}{2}[\boldsymbol{i} + (\delta \boldsymbol{F})_{n+1}(\boldsymbol{x}, t_n)]. \tag{2-68}$$

Similarly, we approximate the displacement between $t_{n+\frac{1}{2}}$ and t_{n+1} as

$$\begin{aligned}(\delta \boldsymbol{u})_{n+1}\left(\boldsymbol{x}', t_{n+\frac{1}{2}}\right) &= \boldsymbol{\phi}(\boldsymbol{X}, t_{n+1}) - \boldsymbol{\phi}\left(\boldsymbol{X}, t_{n+\frac{1}{2}}\right) \\ &\simeq \frac{1}{2}(\delta \boldsymbol{u})_{n+1}(\boldsymbol{x}, t_n) = \frac{1}{2}[\boldsymbol{\phi}(\boldsymbol{X}, t_{n+1}) - \boldsymbol{\phi}(\boldsymbol{X}, t_n)],\end{aligned} \tag{2-69}$$

where $x' = \boldsymbol{\phi}\left(\boldsymbol{X}, t_{n+\frac{1}{2}}\right)$ and it is understood that the displacement $\frac{1}{2}(\delta \boldsymbol{u})_{n+1}(\boldsymbol{x}, t_n)$ must be *parallel translated* from $x = \boldsymbol{\phi}(X, t_n)$ to $x' = \boldsymbol{\phi}\left(X, t_{n+\frac{1}{2}}\right)$. The corresponding incremental deformation gradient is

$$(\delta \boldsymbol{F})_{n+1}\left(\boldsymbol{x}', t_{n+\frac{1}{2}}\right) = \boldsymbol{i} + \frac{1}{2}\overline{\nabla}'(\delta \boldsymbol{u})_{n+1}(\boldsymbol{x}, t_n) \tag{2-70}$$

where $\overline{\nabla}'$ denotes the gradient operator at $\boldsymbol{x}' = \boldsymbol{\phi}\left(\boldsymbol{X}, t_{n+\frac{1}{2}}\right)$, as opposed to the gradient operator $\overline{\nabla}$ at $\boldsymbol{x} = \boldsymbol{\phi}(\boldsymbol{X}, t_n)$.

Using the incremental deformation gradients $(\delta \boldsymbol{F})_{n+1}(\boldsymbol{x}, t_n)$ and $(\delta \boldsymbol{F})_{n+1}\left(\boldsymbol{x}', t_{n+\frac{1}{2}}\right)$, we can write the multiplicative decomposition

$$\boldsymbol{F}(\boldsymbol{X}, t_{n+1}) = (\delta \boldsymbol{F})_{n+1}\left(\boldsymbol{x}', t_{n+\frac{1}{2}}\right)(\delta \boldsymbol{F})_{n+\frac{1}{2}}(\boldsymbol{x}, t_n)\boldsymbol{F}(\boldsymbol{X}, t_n), \tag{2-71}$$

Which, comparing with Eq. (2-64) and using Eq. (2-67) and Eq. (2-70), yields

$$(\delta \boldsymbol{F})_{n+1}(\boldsymbol{x}, t_n) = (\delta \boldsymbol{F})_{n+1}\left(\boldsymbol{x}', t_{n+\frac{1}{2}}\right)(\delta \boldsymbol{F})_{n+\frac{1}{2}}(\boldsymbol{x}, t_n)$$

$$= \left[\boldsymbol{i} + \frac{1}{2}\overline{\nabla}'(\delta \boldsymbol{u})_{n+1}(\boldsymbol{x}, t_n)\right]\left[\boldsymbol{i} + \frac{1}{2}\overline{\nabla}(\delta \boldsymbol{u})_{n+1}(\boldsymbol{x}, t_n)\right] \tag{2-72}$$

The midpoint displacement gradient $\overline{\nabla}'(\delta \boldsymbol{u})_{n+1}(\boldsymbol{x}, t_n)$ is evaluated from Eq. (2-72), considering Eq. (2-68), as

$$\nabla'(\delta \boldsymbol{u})_{n+1}(\boldsymbol{x}, t_n) = 4(\delta \boldsymbol{F})_{n+1}(\boldsymbol{x}, t_n)[i + (\delta \boldsymbol{F})_{n+1}(\boldsymbol{x}, t_n)]^{-1} - 2\boldsymbol{i} \tag{2-73}$$

The velocity in the configuration $\mathbb{B}_{n+\frac{1}{2}}$ is approximated by the midpoint discrete derivative

$$\boldsymbol{v}\left(\boldsymbol{x}', t_{n+\frac{1}{2}}\right) = \dot{\boldsymbol{\phi}}\left(\boldsymbol{X}, t_{n+\frac{1}{2}}\right) \simeq \frac{\boldsymbol{\phi}(\boldsymbol{X}, t_{n+1}) - \boldsymbol{\phi}(\boldsymbol{X}, t_n)}{(\delta t)_n} = \frac{\delta \boldsymbol{u}_{n+1}(\boldsymbol{x}, t_n)}{(\delta t)_n}, \tag{2-74}$$

where, again, the parallel translation from $x = \boldsymbol{\phi}(X, t_n)$ to $x' = \boldsymbol{\phi}\left(X, t_{n+\frac{1}{2}}\right)$ is understood. Based on this approximation, the velocity gradient in the midpoint configuration $\mathbb{B}_{n+\frac{1}{2}}$ is given by

$$\boldsymbol{\ell}\left(\boldsymbol{x}', t_{n+\frac{1}{2}}\right) = \overline{\nabla}'\boldsymbol{v}\left(\boldsymbol{x}', t_{n+\frac{1}{2}}\right) \simeq \frac{1}{(\delta t)_n}\overline{\nabla}'(\delta \boldsymbol{u})_{n+1}(\boldsymbol{x}, t_n), \tag{2-75}$$

With $\nabla'(\delta \boldsymbol{u})_{n+1}(\boldsymbol{x}, t_n)$ given by Eq. (2-73). The corresponding deformation rate and spin are

$$\boldsymbol{d}\left(\boldsymbol{x}', t_{n+\frac{1}{2}}\right) \simeq \frac{1}{2(\delta t)_n}[\nabla'(\delta \boldsymbol{u})_{n+1}(\boldsymbol{x}, t_n) + [\nabla'(\delta \boldsymbol{u})_{n+1}]^T(\boldsymbol{x}, t_n)], \tag{2-76 a}$$

$$\boldsymbol{w}\left(\boldsymbol{x}', t_{n+\frac{1}{2}}\right) \simeq \frac{1}{2(\delta t)_n}[\nabla'(\delta \boldsymbol{u})_{n+1}(\boldsymbol{x}, t_n) - [\nabla'(\delta \boldsymbol{u})_{n+1}]^T(\boldsymbol{x}, t_n)]. \tag{2-76 b}$$

The infinitesimal strain increment $\delta\epsilon_n$ is the tensor corresponding to the UMAT-subroutine variable DSTRAN and is obtained from the midpoint deformation rate (2-76a) by multiplying by the time increment $(\delta t)_n$:

$$\delta\boldsymbol{\epsilon}_n \equiv \boldsymbol{d}\left(\boldsymbol{x}', t_{n+\frac{1}{2}}\right)(\delta t)_n = \frac{1}{2}[\nabla'(\delta\boldsymbol{u})_{n+1}(\boldsymbol{x}, t_n) + [\nabla'(\delta\boldsymbol{u})_{n+1}]^T(\boldsymbol{x}, t_n)] \qquad (2\text{-}77)$$

The midpoint spin Eq. (2-76 b) is instead used to calculate the incremental rotation tensor $\boldsymbol{Q}_n$ corresponding to the UMAT-subroutine variable DROT, according to the Hughes–Winget algorithm (see Hughes and Winget [26] and Section 14.10.6 of Neto et al. [25]), as

$$\boldsymbol{Q}_n \equiv \left[\boldsymbol{i} - \frac{1}{2}(\delta t)_n \boldsymbol{w}\left(\boldsymbol{x}', t_{n+\frac{1}{2}}\right)\right]^{-1}\left[\boldsymbol{i} + \frac{1}{2}(\delta t)_n \boldsymbol{w}\left(\boldsymbol{x}', t_{n+\frac{1}{2}}\right)\right], \qquad (2\text{-}78)$$

The usage of which will be explained in the Section 2.3.3.

2.3.3 UMAT-subroutine variable STRESS

The stress array STRESS is the key UMAT-subroutine variable that provides the user with the components of the Cauchy stress tensor at the beginning of an increment. The user is, then, required to update the STRESS array with the components of the Cauchy stress tensor at the end of the increment. In some cases, such as that of hyperelastic constitutive models, the user can easily utilize the deformation gradient at the end of the increment, i.e. UMAT-subroutine variable DFGRD1, to calculate the Cauchy stress components. However, for rate-dependent constitutive equations, updating the STRESS array requires careful consideration on part of the user.

ABAQUS uses the *Hughes–Winget algorithm* to integrate the rate-form constitutive equations and update the STRESS array (see Section 3.2.2 of ABAQUS Theory Manual [7]). Based on the Hughes–Winget algorithm, the stress update reads [26]

$$\boldsymbol{\sigma}_{n+1} = \boldsymbol{Q}_n \boldsymbol{\sigma}_n \boldsymbol{Q}_n^T + \mathbb{c}_n^{\sigma^\nabla} : \delta \boldsymbol{\varepsilon}_n, \tag{2-79}$$

where $\boldsymbol{\sigma}_n$ and $\boldsymbol{\sigma}_{n+1}$ are the Cauchy stress tensor at time t_n and t_{n+1}, respectively, $\boldsymbol{Q}_n$ is the incremental rotation tensor and $\mathbb{c}_n^{\sigma^\nabla}$ is the elasticity tensor relating the Jaumann rate $\boldsymbol{\sigma}^\nabla$ of the Cauchy stress to the rate of deformation $\boldsymbol{d}$ (see Eq. (A-14)). By defining

$$\tilde{\boldsymbol{\sigma}}_n = \boldsymbol{Q}_n \boldsymbol{\sigma}_n \boldsymbol{Q}_n^T, \tag{2-80}$$

We can write Eq. (2-79) in the form

$$\boldsymbol{\sigma}_{n+1} = \tilde{\boldsymbol{\sigma}}_n + \mathbb{c}_n^{\sigma^\nabla} : \delta \boldsymbol{\varepsilon}_n. \tag{2-81}$$

The tensor $\tilde{\boldsymbol{\sigma}}_n$ is the quantity corresponding to the UMAT-subroutine variable STRESS (see Section 1.1.44 of the ABAQUS User Subroutines Reference Guide [7]). Based on Eq. (2-56), relating $\mathbb{c}_n^{\sigma^\nabla}$ to the consistent Jacobian $\mathbb{D}$, we have

$$\mathbb{c}_n^{\sigma^\nabla} = \mathbb{D}_n - \boldsymbol{\sigma}_n \otimes \boldsymbol{i}, \ \left(\mathbb{c}_n^{\sigma^\nabla}\right)_{ijkl} = (\mathbb{D}_n)_{ijkl} - (\boldsymbol{\sigma}_n)_{ij}\delta_{kl}, \tag{2-82}$$

Where $\mathbb{D}_n$ and $\boldsymbol{\sigma}_n$ are the consistent Jacobian and the stress at the beginning of step n, respectively. Using Eq. (2-82), we can write Eq. (2-81) in terms of $\mathbb{D}_n$ as

$$\boldsymbol{\sigma}_{n+1} = \tilde{\boldsymbol{\sigma}}_n + (\mathbb{D}_n - \boldsymbol{\sigma}_n \otimes \boldsymbol{i}) : \delta \boldsymbol{\epsilon}_n. \tag{2-83}$$

The form of the consistent Jacobian $\mathbb{D}_n$ depends on the selected hypoelastic model, see Eq. (2-54) to Eq. (2-59).

2.4 Results and discussion

Four simulations are performed in ABAQUS to validate the update procedure of the Cauchy stress array STRESS and the Jacobian matrix DDSDDE for the hypoelastic constitutive equations. Each model consists of only one eight-node brick element C3D8 with unit dimensions $L = 1$ (Figure 2-1). The models are divided into *displacement-based models* and *force-based models*. The displacement-based models are used to check the correctness of the updated Cauchy stress tensor. In these models, the iterative procedure is not involved and, thus, the Jacobian matrix does not affect the material response. In contrast, in the force-based models, the implementation of the correct Jacobian matrix plays a crucial part in the convergence of the analysis. Employing the force-based models serves to validate the Jacobian matrices used in the hypoelastic constitutive equations and to show the consequences of using a Jacobian matrix that does not correspond to that required by the element type (for solid elements, that related to the Jaumann rate).

In ABAQUS, the Static-General step employs the *Newton-Raphson method* for the iteration. For the force-based models, the *incrementation type* is set to *automatic*, and, for the displacement-based models, the *fixed incrementation type* is used. For automatic incrementation, the *initial increment size* is selected 100 times smaller than the *maximum increment size* and the *minimum increment size* is chosen 100 times smaller than the initial increment size. The hypoelastic

constitutive equations used in these four models are based on: (1) the Jaumann rate of the Cauchy stress, (2) the Jaumann rate of the Kirchhoff stress, (3) the Truesdell rate of the Cauchy stress, (4) the Truesdell rate of the Kirchhoff stress, (5) the Green–Naghdi rate of the Cauchy stress, and (6) the Green–Naghdi rate of the Kirchhoff stress. The constitutive equations are all *zero-graded*. The Young's modulus E and Poisson's ratio ν are, respectively, set to 20 (with consistent units) and 0.2. We verified analytically that, for the cases studied, the material parameters E and ν appear linearly in the expressions of the Cauchy stress and, therefore, varying their magnitude does not introduce any further nonlinearity. Therefore, the conclusions drawn in this section are valid for arbitrary (and, naturally, physically admissible) values of the Young's modulus and the Poisson's ratio. In the *first model* (Figure 2-1 (a)), the nodes located on the bottom surface of the element are fixed in all directions, the nodes on the upper surface are fixed in x_2 and x_3 directions and a displacement equal to 5 is applied at the upper nodes in x_1 direction. This model is a displacement-based model subjected to simple shear. Using the zero-graded hypoelastic constitutive equations in this model, the *numerical* Cauchy stress tensors can be checked with the *analytical* counterparts provided in [2, 3] (see

Figure 2-2 for the analytical solutions of the zero-graded hypoelastic constitutive equations under simple shear).

In simple shear, the *local volume* does not change (i.e. $J = 1$) and, thus, the Kirchhoff stress tensor coincides with the Cauchy stress tensor. Therefore, the hypoelastic constitutive equations based on the Kirchhoff stress tensor are equivalent to those based on the Cauchy stress tensor. Figure 2-3 compares the analytical solutions (CASE 4) with the numerical ones, considering the

fixed increment size as 0.1 (CASE 1), 0.01 (CASE 2), and 0.001 (CASE 3). For all hypoelastic constitutive equations, the numerical solutions corresponding to the increment size of 0.001 lie on the analytical solutions. For the hypoelastic models associated with the Jaumann and Green–Naghdi rates, the convergence occurs at the increment size of 0.01 (CASE 2).

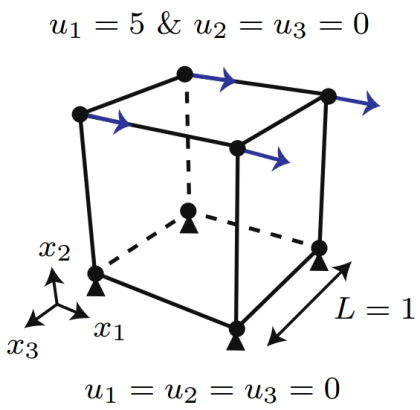

(a) Displacement-based, simple-shear

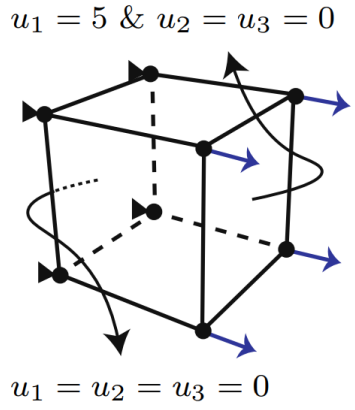

(b) Displacement-based, uniaxial-extension

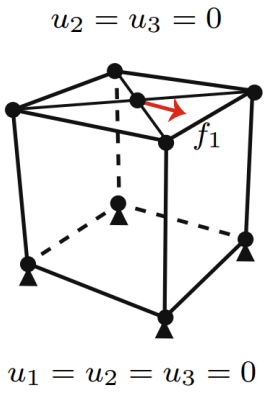

(c) Force-based, simple-shear

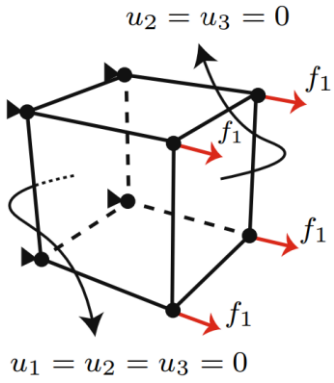

(d) Force-based, uniaxial-extension

Figure 2-1: ABAQUS models for checking the correctness of the Cauchy stress array STRESS and the Jacobian matrix DDSDDE

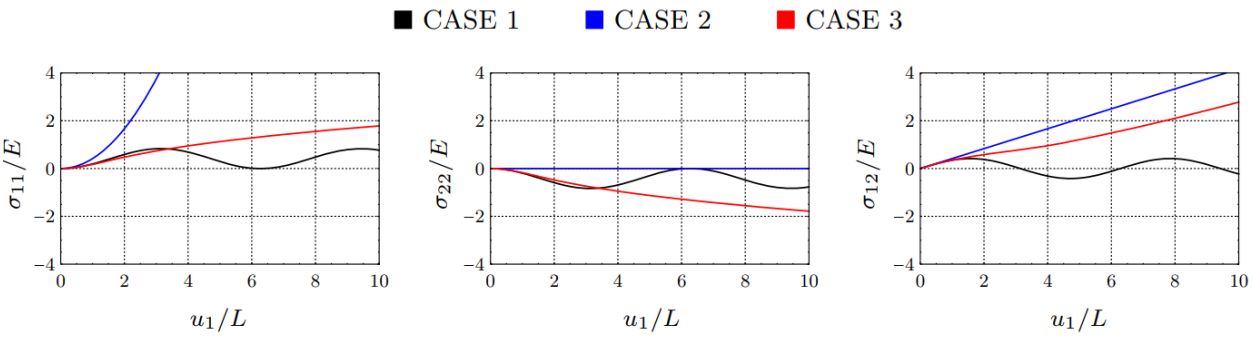

Figure 2-2: Analytical solutions of the Cauchy stress tensor in a material body subjected to simple shear; zero-graded hypoelastic constitutive equations based on: the Jaumann rate of the Cauchy stress (CASE 1); the Truesdell rate of the Cauchy stress (CASE 2); and the Green–Naghdi rate of the Cauchy stress (CASE 3)

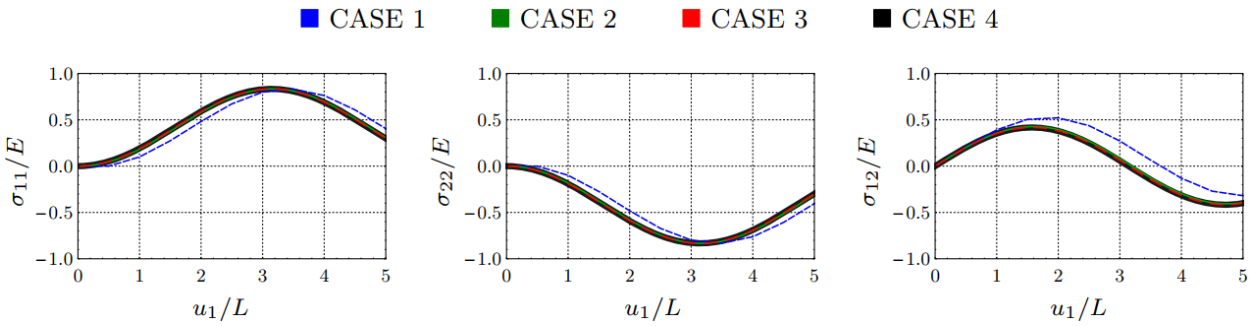

(a) Jaumann rate of the Cauchy or Kirchhoff stress tensors

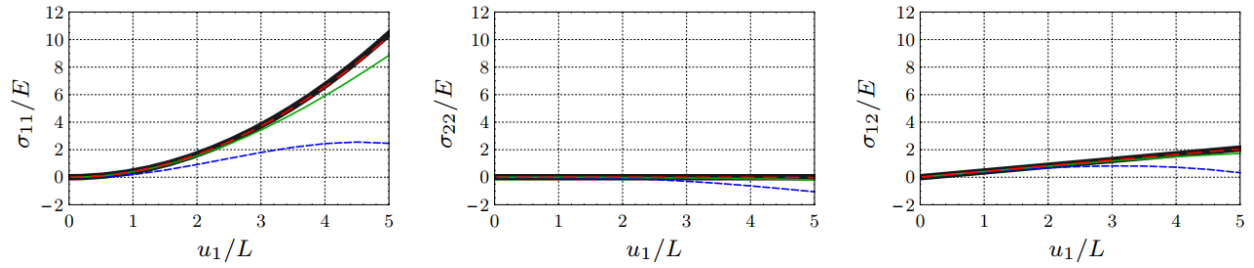

(b) Truesdell rate of the Cauchy or Kirchhoff stress tensors

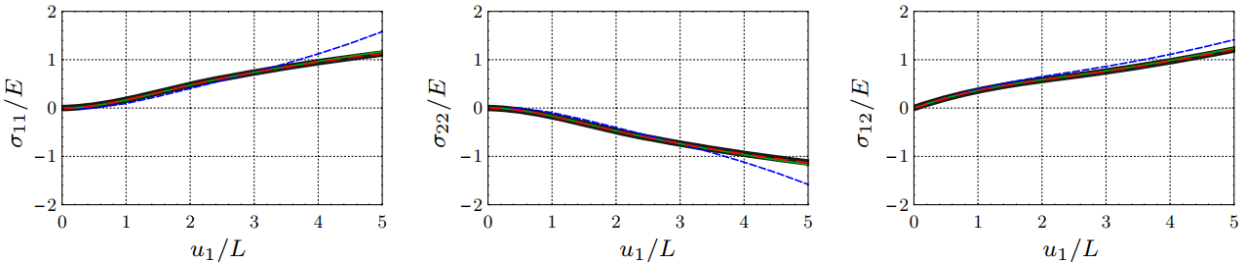

(c) Green-Naghdi rate of the Cauchy or Kirchhoff stress tensors

Figure 2-3: The Cauchy stress components in the displacement-based model subjected to simple shear; zero-graded hypoelastic constitutive equations based on various rates (a–c); numerical solutions with fixed increment sizes of 0.1 (CASE 1), 0.01 (CASE 2), and 0.001 (CASE 3) in comparison with the analytical solutions (CASE 4)

In the *second model* (Figure 2-1 (b)), the nodes on the back surface are fixed in all directions; the nodes on the front surface are fixed in x_2 and x_3 directions and a displacement equal to 5 is applied in x_1 direction. This model is a displacement-based model subjected to uniaxial extension, which we use to double-check the update procedure of the Cauchy stress tensor for the zero-graded hypoelastic constitutive equations. In uniaxial extension, the eigenvectors of the right stretch tensor $\boldsymbol{U}$ remain constant during the motion and thus the eigenvectors of $\dot{\boldsymbol{U}}$ coincide with those of $\boldsymbol{U}$. Consequently, $\boldsymbol{U}$ and $\dot{\boldsymbol{U}}$ *commute* and the spin tensor $\boldsymbol{w}$ reduces to the rigid spin $\boldsymbol{\Omega}$, as can be seen from Eq. (2-10). Accordingly, in uniaxial extension, the hypoelastic constitutive equations based on the Jaumann rates show the same mechanical behaviour as those based on the Green–Naghdi rates. Figure 2-4 represents the numerical solutions considering the fixed increment size as: 0.1 (CASE 1), 0.01 (CASE 2), 0.001 (CASE 3), and 0.0001 (CASE 4). For all hypoelastic constitutive equations, the increment sizes of 0.01, 0.001, and 0.0001 result in the same responses.

In the *third model* (Figure 2-1 (c)), the bottom nodes are fixed in all directions; by defining a *rigid body constraint*, the upper nodes are *rigidly constrained* to a *reference point* located at the center of the upper surface and a concentrated force in the x_1-direction is applied to the reference point. The reason behind the employment of the rigid constraint is that the application of equal concentrated forces at the upper nodes does not produce simple shear deformation. This is a force-based model, used to check the correctness of the Jacobian matrix for the zero-graded hypoelastic constitutive equations. In this model, the applied force is in equilibrium with the shear Cauchy stress component, i.e. σ_{12} (Figure 2-1 (c)). Noting that the iterative procedure, i.e. the Newton–Raphson method, is unable to pass the *critical points* (e.g. snap-through), for each hypoelastic constitutive equation, the value of the applied force must be selected based on the shear stress response in the displacement-based model under simple shear. Based on Figure 2-3 (b) and Figure 2-3 (c), for the hypoelastic constitutive equations associated with the Truesdell and Green–Naghdi rates, the shear stress is increasing in the course of the simple shear motion and its maximum value occurs at $u_1 = 5$. Nevertheless, for the hypoelastic constitutive equations associated with the Jaumann rates, the maximum shear stress occurs at a critical point located at $u_1 = 1.57$ (Figure 2-3 (a)). Employing the zero-graded hypoelastic constitutive equations and the corresponding applied force values into the model, in Figure 2-5, a comparison is provided between the analytical solutions (CASE 4) and the numerical solutions using the automatic incrementation with maximum increment sizes as: 0.1 (CASE 1), 0.01 (CASE 2), and 0.001 (CASE 3). For all hypoelastic constitutive equations, the maximum increment size of 0.001 (CASE 3) provides numerical solutions which are located on the analytical solutions. For the hypoelastic constitutive

equations based on the Jaumann and Green–Naghdi rates, even the numerical solutions associated with the maximum increment size of 0.1 lie on the analytical counterparts (Figure 2-5 (a) and Figure 2-5 (b).

For the *fourth model* (Figure 2-1 (d)), the nodes in the back surface are fixed in all directions, the nodes in the front surface are restricted in x_2 and x_3 directions and, in the remaining degrees of freedom (DOFs), i.e. DOFs in x_1 direction at the nodes in the front, equal concentrated forces f_1 are applied. This model is a force-based model subjected to uniaxial extension, used to double-check the correctness of the Jacobian matrix for the zero-graded hypoelastic constitutive equations.

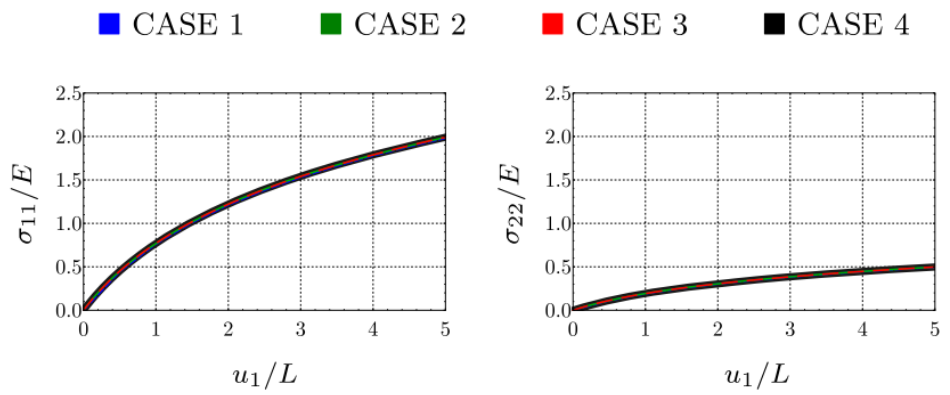

(a) Jaumann or Green-Naghdi rate of the Cauchy stress tensor

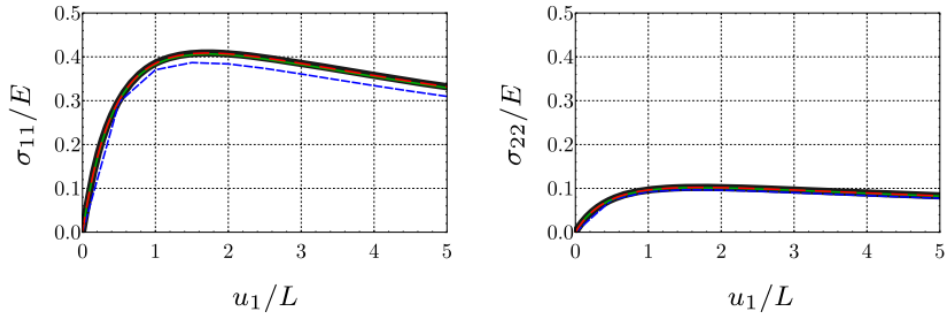

(b) Jaumann or Green-Naghdi rate of the Kirchhoff stress tensor

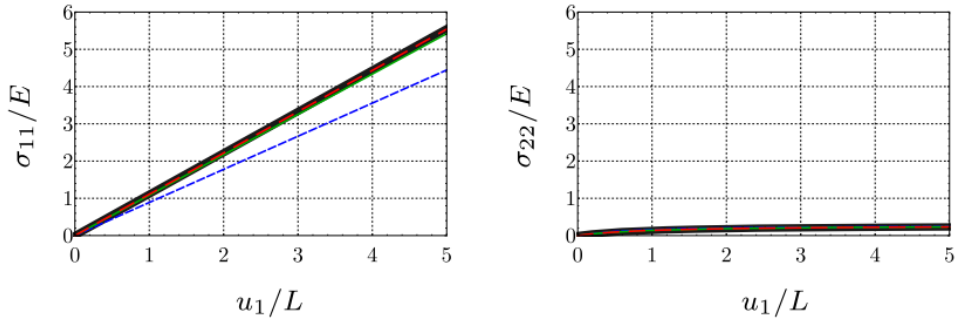

(c) Truesdell rate of the Cauchy stress tensor

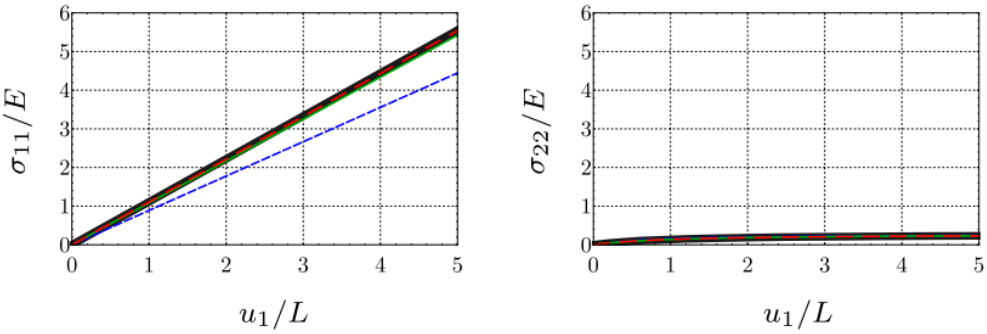

(d) Truesdell rate of the Kirchhoff stress tensor

Figure 2-4: The Cauchy stress components in the displacement-based model subjected to uniaxial extension deformation; zero-graded hypoelastic constitutive equations based on various rates (a–d); comparing numerical solutions with fixed increment sizes as: 0.1 (CASE 1), 0.01 (CASE 2), 0.001 (CASE 3), and 0.0001 (CASE 4)

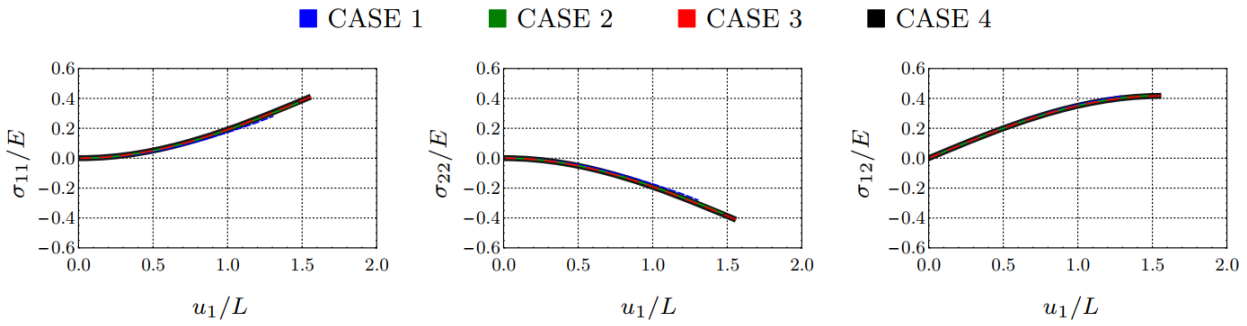

(a) Jaumann rate of the Cauchy or Kirchhoff stress tensors

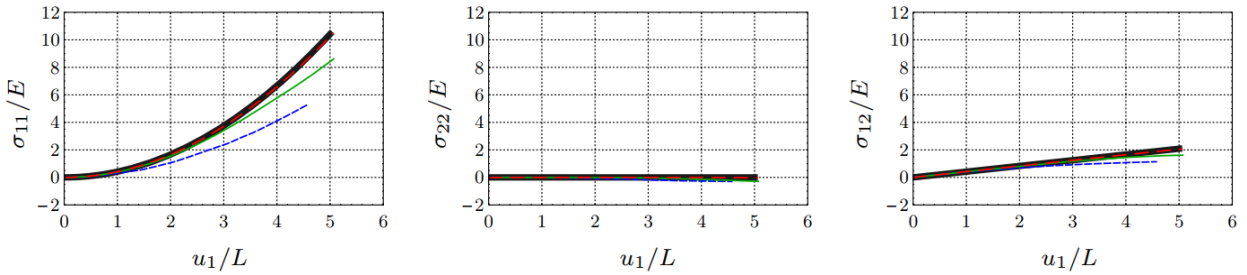

(b) Truesdell rate of the Cauchy or Kirchhoff stress tensors

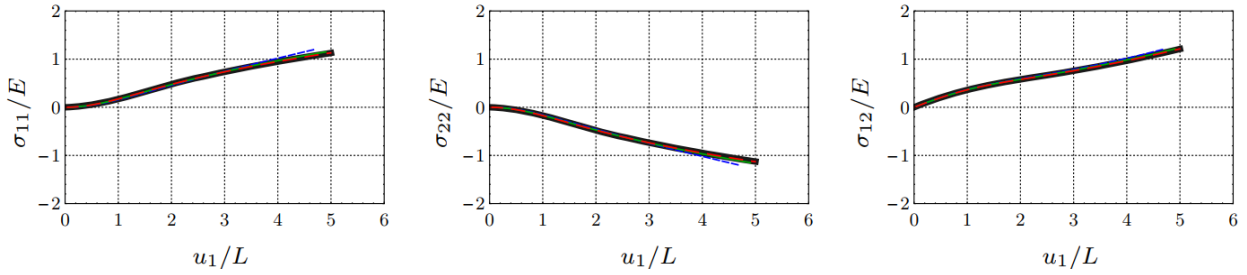

(c) Green-Naghdi rate of the Cauchy or Kirchhoff stress tensors

Figure 2-5: The Cauchy stress components in the force-based model subjected to simple shear; zero-graded hypoelastic constitutive equations based on various rates (a-c); numerical solutions using automatic incrementation with maximum increment sizes of 0.1 (CASE 1), 0.01 (CASE 2), and 0.001 (CASE 3) in comparison with analytical solutions (CASE 4)

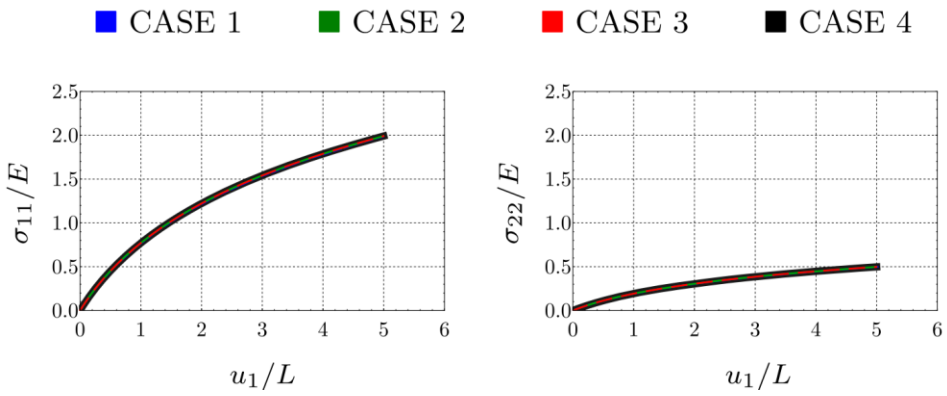

(a) Jaumann or Green-Naghdi rate of the Cauchy stress tensor

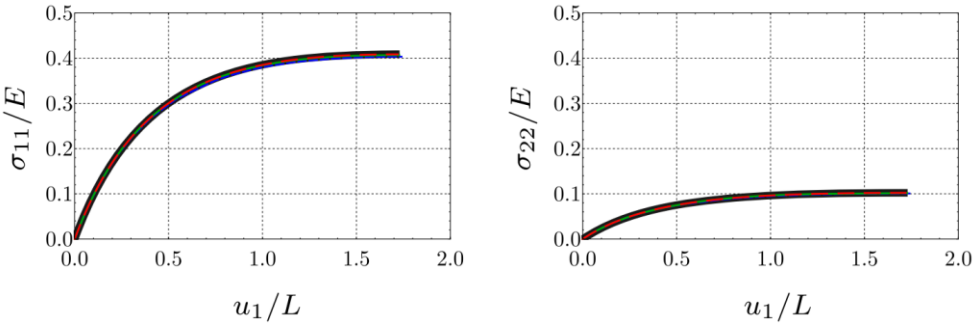

(b) Jaumann or Green-Naghdi rate of the Kirchhoff stress tensor

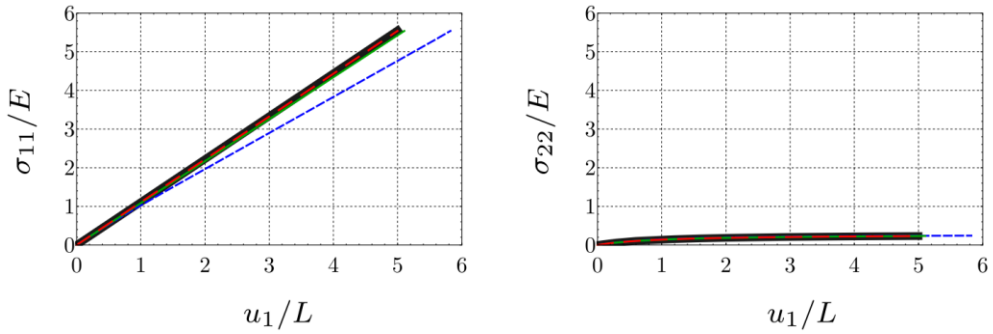

(c) Truesdell rate of the Cauchy stress tensor

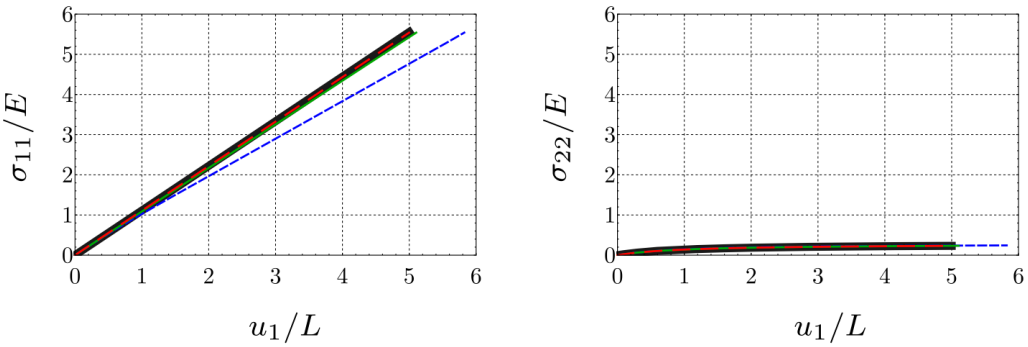

(d) Truesdell rate of Kirchhoff stress tensor

Figure 2-6: The Cauchy stress components in the force-based model subjected to uniaxial extension deformation; zero-graded hypoelastic constitutive equations based on various rates (a–d); using automatic incrementation with the maximum increment sizes of 0.1 (CASE 1), 0.01 (CASE 2), 0.001 (CASE 3), and 0.0001 (CASE 4)

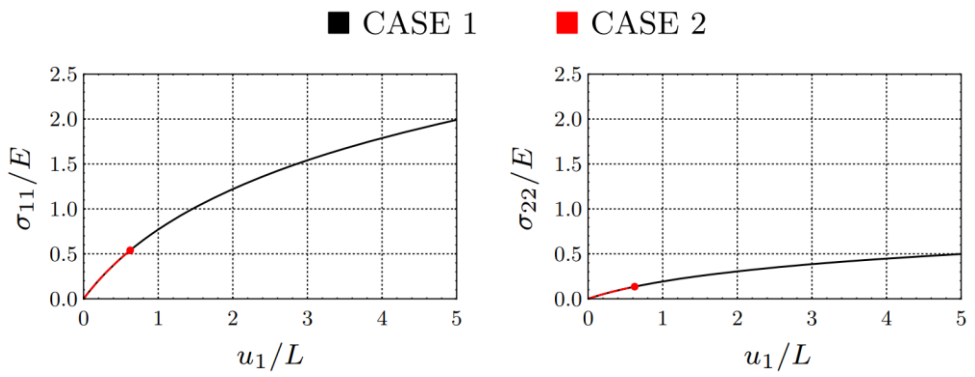

(a) Jaumann or Green-Naghdi rate of the Cauchy stress tensor

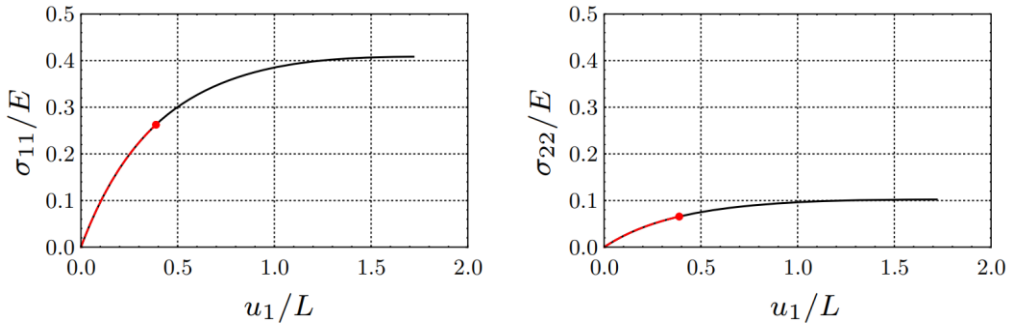

(b) Jaumann or Green-Naghdi rate of the Kirchhoff stress tensor

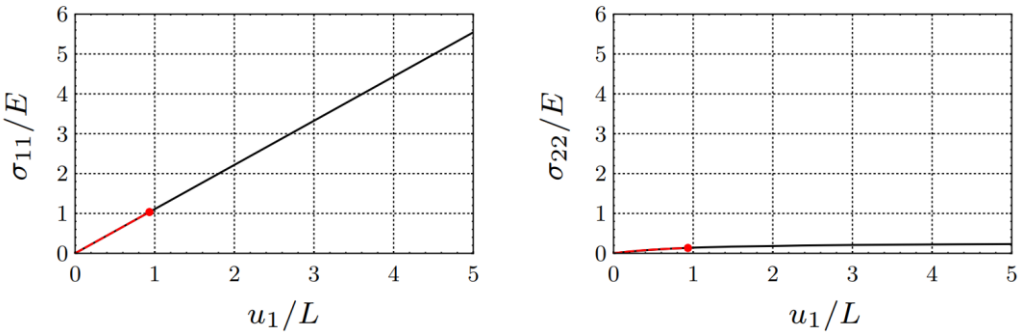

(c) Truesdell rate of the Cauchy stress tensor

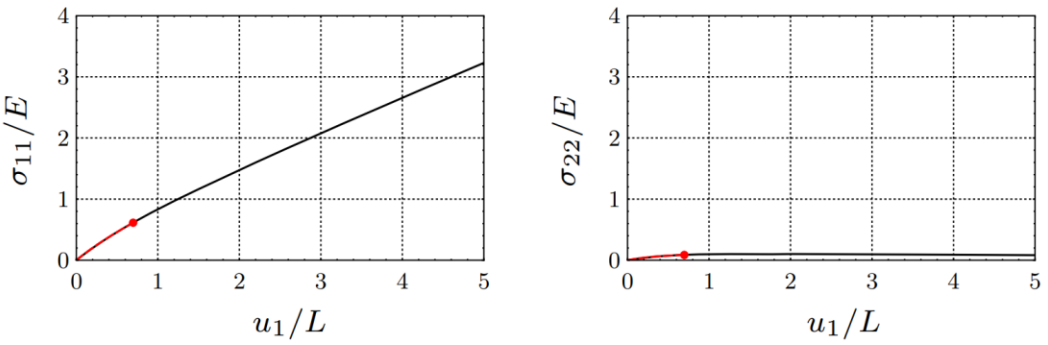

(d) Truesdell rate of the Kirchhoff stress tensor

Figure 2-7: Cauchy stress components in the force-based model subjected to uniaxial extension based on: the correct Jacobian $\mathbb{D}_{\mathrm{n}}$, based on the Jaumann rate of the Kirchhoff stress from Eq. (2-57) (CASE 1), and the incorrect version of the Jacobian, based on the Jaumann rate of the Cauchy stress $\mathbb{c}_{\mathrm{n}}^{\sigma^{\nabla}} = \mathbb{D}_{\mathrm{n}} - \boldsymbol{\sigma}_{\mathrm{n}} \otimes \boldsymbol{i}$ from Eq. (2-56) (CASE 2). The zero-graded hypoelastic constitutive equations based on various rates (a–d); using the automatic incrementation with the maximum increment size of 0.001. Note how the simulation based on the incorrect Jacobian $\mathbb{c}_{\mathrm{n}}^{\sigma^{\nabla}} = \mathbb{D}_{\mathrm{n}} - \boldsymbol{\sigma}_{\mathrm{n}} \otimes \boldsymbol{i}$ fails to converge (the red dot indicates where the simulation stops)

In this model, the sum of the concentrated forces, i.e. $4f_1$, is in equilibrium with the normal Cauchy stress component σ_{11}(Figure 2-1 (d)). Thus, for each hypoelastic constitutive equation, the value of f_1 must be selected based on the response of the stress component σ_{11} in the displacement-based model subjected to uniaxial extension (Figure 2-4). As is clear from Figure 2-4 (b), for the hypoelastic constitutive equations based on the Jaumann or Green–Naghdi rates of the Kirchhoff stress tensor, a critical point (snap-through) exists at $u_1 = 1.71$, whereas the stress component σ_{11} is increasing during the uniaxial extension motion in other constitutive equations (Figure 2-4 (a), Figure 2-4 (c), and Figure 2-4 (d)). In Figure 2-6, employing the zero-graded hypoelastic constitutive equations alongside the proper values of f_1, the numerical solutions for the maximum increment sizes of 0.1 (CASE 1), 0.01 (CASE 2), 0.001 (CASE 3), and 0.0001

(CASE 4) are compared. It is clear from Figure 2-6 that, for all of the hypoelastic constitutive equations, the numerical solutions corresponding to the maximum increment sizes of 0.01 to 0.0001, i.e. CASE 2 to CASE 4, are the same. For the hypoelastic constitutive equations associated with the Jaumann or Green–Naghdi rates, even the first case, i.e. the numerical solutions with the maximum increment size of 0.1 are the same as the rest of the numerical solutions.

The elasticity tensor $\mathbb{c}_n^{\sigma^\nabla}$ describes the relation between the Jaumann rate of the Cauchy stress and the rate of deformation (see Eq. (A.14)) and is related to the consistent Jacobian $\mathbb{c}_n^{\sigma^\nabla} = \mathbb{D}_n - \boldsymbol{\sigma}_n \otimes \boldsymbol{i}$ via Eq. (2-56). Since $\mathbb{c}_n^{\sigma^\nabla}$ is used in the Hughes–Winget algorithm [26] to update the stress (Eq. (2-79)), a possible coding error is to use $\mathbb{c}_n^{\sigma^\nabla}$ in place of the consistent Jacobian $\mathbb{D}_n$ (Eq. (2-57)). Figure 2-7 compares the numerical solutions based on the correct Jacobian $\mathbb{D}_n$ (CASE 1) and the incorrect Jacobian (CASE 2) for the force-based model subjected to uniaxial extension.

Figure 2-7 shows how using the wrong Jacobian matrices results in *non-convergence* of the analyses at the early stages of the loading. Nevertheless, before the simulation fails to converge and stops (which is indicated by the red dots in the CASE 2 plots in Figure 2-7), the Cauchy stress components are identical in both cases of the correct and incorrect Jacobian matrices. Therefore, the correctness of the Jacobian matrix is crucial for the convergence of the analyses, but has no effect on the correctness of the updated Cauchy stress tensor.

2.5 Chapter conclusion

In this study, we implement various hypoelastic constitutive models into the finite element analysis software ABAQUS through the user subroutine UMAT. For the formulation of the consistent Jacobian, i.e. the matrix DDSDDE, ABAQUS uses the elasticity tensor relating the Jaumann rate of the Kirchhoff stress to the rate of deformation for solid elements and the elasticity tensor relating the Green–Naghdi rate of the Kirchhoff stress to the rate of deformation for shell elements. Therefore, it is essential to relate the elasticity tensor of various hypoelastic constitutive models to the elasticity tensor associated with the consistent Jacobian. In regard to the importance of the consistent Jacobian, it is shown that the usage of wrong Jacobian matrices would give rise to the non-convergence of the analyses in the early stages of loading.

Additionally, in order to update the Cauchy stress in the various hypoelastic models presented, the comprehension of ABAQUS co-rotational framework and UMAT-subroutine variables such as STRESS, DSTRAN, and DROT is essential, and this is why they were all described in detail. The correctness of the stress array STRESS and Jacobian matrix DDSDDE in the zero-graded hypoelastic constitutive equations is checked using displacement-based and force-based models subjected to simple shear and uniaxial extension. This work is aimed at providing a step-by-step guide to the implementation of hypoelastic materials in ABAQUS, but the procedures shown can be adapted to the modelling of hyperelastic materials as well.

References

[1] Truesdell, C., Noll, W., Truesdell, C., & Noll, W. (2004). The non-linear field theories of mechanics (pp. 1-579). Springer Berlin Heidelberg.

[2] Dienes, J. K. (1979). On the analysis of rotation and stress rate in deforming bodies. Acta mechanica, 32(4), 217-232.

[3] Johnson, G. C., & Bammann, D. J. (1984). A discussion of stress rates in finite deformation problems. International Journal of Solids and Structures, 20(8), 725-737.

[4] Nguyen, N., & Waas, A. M. (2016). Nonlinear, finite deformation, finite element analysis. Zeitschrift für angewandte Mathematik und Physik, 67, 1-24.

[5] Prot, V., Skallerud, B., & Holzapfel, G. A. (2007). Transversely isotropic membrane shells with application to mitral valve mechanics. Constitutive modelling and finite element implementation. International journal for numerical methods in engineering, 71(8), 987-1008.

[6] Bellini, C., & Federico, S. (2015). Green-Naghdi rate of the Kirchhoff stress and deformation rate: the elasticity tensor. Zeitschrift für angewandte Mathematik und Physik, 66, 1143-1163.

[7] Manual, A. U. (2010). Dassault Systems Simulia Corporation. Providence USA.

[8] Pinsky, P. M., Ortiz, M., & Pister, K. S. (1983). Numerical integration of rate constitutive equations in finite deformation analysis. Computer Methods in Applied Mechanics and Engineering, 40(2), 137-158.

[9] Mehrabadi, M. M., & Nemat-Nasser, S. (1987). Some basic kinematical relations for finite deformations of continua. Mechanics of Materials, 6(2), 127-138.

[10] Freed, A. (2008). Anisotropy in hypoelastic soft-tissue mechanics, I: theory. Journal of Mechanics of Materials and Structures, 3(5), 911-928.

[11] Freed, A. D. (2010). Hypoelastic soft tissues. Part I: theory. Acta Mechanica, 213(1-2), 189-204.

[12] Hughes, T. J., & Marsden, J. E. (1983). Mathematical foundations of elasticity. Englewood Cliffs: Prentice-Hall.

[13] Bonet, J., & Wood, R. D. (1997). Nonlinear continuum mechanics for finite element analysis. Cambridge university press.

[14] Bonet, J., Gil, A. J., & Wood, R. D. (2021). Nonlinear solid mechanics for finite element analysis: dynamics. Cambridge University Press.

[15] Epstein, M. (2010). The geometrical language of continuum mechanics. Cambridge University Press.

[16]Noll, W. (2006). A frame-free formulation of elasticity. Journal of Elasticity, 83, 291-307.

[17] Hashiguchi, K., & Yamakawa, Y. (2012). Introduction to finite strain theory for continuum elasto-plasticity. John Wiley & Sons.

[18] Federico, S., Alhasadi, M. F., & Grillo, A. (2019). Eshelby's inclusion theory in light of Noether's theorem. Mathematics and Mechanics of Complex Systems, 7(3), 247-285.

[19] Kröner, E. (1959). Allgemeine kontinuumstheorie der versetzungen und eigenspannungen. Archive for Rational Mechanics and Analysis, 4, 273-334.

[20] Eringen, A. C. (1980). Mechanics of Continua. Robert E. KriegerPublishing Company, Huntington, New York, 762-76g.

[21] Curnier, A., He, Q. C., & Zysset, P. (1994). Conewise linear elastic materials. Journal of Elasticity, 37, 1-38.

[22] Sun, W., Chaikof, E. L., & Levenston, M. E. (2008). Numerical approximation of tangent moduli for finite element implementations of nonlinear hyperelastic material models. Journal of Biomechanical Engineering, 130, 061003.

[23] Ji, W., Waas, A. M., & Bazant, Z. P. (2013). On the importance of work-conjugacy and objective stress rates in finite deformation incremental finite element analysis. Journal of Applied Mechanics, 80(4), 041024.

[24] Zhou, X., & Tamma, K. K. (2003). On the applicability and stress update formulations for corotational stress rate hypoelasticity constitutive models. Finite elements in analysis and design, 39(8), 783-816.

[25] de Souza Neto, E. A., Peric, D., & Owen, D. R. (2011). Computational methods for plasticity: theory and applications. John Wiley & Sons.

[26] Hughes, T. J., & Winget, J. (1980). Finite rotation effects in numerical integration of rate constitutive equations arising in large ‐ deformation analysis. International journal for numerical methods in engineering, 15(12), 1862-1867.

CHAPTER 3: MORPHOLOGICAL STUDY OF THE PELVIS USING STATISTICAL SHAPE MODELS: ANATOMICAL VARIATION, ASYMMETRY, AND SEXUAL DIMORPHISM

This chapter is derived from the paper in prepration:

M. Palizi, M. S. Ead, J. L. Jaremko, L. Westover, S. Adeeb, Quantitative assessment of pelvic morphology using statistical shape modelling.

Abstract

The human pelvis is a complex anatomical structure with geometric variability due to the shape, size, location, and orientation of its components. Statistical shape modelling describes anatomical variation in compact mathematical form, called statistical shape models (SSMs). This study uses the dataset of 40 pelves (20 male and 20 female) to construct SSMs for the hemipelvis at three different levels and quantify inter- and intra-individual, as well as sexual dimorphism. Our study included the following structures: the hemipelvic shape, the hemipelvis with actual size, and the left-right hemipelves in the pelvic girdle structure. In addition to the patterns, anatomical variation and asymmetry are measured locally. Non-parametric statistical tests and permutation-based analyses are utilized to assess the significance of the observations. The results show that (1) change of size is the first mode of anatomical variation for both hemipelvis and pelvis with higher

dominance within the male group, (2) the dominant mode of anatomical variation on the hemipelvis shape involves changes in iliac breadth for both groups, (3) Anterior Superior Iliac Spine (ASIS) exhibits the highest anatomical variation in all three structures for both male and female groups, with its lateral-medial movement being a significant pattern of anatomical variation in all studied structures, (4) the main pattern of bilateral asymmetry for both the male and female groups was linked to the arrangement/orientation of the left-right hemipelves (an elevation/depression for the male group, and an oblique rotation for the female group), and (5) for the hemipelvic shape, the male average model displayed a narrower sciatic notch and upright ilium, while the female group exhibited a curved and shorter ilium with longer and thinner superior pubic and ischiopubic rami. This study is relevant to implant design companies, preoperative planning of unilateral pelvic injuries, and assessment of anatomical restoration following pelvic surgeries and difficult childbirth. Additionally, there are potential applications in educational contexts.

Keywords: statistical shape modelling; pelvic morphometrics; inter-individual variation; matching asymmetry; bilateral asymmetry; sexual dimorphism.

3.1 Introduction

The pelvis is a complex anatomical structure that consists of two innominate bones, the sacrum, and the coccyx [1]. Each innominate bone, referred to as the *hemipelvis*, is made up of three parts: the ilium, ischium, and pubis. These components are initially separated at birth but merge by the end of puberty, forming the complete hemipelvis [1]. The variation in pelvic

morphology (or geometry) arises from the differences in the shape, size, position, and orientation of its components. Furthermore, pelvic morphology has significant differences between men and women [2]. The *sexual dimorphism* of the pelvis is related to childbirth which exerted evolutionary pressure on the female pelvis [2].

Morphometrics is an old topic in biology that quantifies the morphology (or geometry) of bones, organs, and anatomical structures [3]. Traditional morphometric studies typically employed statistical analyses on sets of distances, angles, and/or distance ratios [3]. The distances and angles were defined between a set of anatomically meaningful points that were common and distinguishable within samples, referred to as *landmarks* [3]. Despite insightful findings of traditional morphometrics, analyses of these discrete measurements failed to represent the complete three-dimensional geometry of bones [4]. To overcome this limitation, *geometric morphometrics* (GM) emerged as a promising approach for the analysis of bone geometry. The key idea of GM was to directly analyze the coordinates of the landmarks, instead of distances and angles [4]. With advancements in 3D medical imaging and shape analysis, GM expanded its scope from analyzing a limited number of landmarks to a dense set of features [4].

Statistical Shape Model (SSM) is one of the promising tools in modern GM to quantify bone morphology [5]. An SSM provides a concise yet comprehensive representation of the average geometry of a bone and its main types of variation [5]. In the last decade, researchers have employed SSMs to investigate various aspects of pelvic morphology. The majority of the studies have been focused on the *anatomical variation* of the pelvis within European and Asian populations, which proved to be highly beneficial in orthopaedics [6-10]. As an example, Artificial

Bone Models (ABMs) are widely used to teach fracture management principles, explore the biomechanics of the human skeletal system, and evaluate implant component efficiency through mechanical experiments [7]. However, the commercially available ABMs were limited to the European population [7]. To address this limitation, Ahrend et. al. used SSM to study the anatomical variation of the pelvis in the Asian population and manufactured a generic Asian pelvic ABM for educational and research purposes [7].

In addition to the anatomical variation, some studies have investigated the *sexual dimorphism* of the pelvis using SSM-based approaches [6, 8, and 10]. Arand et. al. created an overall (male and female) pelvic SSM for 50 Japanese adults, and alongside anatomical variation, they compare the average models for the male and female groups [8]. Veldhuizen et al. created an overall SSM for the hemipelvis, using a database of 100 men and 100 women in a Caucasian population, and compare the scores of the male and female groups in each SSM mode [10].

Asymmetry of the pelvis is another area where SSM-based approaches have been proposed [6, 11]. Handrich et al. created pelvic SSMs for male and female adults in Asian and European populations (four models) and identified the patterns of asymmetry within the modes of anatomical variation using visual judgment [11]. Assessing pelvic asymmetry is highly valuable for the preoperative planning of unilateral pelvic injuries, where the pelvic morphology of the intact side serves as a template for decision-making regarding the treatment and implant component selection [11].

In this study, we present a comprehensive SSM-based approach to investigate pelvic morphology in terms of anatomical variation, asymmetry, and sexual dimorphism. Unlike previous studies which have assessed either the entire pelvic structure or the hemipelvis, we analyze the pelvis geometry at different levels. Our study includes the following structures: (1) the hemipelvis without size, referred to as the *hemipelvic shape* hereinafter, (2) the hemipelvis at its actual scale, referred to as the *hemipelvis*, and (3) the left-right hemipelves within the pelvic structure, called the *pelvis*, hereinafter. The multi-level analysis provides a deeper understanding of pelvic morphology. Furthermore, we analyze the anatomical variation and asymmetry in the male and female groups separately to explore the similarities/differences between the two groups. Despite the extensive studies on pelvic morphology, the knowledge about the differences/similarities of the anatomical variation and specially asymmetry between the male and female pelvis is limited.

The remaining sections of this study are structured as follows: section 3.2 presents the computational pipeline to construct the models and assess the significance of the findings. In section 3.3, we present the significant patterns and areas related to anatomical variation, asymmetry, and sexual dimorphism. Section 3.4 discusses the findings of the study, compares them to other studies, and explores the potential applications of the study.

3.2 Materials and methods

The computational pipeline of the study included two major steps: (1) conversion of the image database into the samples of the studied structures, and (2) multivariate analyses. Figure 3-1 illustrates these steps in detail.

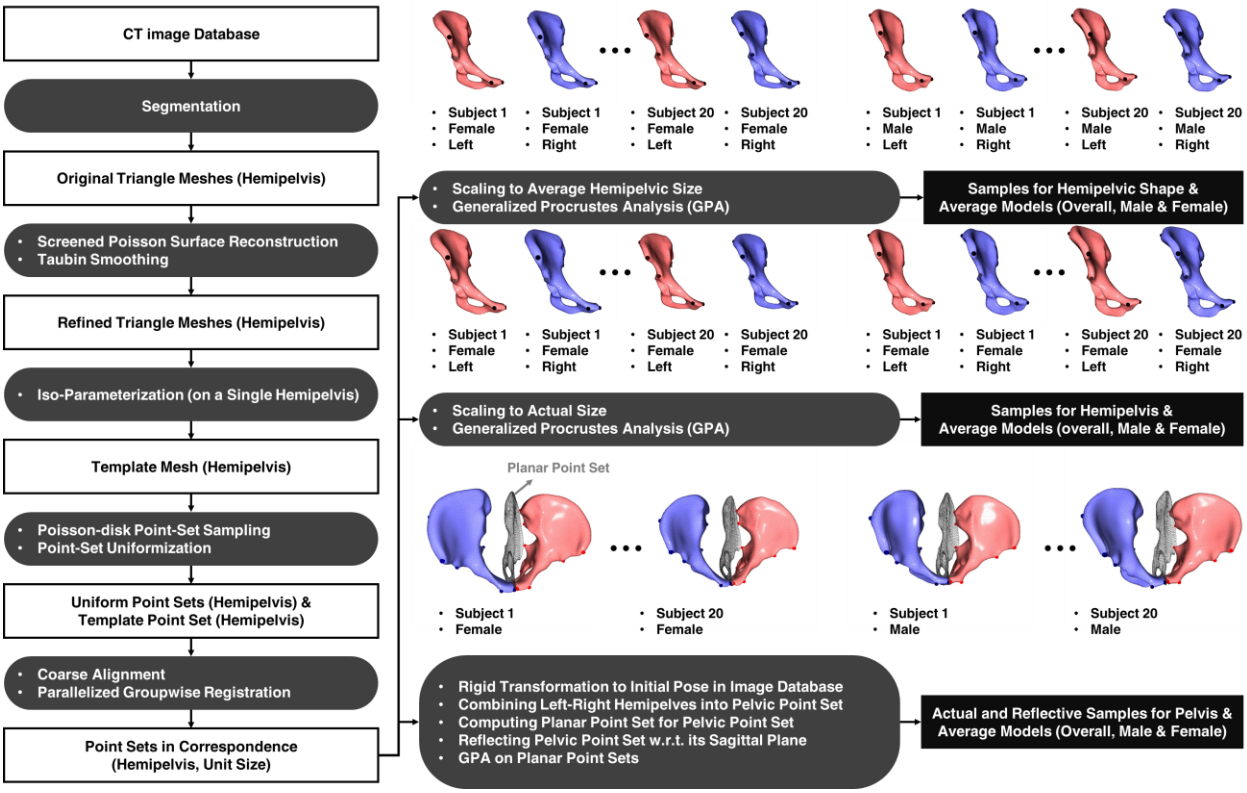

(a) Conversion of the image database into the samples.

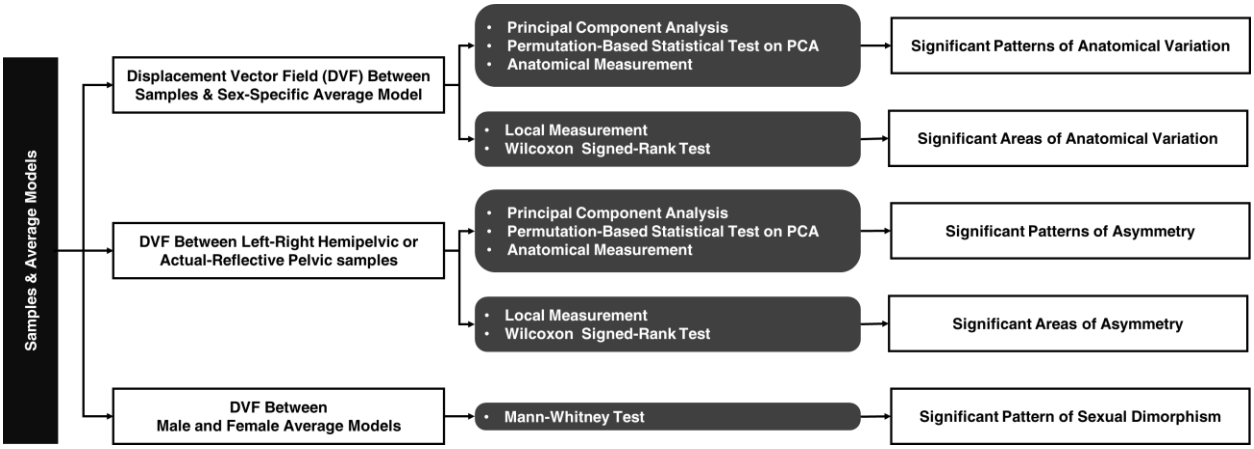

(b) Multivariate analyses.

Figure 3-1: Computational pipeline to study the pelvic morphology using SSM

3.2.1 Image dataset, triangle meshes, and point sets

The study used Computed Tomography (CT) images of the pelvic regions of 40 individuals (20 men, 20 women) with ages ranging from 18 to 25 years (average age: 21.3 years). The difference between the average age of the male and female groups was non-significant ($P = 0.912$, two-sided Mann-Whitney test). Approval to use the database was obtained from the Health Research Ethics Board at the University of Alberta with a waiver of consent. The study was conducted in line with the Declaration of Helsinki [12].

The CT scans were converted into triangle meshes using a semi-automated segmentation method [13]. Each segmented mesh represented the left or right hemipelvis of an individual. These original meshes contained geometric and topological noises. The screened Poisson surface

reconstruction technique [14] was used to convert each original mesh into a watertight mesh. Each watertight mesh was then smoothed using the Taubin method [15].

A *template* was required to establish correspondence as well as visualization purposes, for which one of the smoothed meshes was selected. Using a parameterization technique [16], the template mesh was converted into a mesh with optimal tessellation quality, i.e. uniform vertex distribution and equilateral triangles.

A dense uniform point set was sampled on each smoothed mesh and the template. To achieve uniform point distribution, the Poisson-disk point-set sampling method [17] was used to sample well-distributed points on the meshes. Then, the uniformization technique proposed in [18] was used to further homogenize the point distribution over the meshes.

3.2.2 Correspondence

The point sets (representing the hemipelves and the template hemipelvis) were coarsely aligned w.r.t. translation, scaling, and rotation. Each point set was first translated such that its centroid was moved to the origin of a global coordinate system. Next, each point set was scaled to have a unit centroid size. Afterward, each point set was rotated such that its principal axes aligned with the axes of the global coordinate system (see [19] for the computation of the centroid, centroid size, and principal axes of a point set). To align the right and left hemipelvic point sets, the point sets of the left hemipelves underwent an additional reflection.

After normalization, a parallelized groupwise registration scheme [20] was used to establish correspondence between the hemipelvic point sets. The scheme was an iterative process with two main steps: (1) the rigid alignment of the hemipelvic point sets on an average point set, and (2) the non-rigid alignment of the average point set on the hemipelvic point sets. Initially, the template point set served as the average point set, and after each iteration, the average point set was updated [20]. Convergence of the average point set was achieved in two iterations. The Coherent Point Drift (CPD) method [21] was used for the rigid and non-rigid registration tasks in the scheme. Using this parallelized registration scheme [20], we obtained a set of point sets in *correspondence* that represented the hemipelves in a common high-dimensional space (as the deformed versions of the template).

3.2.3 Samples

3.2.3.1 Hemipelvic-Shape Samples

The point sets in correspondence had unit centroid size. Using these point sets, the geometry of the *hemipelvic shape* was investigated. To facilitate the comparison between the hemipelvic shape and the structures with actual scale, all of the point sets in correspondence were scaled using the average centroid size of the hemipelves. Generalized Procrustes Analysis (GPA) was then employed to remove the redundant rigid transformations within the set [22].

3.2.3.2 Hemipelvic Samples

The point sets in correspondence were rigidly transformed to their actual scales. Next, GPA was applied to remove the redundant rigid transformations within the set.

3.2.3.3 Pelvic Samples

The point sets in correspondence were first transformed to their original location, orientation, and scale in the image dataset (using the computed parameters of the rigid registrations and normalization). Next, the left and right hemipelvic point sets belonging to each subject were combined into a single point set, representing the pelvis. In addition, the average of the left-right hemipelvic point sets was computed for each subject, which depicts a planar point set mirroring the contralateral (opposite) hemipelves. For each subject, the pelvic point set was reflected w.r.t to its sagittal plane; the sagittal plane was defined using the centroid and the smallest eigenvector of the planar point set. GPA was then applied on the planar point sets to remove the rigid transformation within the set.

3.2.4 Displacement Vector Fields (DVF)

For each structure, the Displacement Vector Field (DVF) between the samples and their sex-specific average point sets was used to study the *anatomical variation*. For the hemipelvic shape

and the hemipelvis, the DVF between the left-right point sets belonging to each subject was used to investigate the *matching asymmetry* of the hemipelvis (with and without size) [6]. For the pelvis, the DVF between the actual and reflected pelvic point sets was used to study the *bilateral asymmetry* on the pelvis [23, 24]. Lastly, the displacement between the male and female average point sets was used to characterize *sexual dimorphism*.

3.2.5 Multivariate analyses

Principal Component Analysis (PCA) is a dimension-reduction technique that identifies the main modes of variation within a dataset (see [22] for a description of PCA). In PCA, the modes of variation, referred to as the *principal components* (PCs), are arranged sequentially based on their contribution to the total variance within the dataset [22]. PCA was used to identify the main modes of anatomical variation and asymmetry in all of the studied structures, using the associated DVFs. The significance of the principal component analyses was assessed using a permutation-based statistical test proposed by [25]. In this test, firstly, the overall significance of the PCA was assessed by two statistics, ensuring the correlational structure exists in the DVFs [25]. Next, the PCs of valid variation were distinguished from the PCs reflecting the random noise [25].

In addition to the PCA, the anatomical variation and asymmetry were assessed *locally*. To measure the *local anatomical variation* on each structure, the distance between each sample and its sex-specific average model was recorded (i.e. the Euclidean norm of the DVFs related to anatomical variation). At each point, the average of such distances was measured as the *local*

anatomical variation. Similarly, the *local asymmetry* was measured at each point as (1) the average of the distance between the left-right hemipelvic samples (for the matching asymmetry of the hemipelvis, with and without size), and (2) the average of the distance between the pairs of actual-reflective pelvic samples for the bilateral asymmetry. It should be noted that PCA shows the main *patterns* of variation which explain the anatomical variation or asymmetry, while the local measures exhibit variance at each point on the structures.

To assess the statistical significance of the local measure at each point, we assumed that no significant difference exists between the local measure at that point and the overall average value over the whole structure (separate values for the male and female groups). The Wilcoxon signed-rank test [26] was then employed to assess this hypothesis by comparing the distance records at the point with the overall average value. To address the issue of multiple comparisons and control the false-positive rate [27], the threshold of considering the points as significance locations were considered as 1e-5 [27].

To model the *sexual dimorphism* on each structure, the DVF between the average male and female models was computed, intensified, and visualized. To determine the statistical significance of the *sex-related DVF* for each structure, the displacement field between the samples and the overall average model was projected on the sex-related DVF, and using the Mann-Whitney test, the difference between the projections for the male and female was assessed.

3.3 Results

3.3.1 Significant regions of anatomical variation

Figure 3-2 shows the color map plots for the *local anatomical variation* on each structure. The plots for the male and female groups are presented separately. Table 3-1 reports the overall statistics of the local anatomical variation. The p-values of the statistical tests on the significance of the local anatomical variation are plotted in Figure B-0-1 in Appendix B.

For all structures, the male group showed higher variation in comparison with the female group (Table 3-1 and Figure 3-2). The maximum variation for all of the structures was located around the Anterior Superior Iliac Spine or ASIS (red dots in Figure 3-2). For the *hemipelvic shape*, the variation around the ASIS reached 9.2 mm for the male group and 7.5 mm for the female group (Figure 3-2 and Table 3-1). In addition, the posterior side of the ilium, the pubic symphysis, and the ischial tuberosity (only for the male group) exhibited high variation (Figure 3-2 and Figure B-0-1).

For the *hemipelvis*, the local anatomical variation around the ASIS reached 10.7 mm for the male group and 8.2 mm for the female group (Figure 3-2 and Table 3-1). High variations were also observed at the top and bottom of the hemipelvis (Figure 3-2 and Figure B-0-1).

For the *pelvis*, both groups showed high variation around the ASIS, with the maximum local anatomical variation of 15.5 mm for the male group and 12.9 mm for the female group (Table 3-1 and Figure 3-5). For the pelvis, the variations in other regions were non-significant (Figure B-0-1).

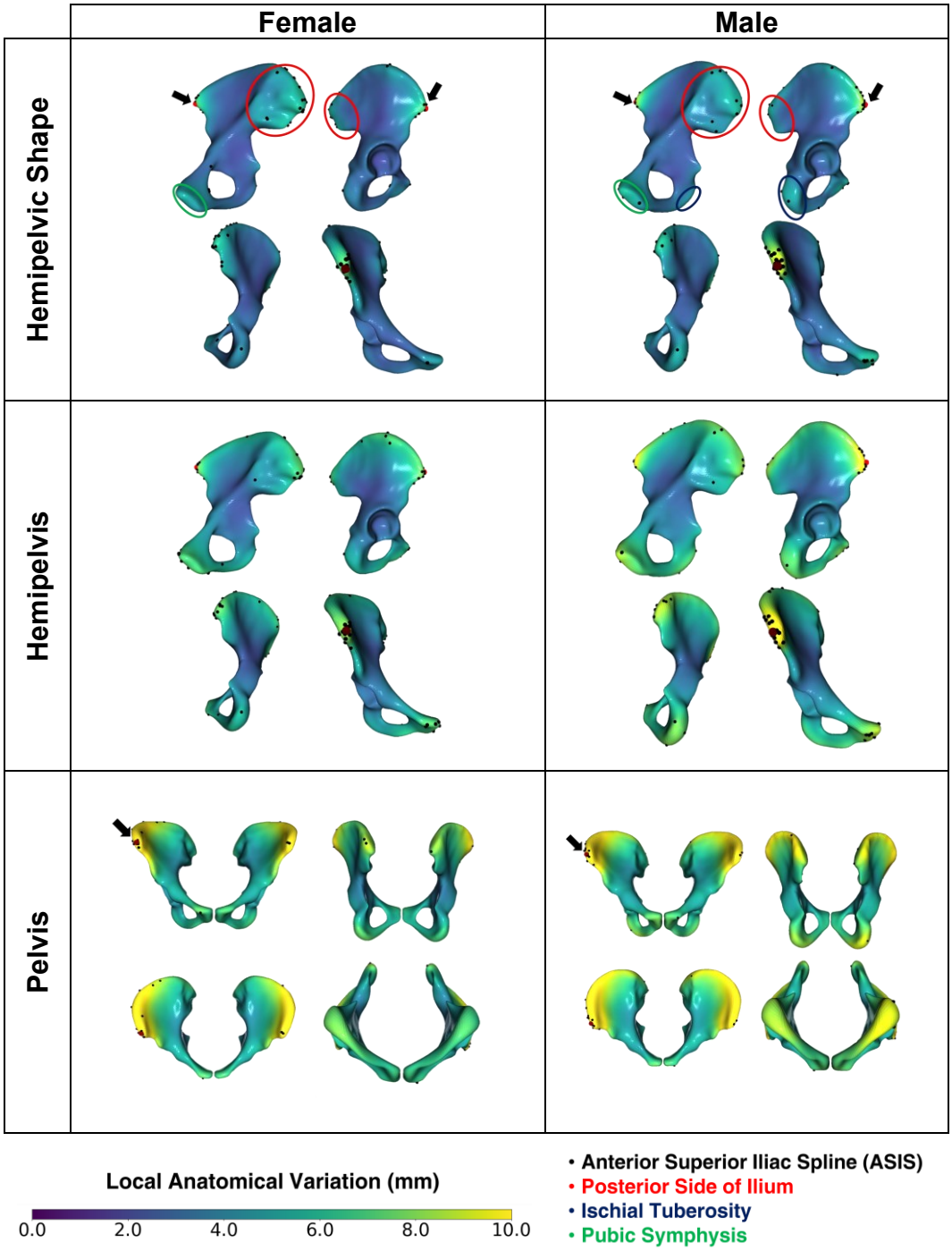
Female
Male
Hemipelvic Shape
Hemipelvis
Pelvis
Local Anatomical Variation (mm)
0.0
2.0
4.0
6.0
8.0
10.0
• Anterior Superior Iliac Spline (ASIS)
• Posterior Side of Ilium
• Ischial Tuberosity
• Pubic Symphysis

Figure 3-2: Color map plots for the local anatomical variation on the studied structures. The red dot shows the location of the maximum local anatomical variation. The black dots show the locations where each sample has the maximum distance from its sex-specific average model. The hemipelvis is visualized from lateral (top-left), medial (top-right), posterior (bottom-left) and anterior views (bottom-right). The views of the pelvis include anterior (top-left), posterior (top-right), inlet (bottom-left) and outlet (bottom-right).

Table 3-1: Statistics of the local anatomical variation for the studied structures

Structure	**Sex**	**Mean (mm)**	**SD (mm)**	**Min (mm)**	**Max (mm)**
Hemipelvic Shape	Female	3.4	0.9	2.0	7.5
	Male	3.6	1.0	2.0	9.2
Hemipelvis	Female	4.5	1.4	2.2	8.2
	Male	5.3	1.7	2.4	10.7
Pelvis	Female	6.2	1.9	3.1	12.9
	Mala	7.0	2.0	4.1	15.5

3.3.2 Patterns of anatomical variation

Table 3-2 presents the results of PCA analyses and permutation-based tests for the *anatomical variation* on each structure. In Figure 3-3 to Figure 3-5, the first three modes (principal component or PC) of the anatomical variation are depicted for each structure. Each PC is shown within the range of ±3 Standard Deviation (SD), encompassing 99.7% of the instances represented by that PC (see [22] for a description of PCA and the shape instance associated with a SD). The permutation-based tests showed significant correlational structure in all of the datasets (P-value

for the psi and phi statistics [25], Table 3-2). In addition, at least the first three PCs were meaningful modes that explain the anatomical variation (and not random noise) (Table 3-2).

For the *hemipelvic shape*, the first PC accounted for 31.0% of the total variance for the male group and 22.1% in the female group (Table 3-2). In both groups, PC1 mainly influenced the iliac breadth. For the male group, an increase in the iliac breadth was accompanied by a lateral movement of the ASIS, and the rotation of the pubis and ischium as a unit (Figure 3-3, PC1-Male). For the female group, an increase in the iliac breadth was associated with notable movements at the ASIS and PSIS (Posterior Superior Iliac Spine) and the elevation of the pubis and ischium as a unit (Figure 3-3, PC1-Female).

The second PC explained 12.2% of the total variance in the male group and 13.0% in the female group. For the male group, PC2 mainly influenced the curvature of the gluteal surface and iliac fossa, alongside notable movements at PSIS, ASIS, and ischium (Figure 3-3, PC2-Male). For the female group, PC2 mainly affects the posterior side of the ilium (sacroiliac or SI joint surface) as well as the acetabulum (Figure 3-3, PC2-Female). The third PC accounted for 10.0% of the total variation for the male group and 11.1% in the female group. For both groups, PC3 represents a movement at the ASIS in the anteroposterior direction (Figure 3-3, PC3-Female and Male).

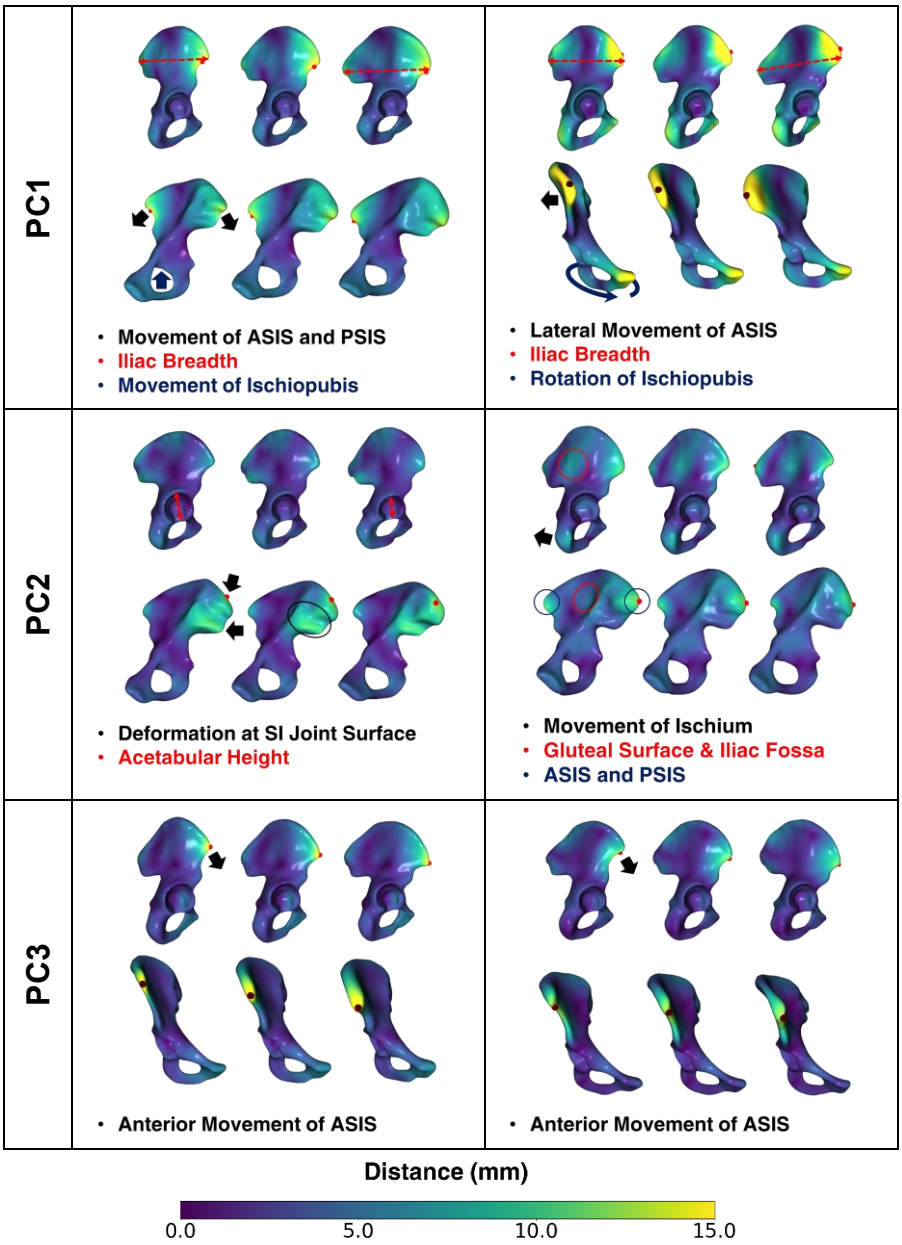

Figure 3-3: The first three PCs for the anatomical variation on the hemipelvic shape. The PCs are presented within the range of ±3 SD. The color mapping shows the distance between the extreme instances (associated with ±3SD) and the average model. The red dot shows the location of the maximum distance.

For the *hemipelvis*, the first PC primarily represented changes in size, accounting for 61.1% and 52.1% of the total variance in the male and female groups, respectively (Table 3-2 and Figure 3-4, PC1-Female and Male). For PC1, the maximum displacement was located on the ischium for the male group and the iliac crest for the female group (Figure 3-4, PC1-Female and Male). For both groups, PC2 shared the same traits as those in PC1 for the hemipelvic shape (Figure 3-4).

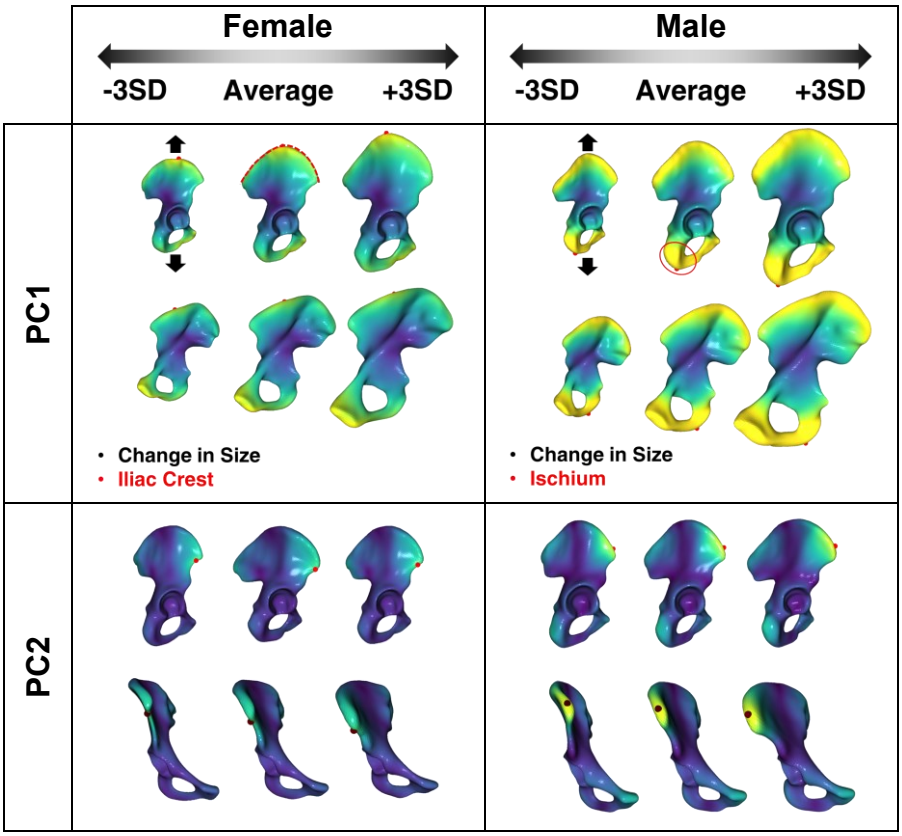

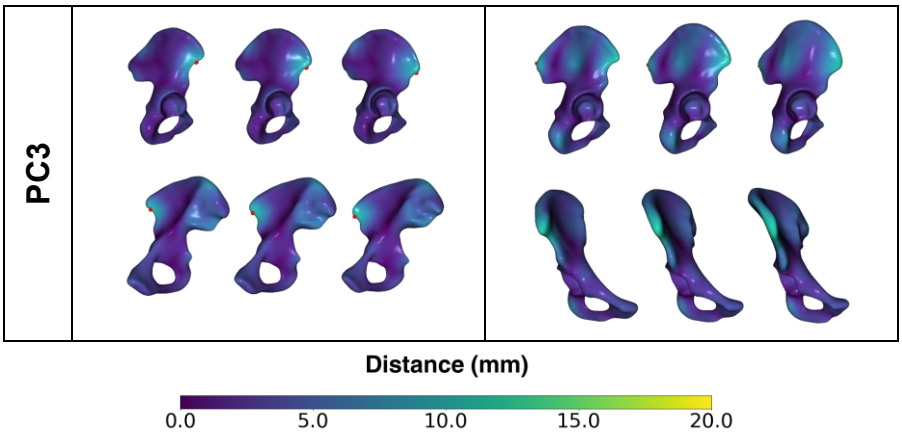

Figure 3-4: The first three PCs for the anatomical variation on the hemipelvis. The PCs are presented within the range of ±3 Standard Deviation (SD). The color mapping shows the distance between the extreme instances (associated with ±3SD) and the average model. The red dot shows the location of the maximum distance.

For the *pelvis*, the first mode dominantly showed differences in size; PC1 accounted for 53.9% and 55.0% of the total variance in the male and female groups, respectively (Table 3-2 and Figure 3-5, PC1-Female and Male). The second mode described 19.2% of the variance in the male group and 16.2% in the female group (Table 3-2). PC2 was dominantly the lateral-medial movements of the left-right ASISs (Figure 3-5, PC2-Female and Male). For the male group, the lateral movement of the ASIS was accompanied by an increase in the transverse diameter of the pelvic inlet and outlet (Figure 3-5, PC2-Male). For the female group, as ASIS moved laterally, the transverse dimension of the inlet did not change and the transverse diameter of the outlet decreased (Figure 3-5, PC2-Female). The modal contribution of the third PC was 5.6% for the male group and 7.2% for the females (Table 3-1). For the male group, PC3 was the lateral-medial movement of the left-right ischium (Figure 3-5, PC3-Male). For the female group, PC3 represents the lateral-medial movement of the posterior side of the ilium (Figure 3-5, PC3-Female).

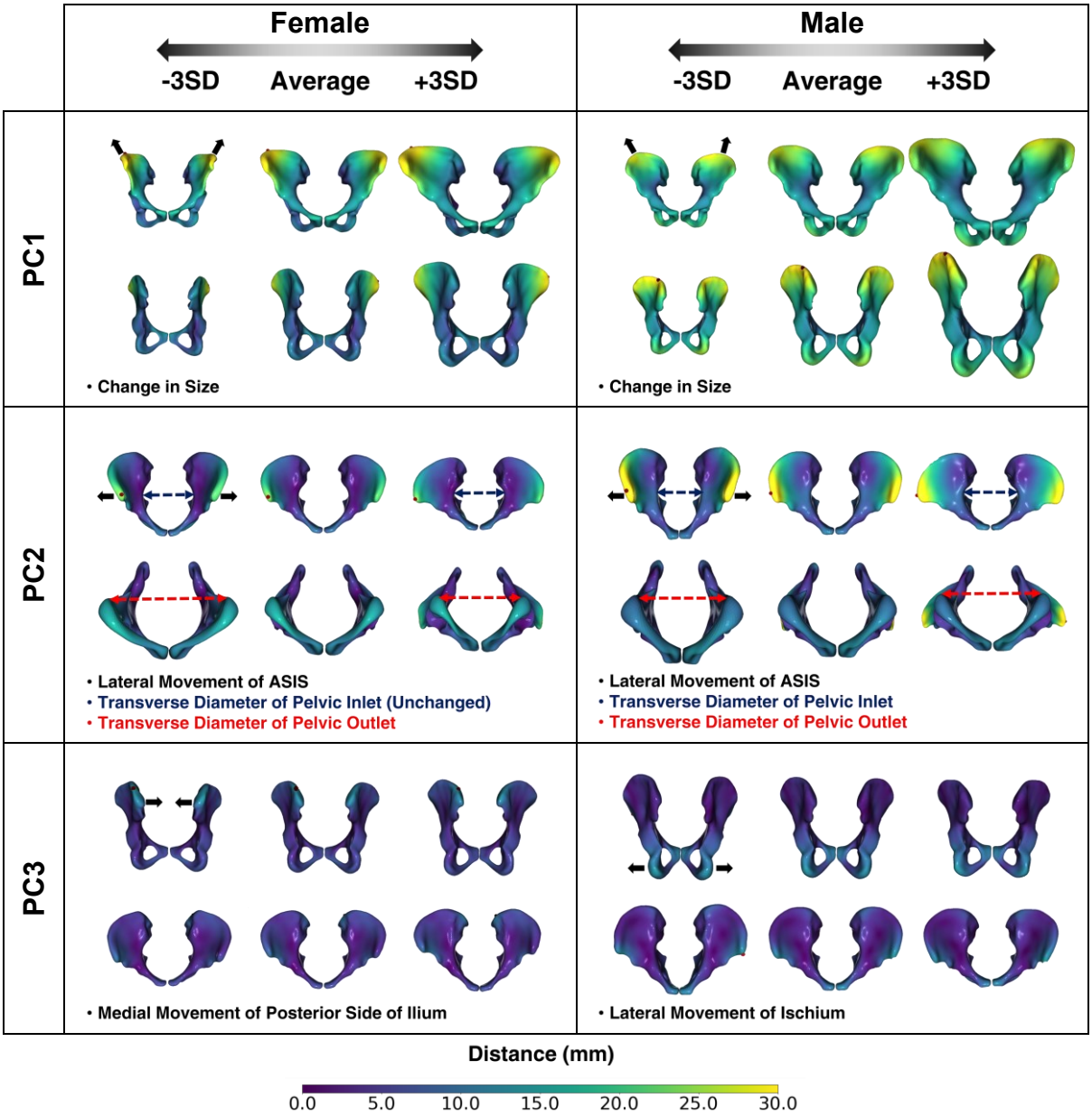

Figure 3-5: The first three PCs for the anatomical variation on the pelvis. The PCs are presented within the range of ±3 SD. The color mapping shows the distance between the extreme instances (associated with ±3SD) and the average model. The red dot shows the location of the maximum distance.

Table 3-2: The results of the principal component analyses for the anatomical variations. For the first five PCs, the modal contribution as well as the average and maximum distance between the average model and the extreme instance (associated with ±3SD) are reported. In addition, the total variance is reported (normalized). Furthermore, the results of the permutation-based tests are reported, which include the p-value of two statistics of the correlation matrix (Psi and Phi, one-tail t-student test), the number of valid PCs, and their cumulative contribution.

Quantity	PC	Hemipelvic Shape		Hemipelvis		Pelvis	
		Female	Male	Female	Male	Female	Male
Modal Contribution (%)	1	22.1	31.0	52.1	61.1	53.9	55.0
	2	13.0	12.2	11.8	10.2	16.2	20.0
	3	11.1	10.0	5.9	5.2	7.2	5.6
	4	9.2	7.0	5.1	3.9	4.1	3.8
	5	7.2	5.6	4.1	3.0	3.7	2.9
Average Distance (mm)	1	4.8	5.9	10.3	14.3	14.5	18.3
	2	3.7	4.0	4.7	5.3	7.6	9.4
	3	3.3	3.5	3.3	4.0	5.6	5.4
	4	3.2	3.1	3.1	3.2	4.0	4.3
	5	2.9	2.7	2.8	3.2	3.7	3.7
Maximum Distance (mm)	1	14.5	20.8	20.4	27.1	33.2	32.9
	2	11.6	11.6	13.9	18.2	24.0	36.9
	3	12.9	14.9	11.1	12.0	13.3	15.0
	4	7.9	7.1	10.2	16.1	13.5	14.1
	5	7.0	7.2	8.7	7.0	13.3	16.0
Total Variance		0.0	0.24	0.36	0.58	0.74	1.00
Psi, P-value		0*	0	0	0	0	0
Phi, P-value		0	0	0	0	0	0
Nr. of Significant PCs		10	9	6	5	3	3
Cumulative Variance (%)		80.7	80.0	82.4	83.4	77.3	80.7
* Less than machine epsilon							

3.3.3 Significant regions of asymmetry

Figure 3-6 shows the color map plots for the *local asymmetry* on the studied structures. The overall statistics of the local asymmetry are reported in Table 3-2. The color map plots for the statistical significance of the local asymmetry are presented in Figure B-0-2.

The matching asymmetry of the *hemipelvic shape* was at the same level for the male and female groups, with an average value of 1.1 mm for both groups (Table 3-3). For the female group, the local asymmetry reached the maximum value of 2 mm at the iliac tuberculum, and for the male group, the maximum value was equal to 1.9 mm at the ASIS (Figure 3-6, and Table 3-3). In addition to the ASIS and iliac tuberculum, (1) the posterior side of the ilium, (2) the pubic tubercle, and (3) ischial tuberosity (only for the male group) showed significant asymmetry (Figure 3-6). For the *hemipelvis*, the patterns of local asymmetry were similar to those for the hemipelvic shape (Figure 3-6). Comparing the hemipelvic models with and without size, the location of the maximum distance between the left-right samples did not change noticeably (black dots in Figure 3-6).

For the *pelvis*, the average value for the local (bilateral) asymmetry was 1.7 mm for the female group and 1.6 mm for the male group (Table 3-3). For the female pelvis, the local asymmetry reached the maximum value in the neighborhood of PSIS (Figure 3-6). For the male group, the maximum asymmetry was located on the bottom of the ischium (Figure 3-6). Other regions did not show significant local asymmetry (Appendix B).

	Female	Male

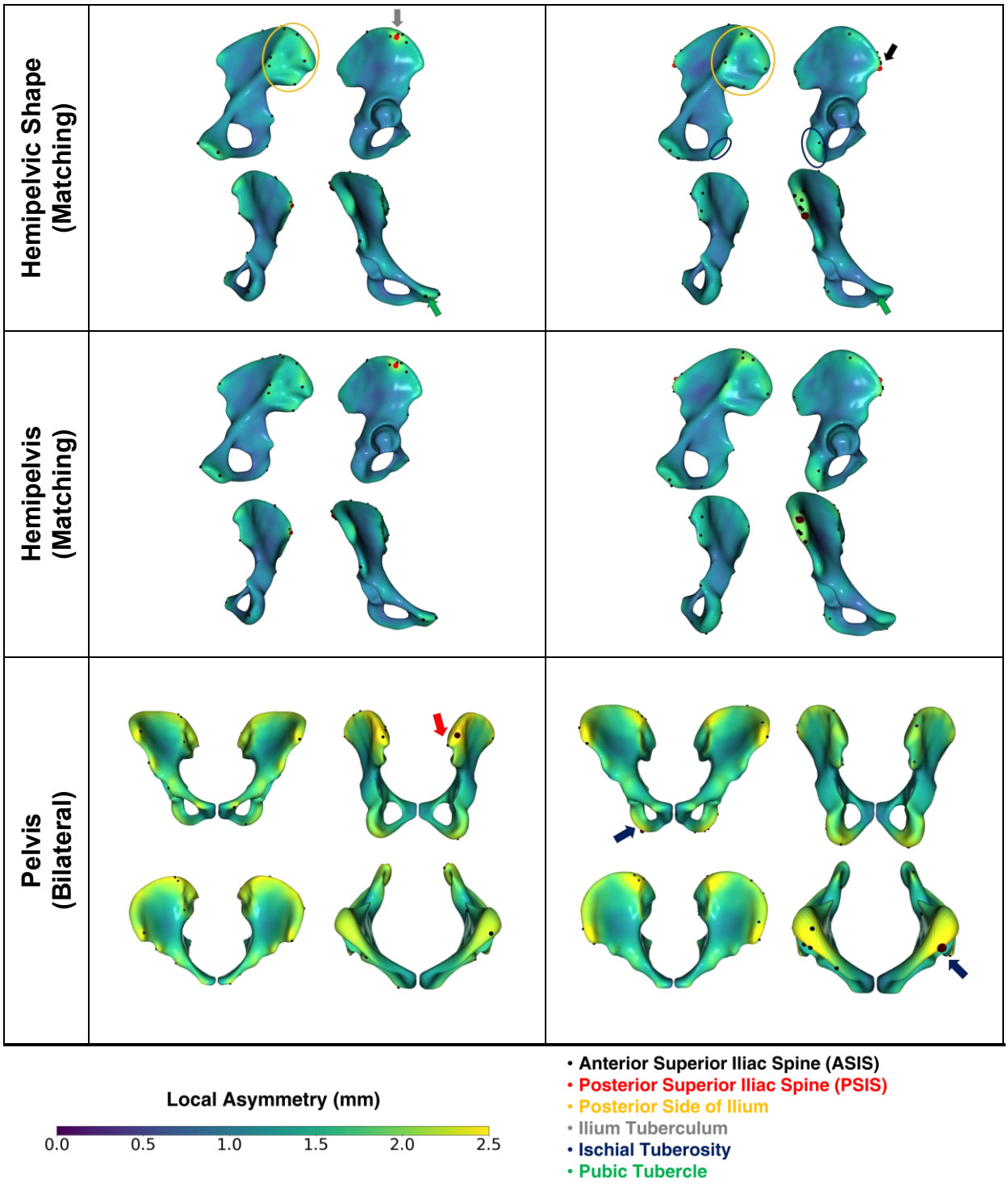

Figure 3-6: Color map plots for the local asymmetry of the studied structures: matching asymmetry on the hemipelvic shape, matching asymmetry on the hemipelvis, and the bilateral asymmetry on the pelvis. The red dot shows the location of the maximum local asymmetry. The

black dots show the locations of the maximum distance between the paired samples (left-right samples for matching asymmetry of the hemipelvis and actual-reflective samples for bilateral asymmetry of the pelvis). The hemipelvis is visualized from lateral (top-left), medial (top-right), posterior (bottom-left) and anterior views (bottom-right). The views of the pelvis include anterior (top-left), posterior (top-right), inlet (bottom-left) and outlet (bottom-right).

Table 3-3: Statistics of the local asymmetry on the studied structures (mm).

Structure	Sex	Mean (mm)	SD (mm)	Min (mm)	Max (mm)
Hemipelvic Shape	Female	1.1	0.3	0.6	2.0
	Male	1.1	0.2	0.6	1.9
Hemipelvis	Female	1.1	0.3	0.6	2.0
	Male	1.2	0.3	0.6	2.0
Pelvis	Female	1.7	0.3	1.1	2.8
	Mala	1.6	0.3	0.9	2.6

3.3.4 Patterns of asymmetry

Figure 3-7 and Figure 3-8 presents the first three PCs for the *asymmetry of the hemipelvis and pelvis*, in the range of ±3 SD. The PCs for the *asymmetry of the hemipelvic shape* were similar to the patterns in the hemipelvis and not reported here. The results of the PCA analyses and permutation-based tests are provided in Table 3-4. Based on the tests, correlational structure exists in all of the datasets, and at least, the first three PCs represented significant patterns of asymmetry in the datasets (Table 3-4).

For the *matching asymmetry of the hemipelvis*, the first mode explained 17.1% of the total variance for the male group and 16.8% in the female group (Table 3-4). For the male group, PC1 showed comparable traits to those observed in PC1 for the anatomical variation on the hemipelvic

shape, i.e. the lateral-medial movement of the ASIS and the rotation of the ischio-pubic unit (Figure 3-7, PC1-Male). For the female group, PC1 included (1) the elevation/depression of the pubic symphysis, (2) a change in the curvature of the iliac crest, and (3) a notable movement on the ilio-pubic eminence (Figure 3-7, PC1-Female). In PC1 for the female group, as the pubic symphysis moved downward, the S-shaped pattern on the iliac crest became more pronounced (Figure 3-7, PC1-Female).

The second mode contributed to 12.3% of the total variance in the male group and 15.3% in the female group (Table 3-4). For the male group, PC2 affected the innominate length by the opposite elevation/depression of the iliac crest and ischio-pubic unit (Figure 3-7, PC2-Male). For the female group, PC2 influenced the iliac breadth, with notable movement at the iliac tubercle and PSIS (Figure 3-7, PC2-Female). The third mode explained 8.8% and 9.9% of the total variance in the male and female groups, respectively (Table 3-4). For the male group, PC3 included a noticeable movement on the medial border of the ilium that separates the iliac fossa from the posterior side of the ilium (Figure 3-7, PC3-Male). For the female group, PC3 affected the innominate length with an elevation/depression of the iliac crest; unlike PC2 for the male group, we did not observe a notable movement on the ischium and pubis in this mode (Figure 3-7, PC3-Female).

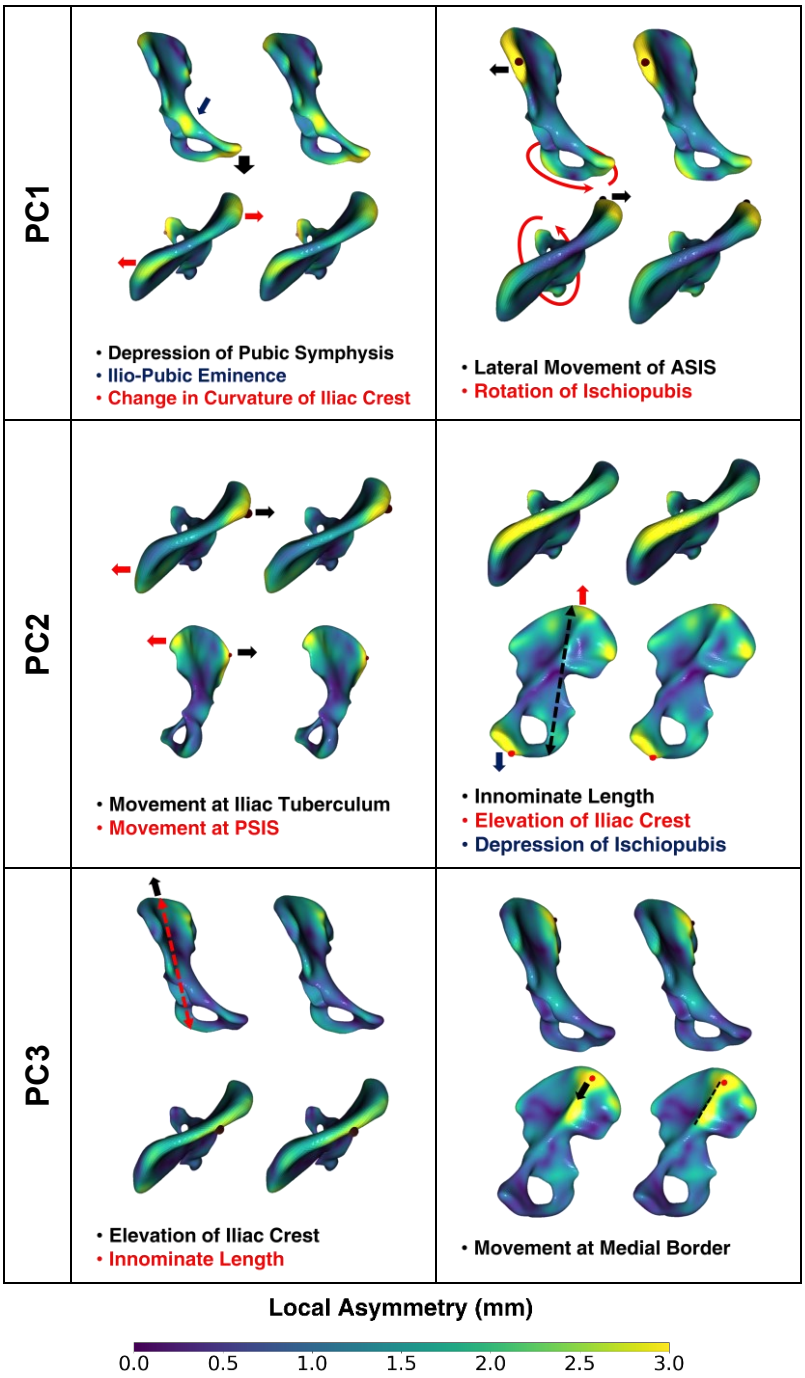

Figure 3-7: The first three PCs of the matching asymmetry of the hemipelvis. The color mapping shows the distance between the average model and the extreme instances associated with ±3 SD. Only the extreme instances are drawn for each PC. The red dot shows the location of the maximum displacement for each PC.

For the *bilateral asymmetry of the pelvis*, the first PC contributed to 28.7% and 37.6% of the total variance in the male and female groups, respectively (Table 3-4). For the male group, PC1 was the elevation/depression of the left-right hemipelves in opposite directions (Figure 3-8, PC1-Male). For the female group, PC1 was the rotation of the left-right hemipelves around the oblique axes (Figure 3-8, PC1-Female). The second mode contributed to 18.9% of the total variance in the male group and 21.2% in the female group. For the male group, PC2 included a lateral-medial movement of the ischium (Figure 3-8, PC2-Male). For the female group, PC2 showed lateral-medial movements on the ischium and iliac crest (Figure 3-8, PC2-Female). The third mode explained 12.1% of the variance in the male group and 11.8% in the female group. For the male group, PC3 was the lateral-medial movement of the ASIS with noticeable changes on the sacroiliac (SI) joint surface (Figure 3-8, PC3-Male). For the female group, PC3 was the anteroposterior movement of the ischium (Figure 3-8, PC3-Female).

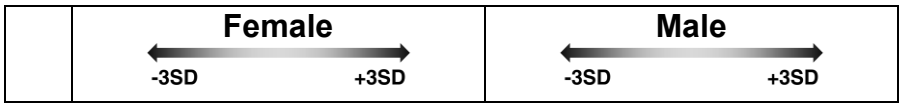

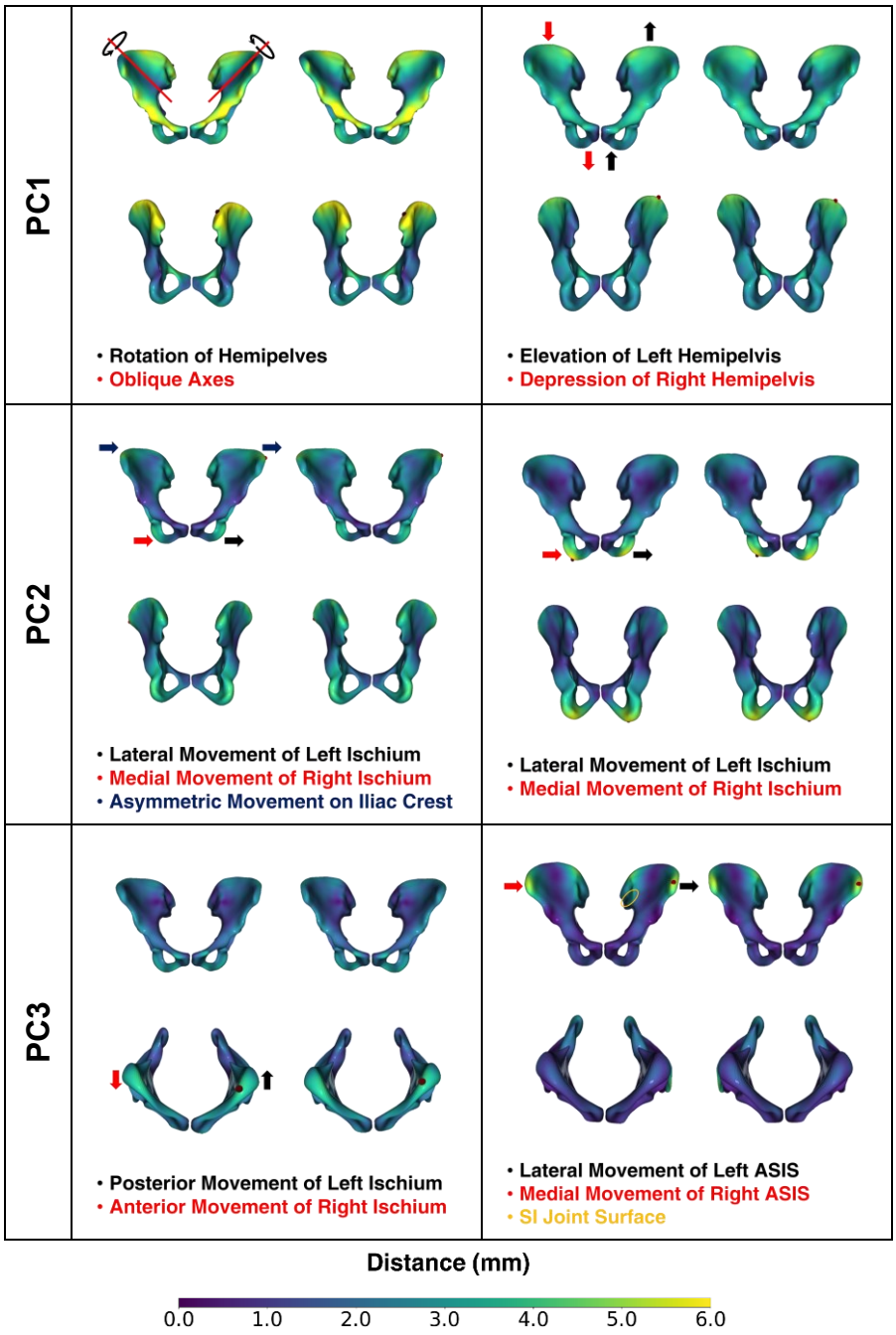

Figure 3-8: The first three PCs for the bilateral asymmetry of the pelvis. The color mapping shows the distance between the average instance and the extreme instances associated with ±3 SD. The red dot shows the location of the maximum movement on each PC.

Table 3-4: The results of the principal component analyses for the asymmetry (matching and bilateral). For the first five PCs, the modal contribution as well as the average and maximum distance between the average model and the extreme instance (associated with ±3SD) are reported. Furthermore, the results of the permutation-based tests are reported, which include the p-value of two statistics of the correlation matrix (Psi and Phi, one-tail t-student test), the number of valid PCs, and their cumulative contribution. The total variance is also reported (normalized).

Quantity	PC	Hemipelvic Shape		Hemipelvis		Pelvis	
		Female	Male	Female	Male	Female	Male
Modal Contribution (%)	1	18.8	16.6	17.1	16.8	37.6	28.7
	2	15.6	11.6	15.3	12.3	21.2	18.9
	3	8.1	8.9	9.9	8.8	11.8	12.1
	4	7.3	8.0	7.9	7.8	5.4	6.5
	5	5.8	6.5	6.4	6.8	4.0	4.5
Average Distance (mm)	1	1.5	1.3	1.4	1.4	3.5	2.8
	2	1.3	1.1	1.3	1.3	2.6	2.1
	3	1.0	1.0	1.1	1.0	1.9	1.6
	4	0.9	0.9	1.0	1.0	1.2	1.3
	5	0.8	0.9	0.8	0.9	1.1	1.1
Maximum Distance (mm)	1	4.8	4.2	4.2	4.6	6.1	5.0
	2	4.4	3.9	3.6	3.4	5.6	6.4
	3	2.8	3.8	2.7	3.9	4.0	5.2
	4	3.1	2.5	2.6	2.8	4.3	3.8
	5	2.8	2.7	2.9	3.0	3.6	2.6
Total Variance		0.40	0.38	0.40	0.42	1.00	0.83
Psi, P-value		0.0	0.0	0.0	0.0	0.0	0.0
Phi, P-value		0.0	0.0	0.0	0.0	0.0	0.0
Nr. of Significant PCs		5	6	5	6	4	4
Cumulative Variance (%)		55.7	57.2	56.6	58.4	75.9	66.3

3.3.5 Sexual dimorphism

In Figure 3-9, the DVF between the male and female average models is intensified and visualized for each structure. The results of the sex-related DVFs and Mann-Whitney tests are presented in Table 3-5. For all three structures, the displacement field was significant (Table 3-5).

For the *hemipelvic shape*, the maximum distance between the male and female average models was 8.0 mm, located on the posterior Inferior Iliac Spine or PIIS. For the male group, the PIIS was located at a lower position, and the sciatic notch was narrower (Figure 3.9). For the average male model, the ilium was upright, while the average female model had a curved and shorter ilium in comparison (Figure 3.9). The superior pubic and the ischiopubic rami were longer and thinner for the female group (Figure 3.9).

For the *hemipelvis*, the maximum distance between the male and female average models was 12.3 mm, located on the ischium (Figure 3.9). The average male model was larger than the model of the female group and the differences in the ilium, pubis, and ischium followed the same patterns as those described for the hemipelvic shape (Figure 3.9).

For the *pelvis*, the maximum distance between the male and female average models was also located on the ischium, 12.8 mm. The average pelvis for the male group was larger than the average female pelvis. The subpubic angle, which is formed by the inferior pubic rami was wider for the female group. Despite the smaller size of the average female pelvis, the pelvic inlet and outlet were wider for the female group.

Table 3-5: The average and maximum distance between the male and female average models; the P-value for the Mann-Whitney tests on the projection of the DVFs defined between the samples and the overall average with the DVF defined between the male and female samples.

Structure	Average Distance (mm)	Maximum Distance (mm)	P-value
Hemipelvic Shape	2.7	8.0	9.69e-15
Hemipelvis	5.3	12.3	2.34e-8
Pelvis	5.9	12.8	2.34e-5

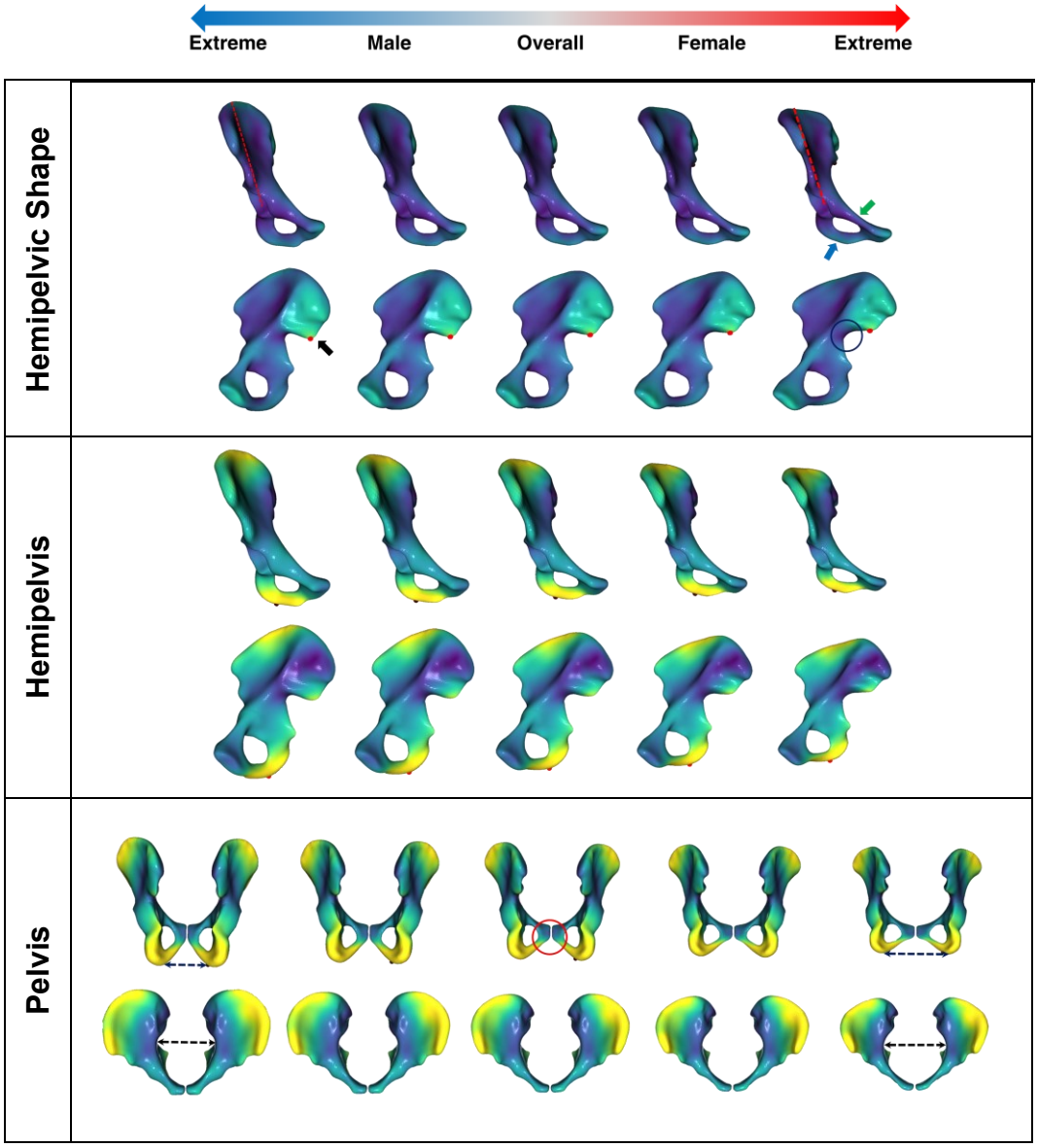

Figure 3-9: The intensified DVF between the male and female average models for the studied structures. The color mapping shows the distance between the sex-specific average model

(female or male). The red dot shows the location of the maximum distance between the average models.

3.4 Discussion

The traditional pelvic morphometrics was limited to the assessment of discrete measurements, which did not fully capture the complex 3D geometry of the pelvis [4]. The emergence of GM and advancements in 3D data acquisition and computations facilitated the morphological study of the entire pelvic geometry [4]. In the last two decades, SSMs have been employed to assess various aspects of pelvic morphology [6-11].

The objective of this study was to investigate the anatomical variation, asymmetry, and sexual dimorphism of the male and female pelvis, using statistical shape modelling. We analyzed the pelvis geometry at three different levels: the hemipelvis with normalized size (hemipelvic shape), the hemipelvis with actual size (hemipelvis), and the left-right hemipelves in the pelvic structure (referred to as the pelvis). Using a computational pipeline, the CT image database from 40 subjects (20 male, 20 female) was transformed into tangible representations in correspondence (triangle mesh with high-quality tessellation). Using the GPA, we extracted DVFs related to anatomical variation, asymmetry, and sexual dimorphism. PCA was then employed to identify the dominant patterns of anatomical variation and asymmetry. Using local measurements of the DVFs, the areas of significant anatomical variation and asymmetry were identified. Sexual dimorphism was also investigated using the intensified DVF between the male and female average models. The

models for the local anatomical variation, local asymmetry, and patterns of bilateral asymmetry on the pelvis were novel contributions of this study.

Our results regarding *anatomical variation* showed that the Anterior Superior Iliac Spine (ASIS) was the location of highest anatomical variation in all three structures for both male and female groups (Figure 3-2). ASIS movement, especially the lateral-medial movement, was among the main patterns of anatomical variation in all three structures. This pattern has been reported in previous studies, e.g. PC2 for an overall pelvic model for 50 Japanese subjects (male and female) [8]. The most dominant mode of anatomical variation for the hemipelvis and pelvis was related to changes in scale, which has been reported by previous studies [6-10].

The analyses of pelvic asymmetry revealed that ASIS, iliac tuberculum, pubic tubercle, the posterior side of the ilium, and ischial tuberosity (only for men) were areas of significant matching asymmetry. Our results for the matching asymmetry of the hemipelvis were in line with a study by Audenaert et. al. [6], in which the insertion sites of muscle groups were reported as the areas of high matching asymmetry (the ASIS attached to the sartorius, iliac crest to abdominal muscles, pubis to adductor muscles, and ischium to hamstrings).

The dominant mode of bilateral asymmetry for both the male and female groups was related to the positioning/orientation of the left-right hemipelves (an elevation/depression for the male group and an oblique rotation for the female group). Our models for the bilateral asymmetry of the pelvis included traits reported by Handrich et. al. [11] who identified six distinct asymmetry patterns based on the visual inspection of 4 pelvic models for anatomical variation (European and

Asian, male and female) [11]. These regions included the sacrum, iliac crest, pelvic brim, pubic symphysis, inferior pubic ramus, and acetabulum, all of which showed high asymmetric movements in our study as well (with exception fo the sacrum which was not included in our study).

Our results for the sexual dimorphism of the pelvis were in line with the distance color plots presented in Aarand et. al. [8]. Furthermore, our models exhibited similar traits as those extensively explained in traditional morphometric studies [27].

For all structures, the male group showed higher anatomical variation in comparison with the female group (statistics of the local anatomical variation in Table 3.1, total variance of the anatomical variation in Table 3.2). For the structures with actual size, the change of size was more dominant in the male group (modal contribution of PC1 in Table 3.2).

The matching asymmetry was at the same level for the male and female groups, while the bilateral asymmetry was slightly higher for women (statistics of the local asymmetry in Table 3.3, total variance of asymmetric patterns in Table 3.4).

When incorporating the pose of the hemipelvis to its shape-size, the average local anatomical variation increases by 32% for the male group and 37% for the female group (Table 3.1); comparing the bilateral asymmetry of the pelvis and matching asymmetry of the hemipelvis, the average local asymmetry increases 33% for the male group and 54% for the female group (Table 3.3).

This study had two limitations: first, we did not have access to the sacrum and coccyx in our database; second, the sample size was limited to 20 male and 20 female individuals. The adequate sample size to cover the entire variation within a population is suggested to be around 200 for the lower-limb bones and the pelvis [6]. Admittedly, there could be patterns of anatomical variation or asymmetry which were not covered in this study. Nevertheless, using the statistical tests, we demonstrated that the reported patterns represented meaningful features within the pelvic bone.

Our models for the patterns of anatomical variation could be of interest to implant design companies to generate artificial bone models and provide better-fitting implants for patients requiring implant surgeries. Our asymmetry analyses are relevant to unilateral surgeries of the pelvis, in which the intact side of the pelvis serves as a reference for surgical planning. In addition, our computational pipeline to assess asymmetry could be used as a quantification tool for the follow-up of pelvic surgeries. The significant patterns of anatomical variation, asymmetry, and sexual dimorphism are animated, providing informative sources for the medical community in general.

3.5 Chapter conclusion

This study used SSM to investigate the female and male pelvic morphology in terms of anatomical variation, asymmetry, and sexual dimorphism. We analyzed the pelvis at three levels including the hemipelvis (with and without size) and the pelvis (without sacrum and coccyx). For each structure, the significant patterns of anatomical variation and asymmetry, as well as

significant areas, were identified. This study provides beneficial models for implant-design companies and is informative for unilateral surgeries related to the pelvis and educational purposes in general.

Reference

[1] Ead, M. S. (2020). Virtual Reconstruction of Pelvic Fractures.

[2] Wittman, Anna Blackburn, and L. Lewis Wall. "The evolutionary origins of obstructed labor: bipedalism, encephalization, and the human obstetric dilemma." Obstetrical & gynecological survey 62, no. 11 (2007): 739-748.

[3]Dryden, I. L., & Mardia, K. V. (2016). Statistical shape analysis: with applications in R (Vol. 995). John Wiley & Sons.

[4] Slice, Dennis E. "Geometric morphometrics." Annu. Rev. Anthropol. 36 (2007): 261-281.

[5] Ambellan, Felix, Hans Lamecker, Christoph von Tycowicz, and Stefan Zachow. Statistical shape models: understanding and mastering variation in anatomy. Springer International Publishing, 2019.

[6] Audenaert, Emmanuel A., Christophe Pattyn, G. Steenackers, Joris De Roeck, Dirk Vandermeulen, and Peter Claes. "Statistical shape modelling of skeletal anatomy for sex discrimination: their training size, sexual dimorphism, and asymmetry." Frontiers in bioengineering and biotechnology 7 (2019): 302.

[7] Ahrend, Marc-Daniel, Hansrudi Noser, Rukmanikanthan Shanmugam, Felix Burr, Lukas Kamer, Tunku Kamarul, Heinz Hügli, Andreas Nagy, Robert Geoff Richards, and Boyko Gueorguiev-Rüegg. "Development of generic Asian pelvic bone models using CT-based 3D statistical modelling." Journal of orthopaedic translation 20 (2020): 100-106.

[8] Arand, Charlotte, Daniel Wagner, Robert Geoff Richards, Hansrudi Noser, Lukas Kamer, Takeshi Sawaguchi, and Pol M. Rommens. "3D statistical model of the pelvic ring–a CT-based statistical evaluation of anatomical variation." Journal of Anatomy 234, no. 3 (2019): 376-383.

[9] Brynskog, Erik, Johan Iraeus, Matthew P. Reed, and Johan Davidsson. "Predicting pelvis geometry using a morphometric model with overall anthropometric variables." Journal of biomechanics 126 (2021): 110633.

[10] van Veldhuizen, Willemina A., Hylke van der Wel, Hennie Y. Kuipers, Joep Kraeima, Kaj Ten Duis, Jelmer M. Wolterink, Jean-Paul PM de Vries, Richte CL Schuurmann, and Frank FA IJpma. "Development of a Statistical Shape Model and Assessment of Anatomical Shape Variations in the Hemipelvis." Journal of Clinical Medicine 12, no. 11 (2023): 3767.

[11] Handrich, Kristin, Lukas Kamer, Keith Mayo, Takeshi Sawaguchi, Hansrudi Noser, Charlotte Arand, Daniel Wagner, and Pol M. Rommens. "Asymmetry of the pelvic ring evaluated by CT-based 3D statistical modelling." Journal of anatomy 238, no. 5 (2021): 1225-1232.

[12] Von Elm, Erik, Douglas G. Altman, Matthias Egger, Stuart J. Pocock, Peter C. Gøtzsche, Jan P. Vandenbroucke, and Strobe Initiative. "The Strengthening the Reporting of Observational Studies in Epidemiology (STROBE) Statement: guidelines for reporting observational studies." International journal of surgery 12, no. 12 (2014): 1495-1499.

[13] Ead, M. S., Palizi, M., Jaremko, J. L., Westover, L. & Duke, K. K. Development and application of the average pelvic shape in virtual pelvic fracture reconstruction. Int. J. Med. Robot. **17,** e2199 (2021).

[14] Kazhdan, M., Bolitho, M. & Hoppe, H. Poisson surface reconstruction in Proceedings of the fourth Eurographics symposium on Geometry processing, **7** (2006).

[15]Taubin, G. (1995, June). Curve and surface smoothing without shrinkage. In Proceedings of IEEE international conference on computer vision (pp. 852-857). IEEE.

[16] Pietroni, Nico, Marco Tarini, and Paolo Cignoni. "Almost isometric mesh parameterization through abstract domains." IEEE Transactions on Visualization and Computer Graphics 16, no. 4 (2009): 621-635.

[17] Yuksel, C. (2015, May). Sample elimination for generating Poisson disk sample sets. In Computer Graphics Forum (Vol. 34, No. 2, pp. 25-32).

[18] Luo, C., Ge, X., & Wang, Y. (2018, February). Uniformization and density adaptation for point cloud data via graph Laplacian. In Computer Graphics Forum (Vol. 37, No. 1, pp. 325-337).

[19] Laga, H., Guo, Y., Tabia, H., Fisher, R. B., & Bennamoun, M. (2018). 3D Shape analysis: fundamentals, theory, and applications. John Wiley & Sons.

[20] van de Giessen, M., Vos, F. M., Grimbergen, C. A., van Vliet, L. J., & Streekstra, G. J. (2012). An efficient and robust algorithm for parallel groupwise registration of bone surfaces. In Medical Image Computing and Computer-Assisted Intervention–MICCAI 2012: 15th International Conference, Nice, France, October 1-5, 2012, Proceedings, Part III 15 (pp. 164-171). Springer Berlin Heidelberg.

[21] Myronenko, A., & Song, X. (2010). Point set registration: Coherent point drift. IEEE transactions on pattern analysis and machine intelligence, 32(12), 2262-2275.

[22] Cootes, T. F., Taylor, C. J., Cooper, D. H., & Graham, J. (1995). Active shape models-their training and application. Computer vision and image understanding, 61(1), 38-59.

[23] Mardia, K. V., Bookstein, F. L., & Moreton, I. J. (2000). Statistical assessment of bilateral symmetry of shapes. Biometrika, 87(2), 285-300.

[24] Baclig, M. M., Westover, L., & Adeeb, S. (2019). Categorizing three-dimensional symmetry using reflection, rotoinversion, and translation symmetry. Symmetry, 11(9), 1132.

[25] Camargo, A. (2022). PCAtest: testing the statistical significance of principal component analysis in R. PeerJ, 10, e12967.

[26] Conover, W. J. (1999). Practical nonparametric statistics (Vol. 350). john wiley & sons.

[27] Styner, M., Lieberman, J. A., Pantazis, D., & Gerig, G. (2004). Boundary and medial shape analysis of the hippocampus in schizophrenia. Medical image analysis, 8(3), 197-203.

[28] Bruzek, J. (2002). A method for visual determination of sex, using the human hip bone. American Journal of Physical Anthropology: The Official Publication of the American Association of Physical Anthropologists, 117(2), 157-168.

CHAPTER 4: QUALITY MEASURES OF STATISTICAL SHAPE MODELS FOR HEMIPELVIS AND TALUS

This chapter is derived from the paper in preparation:

Palizi, M. & Adeeb S. (2023). Quality measurement of anatomical shape models in simulation of training shapes and unseen shapes (hemipelvis and talus).

Abstract

Statistical shape models describe geometric variations on anatomical structures and facilitate orthopaedic applications such as image segmentation, virtual bone reconstruction, and the design of implant components. The present study aims to measure the quality of statistical shape models in simulating the in-training samples (accuracy) as well as predicting unseen samples (generalization ability) for two bone structures, the hemipelvis, and the talus. Our study distinguishes between the original and registered representations of the shape samples and evaluates the accuracy and generalization ability by comparing the SSM instances with the original representations of the samples. Coherence point drift (CPD) is employed to establish correspondence between the training samples. Principal component analysis (PCA) is used to create 12 models (hemipelvis/talus, shape/shape-size, male/female/overall). The model properties including compactness, accuracy, and generalizability are characterized and evaluated. Our results show that (1) the accuracy of the models, when all of the PCs are included, is in the range of 0.23-

0.26 mm for the talus and 0.69-0.71 mm for the hemipelvis (shape/shape-size, male/female/overall), (2) the accuracy of the average shape models and the shape-size models with PC1 is in the range of 0.58-0.68 mm for the talus and 1.72-2.04 mm for the hemipelvis (male/female/overall), (3) the generalizability of sex-specific models with full capacity is in the range of 0.37-0.41 mm for the talus and 1.26-1.47 mm for the hemipelvis (shape/shape-size), and (4) the incorporation of the male and female datasets into overall models improves the generalization ability, 0.28-0.32 mm for the talus and 1.03-1.18 for the hemipelvis (shape/shape-size).

Keywords: statistical shape models; talus; pelvis; compactness; accuracy; generalization ability.

4.1 Introduction

Statistical shape models (SSMs) describe geometric variations on anatomical structures in a computational format. Statistical models of shape have a wide and growing range of clinical applications. Medical imaging (MI) technologies such as computed tomography (CT) and magnetic resonance imaging (MRI) scan the shape of human organs and skeletal structures in 3D images. Conversion of such images into more tangible shape representations such as triangle meshes is highly demanding; SSM-based approaches have been developed to facilitate the automation of such clinical routines (see [1] for a survey on the application of statistical shape models in image segmentation). SSMs and their average models have been employed in reconstructing the shape of bones with defects [2-5]. Statistical models for 3D shapes have been

used in morphological studies of human bones and organs, upgrading such studies from investigating discrete measurements based on landmarks to 3D morphometric analyses [6-9]. SSMs and their augmented version such as statistical shape and appearance models (SSAMs) have been incorporated into finite element (FE) simulation of skeletal structures to evaluate the risk of bone injuries [10] and reveal the connection between geometry and biomechanics [11-12].

A key factor in the performance of SSM-based algorithms is the plausibility of the generated instances by the SSM. Davies et. al. initially quantified the ability of an SSM to generate "valid" shape instances using measures such as compactness, accuracy, and generalizability [13]. Compactness measures the model's ability to explain the majority of the geometric variance with the smallest number of modes [13]; accuracy measures the quality of the model in explaining the training samples [13]; and, generalizability evaluates the model's performance in predicting unknown samples [13].

Based on the medical application of an anatomical SSM, certain measures become more important. For example, morphological studies favor compact models which capture the majority of geometric variation with the smallest number of modes, possible. Accuracy is relevant to the design of implant components; implant-design companies are in the pursuit of static anatomical templates, scalable templates, and SSMs with only a limited number of modes that model an anatomical entity for a population within a specific distance error threshold. Generalization ability is essential for an accurate fitting of SSMs on image datasets or meshes with missing parts. When the generalizability of a model is close to its accuracy, indicates that the SSM adequately represents the sample population.

This study aims to evaluate the compactness, accuracy, and generalizability of SSMs for two bone structures: the hemipelvis and talus. We develop an automated workflow to construct various types of SSMs (sex-specific and overall models, models with and without size) for the CT image database of 40 pelves (20 male and 20 female) and 96 tali (41 female and 56 male). For these two bone structures, previous studies have measured the SSM qualities by comparing the SSM instances with a representation of the shape samples that were used to construct the SSM [2, 3, 4, 6]. However, the registered representation of the shape samples is computed by a deformable registration process which introduces a deviation from the original geometry of the shape samples. Our study distinguished between the original and registered representations of the shape samples and evaluates the accuracy and generalization ability of the models by comparing the original representation of the shape samples, referred to as the ground truth hereinafter, with the SSM instances.

The remainder of this study is organized as follows: Section (4.2) presents the computational pipeline to convert the image dataset of two bone structures into various types of SSMs as well as the characterization of quality measures. Section (4.3) presents the assessments of the quality measures. In section (4.4), we discuss the findings of the study and compare our results with previous research.

4.2 Materials and methods

Figure 4-1 presents the computational pipeline of the study in detail. The computational process included: (1) conversion of the image dataset into refined triangle meshes and uniform point set, (2) establishment of correspondence, and (3) construction of various models and quality measurements

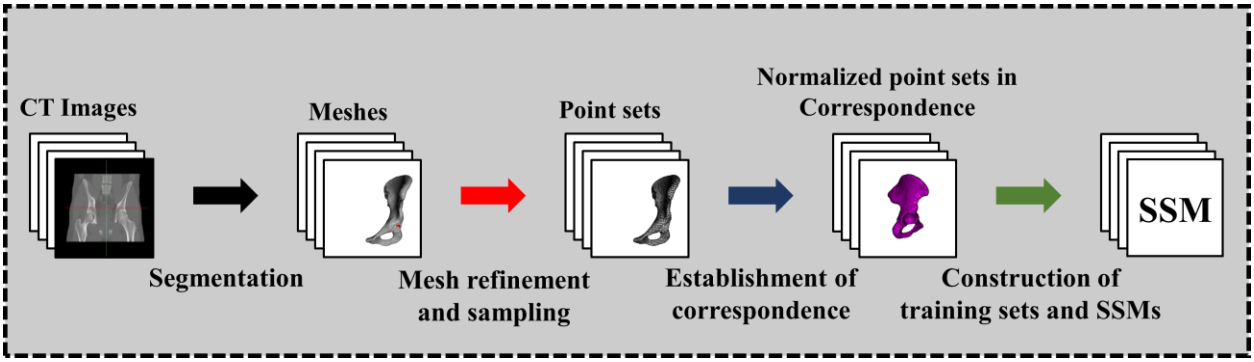

(a)

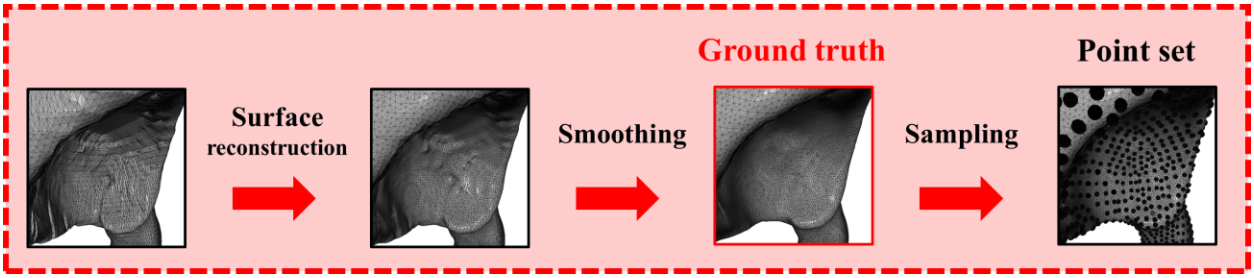

(b)

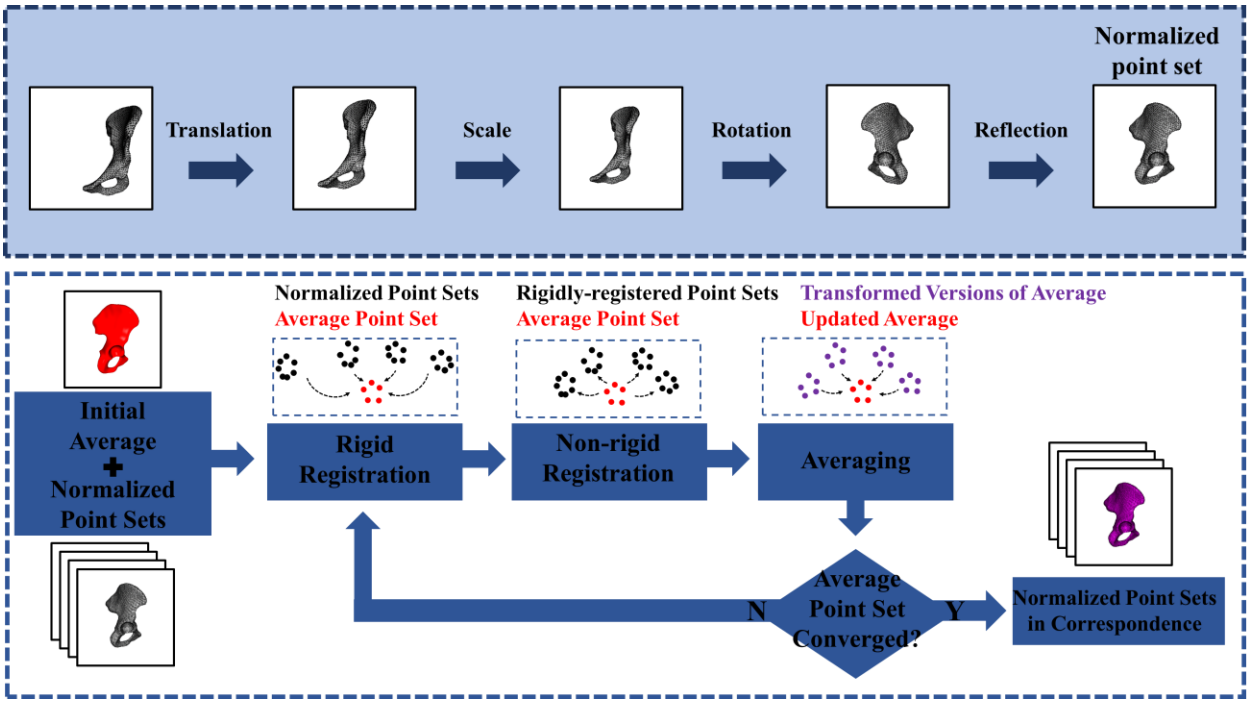

(c)

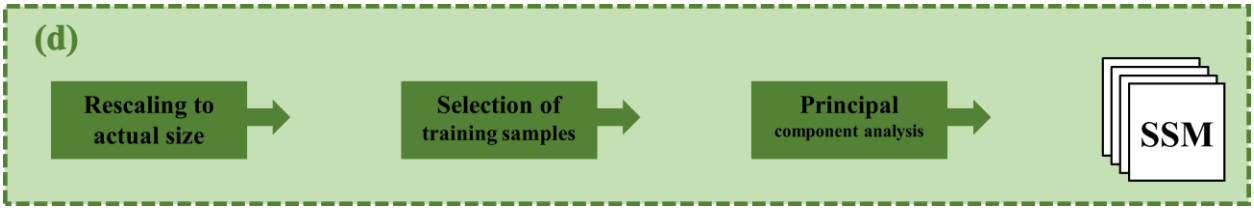

(d)

Figure 4-1: Computational pipeline to build 12 anatomical models. In (a), the main steps to build models are presented for the hemipelvis (starting from the CT images). In (b), the refinement of a segmented mesh is shown around the acetabulum of a hemipelvis. In (c), the coarse alignment of a hemipelvic sample and the schematic diagram to establish correspondence are shown. In (d), the alternatives to generate different training sets and models are presented

4.2.1 Image datasets, refined meshes, and point sets

The study used computed tomography (CT) images of 40 pelvises (20 male and 20 female, age range 18-25 years) and 96 tali (55 male and 41 female, age range of 12-65 years). The approval to use the CT images was obtained from the Health Research Ethics Board at the University of Alberta with the waiver of consent. The images were obtained from different scanning devices; the in-plane pixel length for the images was in the range of 0.44-0.93 millimetre (mm) for the pelvis and equal to 0.39 mm for the talus; the thickness between the image slices was in the range of 1.00-3.00 mm for the hemipelvis and equal to 0.60 mm for the talus.

The CT images of the two bone structures were converted into three-dimensional triangle stereolithography (STL) meshes in two previous studies ([14] for the hemipelvis, and [7] for the talus). Using a parameterization technique [15] and Taubin smoothing [16], the original triangle meshes were converted into watertight meshes with high-quality tessellation. The number of vertices on each refined mesh was approximately 20,000. The resulting refined meshes served as the golden standard or ground truth for measuring the accuracy and generalizability of the SSMs. Using a Poisson-disk point-set sampling algorithm, equipped with uniformization, a uniform point set with 10,000 points was sampled on each refined mesh. The left-right hemipelves belonging to each individual were similar and to avoid introducing bias in the generalizability evaluation, only the information for the left hemipelves was used in the study. In addition, the initial training set of the talus includes 97 subjects; a male subject was removed from the dataset due to local abnormalities (visual inspection of the samples).

4.2.2 Establishment of correspondence

For a set of homologous shape samples, finding invertible and plausible mappings between the shape samples is a crucial step to construct an SSM. By finding such mappings, called correspondence, the samples are described in a common space. To establish correspondence between the samples, firstly, the uniform point sets were coarsely aligned; next, correspondence was established between the coarsely aligned (or normalized) point sets using a groupwise point-set registration method [17].

For the coarse alignment of samples, the centroid, centroid size, and principal axes of uniform point sets were computed (see [18] for the definition of these global descriptors of a point set). The point sets were then normalized w.r.t. translation, scaling, and rotation such that: (1) all of the point sets were centered at the origin, (2) they all had unit centroid size, and (3) their principal axes (ordered from largest to smallest) were aligned with XYZ axes of a global coordinate system. The shape samples for the talus represented the left or right bone for each individual, and an additional reflection was required to align them.

After coarse alignment, the groupwise point-set registration algorithm [17] was performed to establish correspondence between the samples. The groupwise registration algorithm was an iterative process in which (1) each normalized point set was rigidly registered on the average point set, and (2) the average point set was non-rigidly registered on the normalized point sets. Initially, the average point set was selected as the normalized point set with the minimum distance from

other point sets (average point-to-point Euclidean distance between two point sets). Through the non-rigid registration step, the average point set was transformed to capture the geometry of the samples. After each iteration, the arithmetic average of the transformed versions was computed as the updated average point set. For both bone structures, two iterations were sufficient to achieve convergence for the average point set. The transformed versions of the average point set represented the shape samples in correspondence; these point sets are referred to as the point sets in correspondence. For the rigid and non-rigid registration tasks, the Coherent Point Drift (CPD) registration method [19, 20] was used. The parameters of the CPD registration method were adjusted as $\omega=0$,$\beta=2$, and $\lambda=2$ (see Appendix (3) for a detailed description of the CPD registration method).

The converged point set and the normalized point set which was used as the initial average point set were in correspondence and had a dense set of paired points. Using these corresponding pairs and the thin-plate spline transformation [21], the refined mesh for the normalized point set was converted into a mesh representing the average point set, called the average mesh. In a similar process, the average mesh was converted into a mesh representing each one of the shape samples, referred to as the simulated mesh.

Therefore, each shape sample had two meshes: (1) the ground-truth mesh which was extracted from the image dataset and refinement process, and (2) the simulated mesh which was computed in the registration process. During the process of establishing correspondence, the point set for the shape samples underwent a series of rigid transformations (coarse alignment and rigid

registrations). For each sample, these rigid transformations were applied to the ground-truth mesh as well.

4.2.3 Construction of SSMs and quality measures

Using principal component analysis (PCA), six models were constructed for each bone (talus/hemipelvis), including male, female, and overall models for the shape and shape-size of the bone. In a shape model, the geometric information regarding the size of the samples was removed. In comparison, the shape-size models encompass the geometric information regarding the shape as well as the size of the samples. To build a shape model, the point sets in correspondence were considered as the training samples; these point sets shared unit centroid size. To construct shape-size models, the actual size of each sample was restored by scaling, using the original centroid size of the sample. Sex-specific models refer to the models in which only the male or female dataset was used. These models only consider the geometric variation of an anatomical structure within the male or female groups. In comparison, the overall models include all of the samples (regardless of their sex) and describe the modes related to sexual dimorphism (if exists) of a bone as well as the inter-individual variations.

After preparing each training set, the Generalized Procrustes Analysis (GPA) was performed to remove the redundant rigid transformation due to translation and rotation from each training set. To build SSM for each training set, the XYZ coordinates of each sample were arranged into a single vector [13]:

$$\boldsymbol{x}_i = \begin{bmatrix} x_i^{(1)} & y_i^{(1)} & z_i^{(1)} & \dots & x_i^{(n_P)} & y_i^{(n_P)} & z_i^{(n_P)} \end{bmatrix}^T, \ i = 1, \dots, n_S \tag{4-1}$$

in which, n_P is the number of points on a single sample, and n_S is the number of samples, referred to as the *training size*. The average of the sample vectors, denoted by $\boldsymbol{\mu}$, and the (centered) covariance matrix of samples vectors, denoted by $\boldsymbol{\Sigma}$, were computed as follows [13]:

$$\boldsymbol{\mu} = \frac{1}{n_S} \sum_{i=1}^{n_S} \boldsymbol{x}_i \tag{4-2}$$

$$\boldsymbol{\Sigma} = \frac{1}{n_S} \sum_{i=1}^{n_S} (\boldsymbol{x}_i - \boldsymbol{\mu})(\boldsymbol{x}_i - \boldsymbol{\mu})^T \tag{4-3}$$

The rank of the covariance matrix $\boldsymbol{\Sigma}$, denoted by n_M, was noticeably lower than the dimension of a sample vector, i.e. $3n_P$, and equal to $n_S - 1$. Using a standard technique for the low-rank real symmetric matrices [22], the covariance matrix was decomposed into its eigensystem [13]:

$$\boldsymbol{\Sigma} = \sum_{m=1}^{n_M} \lambda_m \boldsymbol{v}_m \boldsymbol{v}_m^T \tag{4-4}$$

$$\boldsymbol{v}_m^T \boldsymbol{v}_n = \delta_{mn} \ , \ \ m, n = 1, \dots, n_M \tag{4-5}$$

in which, λ_m and $\boldsymbol{v}_m$ are m^{th} eigenvalue and (normalized) eigenvector of the covariance matrix and δ_{mn} is the Kronecker delta. The eigenvectors $\boldsymbol{v}_m$ are referred to as the *Principal Components* (PCs). Using the set of orthonormal PCs, each sample vector $\boldsymbol{x}_i$ was expressed as follows [13]:

$$\boldsymbol{x}_i = \boldsymbol{\mu} + \sum_{m=1}^{n_M} b_{im}\boldsymbol{v}_m \quad , \quad i = 1, \dots, n_S \tag{4-6}$$

in which, b_{im} is the score of the i^{th} sample vector on the m^{th} PC [13]:

$$b_{im} = (\boldsymbol{x}_i - \boldsymbol{\mu})^T \boldsymbol{v}_m \tag{4-7}$$

Next, the *total variance*, denoted by Var, was computed as follows [13]:

$$Var = \frac{1}{n_S}\sum_{i=1}^{n_S}(\boldsymbol{x}_i - \boldsymbol{\mu})^T(\boldsymbol{x}_i - \boldsymbol{\mu}) = \sum_{m=1}^{n_M}\lambda_m \tag{4-8}$$

The *modal contribution* of the m^{th} PC and the *cumulative modal contribution* of the first m PCs were computed as follows [13]:

$$Modal\ Contribution(m) = \frac{\lambda_m}{Var} \quad , \quad m = 1, \dots, n_M \tag{4-9}$$

$$Cumulative\ Modal\ Contribution(m) = \frac{\sum_{i=1}^{m}\lambda_i}{Var} \quad , \quad m = 1, \dots, n_M \tag{4-10}$$

C*ompactness* was defined as the minimum number of PCs required to reach 90% of the cumulative modal contribution. Using the first m PCs, a sample vector $\boldsymbol{x}_i$ was approximated as follows [13]:

$$\hat{\boldsymbol{x}}_i(m) = \boldsymbol{\mu} + \sum_{j=1}^{m} b_{ij}\boldsymbol{v}_j \tag{4-11}$$

in which, $\hat{\boldsymbol{x}}_i(m)$ is the approximation of $\boldsymbol{x}_i$ using the first m PCs and b_{in} is computed in Eq. (4-2). Denoting the mesh associated with the approximation of i^{th} shape vector by $\widehat{M}_i(m)$ and the

ground truth mesh of the sample by M_i, the *accuracy* was defined w.r.t. the number of included PCs, m, as follows:

$$Accuracy(m) = \frac{1}{n_S}\sum_{i=1}^{n_S}\widehat{\mathcal{D}}_i(m) \tag{4-12}$$

$$\widehat{\mathcal{D}}_i(m) = \frac{1}{2}\left[d\left(M_i, \widehat{M}_i(m)\right) + d\left(\widehat{M}_i(m), M_i\right)\right] \tag{4-13}$$

in which, $d\left(M_i, \widehat{M}_i(m)\right)$ was the average of the Euclidean distances between the vertices of M_i and the nearest points on the triangles of the mesh $\widehat{M}_i(m)$. The distance measure d was not commutative, i.e. $d\left(M_i, \widehat{M}_i(m)\right)$ and $d\left(\widehat{M}_i(m), M_i\right)$ were not necessarily equal, while $\widehat{\mathcal{D}}_i(m)$ provided a commutative distance measurement between two meshes [23].

Finally, the generalizability of each SSM was computed by a set of leave-one-out tests [13]. In each test, (1) a new training set was created by excluding an individual sample from the original training set, (2) an SSM was constructed for the new training set, and (3) the excluded shape sample was predicted using the model for the new training set. Similar to the characterization of accuracy, denoting the ground-truth mesh of the i^{th} sample by M_i and the mesh associated with the prediction of the excluded shape by $\widetilde{M}_i$, the generalization ability was defined as follows:

$$generlizability = \frac{1}{n_s}\sum_{i=1}^{n_S}\widetilde{\mathcal{D}}_i \tag{4-14}$$

$$\widetilde{\mathcal{D}}_i = \frac{1}{2}\left[d\left(M_i, \widetilde{M}_i\right) + d\left(\widetilde{M}_i, M_i\right)\right] \tag{4-15}$$

in which, d has the same definition as in Eq. (4-7).

Lastly, the comparison of compactness between the two SSMs was meaningful only if the models shared the same training size. To compare two models with different training sizes, the same number of samples was randomly selected from the training sets of two models, the random selection was repeated 100 times, SSMs were constructed for the randomly-selected training sets, and the compactness was compared between the random SSMs (with fixed training size).

4.3 Results

4.3.1 Compactness

Figure 4-2 presents two types of plots: (1) the cumulative modal contribution w.r.t. the number of included PCs for 12 models (talus/hemipelvis, male/female/overall, and shape/shape-size); and (2) the maximum-minimum range of the cumulative modal contribution for the randomized models, referred to as the range plots. In the range plots in Figure 4-2, the randomized models have 15 samples for the talus and 30 samples for the hemipelvis (male/female/overall, shape/shape-size). To draw each plot, the random selection was repeated 50 times. Each range plot compares the compactness between the sex-specific and overall models for a structure (talus/hemipelvis, shape/shape-size). In Figure 4-3, the range plots compare the compactness of the shape/shape-size models for the two studied bones; each range plot is based on 50 experiments, and in each experiment, 30 samples were selected from the overall training sets (shape/shape-size, hemipelvis/talus).

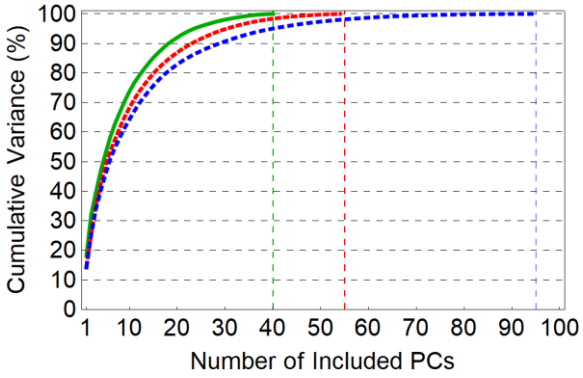

(a) Talus, shape

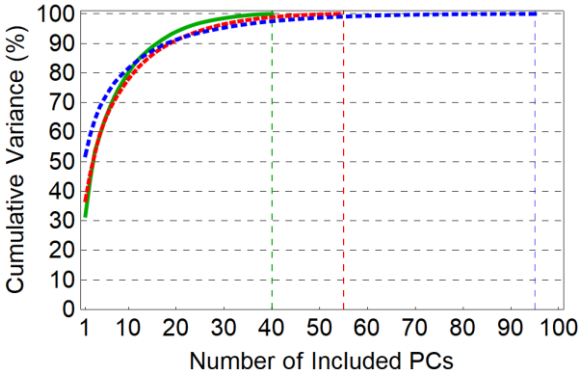

(b) Talus, shape-size

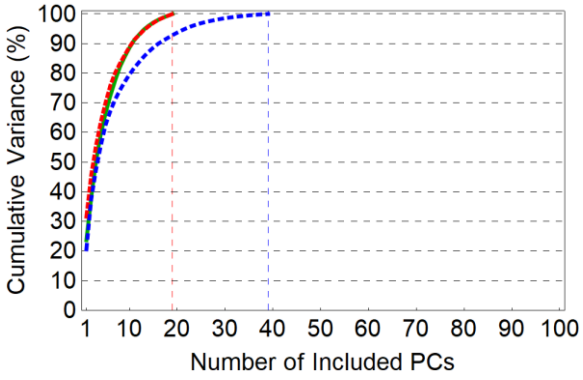

(c) Hemipelvis, shape

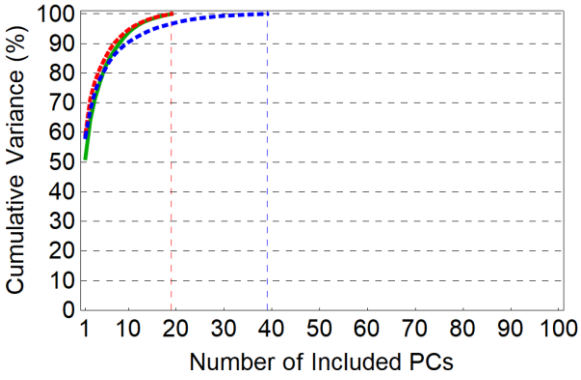

(d) Hemipelvis, shape-size

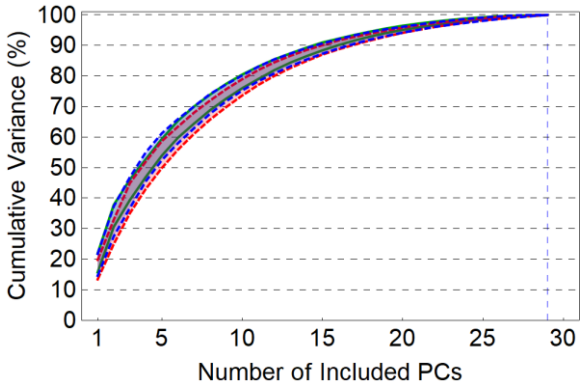

(e) Talus, shape (random)

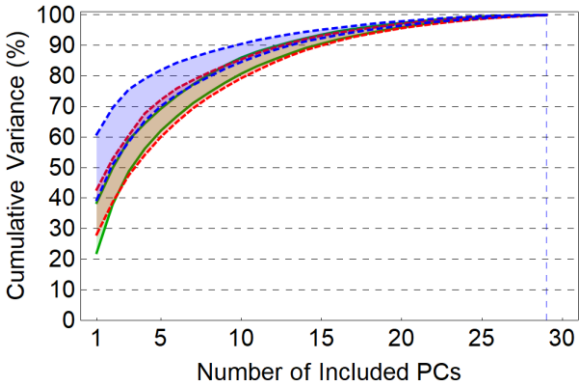

(f) Talus, shape-size (random)

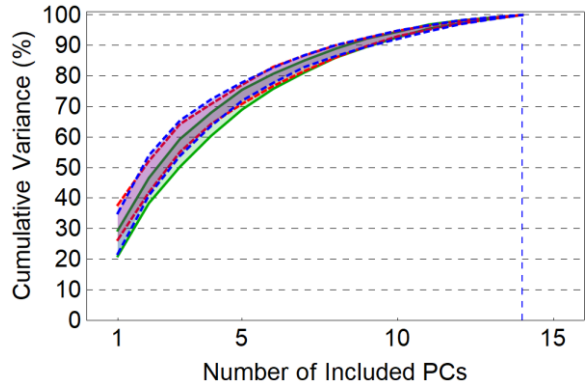

(g) Hemipelvis, shape (random)

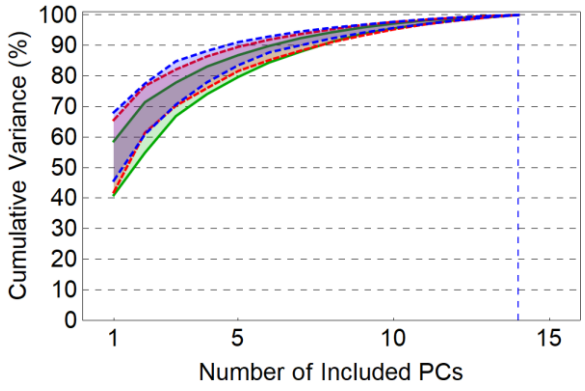

(h) Hemipelvis, shape-size (random)

Figure 4-2: Cumulative modal contribution w.r.t. the number of included PCs for 12 models (a-d) and the maximum-minimum range of cumulative modal contribution for models constructed by random selection of training samples (e-h). The number of randomly-selected samples is 30 for the talus (e and f) and 15 for the hemipelvis (g and h). The random selection was repeated 50 times for each range plot (e-h). In each plot, the models for the male, female, and overall training sets are compared for a structure (shape/shape-size, hemipelvis/talus) (a-h).

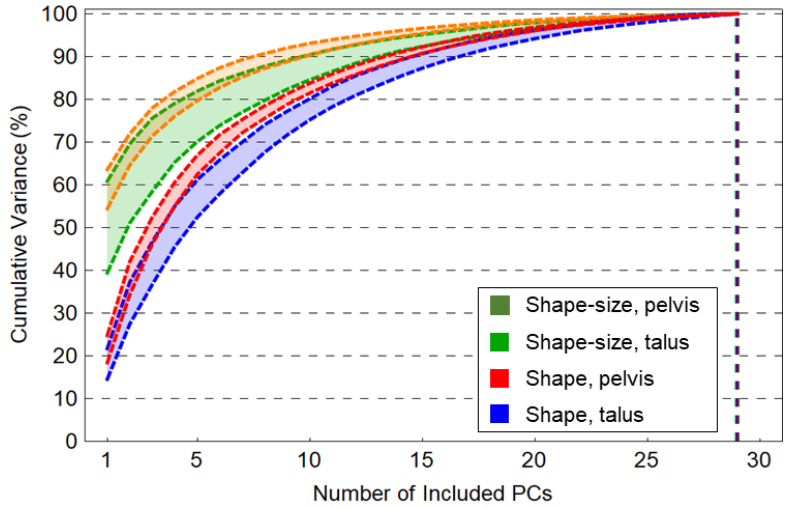

Figure 4-3: Range plots to compare the overall models for the structures (shape/shape-size, hemipelvis/talus). For each structure, 30 samples are randomly selected and the process is repeated 50 times.

In Table (4.1), the model properties such as (1) the total variance, (2) the modal contribution of PC1, (3) the number of PCs required to explain 90% of the total variance, and (4) the average centroid size of the training samples are reported. The total variance of an SSM is reported in two formats: (1) Total variance: the values are only normalized w.r.t. the largest value. (2) Total variance (Norm.): the average centroid size is firstly used to normalize the values of total variance for each model (w.r.t scale), and afterward, all values are normalized w.r.t. the largest value. Based on Eq. (4.3), when all of the training samples of a model are scaled by a single factor, the total variance is proportional to the squared value of the scaling factor. Table (4.1) also reports the number of PCs required to explain 90% of the total variance for the random models (with the same training size), providing a measure of the compactness.

Table 4-1: Total variance, the modal contribution of PC1, the number of PCs required to achieve 90% of the total variance, the average centroid size for 12 models, and the compactness of randomly-selected models.

Bone	Size included?	Sex	Training size	Total variance	Total variance (Norm.)	Modal contribution of PC1 (%)	Nr. of PCs explaining 90% variance	Average centroid size (mm)
Talus	N	F	41	0.00	0.43	18.18	19	1.00
		M	55	0.00	0.43	14.24	24	1.00
		F/M	96	0.00	0.43	14.24	29	1.00
	Y	F	41	0.06	0.61	31.75	16	20.4
		M	55	0.08	0.66	36.94	19	22.6
		F/M	96	0.10	0.92	52.15	18	21.6
Pelvis	N	F	20	0.00	0.38	23.66	11	1.00
		M	20	0.00	0.44	31.61	11	1.00
		F/M	40	0.00	0.47	20.58	17	1.00
	Y	F	20	0.64	0.68	51.33	9	63.6
		M	20	1.00	0.93	59.37	7	68.6
		F/M	40	1.00	1.00	58.43	10	66.2

Talus	N	F/M	30	-	-	14.6-21.8	15-17	-
Talus	Y	F/M	30	-	-	39.4-60.9	10-14	-
Pelvis	N	F/M	30	-	-	18.4-24.8	14-15	-
Pelvis	Y	F/M	30	-	-	54.4-63.6	8-10	-

Figure 4-2 shows that the larger training size of the overall models, in comparison with the sex-specific models, is accompanied by the larger number of PCs required to achieve 90% of the total variance (with exception for talus shape-size, Figure 4-1 (a)-(d)); however, when the effect of training size is nullified by considering random models with the same training size, no specific pattern of compactness is observed between the sex-specific and overall models for the hemipelvic shape, hemipelvic shape-size, and talus shape (Figure 4-1 (e) (g) and (h)). The only exception was the talus shape-size, for which the overall model was more compact (Figure 4-1 (f)); even with the initial training size of 96, 18 PCs are required to achieve 90% of the total variance in the overall model of talus shape-size, while the number of required PCs is 19 for the associated male model (Table 4.1).

For both bones, the male samples were on average larger than the female samples, e.g. the average centroid size of the hemipelvis was 68.6 mm for the male group and 63.6 mm for the female group (Table 4.1, average centroid size). For all of the shape-size models, the first PC was dominantly a change of size. For the hemipelvis, the size was more dominant for the male group in comparison with the females (59.37% for men and 51.33% for women, Table 4.1).

Comparing the associated shape and shape-size models (male/female/overall) shows that the shape-size model required a smaller number of PCs to achieve 90% of the total variance; for

example, for the female talus, the shape model needs 19 PCs to achieve 90% of the total variance, while the shape-size model only requires 16 PCs (Table 4.1).

Figure 4-3 shows a pattern of compactness between the random models created from the overall dataset for the shape/shape-size of the hemipelvis and talus; the models for the shape-size of the hemipelvis have higher compactness in comparison with the shape-size of the talus; similarly, the model for the shape of the hemipelvis is more compact compared to the shape model for the talus.

4.3.2 Accuracy

The accuracy of a model is characterized as the average of the (average) distances $\widehat{\mathcal{D}}_i$ between the simulated and ground-truth meshes (Eq. 4-7). In Figure 4-4, the statistics of the distances $\widehat{\mathcal{D}}_i$, including the maximum, median, minimum, 25th, and 75th percentile, are shown w.r.t.the number of included PCs. Table (4.2) presents the accuracy of models w.r.t the number of included PCs as well as the maximum distance record $\widehat{\mathcal{D}}_i$. For the shape models, the distance $\widehat{\mathcal{D}}_i$ between each simulation and its ground truth are scaled using the centroid size of the sample.

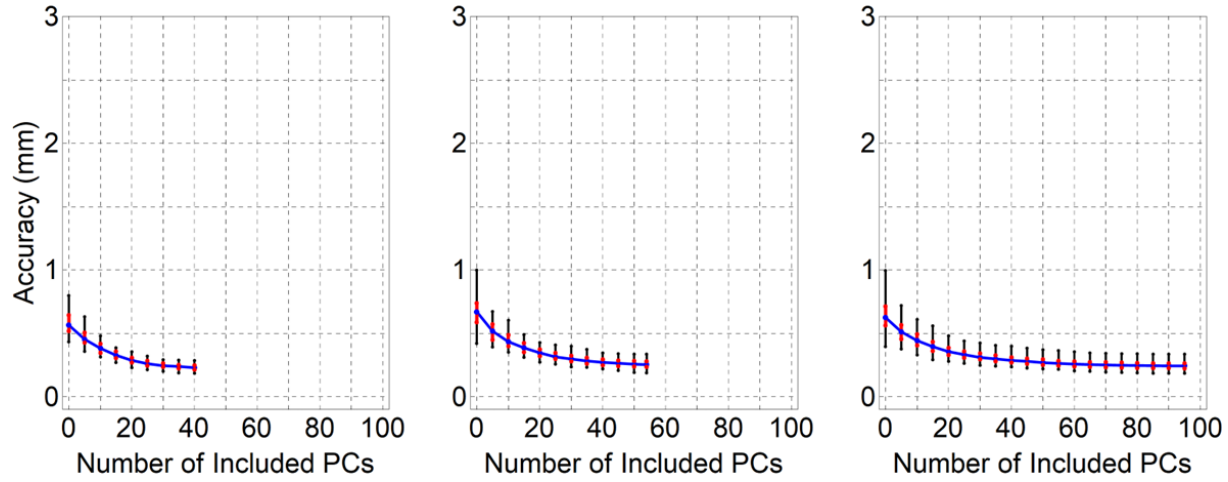

(a) Talus, shape

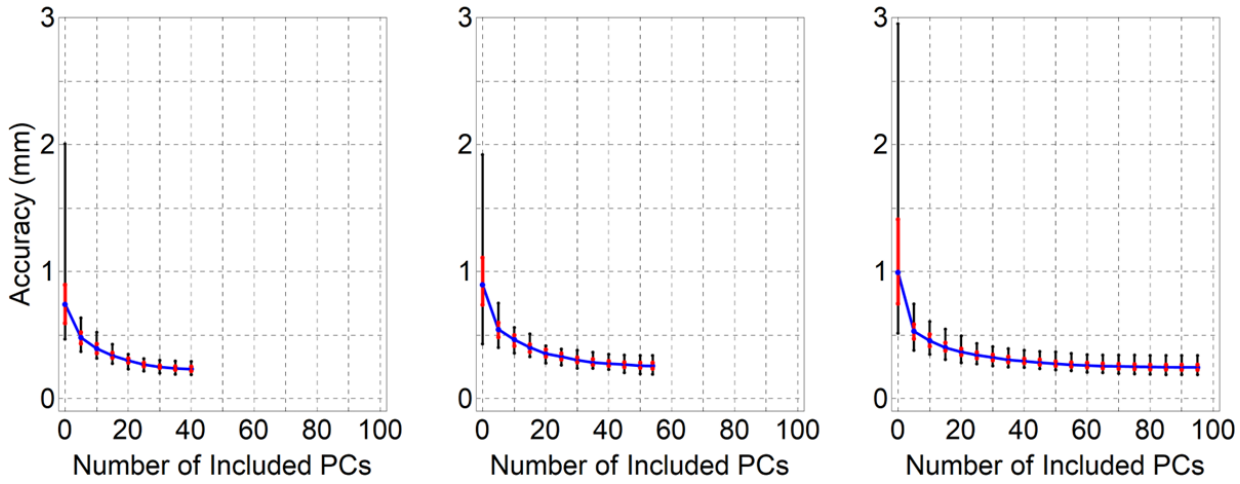

(b) Talus, shape-size

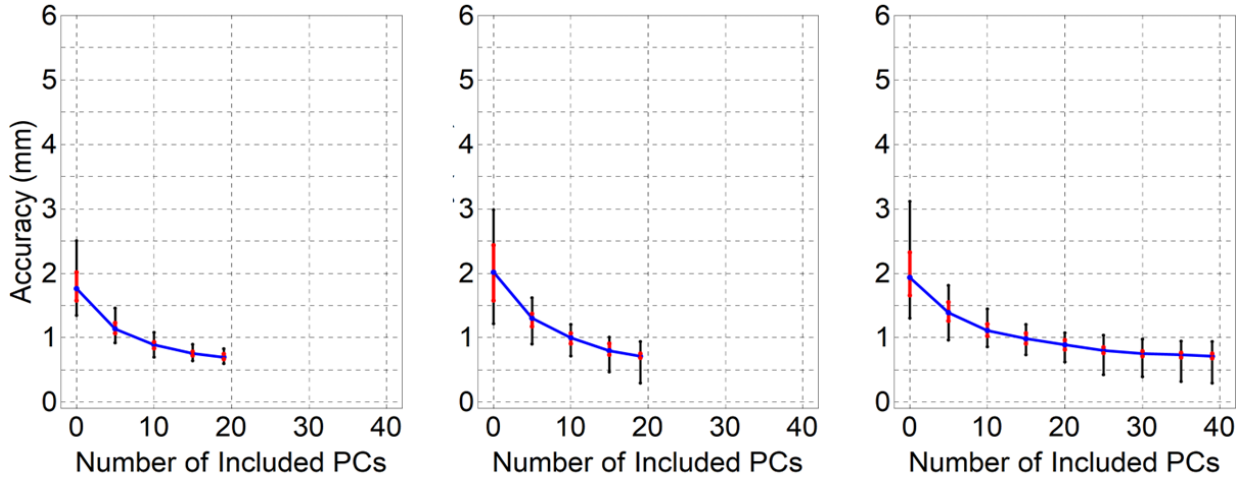

(c) Hemipelvis, shape

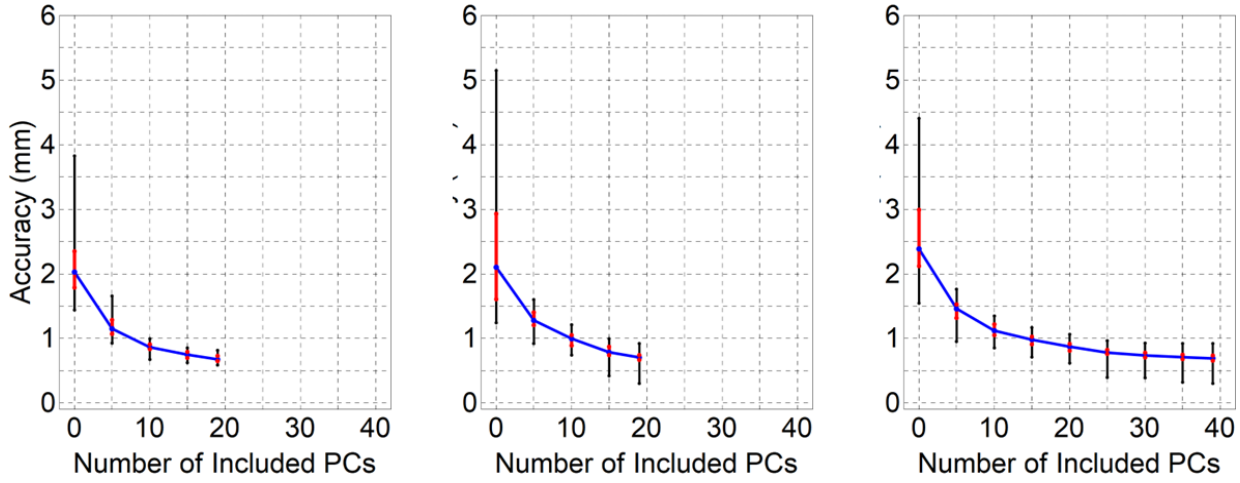

(d) Hemipelvis, shape-size

Figure 4-4: Accuracy evolution plots for 12 models. In each plot, the black line shows the minimum-maximum range of the distances $\widehat{\mathcal{D}}_i$;; the red lines represent the interval between the 25th and 75th percentile, and the blue line shows the evolution of the median as more PCs are included in the model. In each plot, the models for the female, male, and overall training sets are shown from left to right.

Table 4-2: Accuracy of 12 models in millimeters (mm). The accuracy, i.e. the average of the distances $\widehat{\mathcal{D}}_i$ are reported for the cases in which 0, 1, 5, 10, 15, and all of the PCs are included in

the simulation of the samples. The maximum distance $\widehat{\mathcal{D}}_i$ are also documented for the extreme cases in which none/all of the PCs are included.

			Accuracy (Avg.)						Max Avg.	
			Number of Included PCS						Nr. PCs	
SSM	**Size?**	**Sex**	**0**	**1**	**5**	**10**	**15**	**all**	**0**	**all**
Talus	N	F	0.58	0.55	0.47	0.39	0.33	0.23	0.80	0.29
		M	0.68	0.65	0.52	0.45	0.39	0.26	1.00	0.34
		F/M	0.64	0.62	0.52	0.45	0.40	0.25	1.00	0.34
	Y	F	0.80	0.59	0.49	0.40	0.34	0.24	2.00	0.29
		M	0.97	0.68	0.54	0.46	0.40	0.26	1.92	0.34
		F/M	1.14	0.65	0.54	0.47	0.41	0.25	2.95	0.34
Pelvis	N	F	1.83	1.65	1.18	0.89	0.76	0.71	3.07	1.12
		M	2.04	1.71	1.29	0.99	0.81	0.72	3.88	1.29
		F/M	2.04	1.84	1.41	1.13	0.99	0.71	4.10	1.29
	Y	F	2.14	1.72	1.20	0.87	0.75	0.69	4.82	1.10
		M	2.49	1.95	1.31	0.98	0.80	0.70	7.14	1.26
		F/M	2.61	1.95	1.44	1.13	0.97	0.70	6.11	1.26

F: female
M: Male

For all 12 SSMs, the accuracy evolution plots show a similar pattern (Figure 4-3); as the first few PCs are added to the models, the distance error between the simulated and ground-truth meshes rapidly decreases and then converges to a specific value. The accuracy, for the case in which all of the PCs are included in the models, is in the range of 0.23-0.26 mm for the talus and 0.69-0.72 mm for the hemipelvis (male/female/overall, shape/shape-size, Table 4.2).

For the cases in which none of the PCs are included in the model, the records are simply the distance $\mathcal{D}_i$ between the average model of an SSM and the training samples; the values for the sex-specific models of the talus shape show that, given the size of a sample, the male and female average models for the talus shape could serve as a template to simulate a sample with less than 1 mm distance error, 0.58 mm for women and 0.68 for men (Table 4.2). For the talus shape-size, the

inclusion of the first PC in the models results in the same accuracy, 0.59 mm for the women and 0.68 mm for men (Table 4.2); interestingly, for the hemipelvis, the inclusion of the first PC in the shape-size models shows slightly better performance in simulating the samples compared to the average model of the shape models, which is possibly due to the effect of Allometry in the hemipelvic models (Table 4.2).

4.3.3 Generalizability

Similar to the accuracy of a model, generalizability is defined as the average of the distances $\widetilde{\mathcal{D}}_i$ between the predicted meshes and the ground-truth meshes. In Figure 4-5, the statistics of such distances $\widetilde{\mathcal{D}}_i$ are reported for various models which are used to predict the male and female samples. For the leave-one-out experiments on the shape models, the centroid size of each sample is used to scale the computed distance $\widetilde{\mathcal{D}}_i$ between the prediction and the ground-truth representation. In addition, the generalization ability of the models is assessed at two levels: (i) the case in which all of the PCs are included, and (ii) the case in which the included PCs explain 90% of the total variability. In Table (4.2), the average of the recorded distances $\widetilde{\mathcal{D}}_i$, i.e. the generalizability, as well as the maximum distance $\widetilde{\mathcal{D}}_i$ are reported for the cases in which the sex-specific or overall models are employed in a leave-one-out setting to predict the male or female samples.

Table 4-3: Assessment of the generalization ability of the SSMs.

Var = 100 %	**Var = 90%**

Bone	Size included?	Training size	Predictor model	Nr. of PCs	Avg. Mean (mm)	Avg. Max. (mm)	Nr. of PCs	Avg. Mean (mm)	Avg. Max. (mm)
Talus	N	F	F	40	0.37	0.5	18-19	0.44	0.58
			F/M	95	0.28	0.35	29	0.37	0.49
		M	M	54	0.39	0.53	23-24	0.46	0.66
			F/M	95	0.31	0.43	29	0.43	0.63
	Y	F	F	40	0.38	0.51	16-17	0.47	0.63
			F/M	95	0.28	0.37	18-19	0.42	0.56
		M	M	54	0.41	0.53	19	0.49	0.73
			F/M	95	0.32	0.43	18-19	0.48	0.71
Hemipelvis	N	F	F	19	1.26	1.57	11	1.33	1.74
			F/M	39	1.06	1.26	16-17	1.24	1.55
		M	M	19	1.45	1.95	10-11	1.53	1.98
			F/M	39	1.18	1.43	16-17	1.39	1.65
	Y	F	F	19	1.28	1.73	8-9	1.51	2
			F/M	39	1.03	1.27	10-11	1.37	1.73
		M	M	19	1.47	1.94	7-8	1.69	2.4
			F/M	39	1.17	1.43	10-11	1.5	1.87

Case (training set, model, variance):

1. Female, sex-specific, 100%
2. Female, overall, 100%
3. Female, sex-specific, 90%
4. Female, overall, 90%
5. Male, sex-specific, 100%
6. Male, overall, 100%
7. Male, sex-specific, 90%
8. Male, overall, 90%

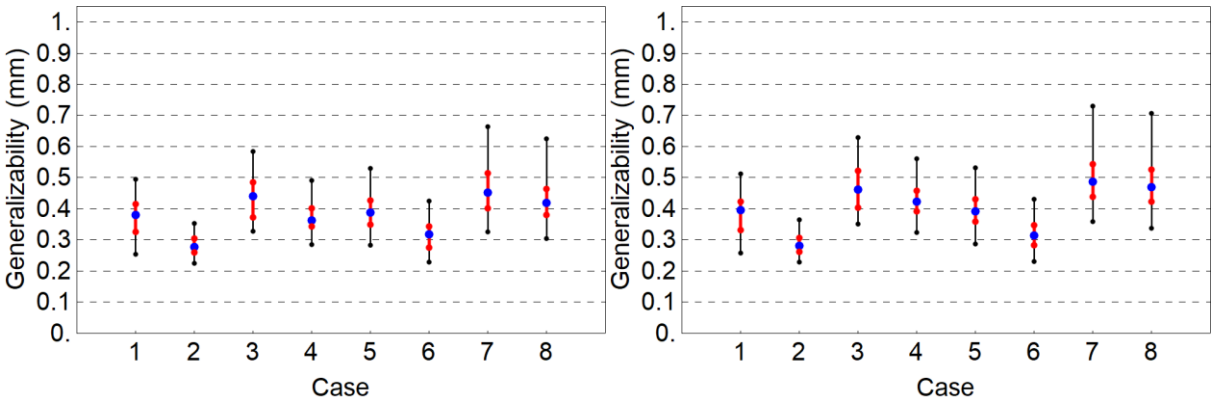

(a) Talus, shape

(b) Talus, shape-size

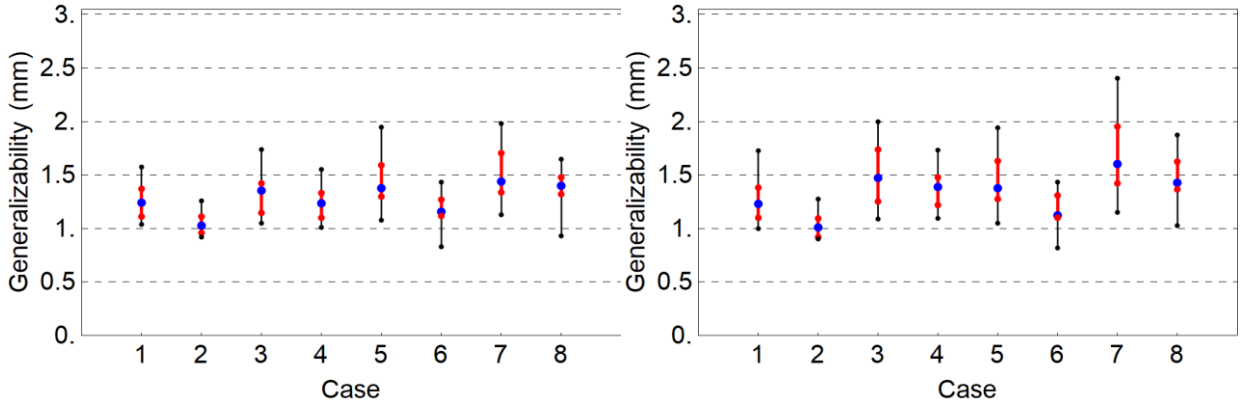

(c) Hemipelvis, shape (d) Hemipelvis, shape-size

Figure 4-5: The statistics of the SSM generalizability for the shape and shape-size of the hemipelvis and talus. In each plot, the male/female training sets are predicted by the associated sex-specific as well as the overall model. In addition, the generalizability of each model is evaluated for the full-capacity model and its compact version associated with 90% of the total variance. For each assessment, the black dots show the minimum-maximum range of the distances $\widetilde{\mathcal{D}}_i$; the red dots exhibit the 25th and 75th percentile, and the blue dot shows the median of the distances.

Table 4-3 shows that the generalization ability of the sex-specific models for the talus with the full capacity (shape/shape-size, all PCs included) is in the range of 0.37-0.41 mm; consideration of the whole datasets (male and female) into total models reduces the average distance error between the prediction and ground truth to the range of 0.28-0.32 mm (Table 4-3). *For the talus models (shape/shape-size), the ability of the models in predicting the male and female subjects (0.28-0.41 mm,* Table 4-3*) is comparable to the in-plane pixel size of the images, i.e. 0.39 mm.* The compact version of the talus models (associated with 90% of total variance) uses a considerably lower number of PCs to predict the samples, while their generalizability is still comparable with the image sizes, i.e. the range of 0.37-0.49 mm.

Similarly, for the hemipelvis, the incorporation of the male and female datasets into total models (form/form-size) reduces the average distance error $\widetilde{\mathcal{D}}_i$ between the ground-truth meshes and their predictions. For example, the prediction of the female hemipelvic shape with the whole dataset (compared with the associated model constructed only by female samples) decreases the average distance error $\widetilde{\mathcal{D}}_i$ from 1.26 mm to 1.06 mm (Table 4-3). Figure 4-5 shows the effects related to the enlargement of the training set and the employment of the compact version of the models on the generalizability of the models.

4.4 Discussion

Statistical shape models (SSMs) are beneficial computational tools to describe the geometric variation of anatomical structures in a compact form. The anatomical SSMs have been successfully employed in a wide spectrum of clinical applications such as medical image segmentation [1], virtual bone reconstruction [2-5], morphological studies of the bones [6-9], and finite element (FE) simulations of skeletal structures and joint biomechanics [10-12]. Davies originally quantified the SSM's ability to model the in-training samples and predict unknown samples which is highly beneficial in applications of anatomical SSM [13].

The objective of the current study was to (i) create various types of SSMs (form/form-size, sex-specific/total) for two anatomical structures (hemipelvis and talus), (ii) to evaluate the important properties of the models (compactness, accuracy, and generalizability) and determine the capacity of the models in simulating the in-training and unseen samples. The study used CT

images of the talus for 96 subjects (41 female and 55 male) (a male talus is removed due to local abnormalities) and the pelvis for 40 subjects (20 male and 20 female).

A difference between our work and the related studies on the quantification of SSM's ability to represent anatomical shapes (with [2-4] or without [6] artificial defects) is the usage of ground truth meshes. In the previous studies [2, 3, 4, 6], the dense correspondence established between the samples is considered the gold standard in the SSM quantification, i.e. when all of the PCs are included in a model, the accuracy of the model is equal to zero. However, during the non-rigid registration tasks, a template point set does not perfectly match the sample point sets and a distance exists between the transformed point sets and the original point set representing the samples. To evaluate the accuracy and generalizability of the models, we tracked the rigid transformations that occurred in the computational workflow for each sample and applied the same rigid transformation to the ground-truth meshes; this approach allowed us to evaluate the accuracy and generalizability of a model more realistically, independent of the established correspondence.

To compare the shape and shape-size models, we used (1) the average centroid size of each training set to compare the total variance of the models and (2) the centroid size of individual samples to compare the accuracy and generalizability measures. Due to the different training sizes, the direct comparison of the compactness between the models was not suitable and the selection of random SSMs with a fixed sample size was necessary.

Our results for the total variance and modal contribution of the models show that the talus shape has the same level of variance for the male and female groups, while the hemipelvic shape

shows higher variations for the male group; the shape-size of the talus/hemipelvis shows slight/noticeable higher geometric variance for the male group; and the size is more dominant for the male group in both anatomical structures (Table 4-1, Total Variance Norm.).

Based on the accuracy measurements, the sex-specific average model for the talus shape have an average distance error of 0.58 and 0.68 mm in simulating the female and male training samples (Table 4-2), while the associated values for the hemipelvic model are 1.83 and 2.04 mm (Table 4-2). The inclusion of all of the PCs in the sex-specific models decreases the accuracy distance errors to 0.23/0.26 mm for the talus (female/male) and 0.71/0.72 mm for the hemipelvis (female/male) (Table 4-2).

For the shape-size SSMs, the average distance between the sex-specific average model and the samples is 0.97 mm for the male tali, 0.80 mm for the female tali, 2.14 mm for the female hemipelvis, and 2.45 mm for the male hemipelvis (Table 4-2). The inclusion of the first PC in the talus models results in the same accuracy as the average model of the shape models (Table 4-2).

The created models in the current study have a generalizability of 0.28/0.32 mm for the female/male talus and a generalizability of 1.03/1.17 mm for the female/male hemipelvis (average error, point-to-plane distance, 100% variance, Table 4-3).

The quantification of the accuracy and generalizability of the constructed SSMs are of great importance for the preoperative planning of bilateral injuries around the pelvis and the talus. For unilateral bone injuries, the researchers have demonstrated that the intact contralateral bone could serve as a reliable patient-specific template for surgical planning, referred to as *mirroring virtual*

reconstruction (see [14] for the pelvis and [24] for the talus). The segmentation of 3D medical image data sets was previously manual, subjective, and time-consuming. Researchers have developed semi-automatic and automatic algorithms to facilitate the medical image segmentation tasks involved in the mirroring reconstruction algorithms (e.g. see [14] for semi-automatic segmentation of the CT scans around the pelvic area and [25] for an SSM-based automatic segmentation of the lower-limb anatomy). However, the mirrored template is unavailable for patients with bilateral bone injuries and virtual reconstruction workflows for surgical planning of bilateral injuries are highly demanding. Using 3D shape analyses, scalable templates have been developed and validated to restore the morphology of an injured bone within a specific error threshold (see [7] for the talus and [14] for the pelvis). Our results for the accuracy of the average shape model (i.e. the accuracy of the shape models with no PC included) and the accuracy of the shape-size models with only the first PC quantify the expected distance error for the virtual bone reconstruction based on such templates. Our results for the generalization ability quantified the capability of the models to simulate a new shape through a cross-validation procedure.

4.5 Chapter conclusion

The current study developed a workflow to measure the quality of statistical shape models in simulating the in-training and unseen shapes for two anatomical datasets (hemipelvis, and talus). We used the CPD algorithm to establish correspondence between the shapes and PCA was used to combine the established correspondence into linear models. The compactness, accuracy, and

generalizability of the constructed models were evaluated using the representation of samples before the registration process and the effects related to the training size, the shape/size of the bones, as well as the sexual dimorphism were investigated by comparing the properties of various models.

Reference

[1] Heimann, T., & Meinzer, H. P. (2009). Statistical shape models for 3D medical image segmentation: a review. Medical image analysis, 13(4), 543-563.

[2] Vanden Berghe, P., Demol, J., Gelaude, F., & Vander Sloten, J. (2017). Virtual anatomical reconstruction of large acetabular bone defects using a statistical shape model. Computer methods in biomechanics and biomedical engineering, 20(6), 577-586.

[3] Krol, Z., Skadlubowicz, P., Hefti, F., & Krieg, A. H. (2013). Virtual reconstruction of pelvic tumor defects based on a gender-specific statistical shape model. Computer aided surgery, 18(5-6), 142-153.

[4] Plessers, K., Berghe, P. V., Van Dijck, C., Wirix-Speetjens, R., Debeer, P., Jonkers, I., & Vander Sloten, J. (2018). Virtual reconstruction of glenoid bone defects using a statistical shape model. Journal of shoulder and elbow surgery, 27(1), 160-166.

[5] Ead, M. S., Palizi, M., Jaremko, J. L., Westover, L., & Duke, K. K. (2021). Development and application of the average pelvic shape in virtual pelvic fracture reconstruction. The International Journal of Medical Robotics and Computer Assisted Surgery, 17(2), e2199.

[6] Audenaert, E. A., Pattyn, C., Steenackers, G., De Roeck, J., Vandermeulen, D., & Claes, P. (2019). Statistical shape modelling of skeletal anatomy for sex discrimination: their training size, sexual dimorphism, and asymmetry. Frontiers in bioengineering and biotechnology, 7, 302.

[7] Liu, T., Jomha, N. M., Adeeb, S., El-Rich, M., & Westover, L. (2020). Investigation of the average shape and principal variations of the human talus bone using statistic shape model. Frontiers in Bioengineering and Biotechnology, 8, 656.

[8] Arand, C., Wagner, D., Richards, R. G., Noser, H., Kamer, L., Sawaguchi, T., & Rommens, P. M. (2019). 3D statistical model of the pelvic ring‐a CT‐based statistical evaluation of anatomical variation. Journal of Anatomy, 234(3), 376-383.

[9] Brynskog, E., Iraeus, J., Reed, M. P., & Davidsson, J. (2021). Predicting pelvis geometry using a morphometric model with overall anthropometric variables. Journal of biomechanics, 126, 110633.

[10] Frazer, L., Nicolella, D. P., & Southwest Research Institute San Antonio United States. (2020). Human Response to High Rate Loading.

[11] Campbell, J. Q., & Petrella, A. J. (2016). Automated finite element modelling of the lumbar spine: using a statistical shape model to generate a virtual population of models. Journal of biomechanics, 49(13), 2593-2599.

[12] Clouthier, A. L., Smith, C. R., Vignos, M. F., Thelen, D. G., Deluzio, K. J., & Rainbow, M. J. (2019). The effect of articular geometry features identified using statistical shape modelling on knee biomechanics. Medical engineering & physics, 66, 47-55.

[13] Davies, R. H., Twining, C. J., Cootes, T. F., Waterton, J. C., & Taylor, C. J. (2002). A minimum description length approach to statistical shape modelling. IEEE transactions on medical imaging, 21(5), 525-537.

[14] Ead, M. S., Westover, L., Polege, S., McClelland, S., Jaremko, J. L., & Duke, K. K. (2020). Virtual reconstruction of unilateral pelvic fractures by using pelvic symmetry. International Journal of Computer Assisted Radiology and Surgery, 15, 1267-1277.

[15] Pietroni, N., Tarini, M., & Cignoni, P. (2009). Almost isometric mesh parameterization through abstract domains. IEEE Transactions on Visualization and Computer Graphics, 16(4), 621-635.

[16] Taubin, G. (1995, June). Curve and surface smoothing without shrinkage. In Proceedings of IEEE international conference on computer vision (pp. 852-857). IEEE.

[17] de Giessen, Martijn, Frans M. Vos, Cornelis A. Grimbergen, Lucas J. van Vliet, and Geert J. Streekstra. "An efficient and robust algorithm for parallel groupwise registration of bone surfaces." In Medical Image Computing and Computer-Assisted Intervention–MICCAI 2012: 15th International Conference, Nice, France, October 1-5, 2012, Proceedings, Part III 15, pp. 164-171. Springer Berlin Heidelberg, 2012

[18] Laga, H., Guo, Y., Tabia, H., Fisher, R. B., & Bennamoun, M. (2018). 3D Shape analysis: fundamentals, theory, and applications. John Wiley & Sons.

[19] Myronenko, A., & Song, X. (2010). Point set registration: Coherent point drift. IEEE transactions on pattern analysis and machine intelligence, 32(12), 2262-2275.

[20] Myronenko, A., Song, X., & Carreira-Perpinan, M. (2006). Non-rigid point set registration: Coherent point drift. Advances in neural information processing systems, 19.

[21] Bookstein, Fred L., and William DK Green. "Thin-plate spline for deformations with specified derivatives." In Mathematical Methods in Medical Imaging II, vol. 2035, pp. 14-28. SPIE, 1993.

[22] Bishop, C. M., & Nasrabadi, N. M. (2006). Pattern recognition and machine learning (Vol. 4, No. 4, p. 738). New York: springer.

[23] Aspert, N., Santa-Cruz, D., & Ebrahimi, T. (2002, August). Mesh: Measuring errors between surfaces using the hausdorff distance. In Proceedings. IEEE international conference on multimedia and expo (Vol. 1, pp. 705-708). IEEE.

[24] Islam, K., Dobbe, A., Komeili, A., Duke, K., El-Rich, M., Dhillon, S., ... & Jomha, N. M. (2014). Symmetry analysis of talus bone: a geometric morphometric approach. Bone & joint research, 3(5), 139-145.

[25] Audenaert, E. A., Van Houcke, J., Almeida, D. F., Paelinck, L., Peiffer, M., Steenackers, G., & Vandermeulen, D. (2019). Cascaded statistical shape model based segmentation of the full lower limb in CT. Computer methods in biomechanics and biomedical engineering, 22(6), 644-657.

CHAPTER 5: EFFECT OF GEOMETRY-AWARE SAMPLING ON THE PERFORMANCE OF THE COHERENT POINT DRIFT REGISTRATION METHOD

This chapter is derived from the paper in preparation:

Palizi, M. & Adeeb, S. (2023). Effect of geometry-aware sampling on the performance of the coherent point drift registration method.

Abstract

Point-set registration is the process of aligning two or multiple point sets by finding a transformation that optimizes a similarity measure between the point sets. Coherent point drift (CPD) is a probabilistic point-set registration method. A limitation of the technique is the alignment of areas of high curvature. Due to the high amount of energy required for local areas, the method might struggle to match the shapes accurately. In this study, we investigate the effect of geometry-aware point-set sampling on the performance of the CPD method. Firstly, we design a set of 2D and 3D synthetic shapes with one or two local features. The shapes have the same global structure and their difference is the location and/or scale of the local features. By manipulating the degree of dissimilarity in these local features, we evaluate the performance of the CPD method in matching shapes with local features. Each experiment is performed using uniform

and geometry-aware point-set sampling. In addition to the synthetic experiments, a set of real-world examples which involve aligning the femur cartilages are considered. For the uniform and geometry-aware sampling in 3D, two automated algorithms are developed that sample point sets from triangle meshes. Our results for the synthetic experiments show that the geometry-aware point set sampling enhances the performance of the CPD method in finding the true correspondence between the local features. Similarly, for real-world experiments, geometry-aware sampling improves the accuracy of alignments.

Keywords: correspondence; probabilistic point-set registration; coherence point drift; point-set sampling; geometry-aware sampling

5.1 Introduction

Point-set registration is the process of aligning two or multiple point sets by finding a transformation that optimizes a similarity measure between the point sets [1]. Point-set registration problems frequently arise in practical applications of computer vision, robotics, and medical imaging [1]. Early methods such as Iterative Closest Point (ICP) [2] were equipped with rigid body motions and used Euclidean distance for similarity measurement. These early methods are beneficial in applications such as scene reconstruction, in which multiple point sets extracted from the same scene are integrated to reconstruct the entire scene [3].

However, many applications require point-set registration with more advanced transformations. For example, 3D modelling of anatomical structures during growth or disease progression needs registration of a sequence of scans with non-linear deformation [3]. Formulating non-rigid point-set registration started with the pioneering work of Bookstein [4], which introduced the *Thin-Plate Spline (TPS) transformation* to simulate flexible deformation within biological entities. The TPS transformation used a set of control points to flexibly warp one point set onto another while minimizing an energy function called the *bending energy of a thin plate* [4].

Point-set registration problems have also been modelled in probabilistic estimation frameworks [3]. Probabilistic registration methods are based on the concept of establishing *soft correspondence* [5]. Unlike *one-to-one* correspondence in the ICP method [2], which assigns each point in one set to a point in the other set, soft correspondence allows for partial assignments, indicating the likelihood or confidence of a match between points [5]. Gaussian Mixture Model Registration (GMMReg) [6] and Coherent Point Drift (CPD) [1, 7] are two probabilistic methods that register point sets in the presence of complex deformation, occlusion, noise, and outliers.

GMMReg models two point sets as isotropic Gaussian Mixture Models (GMMs) and minimizes the L2 divergence between these two GMMs [6]. The CPD method represents one point set as centroids of an isotropic GMM with unknown variance, treating the other set as observed data points [1, 7]. An Expectation-Maximization (EM) algorithm is then used to maximize the likelihood of the GMM given the data points [1, 7]. In recent years, refinements and extensions have been proposed to improve various aspects of the probabilistic methods. For example, Saval-Calvo et al. incorporated color information alongside point coordinates to enhance the estimation

of correspondence in the CPD method [8]. Peng et al. introduced the Shape Context (SC) into the correspondence estimation of the CPD method [9]. Gao et al. proposed an EM algorithm to iteratively evaluate the outlier ratio in the CPD method [10].

One limitation of the probabilistic registration methods, which is relatively unexplored, is relevant to equal treatment of points in the point sets. The areas of high curvature in a point set, referred to as the *geometric features* hereinafter, usually require more intricate transformations to match their counterparts during a registration process. However, due to the equal treatment of all points and the high content of energy demanded, probabilistic methods might struggle to align the geometric features accurately.

To address this, we explore the possibility of enhancing this aspect of the CPD method, i.e. the accurate alignment of geometric features, by using geometry-aware point-set sampling. In geometry-aware sampling, a higher point density (the number of points per unit length/area) is considered on the geometric features which could improve the perception of the point sets in the registration process and increase the accuracy of aligning geometric features.

We first conducted a set of 2D and 3D synthetic experiments that involve registering shapes with different types of local dissimilarities. A measure of true correspondence was defined between these shapes to evaluate the accuracy of the CPD method. In each experiment, two cases of geometry-aware point-set sampling were compared with uniform sampling in terms of registration accuracy. In addition to the synthetic experiments, a set of real experiments was examined which involves the registration of femur cartilage. Our results for both the synthetic and

real examples demonstrated that using geometry-aware sampling improves the performance of the CPD registration method in matching complex geometric features.

The rest of the study is organized as follows: Section (5.2) explains the synthetic experiments, covering the geometry of the synthetic shapes, different types of local dissimilarities, a measure of true correspondence, and the adopted point-set sampling strategies. In Section (5.3), we present the preprocessing of the femur cartilage samples, the distance measurements, and the point-sampling cases. The results for both the synthetic and real examples are presented in section 5.4. Section 5.5 discusses our experimentations on the enhancement of the CPD method using geometry-aware sampling and possible extensions. Lastly, in Appendix A, a summary of the CPD registration method is presented.

5.2 Synthetic experiments

5.2.1 Synthetic Shapes

A series of experiments were performed on synthetic shapes in two and three dimensions to investigate the effect of geometry-aware point-set sampling on the accuracy of the CPD method. In each test, a *source* object was registered on a *target* object. The source and target share the same global structure, a rectangle or a box. One or two local features were considered on the source and target. In 2D experiments, the local features were semi-circular, and in 3D experiments, hemispheres were used. The location and/or size of these local features were the source of

dissimilarity between the source and target objects. In general, four types of objects were used in the study, including a box or rectangle with one or two local features. Figure 5-1 shows the dimensions of these objects and the parameters characterizing their geometries. In all of the experiments, the local features of the source had a unit radius and fixed location (Figure 5-1). The radius and location of the local entities on the target varied within the experiments (Figure 5-1).

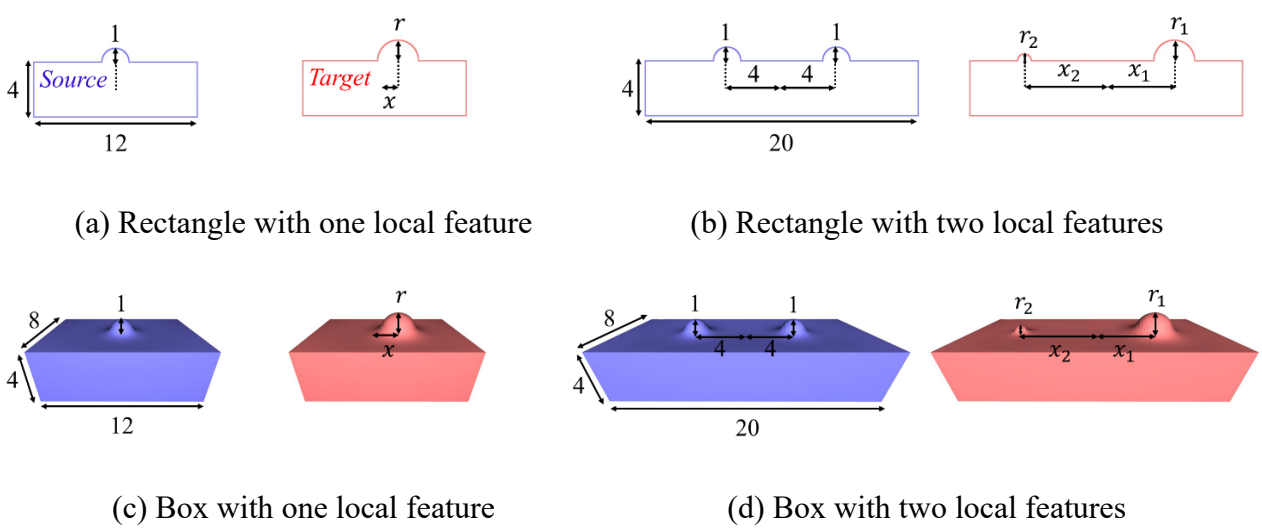

(a) Rectangle with one local feature

(b) Rectangle with two local features

(c) Box with one local feature

(d) Box with two local features

Figure 5-1: Dimensions and characterizing parameters of the synthetic objects. The source and target objects shared identical global shapes (rectangle or box) and their dissimilarity was the location and/or the size of the local features. The local features are semi-circular for 2D objects and hemispherical for 3D objects. The source object is shown in blue and the target object in red.

Figure 5-2 and Figure 5-3 show the source and targets in the *single-feature* and *double-feature* experiments. In each experiment, the local features undergo translation and/or scaling (expansion or shrinkage). Each test was performed at five levels of difficulty by changing the

degree of deformation between the local features of the source and target. This allowed us to monitor the registration accuracy under varying degrees of complexity and assess the efficacy of using geometry-aware point-set sampling in challenging scenarios. Table 5-1 reports the location and radius of the local features on the target for both single- and double-feature experiments.

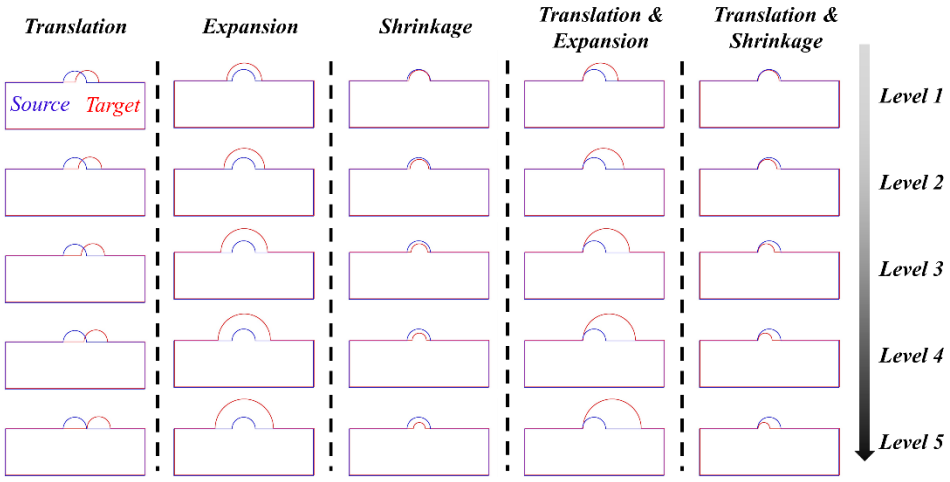

(a) 2D experiments

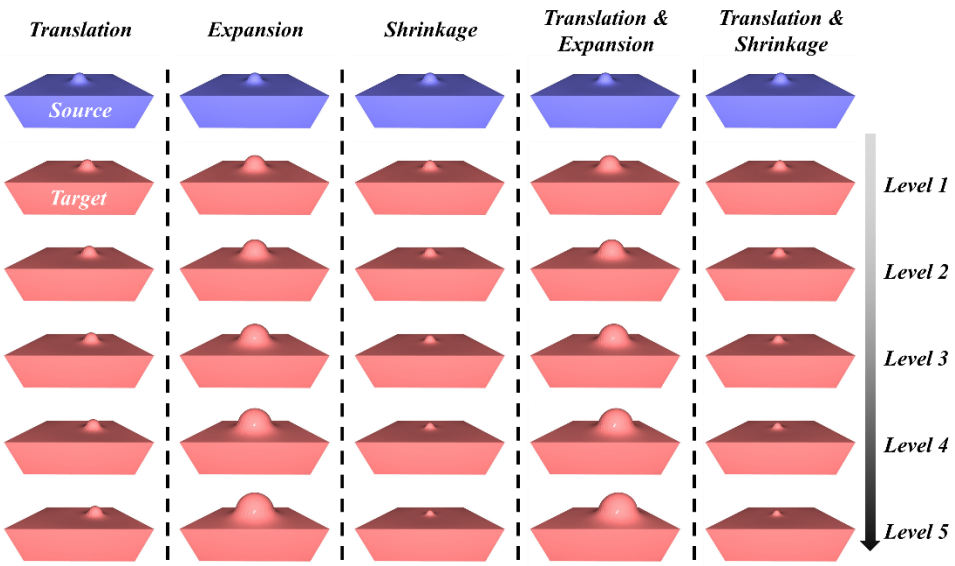

(b) 3D experiments

Figure 5-2: Source and target objects in single-feature experiments. The experiments include the translation and/or scaling (expansion or shrinkage) of a local feature. Each experiment was performed at five levels of difficulty by increasing the degree of deformation between the source and target features. For each test, the source is shown in blue and the targets are shown in red.

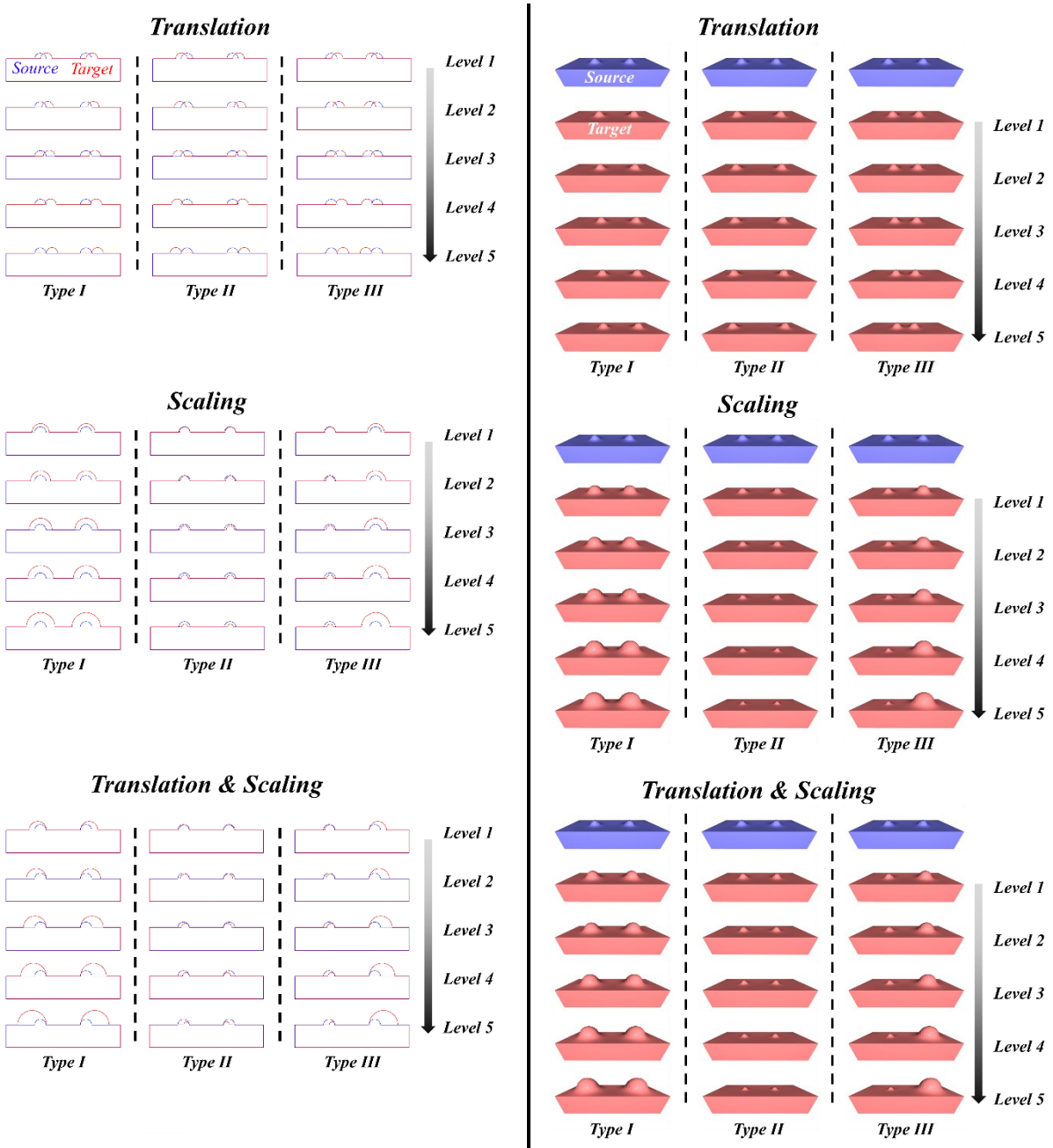

(a) 2D experiments

(b) 3D experiments

Figure 5-3: Source and target objects used in double-feature experiments. Each experiment was performed at five levels of difficulty. The source is shown in blue and the targets are shown in red.

Table 5-1: The location and radius of the target feature in single-feature and double-feature experiments. The same parameters are used for the target in 2D and 3D experiments. The location and radius of target local features are denoted by x and r in single-feature experiments. To differentiate the local entities in double-features experiments, subscripts 1 and 2 are used for the parameters.

Experiment		**Nr. of Levels**	**Target Parameters**				**Parameter Range***
			x		r		
One Feature	Translation	5	α		1		α: 1.0-2.0 (0.25)
	Expansion	5	0		$1+\alpha$		α: 0.5-1.5 (0.25)
	Shrinkage	5	0		$1-\alpha$		α: 0.1-0.5 (0.1)
	Translation & Expansion	5	α		$1+\alpha$		α: 0.5-1.5 (0.25)
	Translation & Shrinkage	5	$-\alpha$		$1-\alpha$		α: 0.1-0.5 (0.1)
Experiment		**Nr. of Levels**	**Target Parameters**				**Parameter Range***
			x_1	r_1	x_2	r_2	
Two Features	Translation I	5	$4+\alpha$	1	$-4+\alpha$	1	α: 1.0-2.0 (0.25)
	Translation II	5	$4+\alpha$	1	$-4-\alpha$	1	
	Translation III	5	$4-\alpha$	1	$-4+\alpha$	1	
	Scaling I	5	4	$1+\alpha_1$	-4	$1+\alpha_1$	α_1: 0.5-1.5 (0.25) α_2: 0.1-0.5 (0.1)
	Scaling II	5	4	$1-\alpha_2$	-4	$1-\alpha_2$	
	Scaling III	5	4	$1+\alpha_1$	-4	$1-\alpha_2$	
	Translation & Scaling I	5	$4+\alpha_1$	$1+\alpha_1$	$-4-\alpha_1$	$1+\alpha_1$	α_1: 0.5-1.5 (0.25) α_2: 0.1-0.5 (0.1)
	Translation & Scaling II	5	$4-\alpha_2$	$1-\alpha_2$	$-4+\alpha_2$	$1-\alpha_2$	
	Translation & Scaling III	5	$4+\alpha_1$	$1+\alpha_1$	$-4+\alpha_2$	$1-\alpha_2$	
* Start-End (Increment)							

5.2.2 Measure of true correspondence

In a *desirable* registration in 2D experiments, each part of the source (straight segment or semi-circle) is transformed on the associated part of the target. Subsequently, the points at the intersection of each two parts on the source will be aligned with the associated points on the target. These points are easily discernable on each object and are referred to as *landmarks*, hereinafter. The landmarks were utilized to measure the registration accuracy in identifying the *true*

correspondence between the source and targets. Similarly, landmarks were defined on 3D objects. In Figure 5-4, the location of the landmarks, as well as two examples of desirable mapping in 2D problems, are illustrated.

To assess the registration accuracy in each test, the following distance was computed between the registered version of the source and the target:

$$d_{RMS} = \sqrt{\frac{1}{n_L}\sum_{i=1}^{n_L} d_i^2} \tag{5-1}$$

Here, d_i is the distance between the i[th] landmark on the registered source and the target, n_L is the number of landmarks, and d_{RMS} is the Root Mean Square (RMS) distance error between the landmarks. The number of landmarks n_L was equal to 7 for the rectangle with one feature, 10 for the rectangle with two features, 13 for the box with one feature, and 18 for the box with two features.

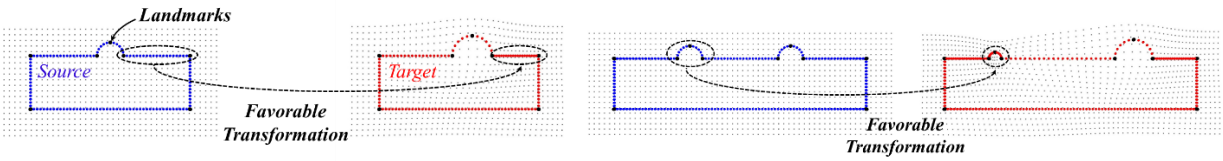

(a) Rectangle with one local feature (b) Rectangle with two local features

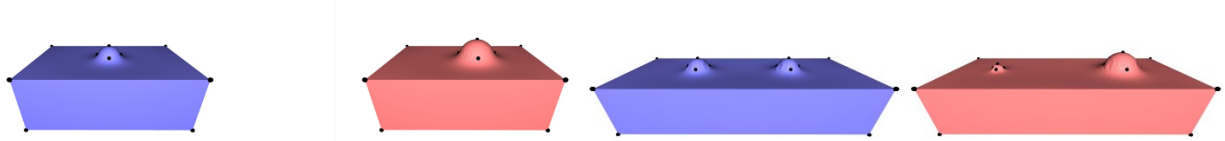

(c) Box with one local feature (d) Box with two local features

Figure 5-4: Defined landmarks on synthetic shapes and examples of desirable transformation between 2D synthetic objects. The black dots show the landmarks on the source and target objects. These points were located at the intersection of distinctive portions of the objects. In (a) and (b), the desirable mapping between the source and target objects was applied to a uniform point set on the source object and a regular grid of points which is shown in gray.

5.2.3 Point-set sampling

Three point-set sampling cases were used to investigate the effect of point distribution on registration accuracy. The first case was uniform sampling in which the same number of points were uniformly sampled from the source and target. The other two cases were geometry-aware sampling in which a higher point density was considered on the geometric features of the source and target. The geometric features include the semi-circles and corners for 2D objects and hemispheres and edges for 3D objects.

The difference between the geometry-aware sampling cases was the ratio of the nearest neighbour distance (NND) on the geometric features and the remaining parts. In the first case, the NND on thegeometric features was half of the NND on the remaining parts. For the second case, this ratio was equal to a quarter. Regardless of the sampling case (uniform or geometry-aware),

the total number of sampled points was equal to 300 and 450 for 2D objects with single and double features, and 4000 and 6000 for 3D objects with single and double features.

For uniform and geometry-aware sampling of 2D objects, each object was manually divided into geometric features and straight segments (using the characterizing parameters of the object in Table 5-1). Each segment was then sampled to achieve uniform point distribution or a specific NND ratio over the object.

The sampling of 3D objects was performed by automated algorithms. For the uniform sampling on 3D objects, firstly, a Poisson-disk sampling method [11] was used to sample well-distributed points on the triangle meshes, while maintaining a minimum distance between the neighbouring points. Then, the uniformization technique proposed by [12] was used to further homogenize the distance between the neighbouring points.

The geometry-aware sampling of 3D objects included two steps: identification of the geometric features and point-set sampling on each division. Using the formula proposed by [13], the mean and Gaussian discrete curvatures were first determined on each triangle of the mesh. The principal curvatures were computed using the mean and Gaussian discrete curvatures. The maximum of the absolute values of the principal curvatures was recorded for each triangle as a measure of curvature. Each triangle was then labeled geometric feature if its curvature measure exceeded the threshold of 0.4 $\frac{1}{mm}$ (the threshold is selected based on the characterizing parameters of 3D objects in Table 5-1). After identifying the geometric features of an object, the surface areas of the geometric features and the remaining parts were computed. The surface areas were then

used to determine the number of points on each section to achieve a specific NND ratio. The sampling on each section was performed using the uniform sampling algorithm. Figure 5-5 shows the resulting uniform and geometry-aware sampling cases on 2D and 3D objects.

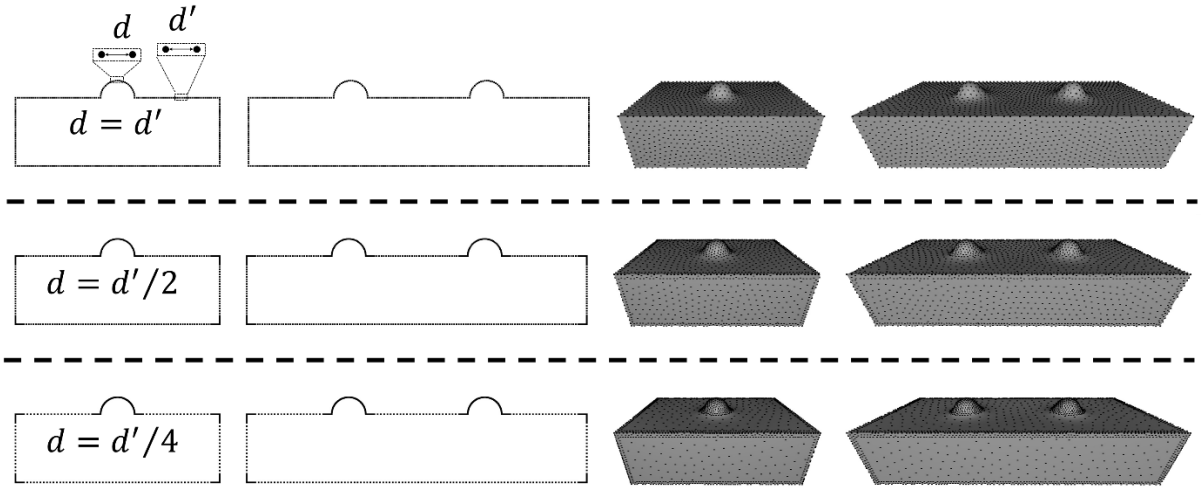

Figure 5-5: Point-set sampling of the synthetic objects in two- and three-dimensions. The first row shows the uniform point-set sampling. The second and third rows show geometry-aware cases, in which, the NND on the local features was half and a quarter of the NND on the remaining parts, respectively.

5.2.4 Registration parameters

For all of the experiments, we used specific values for the registration parameters: β=2, and λ=2. The selected values showed the highest registration accuracy for the uniform sampling case. The number of iterations was set to 100, for which the width of the mixture model σ reached a

constant value in all of the experiments (see Appendix A for a description of the CPD method and the parameters involved in it).

5.3 Real experiments

5.3.1 Preprocessing

The real experiments include the registration tasks within a dataset of femur cartilage belonging to 10 individuals. The dataset of the femur cartilages was obtained from MR images of the Osteoarthritis Initiative (OAI) database [14]. The images were manually segmented into triangle meshes. The triangle meshes were further processed into smooth meshes with high-quality tessellation, using Taubin smoothing [15] and parameterization technique [16]. The discrete curvature operator was applied on each mesh and the geometric features were identified as the triangles with the curvature measure exceeding the threshold of $0.5\ \frac{1}{mm}$. For all of the samples, the selected threshold separated the edges of the cartilages as the areas of high curvature from the remaining parts of the samples. Figure 5-6 shows the color map plots of the curvature measure using the mentioned threshold.

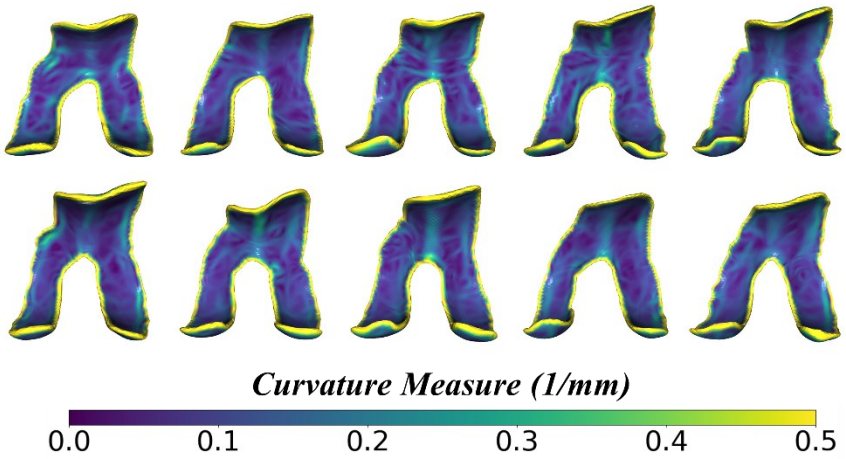

Figure 5-6: Color map plots for the curvature measure on all of the femur cartilage samples.

Using the Poisson-disk point set sampling [11], a sparse point set with only 1,000 points was sampled on each mesh. Using the centroid and centroid size of the sparse point sets [3], all of the samples were normalized w.r.t. scaling and translation. Before performing each registration task, the source was rigidly aligned on the target using the rigid CPD method [7] and the sparse point sets.

5.3.2 Distance measurement

In each experiment, the distance between the registered source and the target was measured using the RMS distance error and the Hausdorff distance [3]. The distances were measured using the vertices of the meshes rather than the point sets, ensuring a consistent measurement approach

for comparing the results of various point-set sampling cases. The Hausdorff distance is a widely-used distance measure between two shapes (mesh or point set) which is defined as follows [3]:

$$d_H(P,Q) = \max\left(\max_{p\in P}\min_{q\in Q} d(p,q)\,,\max_{q\in Q}\min_{p\in P} d(p,q)\right) \tag{5-2}$$

Here, P and Q are the sets of mesh vertices (representing the registered source and the target meshes), p represents a vertex on P, q denotes a vertex on Q, and $d(p,q)$ is the Euclidean distance between the points p and q. The Hausdorff distance shows the maximum distance between the closest points on two shapes.

The RMS of the distances was also defined as follows:

$$d_{RMS}(P,Q) = \sqrt{\frac{1}{n_P+n_Q}\left(\sum_{q\in Q}\min_{p\in P} d(p,q)^2 + \sum_{p\in P}\min_{q\in Q} d(p,q)^2\right)} \tag{5-3}$$

in which, P and Q are the sets of mesh vertices, n_P is the number of vertices on P, n_Q is the number of vertices on Q, and $d(p,q)$ is the Euclidean distance between the points p and q.

5.3.3 Point-set sampling cases

Similar to the synthetic experiments, three cases of point-set sampling were considered for the femur cartilages. The first case was the uniform point-set sampling and the other two cases were geometry-aware sampling. In the first geometry-aware sampling case, the distance between neighboring points (NND) on geometric features was half of the NND in the remaining areas. For

the second case, the NND ratio was reduced to 1/4. The uniform and geometry-aware sampling was performed using the same algorithms as those described for 3D synthetic objects (section 5.2.3). Figure 5-7 presents the point-set sampling cases for all of the femur cartilage samples.

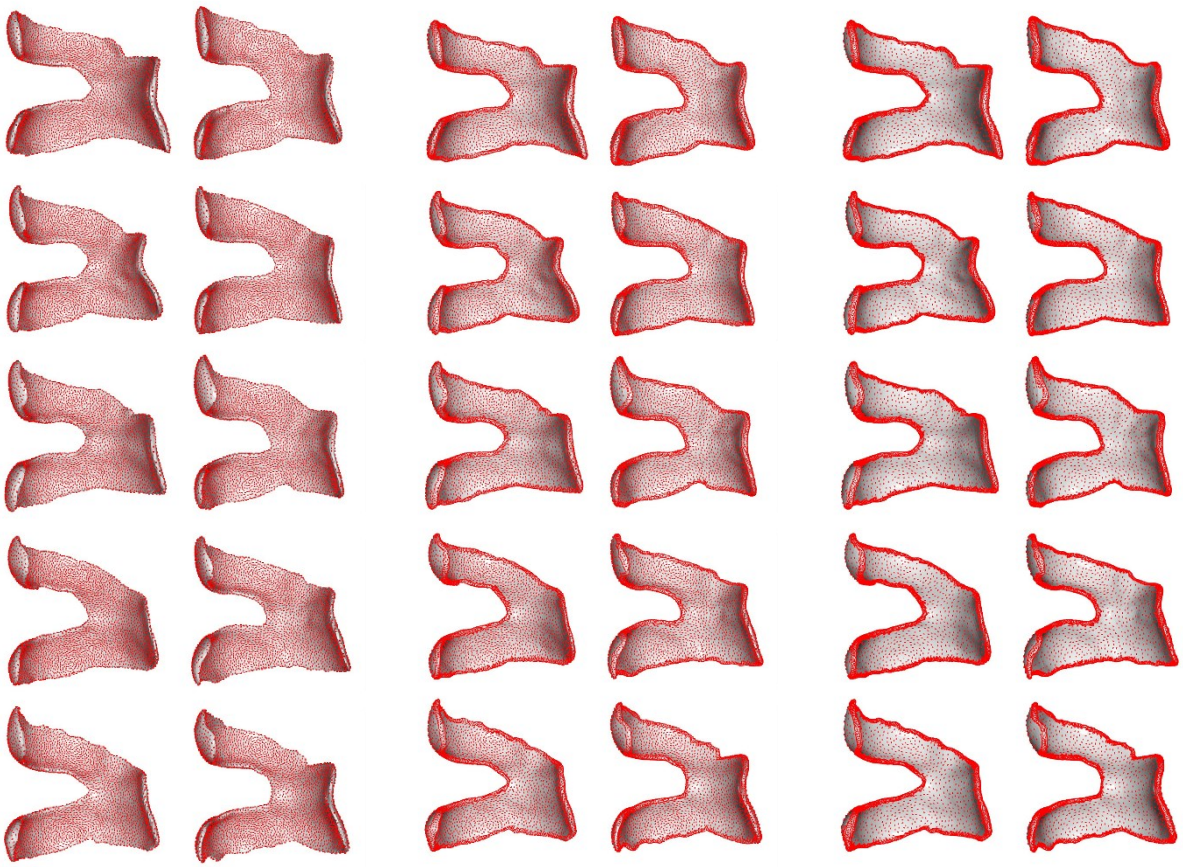

(a) (b) (c)

Figure 5-7: Point-set sampling of the femur cartilage samples: (a) Uniform point-set sampling, (b) Geometry-aware point-set sampling with the NND ratio equal to 1/2, and (c) Geometry-aware point-set sampling with the NND ratio of 1/4.

5.3.4 Registration parameters

In all of the experiments, the registration parameters β and γ were respectively set to 1 and 2 Similar to the synthetic experiments, each registration task was iterated 100 times, for which the sigma value became constant.

5.4 Results

5.4.1 Synthetic experiments

Table 5-2 presents the measured distances in the single-feature and double-features experiments. The reported values are the RMS of the distance between the landmarks of the transformed source and the target (Eq. 5-1). In all 70 experiments (25 single-feature, and 45 double-feature experiments), the geometry-aware sampling improved the performance of the CPD method in matching shapes with local features (Table 5-2). Furthermore, between the two geometry-aware sampling cases, the one with higher point density on the geometric features showed better registration accuracy (Table 5-2).

For the experiments with low degrees of local differences, the registration with both uniform and geometry-aware sampling found the desirable transformation; however, the accuracy was higher for the geometry-aware sampling cases (Table 5-2). For the experiments with high degrees of local transformation, the registration with geometry-aware sampling was mainly successful in

identifying the suitable mapping, while the registration with uniform sampling failed, i.e. non-homologous parts between the source and target were aligned mistakenly.

Figure 5-8 provides examples of the performance enhancement at high levels of difficulty, comparing the registered source for the uniform sampling and the geometry-aware sampling with higher point density on the geometric features (Type II). For the translational experiments at high levels, the registration with uniform sampling failed to recognize the association between the source and target features, and instead of translating the source features, these features were matched on the straight segments of the targets (Figure 5-8 (a)). For the experiments with intense local expansion or shrinkage, the registration with uniform sampling failed to scale the source features onto its target counterparts, resulting in bell-shaped features in expansion and flattened features in shrinkage (Figure 5-8 (b)). Similarly, for the experiments with high degrees of both translation and scaling, by increasing the number of points on the geometric features of the source and target objects, the matching became more accurate (Figure 5-6 (c)). Lastly, upon visual inspection, the edges of the registered source were distorted when uniform sampling was used, while for the geometry-aware cases, the edges were preserved as straight segments (Figure 5-6).

Table 5-2: The registration accuracy in single-feature and double-feature experiments. The registration accuracy was measured as the RMS of the distances between the associated landmarks on the registered source and the target. The sampling cases include uniform sampling (1), geometry-aware sampling with the NND ratio of 1/2 (2), and geometry-aware sampling with the NND ratio of 1/4 (3). The accuracy measures are shaded from lightest (0 mm) to darkest (1.5 mm).

Experiment		Sampling Case	Level (2D)					Level (3D)				
			1	2	3	4	5	1	2	3	4	5
Single-Feature	Translation	1	0.0	0.0	0.0	0.9	0.9	0.2	0.2	0.2	0.3	1.0
		2	0.0	0.0	0.0	0.0	0.8	0.1	0.1	0.1	0.1	0.1
		3	0.0	0.0	0.0	0.0	0.0	0.1	0.0	0.1	0.1	0.1
	Expansion	1	0.1	0.1	0.1	1.3	1.6	0.3	0.5	0.7	1.0	1.3
		2	0.1	0.1	0.1	0.1	1.4	0.2	0.3	0.4	0.8	1.0
		3	0.0	0.0	0.0	0.1	0.1	0.2	0.2	0.2	0.3	0.9
	Shrinkage	1	0.0	0.1	0.1	0.2	0.2	0.1	0.2	0.2	0.2	0.3
		2	0.0	0.0	0.1	0.0	0.1	0.1	0.1	0.1	0.2	0.2
		3	0.0	0.0	0.0	0.0	0.0	0.1	0.1	0.1	0.2	0.1
	Translation & Expansion	1	0.1	0.1	0.6	1.2	1.4	0.3	0.4	0.8	1.1	1.3
		2	0.1	0.1	0.1	0.9	1.3	0.2	0.3	0.5	1.0	1.2
		3	0.0	0.0	0.1	0.7	1.1	0.1	0.1	0.2	0.7	1.1
	Translation & Shrinkage	1	0.1	0.1	0.1	0.2	0.4	0.1	0.2	0.2	0.3	0.4
		2	0.0	0.0	0.1	0.1	0.2	0.1	0.1	0.1	0.2	0.3
		3	0.0	0.0	0.0	0.0	0.0	0.1	0.1	0.1	0.1	0.1
Double-Features	Translation I	1	0.0	0.0	0.0	1.1	1.2	0.2	0.2	0.4	0.4	1.1
		2	0.0	0.0	0.0	0.0	1.2	0.1	0.1	0.2	0.2	0.2
		3	0.0	0.0	0.0	0.0	0.0	0.1	0.1	0.1	0.1	0.1
	Translation II	1	0.0	0.0	0.0	1.0	1.1	0.2	0.3	0.4	0.5	1.2
		2	0.0	0.0	0.0	0.0	1.0	0.1	0.1	0.1	0.2	0.1
		3	0.0	0.0	0.0	0.0	0.0	0.1	0.1	0.1	0.1	0.1
	Translation III	1	0.0	0.0	0.0	0.0	1.2	0.3	0.2	0.3	0.3	1.2
		2	0.0	0.0	0.0	0.0	0.0	0.1	0.1	0.2	0.2	0.3
		3	0.0	0.0	0.0	0.0	0.0	0.1	0.1	0.1	0.1	0.1
	Scaling I	1	0.1	0.1	0.1	1.3	1.8	0.3	0.5	0.8	1.2	1.5
		2	0.0	0.1	0.1	0.1	1.5	0.3	0.4	0.7	0.9	1.3
		3	0.0	0.1	0.0	0.0	1.0	0.2	0.2	0.3	0.3	1.1
	Scaling II	1	0.0	0.1	0.1	0.2	0.2	0.1	0.1	0.2	0.3	0.4
		2	0.0	0.0	0.1	0.1	0.1	0.1	0.1	0.2	0.2	0.3
		3	0.0	0.0	0.0	0.1	0.0	0.1	0.1	0.1	0.1	0.1
	Scaling III	1	0.1	0.1	0.1	1.2	1.6	0.2	0.4	0.6	0.9	1.1
		2	0.1	0.1	0.1	0.1	1.0	0.2	0.3	0.5	0.6	0.9
		3	0.1	0.1	0.1	0.1	0.1	0.1	0.2	0.2	0.5	0.7
	Translation & Scaling I	1	0.1	0.1	0.5	1.4	1.7	0.3	0.6	0.9	1.3	1.5
		2	0.1	0.1	0.1	1.2	1.5	0.3	0.4	0.7	1.1	1.4
		3	0.1	0.0	0.1	1.1	1.5	0.1	0.2	0.3	0.9	1.3
	Translation & Scaling II	1	0.1	0.1	0.1	0.2	0.4	0.1	0.2	0.2	0.3	0.5
		2	0.0	0.0	0.0	0.0	0.3	0.1	0.1	0.2	0.2	0.3
		3	0.0	0.1	0.0	0.1	0.1	0.1	0.1	0.1	0.2	0.2
	Translation & Scaling III	1	0.1	0.1	0.6	0.9	1.2	0.3	0.4	0.7	0.9	1.1
		2	0.1	0.1	0.1	0.7	1.0	0.2	0.2	0.5	0.8	1.0
		3	0.0	0.1	0.1	0.6	0.8	0.1	0.1	0.2	0.6	0.9

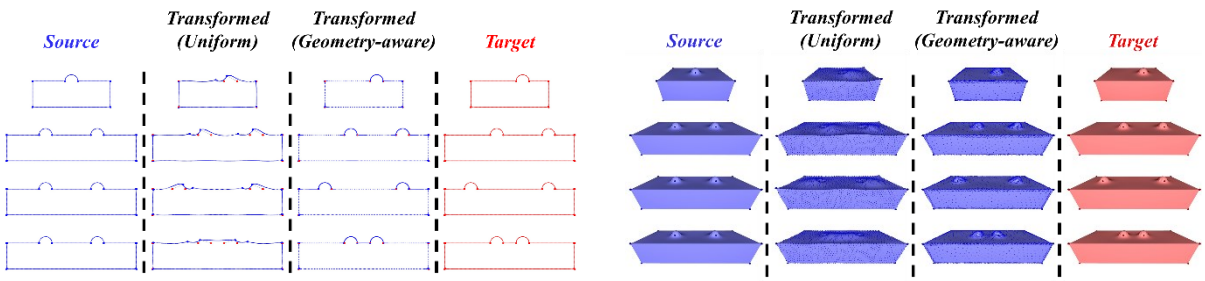

(a) Translation

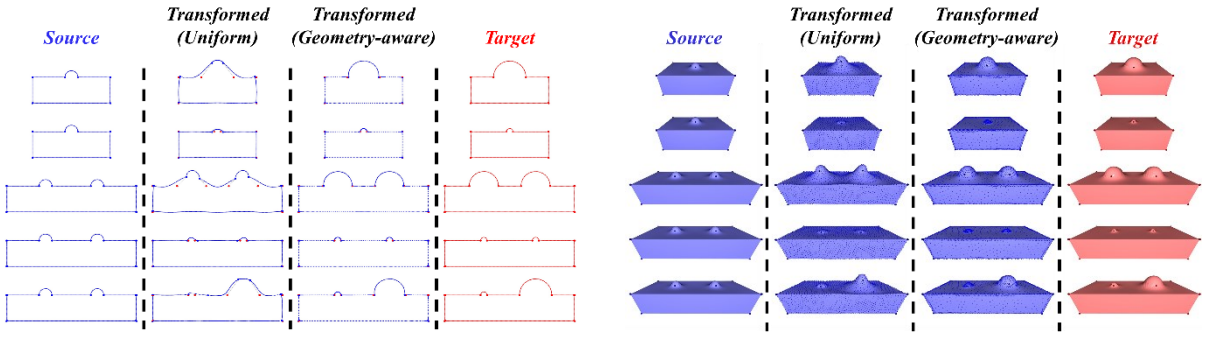

(b) Scaling

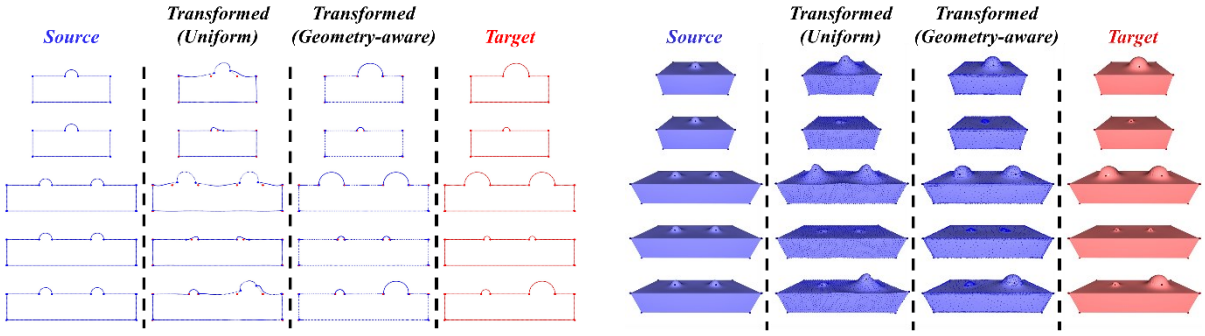

(c) Translation and scaling

Figure 5-8: Examples of the improving effects of geometry-aware point-set sampling on the registration accuracy in experiments with high levels of translation and/or scaling.

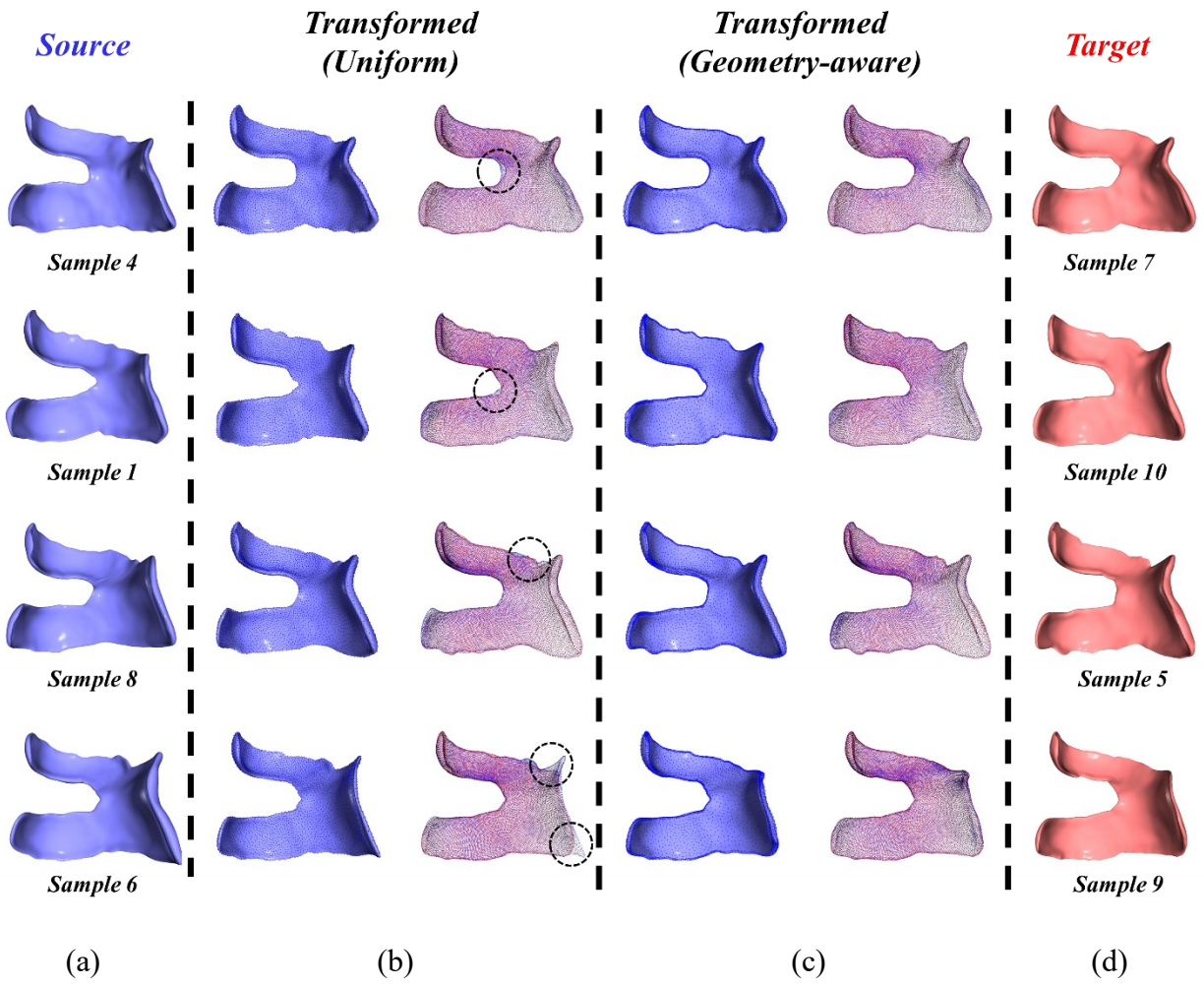

Figure 5-9: Examples of performance enhancement in registering the femur cartilage samples, comparing the uniform sampling with the geometry-aware sampling with higher density (Type II). Each row shows the results of an experiment including (a) the source mesh, (b) the mesh and point set for the registered source, alongside the vertices of the registered source mesh and the target mesh for the uniform sampling, (c) similar items as 2 for the geometry-aware sampling (Type II) and (d) the target mesh. The areas of notable distance error are shown with black circles.

5.4.2 Real experiments

A total number of 90 experiments were performed on the dataset, registering each sample on the rest of the samples. After each registration task, the computed transformation was applied to the source mesh, and the RMS and Hausdorff distances between the registered source and target

were obtained. Table 5-3 presents the measured distances between the registered source and the target for all of the experiments. The results showed that the CPD method performs better in aligning the cartilages using geometry-aware sampling in comparison with uniform sampling. With uniform sampling, there was a notable distance error in matching the edges of the cartilages, while by sampling a larger proportion of points in these areas of high curvature, more accurate alignment was achieved. Figure 5-9 provides some examples of such performance enhancement.

Table 5-3: RMS and Hausdorff distance between the registered source and target for the registration tasks between 10 samples of femur cartilage. In each cell, the first row shows the measured distance for the uniform sampling case, the second row represents the distance for the first type of geometry-aware sampling, and the third row shows the distance for the second type of geometry-aware sampling. The RMS distances are shaded from lightest (zero) to darkest (1 mm). The Hausdorff distances are shaded from the lightest (zero) to the darkest (7 mm).

		Target – RMS Distance										Target – Hausdorff Distance									
		1	**2**	**3**	**4**	**5**	**6**	**7**	**8**	**9**	**10**	**1**	**2**	**3**	**4**	**5**	**6**	**7**	**8**	**9**	**10**
Source	**1**	0.00	0.26	0.26	0.27	0.35	0.29	0.36	0.31	0.30	0.37	0.0	2.2	2.2	2.0	3.5	2.7	3.3	2.7	3.1	3.9
		0.00	0.20	0.21	0.20	0.24	0.24	0.25	0.23	0.22	0.27	0.0	1.1	1.4	1.3	2.7	1.9	2.2	1.4	2.0	3.2
		0.00	0.22	0.22	0.22	0.24	0.26	0.26	0.25	0.22	0.23	0.0	0.9	1.0	1.2	1.6	1.2	1.3	1.2	1.0	1.2
	2	0.27	0.00	0.31	0.19	0.28	0.24	0.22	0.22	0.23	0.23	2.5	0.0	4.5	1.6	2.9	1.8	1.7	1.7	3.1	2.1
		0.21	0.00	0.21	0.17	0.20	0.21	0.18	0.19	0.19	0.19	1.1	0.0	3.2	1.1	2.2	1.1	1.0	1.0	2.8	1.1
		0.24	0.00	0.18	0.20	0.20	0.24	0.20	0.21	0.19	0.21	0.9	0.0	0.9	1.0	1.2	1.4	0.9	0.9	1.6	1.0
	3	0.43	0.31	0.00	0.25	0.33	0.39	0.25	0.21	0.32	0.28	6.4	4.7	0.0	2.6	3.3	5.4	2.0	2.0	4.0	3.3
		0.29	0.23	0.00	0.18	0.22	0.26	0.19	0.18	0.21	0.22	4.3	3.3	0.0	1.3	2.5	2.9	1.2	1.1	2.3	2.9
		0.23	0.18	0.00	0.19	0.23	0.27	0.22	0.21	0.22	0.22	1.1	1.0	0.0	1.0	1.2	1.2	1.2	1.0	1.6	1.4
	4	0.43	0.37	0.25	0.00	0.47	0.43	0.30	0.25	0.42	0.31	4.8	3.5	3.4	0.0	6.2	4.7	3.5	1.8	4.0	3.7
		0.25	0.22	0.21	0.00	0.29	0.33	0.23	0.24	0.22	0.25	2.3	2.2	2.7	0.0	3.6	3.2	2.6	1.9	2.0	2.9
		0.26	0.21	0.21	0.00	0.26	0.31	0.22	0.26	0.23	0.25	1.1	1.4	1.2	0.0	1.5	1.7	1.2	1.8	1.3	2.1
	5	0.36	0.30	0.32	0.25	0.00	0.31	0.32	0.28	0.46	0.41	3.4	2.8	3.2	2.4	0.0	3.4	3.1	2.7	3.9	4.4
		0.24	0.20	0.22	0.20	0.00	0.20	0.21	0.21	0.21	0.24	2.2	2.1	2.0	1.7	0.0	1.6	1.9	1.7	2.0	2.3
		0.23	0.18	0.21	0.22	0.00	0.22	0.23	0.24	0.20	0.22	1.2	1.1	1.2	1.0	0.0	1.6	1.2	1.1	1.1	1.5
	6	0.77	0.80	0.63	0.42	0.38	0.00	0.71	0.26	0.85	0.90	6.6	7.6	5.6	4.5	3.8	0.0	6.5	2.3	7.7	7.1
		0.44	0.63	0.44	0.31	0.19	0.00	0.49	0.21	0.55	0.58	4.6	6.6	4.1	3.3	1.5	0.0	4.5	1.4	5.7	4.9
		0.22	0.20	0.22	0.24	0.20	0.00	0.25	0.24	0.19	0.21	1.0	1.1	1.4	1.5	1.0	0.0	1.3	1.4	1.0	1.3
	7	0.41	0.22	0.26	0.19	0.50	0.26	0.00	0.20	0.38	0.26	4.3	2.1	3.0	1.9	5.3	2.2	0.0	1.6	4.4	2.1
		0.25	0.16	0.18	0.17	0.31	0.23	0.00	0.20	0.21	0.19	2.4	0.9	1.5	1.5	3.8	1.3	0.0	1.3	2.4	1.5
		0.23	0.18	0.18	0.19	0.22	0.25	0.00	0.22	0.19	0.21	1.3	1.0	1.2	1.4	1.3	1.3	0.0	1.2	1.0	1.5
	8	0.49	0.44	0.28	0.22	0.63	0.46	0.41	0.00	0.56	0.42	5.2	5.5	2.7	1.8	7.0	4.1	5.3	0.0	6.1	4.8
		0.30	0.18	0.18	0.17	0.48	0.24	0.19	0.00	0.32	0.30	3.9	1.1	1.9	1.4	5.9	2.2	0.9	0.0	4.1	3.6
		0.22	0.19	0.18	0.19	0.23	0.25	0.21	0.00	0.21	0.21	1.2	0.9	1.0	1.2	1.5	1.3	1.0	0.0	2.3	1.1
	9	0.24	0.22	0.24	0.22	0.26	0.24	0.22	0.24	0.00	0.24	2.0	2.6	2.4	2.2	2.4	1.9	2.2	3.1	0.0	1.9
		0.23	0.17	0.22	0.20	0.22	0.22	0.21	0.22	0.00	0.22	1.3	2.0	2.1	1.7	1.7	1.4	2.0	2.5	0.0	1.7
		0.26	0.20	0.23	0.23	0.23	0.25	0.24	0.24	0.00	0.24	1.1	1.3	1.6	1.2	1.2	1.3	1.3	2.1	0.0	1.3
	10	0.29	0.31	0.26	0.26	0.46	0.30	0.27	0.26	0.32	0.00	3.0	3.4	3.1	2.7	4.4	2.9	2.1	1.8	3.6	0.0
		0.24	0.20	0.24	0.22	0.30	0.25	0.23	0.24	0.23	0.00	1.8	1.2	2.5	2.2	2.6	1.2	1.4	1.5	2.1	0.0
		0.27	0.22	0.24	0.24	0.26	0.29	0.25	0.26	0.24	0.00	1.1	1.0	1.6	1.3	1.6	1.4	1.1	1.4	1.0	0.0

In all 90 experiments, the RMS distance for the first case of geometry-aware sampling was lower than the distance associated with the uniform sampling. In addition, the second case of geometry-aware sampling outperformed the uniform sampling in 80 experiments as measured by the RMS distance. Considering the Hausdorff distance as the accuracy measure, both geometry-aware sampling cases achieved better results in 89 experiments in comparison with uniform sampling. Furthermore, between the two cases of geometry-aware sampling, the first case performed better in terms of RMS distance (63%, 57 out of 90 experiments), while the second case, i.e. the case with higher density on geometric features, had better performance in terms of Hausdorff distance (93%, 84 out of 90 experiments).

5.5 Chapter Discussion

Despite the improvements and refinements proposed for various aspects of the probabilistic registration method, the effect of point distribution on the performance of the Coherent Point Drift (CPD) registration method in matching geometric features is relatively unexplored. This study presented an experimental investigation into the effect of geometry-aware sampling on the performance of the CPD in aligning shapes with various geometric features. The objective of the study was to explore the possibility of enhancing registration accuracy by increasing the point density at salient areas of high curvature. Synthetic experiments were designed in 2D and 3D, involving source and target objects with the same global shape, but local dissimilarities. A set of landmark points were considered on the synthetic shapes, and a measure of true correspondence

was defined and utilized to evaluate the registration accuracy. Two cases of geometry-aware point-set sampling were compared with uniform sampling in terms of registration accuracy.

In addition, real examples involving the alignment of femur cartilages were examined. Similar to the synthetic experiments, each test compared uniform and geometry-aware sampling cases in terms of registration accuracy. However, unlike the synthetic experiments, no measure of true correspondence existed for these real shapes. Instead, widely-used measures such as RMS and Hausdorff distances were utilized to assess the registration accuracy quantitatively. In addition, the registered source and the target were visually inspected in all of the experiments.

The results of the synthetic experiments showed that the geometry-aware sampling improved the performance of the CPD method in matching geometric features. In high degrees of local deformation, the CPD method with uniform sampling usually failed to identify the desirable mapping between the synthetic objects and matched non-homologous parts; while using geometry-aware sampling increased the range for which true correspondence was established between the synthetic objects. In addition, the geometry-aware sampling with higher point density on geometric features (Type II) outperformed the case with the lower density in terms of registration accuracy.

Similarly, for the real examples, the geometry-aware sampling cases performed better than uniform sampling in terms of accuracy measures (RMS and Hausdorff). The alignment of cartilages was notably better on the edges when the second case of geometry-aware sampling was used and the Hausdorff distance was drastically lower for this case of sampling. However, in terms of the RMS distance, the first case of geometry-aware sampling, i.e. the case with lower point

density (Type I)performed slightly better than the case second. To address this, we argue that in the synthetic experiments, areas apart from the geometric features were line segments or planes, and even a sparse set of points in these regions was sufficient to achieve a desirable match (as long as the coherency of the deformation was preserved). However, for the femur cartilages, the curved surface of the cartilage required a higher density of points in these areas to achieve accurate alignment

Overall, by increasing the proportion of points in the geometric features of complex biological entities, the EM algorithm in the CPD method is "encouraged" to match the intricate features, despite the high-level energy of the complex deformations. Conversely, in uniform sampling, it may not be worthwhile to undergo complex deformations (with a high amount of energy) solely to align a few Gaussian Mixture Model (GMM) components on a few points.

In a previous study, Saval-Calvo et. al. developed an extension of the CPD registration method in which color information was used in estimating correspondence. In their study, alongside the main comparisons between their method and the CPD method, they evaluated the registration accuracy for uniform and color-based sampling. Using a face model with large elastic deformation on the eyebrow and lip (colored features of the face), they showed that their extension provides more accurate registration with color-based sampling. Similar to this study, our experiments showed that, for large local deformations, sampling a higher proportion of points on the geometric features could enhance the perception of the point sets and improve the registration accuracy.

Reference

[1] Myronenko, A., & Song, X. (2010). Point set registration: Coherent point drift. IEEE transactions on pattern analysis and machine intelligence, 32(12), 2262-2275.

[2] Besl, P. J., & McKay, N. D. (1992, April). Method for registration of 3-D shapes. In Sensor fusion IV: control paradigms and data structures (Vol. 1611, pp. 586-606). Spie.

[3] Laga, H., Guo, Y., Tabia, H., Fisher, R. B., & Bennamoun, M. (2018). 3D Shape analysis: fundamentals, theory, and applications. John Wiley & Sons.

[4] Bookstein, F. L., & Green, W. D. (1993, June). Thin-plate spline for deformations with specified derivatives. In Mathematical Methods in Medical Imaging II (Vol. 2035, pp. 14-28). SPIE.

[5] Chui, H., & Rangarajan, A. (2003). A new point matching algorithm for non-rigid registration. Computer Vision and Image Understanding, 89(2-3), 114-141.

[6] Jian, B., & Vemuri, B. C. (2005, October). A robust algorithm for point set registration using mixture of Gaussians. In Tenth IEEE International Conference on Computer Vision (ICCV'05) Volume 1 (Vol. 2, pp. 1246-1251). IEEE.

[7] Myronenko, A., & Song, X. (2010). Point set registration: Coherent point drift. IEEE transactions on pattern analysis and machine intelligence, 32(12), 2262-2275.

[8] Saval-Calvo, Marcelo, Jorge Azorin-Lopez, Andres Fuster-Guillo, Victor Villena-Martinez, and Robert B. Fisher. "3D non-rigid registration using color: color coherent point drift." Computer Vision and Image Understanding 169 (2018): 119-135.

[9] Peng, L., Li, G., Xiao, M., & Xie, L. (2016). Robust CPD algorithm for non-rigid point set registration based on structure information. PloS one, 11(2), e0148483.

[10] Wang, P., Wang, P., Qu, Z., Gao, Y., & Shen, Z. (2011). A refined coherent point drift (CPD) algorithm for point set registration. Science China Information Sciences, 54, 2639-2646.

[11] Yuksel, C. (2015, May). Sample elimination for generating Poisson disk sample sets. In Computer Graphics Forum (Vol. 34, No. 2, pp. 25-32).

[12] Luo, C., Ge, X., & Wang, Y. (2018, February). Uniformization and density adaptation for point cloud data via graph Laplacian. In Computer Graphics Forum (Vol. 37, No. 1, pp. 325-337).

[13] Meyer, M., Desbrun, M., Schröder, P., & Barr, A. H. (2003). Discrete differential-geometry operators for triangulated 2-manifolds. In Visualization and mathematics III (pp. 35-57). Springer Berlin Heidelberg.

[14] https://nda.nih.gov/oai/

[15] Taubin, G. (1995, June). Curve and surface smoothing without shrinkage. In Proceedings of IEEE international conference on computer vision (pp. 852-857). IEEE.

[16] Pietroni, N., Tarini, M., & Cignoni, P. (2009). Almost isometric mesh parameterization through abstract domains. IEEE Transactions on Visualization and Computer Graphics, 16(4), 621-635.

[17] Bishop, C. M., & Nasrabadi, N. M. (2006). Pattern recognition and machine learning (Vol. 4, No. 4, p. 738). New York: springer.

[18] Girosi, F., Jones, M., & Poggio, T. (1995). Regularization theory and neural networks architectures. Neural computation, 7(2), 219-269.

CHAPTER 6:CONCLUSIONS

6.1 Summary of research work

This doctoral thesis is in the pursuit of accomplishing four objectives in statistical shape modelling and computational mechanics, all offering advantages for orthopaedics.

Chapter 1 presents a consistent implementation of the hypoelastic constitutive equations into the user-material (UMAT) subroutine in Abaqus. The chapter reviews the concept of objectivity and objective stress rates. Furthermore, the structure of hypoelastic constitutive models and algorithms related to several UMAT variables are covered. To implement a constitutive equation in UMAT, it is essential to reformulate the model as a relationship between the rate of deformation and the Jaumann rate of Kirchhoff stress. This reformation is derived for six hypoelastic constitutive equations and the correctness of the updated Jacobian matrix DDSDDE and the stress matrix STRESS is validated by modelling a solid element under the simple shear and uniaxial extension.

Chapter 2 provides an SSM-based assessment for pelvic morphology. Employing an automated pipeline, the CT image dataset of 40 pelvis (20 men and 20 female) is segmented into smoothed meshes and uniform point sets. A registration procedure is used in which one of the point sets is morphed on the rest of the point sets to establish correspondence. Various Displacement Vector Fields (DVFs) are extracted from the point sets in correspondence: the DVFs

are derived for anatomical variation (sample to sex-specific average), asymmetry (left-right sample), and sexual dimorphism (male to female average). Principal Component Analysis (PCA) identifies the dominant patterns within fields, with their significance assessed via permutation-based statistical tests. The norm of DVFs at each point is measured for all samples and the significance of point-wise variations is determined by comparing records to the overall average value across all points.

Chapter 3 evaluates the ability of anatomical SSMs in predicting unknown samples and modelling in-training samples by comparing refined triangle meshes of the samples with the mesh of SSM instances. Similar to the computational algorithm in Chapter 2, twelve SSMs are constructed for the hemipelvis and talus (sex-specific and overall models with and without size). The key difference in Chapter 3 is the employment of a mesh-tessellation optimization technique to enhance triangle mesh quality for each sample, as these meshes serve as the ground truth for accuracy and generalizability assessments. Additionally, the compactness of the models is assessed. Various models are compared with each other in terms of compactness, accuracy, and generalization ability.

Chapter 4 presents an experimental study on the effect of geometry-aware point-set sampling on the accuracy of the Coherent Point Drift (CPD) registration method. The motivation is to assess the accuracy of the CPD method in registration tasks that requires pronounced local transformations. Using rectangles and boxes with one or two local features, the accuracy of the CPD method is evaluated for uniform and geometry-aware point-set sampling. The geometry-aware approach samples a higher point density at the areas of high curvature. In addition, a group

of 10 femur cartilage samples is registered on one another using uniform and geometry-aware sampling, and the accuracy of the registrations is measured by two metric distances.

6.2 Conclusions of research work

The consistent implementation of a constitutive law requires the user to reformulate the constitutive model as a relationship between the rate of deformation and the Jaumann rate of Kirchhoff stress. In addition, if the user is employing the DSTRAN, which is the incremental rate of deformation based on midpoint integration, the constitutive model is required to be reformulated as a relationship between the rate of deformation and the Jaumann rate of Cauchy stress. A potential mistake in implementing a constitutive equation is using the latter form to update the Jacobian matrix. Simple examples of incorrect implementation (for uniaxial extension) demonstrate that this coding error leads to the divergence of the analyses.

For all of the assessments of pelvic morphology, the significant patterns are greater or equal to three. Local measurements also reveal significant areas of anatomical variation. The Anterior Superior Iliac Spine (ASIS) stands out as a focal point of anatomical variation; particularly the lateral-medial movement of ASIS represents a dominant mode of variation in both sexes. In both the hemipelvis (size included) and pelvis, PC1 primarily indicated size change, with more dominance in the male group. Notably, significant matching asymmetry occurred at the insertion sites of muscle groups on the pubis, ischium, and ilium. Regarding bilateral asymmetry, females exhibited an oblique rotation of the left-right hemipelves, while males demonstrated elevation/depression of hemipelves. The DVF between the average male and female models was

significant in terms of separating the male and female samples and displays recognizable features like the larger size, narrower sciatic notches and subpubic angles, upright ilia, and thicker rami in men, attributes frequently used in forensic sex determination.

The quality measurements of SSMs show that the talus shape displays the same level of total variance for both male and female groups, while the total variance of talus shape-size is slightly higher for the male group. The size dominance is also more pronounced on the male talus. The "static" sex-specific models (average shape-size) could simulate the training samples with an accuracy of 0.97 mm for the female talus and 0.80 mm for the male talus. The "dynamic" sex-specific models (shape-size model with PC1 and average shape with scaling) could simulate the samples with an accuracy of 0.58 mm for the female group and 0.68 mm for the male group. The generalizability of the overall models (shape, shape-size) was 0.28 mm for the female talus and 0.32 mm for the male talus, which is less than the average in-plane dimensions of the image dataset. The shape and shape-size of the hemipelvis exhibit higher variance within the male group. For the hemipelvis, the static sex-specific models (average shape-size) have an accuracy of 1.83 mm for the female hemipelvis and 2.04 mm for the male hemipelvis. As the dynamic sex-specific model, the shape-size model with PC1 is a better choice than the average shape with scaling, which could be due to the allometry in the pelvic bone. For the overall shape-size models, the generalizability is 1.03 mm for the female hemipelvis and 1.17 mm for the male hemipelvis.

The synthetic experiments in 2D and 3D demonstrate the advantageous impact of geometry-aware sampling on enhancing the performance of the CPD method in matching local features. Particularly, under high degree of local deformation, uniform sampling often fails in establishing

desirable mappings between synthetic objects, while employing geometry-aware sampling notably increases the range of dissimilarity for which favorable correspondences could be identified. Similarly, for the matching of femur cartilages, geometry-aware sampling consistently surpassed uniform sampling in accuracy metrics (RMS and Hausdorff). Specifically, when the second geometry-aware sampling approach (with denser point distribution on the local features) is used, the cartilage alignment along edges shows improvement. The consideration of higher point density on local features of objects guides the EM algorithm in the CPD method to prioritize the alignment of local features; on the contrary, with the uniform sampling, the CPD might not engage in high-content energy required for complex deformations, solely to align a few Gaussian Mixture Model (GMM) components on a limited number of points.

6.3 Research contributions and highlights

The reformulation of the Green-Naghdi hypoelastic model into the UMAT subroutine was challenging and the kinematical relations were employed to develop such connections. In addition, the reformation of the Truesdell hypoelastic models could be employed for the simulation of soft biological tissues (hyperelasticity).

The knowledge about the sex-specific anatomical variation and asymmetry of the pelvis at multiple levels was limited, which is addressed by this research. The computational algorithm employed to model bilateral asymmetry serves as a valuable tool for quantifying anatomical restoration after pelvic surgeries and difficult childbirth. The animated patterns of anatomical

variation offer a valuable educational resource for medical students. The measurement of the significance of the displacement field between the average male and female models, a contribution. The assessment for the matching asymmetry of the hemipelvis provides valuable insights for unilateral pelvis surgeries.

The effect of geometry-aware point-set sampling on the non-rigid registration method is relatively unexplored. This research provides an experimental set-up to evaluate the possible enhancement of the CPD method in matching local features. Lastly, the accurate alignment of the femur cartilage through geometry-aware sampling is beneficial for more accurate biomechanical simulation of the knee joints.

6.4 Limitations and recommendations

To study a lower-limb bone and the pelvis, the adequate size of the training set to cover the whole geometric variations within a population is reported as 200. However, the morphological study of the pelvic bone only had access to 20 samples for each sex-specific assessment which might not cover the entire variations in the male and female populations.

For a future study, the established correspondence between hemipelves could be isolated at important anatomical regions, and SSM could be constructed for these regions. As an example, a regional SSM describing only the geometric variation of the acetabulum could be a beneficial tool for the patient-specific implant designs of total hip replacement.

The training size is an important factor in the ability of anatomical structures to predict unknown shapes. The training size of an SSM could be expanded by generating artificial samples. Using the established correspondence between each two samples, a nonlinear path between the samples could be identified and artificial samples could be constructed along this path. This augmentation of the training set could enhance the predictive ability of the models.

BIBLIOGRAPHY

Adeeb, S., & Herzog, W. (2009). Simulation of biological growth. Computer Methods in Biomechanics and Biomedical Engineering, 12(6), 617-626

Ahrend, M. D., Noser, H., Shanmugam, R., Burr, F., Kamer, L., Kamarul, T., ... & Gueorguiev-Rüegg, B. (2020). Development of generic Asian pelvic bone models using CT-based 3D statistical modelling. Journal of orthopaedic translation, 20, 100-106.

Ambellan, F., Lamecker, H., von Tycowicz, C., & Zachow, S. (2019). Statistical shape models: understanding and mastering variation in anatomy (pp. 67-84). Springer International Publishing.

Arand, C., Wagner, D., Richards, R. G., Noser, H., Kamer, L., Sawaguchi, T., & Rommens, P. M. (2019). 3D statistical model of the pelvic ring–a CT-based statistical evaluation of anatomical variation. Journal of Anatomy, 234(3), 376-383.

Aspert, N., Santa-Cruz, D., & Ebrahimi, T. (2002, August). Mesh: Measuring errors between surfaces using the hausdorff distance. In Proceedings. IEEE international conference on multimedia and expo (Vol. 1, pp. 705-708). IEEE.

Audenaert, E. A., Pattyn, C., Steenackers, G., De Roeck, J., Vandermeulen, D., & Claes, P. (2019). Statistical shape modelling of skeletal anatomy for sex discrimination: their training size, sexual dimorphism, and asymmetry. Frontiers in bioengineering and biotechnology, 7, 302.

Baclig, M. M., Westover, L., & Adeeb, S. (2019). Categorizing three-dimensional symmetry using reflection, rotoinversion, and translation symmetry. Symmetry, 11(9), 1132.

Baldwin, M. A., Langenderfer, J. E., Rullkoetter, P. J., & Laz, P. J. (2010). Development of subject-specific and statistical shape models of the knee using an efficient segmentation and mesh-morphing approach. Computer methods and programs in biomedicine, 97(3), 232-240.

Bellini, C., & Federico, S. (2015). Green-Naghdi rate of the Kirchhoff stress and deformation rate: the elasticity tensor. Zeitschrift für angewandte Mathematik und Physik, 66, 1143-1163.

Besl, P. J., & McKay, N. D. (1992, April). Method for registration of 3-D shapes. In Sensor fusion IV: control paradigms and data structures (Vol. 1611, pp. 586-606). Spie.

Bishop, C. M., & Nasrabadi, N. M. (2006). Pattern recognition and machine learning (Vol. 4, No. 4, p. 738). New York: springer.

Bonet, J., Gil, A. J., & Wood, R. D. (2021). Nonlinear solid mechanics for finite element analysis: dynamics. Cambridge University Press.

Bonet, J., & Wood, R. D. (2008). Nonlinear continuum mechanics for finite element analysis, 2nd edition. Cambridge university press.

Bookstein, F. L. (1991). Morphometric tools for landmark data Cambridge University Press. New York

Bookstein, F. L., & Green, W. D. (1993, June). Thin-plate spline for deformations with specified derivatives. In Mathematical Methods in Medical Imaging II (Vol. 2035, pp. 14-28). SPIE.

Bruzek, J. (2002). A method for visual determination of sex, using the human hip bone. American Journal of Physical Anthropology: The Official Publication of the American Association of Physical Anthropologists, 117(2), 157-168.

Brynskog, E., Iraeus, J., Reed, M. P., & Davidsson, J. (2021). Predicting pelvis geometry using a morphometric model with overall anthropometric variables. Journal of biomechanics, 126, 110633.

Camargo, Arley. "PCAtest: testing the statistical significance of principal component analysis in R." PeerJ 10 (2022): e12967.

Campbell, J. Q., & Petrella, A. J. (2016). Automated finite element modelling of the lumbar spine: using a statistical shape model to generate a virtual population of models. Journal of biomechanics, 49(13), 2593-2599.

Chui, Haili, and Anand Rangarajan. "A new point matching algorithm for non-rigid registration." Computer Vision and Image Understanding 89, no. 2-3 (2003): 114-141.

Clouthier, A. L., Smith, C. R., Vignos, M. F., Thelen, D. G., Deluzio, K. J., & Rainbow, M. J. (2019). The effect of articular geometry features identified using statistical shape modelling on knee biomechanics. Medical engineering & physics, 66, 47-55.

Conover, William Jay. Practical nonparametric statistics. Vol. 350. john wiley & sons, 1999.

Cootes, T. F., Taylor, C. J., Cooper, D. H., & Graham, J. (1995). Active shape models-their training and application. Computer vision and image understanding, 61(1), 38-59.

Curnier, A., He, Q. C., & Zysset, P. (1994). Conewise linear elastic materials. Journal of Elasticity, 37, 1-38.

Manual, A. U. (2010). Dassault Systems Simulia Corporation. Providence USA.

Davies, R. H., Twining, C. J., Cootes, T. F., Waterton, J. C., & Taylor, C. J. (2002). A minimum description length approach to statistical shape modelling. IEEE transactions on medical imaging, 21(5), 525-537.

van de Giessen, M., Vos, F. M., Grimbergen, C. A., van Vliet, L. J., & Streekstra, G. J. (2012). An efficient and robust algorithm for parallel groupwise registration of bone surfaces. In Medical Image Computing and Computer-Assisted Intervention–MICCAI 2012: 15th International Conference, Nice, France, October 1-5, 2012, Proceedings, Part III 15 (pp. 164-171). Springer Berlin Heidelberg.

de Souza Neto, E. A., Peric, D., & Owen, D. R. (2011). Computational methods for plasticity: theory and applications. John Wiley & Sons.

Dienes, J. K. (1979). On the analysis of rotation and stress rate in deforming bodies. Acta mechanica, 32(4), 217-232.

Dryden, I. L., & Mardia, K. V. (2016). Statistical shape analysis: with applications in R (Vol. 995). John Wiley & Sons.

Dworzak, J., Lamecker, H., von Berg, J., Klinder, T., Lorenz, C., Kainmüller, D., ... & Zachow, S. (2010). 3D reconstruction of the human rib cage from 2D projection images using a statistical shape model. International journal of computer assisted radiology and surgery, 5, 111-124.

Ead, M. S. (2020). Virtual Reconstruction of Pelvic Fractures.

Ead, M. S., Palizi, M., Jaremko, J. L., Westover, L., & Duke, K. K. (2021). Development and application of the average pelvic shape in virtual pelvic fracture reconstruction. The International Journal of Medical Robotics and Computer Assisted Surgery, 17(2), e2199.

Ead, M. S., Westover, L., Polege, S., McClelland, S., Jaremko, J. L., & Duke, K. K. (2020). Virtual reconstruction of unilateral pelvic fractures by using pelvic symmetry. International Journal of Computer Assisted Radiology and Surgery, 15, 1267-1277.

Epstein, M. (2010). The geometrical language of continuum mechanics. Cambridge University Press.

Eringen, A. C. (1980). ''Mechanics of Continua''Robert E. KriegerPublishing Company, Huntington, New York, 762-76g.

Federico, S., Alhasadi, M. F., & Grillo, A. (2019). Eshelby's inclusion theory in light of Noether's theorem. Mathematics and Mechanics of Complex Systems, 7(3), 247-285.

Fischer, B., & Mitteroecker, P. (2015). Covariation between human pelvis shape, stature, and head size alleviates the obstetric dilemma. Proceedings of the National Academy of Sciences, 112(18), 5655-5660.

Fitzpatrick, C. K., Baldwin, M. A., Laz, P. J., FitzPatrick, D. P., Lerner, A. L., & Rullkoetter, P. J. (2011). Development of a statistical shape model of the patellofemoral joint for investigating relationships between shape and function. Journal of biomechanics, 44(13), 2446-2452.

Frazer, L., Nicolella, D. P., & Southwest Research Institute San Antonio United States. (2020). Human Response to High Rate Loading.

Freed, A. (2008). Anisotropy in hypoelastic soft-tissue mechanics, I: theory. Journal of Mechanics of Materials and Structures, 3(5), 911-928.

Freed, A. D. (2010). Hypoelastic soft tissues. Part I: theory. Acta Mechanica, 213(1-2), 189-204.

Girosi, F., Jones, M., & Poggio, T. (1995). Regularization theory and neural networks architectures. Neural computation, 7(2), 219-269.

Handrich, K., Kamer, L., Mayo, K., Sawaguchi, T., Noser, H., Arand, C., ... & Rommens, P. M. (2021). Asymmetry of the pelvic ring evaluated by CT-based 3D statistical modeling. Journal of anatomy, 238(5), 1225-1232.

Hashiguchi, K., & Yamakawa, Y. (2012). Introduction to finite strain theory for continuum elasto-plasticity. John Wiley & Sons.

Heimann, T., & Meinzer, H. P. (2009). Statistical shape models for 3D medical image segmentation: a review. Medical image analysis, 13(4), 543-563.

Hierl, T., Doerfler, H. M., Huempfner-Hierl, H., & Kruber, D. (2021). Evaluation of the midface by statistical shape modeling. Journal of Oral and Maxillofacial Surgery, 79(1), 202-e1.

Hughes, T. J., & Winget, J. (1980). Finite rotation effects in numerical integration of rate constitutive equations arising in large-deformation analysis. International journal for numerical methods in engineering, 15(12), 1862-1867.

Islam, K., Dobbe, A., Komeili, A., Duke, K., El-Rich, M., Dhillon, S., ... & Jomha, N. M. (2014). Symmetry analysis of talus bone: a geometric morphometric approach. Bone & joint research, 3(5), 139-145.

Ji, W., Waas, A. M., & Bazant, Z. P. (2013). On the importance of work-conjugacy and objective stress rates in finite deformation incremental finite element analysis. Journal of Applied Mechanics, 80(4), 041024.

Jian, B., & Vemuri, B. C. (2005, October). A robust algorithm for point set registration using mixture of Gaussians. In Tenth IEEE International Conference on Computer Vision (ICCV'05) Volume 1 (Vol. 2, pp. 1246-1251). IEEE.

Johnson, G. C., & Bammann, D. J. (1984). A discussion of stress rates in finite deformation problems. International Journal of Solids and Structures, 20(8), 725-737.

Kazhdan, M., Bolitho, M., & Hoppe, H. (2006, June). Poisson surface reconstruction. In Proceedings of the fourth Eurographics symposium on Geometry processing (Vol. 7, p. 0).

Kida, N., & Morishita, Y. (2018). Continuum mechanical modeling of developing epithelial tissues with anisotropic surface growth. Finite Elements in Analysis and Design, 144, 49-60.

Klein, K. F. (2015). Use of parametric finite element models to investigate effects of occupant characteristics on lower-extremity injuries in frontal crashes (Doctoral dissertation, University of Michigan).

Krol, Z., Skadlubowicz, P., Hefti, F., & Krieg, A. H. (2013). Virtual reconstruction of pelvic tumor defects based on a gender-specific statistical shape model. Computer aided surgery, 18(5-6), 142-153.

Kröner, E. (1959). Allgemeine kontinuumstheorie der versetzungen und eigenspannungen. Archive for Rational Mechanics and Analysis, 4, 273-334.

Kurki, H. K. (2017). Bilateral asymmetry in the human pelvis. The Anatomical Record, 300(4), 653-665.

Laga, H., Guo, Y., Tabia, H., Fisher, R. B., & Bennamoun, M. (2018). 3D Shape analysis: fundamentals, theory, and applications. John Wiley & Sons.

Liu, T., Jomha, N. M., Adeeb, S., El-Rich, M., & Westover, L. (2020). Investigation of the average shape and principal variations of the human talus bone using statistic shape model. Frontiers in Bioengineering and Biotechnology, 8, 656.

Luo, C., Ge, X., & Wang, Y. (2018, February). Uniformization and density adaptation for point cloud data via graph Laplacian. In Computer Graphics Forum (Vol. 37, No. 1, pp. 325-337).

Mardia, K. V., Bookstein, F. L., & Moreton, I. J. (2000). Statistical assessment of bilateral symmetry of shapes. Biometrika, 87(2), 285-300.

Hughes, T. J., & Marsden, J. E. (1983). Mathematical foundations of elasticity. Englewood Cliffs: Prentice-Hall.

Marzola, A., Robilotta, C., Volpe, Y., Governi, L., & Furferi, R. (2021). Statistical Shape Model: comparison between ICP and CPD algorithms on medical applications. International Journal on Interactive Design and Manufacturing (IJIDeM), 15, 85-89.

Mehrabadi, M. M., & Nemat-Nasser, S. (1987). Some basic kinematical relations for finite deformations of continua. Mechanics of Materials, 6(2), 127-138.

Meyer, M., Desbrun, M., Schröder, P., & Barr, A. H. (2003). Discrete differential-geometry operators for triangulated 2-manifolds. In Visualization and mathematics III (pp. 35-57). Springer Berlin Heidelberg.

Meynen, A., Matthews, H., Nauwelaers, N., Claes, P., Mulier, M., & Scheys, L. (2020). Accurate reconstructions of pelvic defects and discontinuities using statistical shape models. Computer methods in biomechanics and biomedical engineering, 23(13), 1026-1033.

Myronenko, A., & Song, X. (2010). Point set registration: Coherent point drift. IEEE transactions on pattern analysis and machine intelligence, 32(12), 2262-2275.

Myronenko, A., Song, X., & Carreira-Perpinan, M. (2006). Non-rigid point set registration: Coherent point drift. Advances in neural information processing systems, 19.

Nguyen, N., & Waas, A. M. (2016). Nonlinear, finite deformation, finite element analysis. Zeitschrift für angewandte Mathematik und Physik, 67, 1-24.

Noll, W. (2006). A frame-free formulation of elasticity. Journal of Elasticity, 83, 291-307.

Paprosky, W. G., Perona, P. G., & Lawrence, J. M. (1994). Acetabular defect classification and surgical reconstruction in revision arthroplasty: a 6-year follow-up evaluation. The Journal of arthroplasty, 9(1), 33-44.

Peng, L., Li, G., Xiao, M., & Xie, L. (2016). Robust CPD algorithm for non-rigid point set registration based on structure information. PloS one, 11(2), e0148483.

Pietroni, N., Tarini, M., & Cignoni, P. (2009). Almost isometric mesh parameterization through abstract domains. IEEE Transactions on Visualization and Computer Graphics, 16(4), 621-635.

Pinsky, P. M., Ortiz, M., & Pister, K. S. (1983). Numerical integration of rate constitutive equations in finite deformation analysis. Computer Methods in Applied Mechanics and Engineering, 40(2), 137-158.

Plessers, K., Berghe, P. V., Van Dijck, C., Wirix-Speetjens, R., Debeer, P., Jonkers, I., & Vander Sloten, J. (2018). Virtual reconstruction of glenoid bone defects using a statistical shape model. Journal of shoulder and elbow surgery, 27(1), 160-166.

Prot, V., Skallerud, B., & Holzapfel, G. A. (2007). Transversely isotropic membrane shells with application to mitral valve mechanics. Constitutive modelling and finite element implementation. International journal for numerical methods in engineering, 71(8), 987-1008.

Sarkalkan, N., Weinans, H., & Zadpoor, A. A. (2014). Statistical shape and appearance models of bones. Bone, 60, 129-140.

Saval-Calvo, M., Azorin-Lopez, J., Fuster-Guillo, A., Villena-Martinez, V., & Fisher, R. B. (2018). 3D non-rigid registration using color: color coherent point drift. Computer Vision and Image Understanding, 169, 119-135.

Shui, W., Zhou, M., Maddock, S., He, T., Wang, X., & Deng, Q. (2017). A PCA-Based method for determining craniofacial relationship and sexual dimorphism of facial shapes. Computers in biology and medicine, 90, 33-49.

Slice, D. E. (2007). Geometric morphometrics. Annu. Rev. Anthropol., 36, 261-281.

Slice, D. E. (Ed.). (2006). Modern morphometrics in physical anthropology. Springer Science & Business Media.

Styner, M., Lieberman, J. A., Pantazis, D., & Gerig, G. (2004). Boundary and medial shape analysis of the hippocampus in schizophrenia. Medical image analysis, 8(3), 197-203.

Sun, W., Chaikof, E. L., & Levenston, M. E. (2008). Numerical approximation of tangent moduli for finite element implementations of nonlinear hyperelastic material models.

Taubin, G. (1995, June). Curve and surface smoothing without shrinkage. In Proceedings of IEEE international conference on computer vision (pp. 852-857). IEEE.

Thompson, D. A. W. (1942). On Growth and Form, Cambridge Univ. Press1942.

Tobolsky, V. A., Kurki, H. K., & Stock, J. T. (2016). Patterns of directional asymmetry in the pelvis and pelvic canal. American Journal of Human Biology, 28(6), 804-810.

Truesdell, C., Noll, W., Truesdell, C., & Noll, W. (2004). The non-linear field theories of mechanics (pp. 1-579). Springer Berlin Heidelberg.

Tsin, Y., & Kanade, T. (2004). A correlation-based approach to robust point set registration. In Computer Vision-ECCV 2004: 8th European Conference on Computer Vision, Prague, Czech Republic, May 11-14, 2004. Proceedings, Part III 8 (pp. 558-569). Springer Berlin Heidelberg.

van de Giessen, M., Vos, F. M., Grimbergen, C. A., van Vliet, L. J., & Streekstra, G. J. (2012). An efficient and robust algorithm for parallel groupwise registration of bone surfaces. In Medical

Image Computing and Computer-Assisted Intervention–MICCAI 2012: 15th International Conference, Nice, France, October 1-5, 2012, Proceedings, Part III 15 (pp. 164-171). Springer Berlin Heidelberg.

van Veldhuizen, W. A., van der Wel, H., Kuipers, H. Y., Kraeima, J., Ten Duis, K., Wolterink, J. M., ... & IJpma, F. F. (2023). Development of a Statistical Shape Model and Assessment of Anatomical Shape Variations in the Hemipelvis. Journal of Clinical Medicine, 12(11), 3767.

Vanden Berghe, P., Demol, J., Gelaude, F., & Vander Sloten, J. (2017). Virtual anatomical reconstruction of large acetabular bone defects using a statistical shape model. Computer methods in biomechanics and biomedical engineering, 20(6), 577-586.

Von Elm, E., Altman, D. G., Egger, M., Pocock, S. J., Gøtzsche, P. C., Vandenbroucke, J. P., & Strobe Initiative. (2014). The Strengthening the Reporting of Observational Studies in Epidemiology (STROBE) Statement: guidelines for reporting observational studies. International journal of surgery, 12(12), 1495-1499.

Wang, P., Wang, P., Qu, Z., Gao, Y., & Shen, Z. (2011). A refined coherent point drift (CPD) algorithm for point set registration. Science China Information Sciences, 54, 2639-2646.

Wang, Y., Cao, L., Bai, Z., Reed, M. P., Rupp, J. D., Hoff, C. N., & Hu, J. (2016). A parametric ribcage geometry model accounting for variations among the adult population. Journal of biomechanics, 49(13), 2791-2798.

Wittman, A. B., & Wall, L. L. (2007). The evolutionary origins of obstructed labor: bipedalism, encephalization, and the human obstetric dilemma. Obstetrical & gynecological survey, 62(11), 739-748.

Yuksel, C. (2015, May). Sample elimination for generating Poisson disk sample sets. In Computer Graphics Forum (Vol. 34, No. 2, pp. 25-32).

Zachow, S., Lamecker, H., Elsholtz, B., & Stiller, M. (2005, May). Reconstruction of mandibular dysplasia using a statistical 3D shape model. In International congress series (Vol. 1281, pp. 1238-1243). Elsevier.

Zhang, K., Cao, L., Fanta, A., Reed, M. P., Neal, M., Wang, J. T., ... & Hu, J. (2017). An automated method to morph finite element whole-body human models with a wide range of stature and body shape for both men and women. Journal of biomechanics, 60, 253-260.

Zhou, X., & Tamma, K. K. (2003). On the applicability and stress update formulations for corotational stress rate hypoelasticity constitutive models. Finite elements in analysis and design, 39(8), 783-816.

APPENDIX A: DERIVATION OF CONSISTENT JACOBIANS AND UMAT IMPLEMENTATIONS

For deriving the consistent Jacobian of a hypoelastic model in ABAQUS, the constitutive equation must be expressed in terms of the Jaumann rate of the Kirchhoff stress.

The constitutive equation of *a hypoelastic model based on the Truesdell rate of the Cauchy stress* is

$$\boldsymbol{\sigma}^{\mathrm{o}} = \dot{\boldsymbol{\sigma}} - \boldsymbol{\sigma}\boldsymbol{\ell}^{T} - \boldsymbol{\ell}\boldsymbol{\sigma} + (\mathrm{tr}\boldsymbol{d})\boldsymbol{\sigma} = \mathbb{C}^{\sigma^{\mathrm{o}}} : \boldsymbol{d}, \tag{A-1}$$

In which the elasticity tensor $\mathbb{C}^{\sigma^{\mathrm{o}}}$ is *given*. Considering the expression of the time derivative of the volume ratio, i.e.

$$\dot{J} = J\,\mathrm{tr}\boldsymbol{d} \tag{A-2}$$

Multiplying Eq. (A-1) by J and employing Eq. (2-8), Eq. (2-14), and Eq. (2-21) result in:

$$\boldsymbol{\tau}^{\nabla} = \dot{\boldsymbol{\tau}} + \boldsymbol{\tau}\boldsymbol{w} - \boldsymbol{w}\boldsymbol{\tau} = J\mathbb{C}^{\sigma^{\mathrm{o}}} : \boldsymbol{d} + J\boldsymbol{\sigma}\boldsymbol{d} + J\boldsymbol{d}\boldsymbol{\sigma} = \mathbb{C}^{\tau^{\nabla}} : \boldsymbol{d}. \tag{A-3}$$

Now, representing the last equality in index notation, i.e.

$$J\mathbb{C}^{\sigma^{\mathrm{o}}}_{ijkl} d_{kl} + J\sigma_{im} d_{mj} + J d_{im}\sigma_{mj} = \mathbb{C}^{\tau^{\nabla}}_{ijkl} d_{kl}, \tag{A-4}$$

Rewriting $J\sigma_{im}d_{mj}$ as

$$J\sigma_{im}d_{mj} = J\sigma_{ik}\delta_{jl}d_{kl}, \tag{A-5}$$

And $Jd_{im}\sigma_{mj}$ as

$$Jd_{im}\sigma_{mj} = J\sigma_{jl}\delta_{ik}d_{kl}, \tag{A-6}$$

The following expression will be achieved:

$$\left(J\mathbb{c}^{\sigma^{\circ}}_{ijkl} + J\sigma_{ik}\delta_{jl} + J\sigma_{jl}\delta_{ik}\right)d_{kl} = \mathbb{c}^{\tau^{\nabla}}_{ijkl}d_{kl}. \tag{A-7}$$

Now, based on Eq. (2-53), we can finally write

$$\mathbb{c}^{\sigma^{\circ}}_{ijkl} + \sigma_{ik}\delta_{jl} + \sigma_{jl}\delta_{ik} = \mathbb{D}_{ijkl}, \tag{A-8}$$

Which coincides with Eq. (2-54).

For *a hypoelastic model associated with the Truesdell rate of the Kirchhoff stress*, the constitutive equation is

$$\boldsymbol{\tau}^{\circ} = \mathbb{c}^{\tau^{\circ}} : \boldsymbol{d}. \tag{A-9}$$

Considering Eq. (2-14), Eq. (2-18), Eq. (2-19), and Eq. (A-2), we can easily obtain the expression

$$\boldsymbol{\tau}^{\circ} = J\boldsymbol{\sigma}^{\circ}, \tag{A-10}$$

Which, substituted into Eq. (A-9), yields

$$\boldsymbol{\sigma}^{\circ} = J^{-1}\mathbb{c}^{\tau^{\circ}} : \boldsymbol{d} = \mathbb{c}^{\sigma^{\circ}} : \boldsymbol{d}, \tag{A-11}$$

And, therefore:

$$J^{-1}\mathbb{c}^{\tau^{\circ}}_{ijkl} = \mathbb{c}^{\sigma^{\circ}}_{ijkl}. \tag{A-12}$$

Now, employing the above relation into Eq. (A-8) leads to,

$$J^{-1}\mathbb{c}^{\tau^{\circ}}_{ijkl} + \sigma_{ik}\delta_{jl} + \sigma_{jl}\delta_{ik} = \mathbb{D}_{ijkl}, \tag{A-13}$$

i.e. Eq. (2-55).

For *a hypoelastic model based on the Jaumann rate of the Cauchy stress*, the constitutive equation is

$$\boldsymbol{\sigma}^{\nabla} = \dot{\boldsymbol{\sigma}} + \boldsymbol{\sigma w} - \boldsymbol{w\sigma} = \mathbb{c}^{\sigma^{\nabla}} : \boldsymbol{d}. \tag{A-14}$$

Multiplying Eq. (A-14)) by J, adding $(J\,\boldsymbol{tr d})\boldsymbol{\sigma}$ to both sides of the equation and employing Eq. (2-14) and (2-21), we obtain

$$\boldsymbol{\tau}^{\nabla} = \dot{\boldsymbol{\tau}} + \boldsymbol{\tau w} - \boldsymbol{w\tau} = J\mathbb{c}^{\sigma^{\nabla}} : \boldsymbol{d} + (J\ \mathrm{tr}\boldsymbol{d})\boldsymbol{\sigma} = \mathbb{c}^{\tau^{\nabla}} : \boldsymbol{d}. \tag{A-15}$$

Now, expressing the last equality in index notation

$$J\mathbb{c}^{\sigma^{\nabla}}_{ijkl} d_{kl} + J\sigma_{ij} d_{mm} = \mathbb{c}^{\tau^{\nabla}}_{ijkl} d_{kl}, \tag{A-16}$$

Rewriting the term $J\sigma_{ij} d_{mm}$ as

$$J\sigma_{ij} d_{mm} = J\sigma_{ij}\delta_{kl} d_{kl}, \tag{A-17}$$

And eliminating d_{kl} from both sides of Eq. (A-16), we obtain

$$J\mathbb{c}^{\sigma^{\nabla}}_{ijkl} + J\sigma_{ij}\delta_{kl} = \mathbb{c}^{\tau^{\nabla}}_{ijkl}. \tag{A-18}$$

Finally, considering Eq. (2-53), the elasticity tensor $\mathbb{c}^{\sigma^{\nabla}}$ of the hypoelastic model, which is *known*, could be related to the tensorial version of the consistent Jacobian, i.e.

$$\mathbb{c}^{\sigma^{\nabla}}_{ijkl} + \sigma_{ij}\delta_{kl} = \mathbb{D}_{ijkl}. \tag{A-19}$$

Which coincides with Eq. (2-56).

The constitutive equation of *a hypoelastic model based on the Green–Naghdi rate of the Cauchy stress* is

$$\boldsymbol{\sigma}^{\Delta} = \dot{\boldsymbol{\sigma}} + \boldsymbol{\sigma}\boldsymbol{\Omega} - \boldsymbol{\Omega}\boldsymbol{\sigma} = \mathbb{c}^{\sigma^{\Delta}} : \boldsymbol{d}. \tag{A-20}$$

Based on Eq. (2-62), we have

$$\dot{\boldsymbol{\sigma}} + \boldsymbol{\sigma}\left(\boldsymbol{w} + \sum_{\alpha,\beta=1}^{3} \frac{\lambda_\beta - \lambda_\alpha}{\lambda_\beta + \lambda_\alpha} \boldsymbol{b}_\alpha \boldsymbol{d} \boldsymbol{b}_\beta\right) - \left(\boldsymbol{w} + \sum_{\alpha,\beta=1}^{3} \frac{\lambda_\beta - \lambda_\alpha}{\lambda_\beta + \lambda_\alpha} \boldsymbol{b}_\alpha \boldsymbol{d} \boldsymbol{b}_\beta\right)\boldsymbol{\sigma} = \mathbb{c}^{\sigma^{\Delta}} : \boldsymbol{d}, \tag{A-21}$$

From which, rearranging the terms,

$$\begin{aligned} &\mathbb{c}^{\sigma^{\Delta}} : \boldsymbol{d} - \boldsymbol{\sigma}\left(\sum_{\alpha,\beta=1}^{3} \frac{\lambda_\beta - \lambda_\alpha}{\lambda_\beta + \lambda_\alpha} \boldsymbol{b}_\alpha \boldsymbol{d} \boldsymbol{b}_\beta\right) \\ &+ \left(\sum_{\alpha,\beta=1}^{3} \frac{\lambda_\beta - \lambda_\alpha}{\lambda_\beta + \lambda_\alpha} \boldsymbol{b}_\alpha \boldsymbol{d} \boldsymbol{b}_\beta\right)\boldsymbol{\sigma} = \dot{\boldsymbol{\sigma}} + \boldsymbol{\sigma}\boldsymbol{w} - \boldsymbol{w}\boldsymbol{\sigma}. \end{aligned} \tag{A-22}$$

Now, using Eq. (2-20) and Eq. (A-14) and index notation, we obtain

$$\begin{aligned} &\mathbb{c}_{ijkl}^{\sigma^{\Delta}} d_{kl} - \sigma_{im}\left(\sum_{\alpha,\beta=1}^{3} \frac{\lambda_\beta - \lambda_\alpha}{\lambda_\beta + \lambda_\alpha} (b_\alpha)_{mk} d_{kl} \left(b_\beta\right)_{lj}\right) \\ &+ \left(\sum_{\alpha,\beta=1}^{3} \frac{\lambda_\beta - \lambda_\alpha}{\lambda_\beta + \lambda_\alpha} (b_\alpha)_{ik} d_{kl} \left(b_\beta\right)_{lm}\right)\sigma_{mj} = \mathbb{c}_{ijkl}^{\sigma^{\nabla}} d_{kl}. \end{aligned} \tag{A-23}$$

Employing Eq. (2-60) and eliminating d_{kl} from both sides, we get

$$\mathbb{C}_{ijkl}^{\sigma^{\Delta}} - \sigma_{im}B_{mjkl} + \sigma_{jm}B_{imkl} = \mathbb{C}_{ijkl}^{\sigma^{\nabla}}, \tag{A-24}$$

And, finally, based on Eq. (A-19), we obtain Eq. (2-58)

$$\mathbb{C}_{ijkl}^{\sigma^{\Delta}} - \sigma_{im}B_{mjkl} + \sigma_{jm}B_{imkl} + \sigma_{ij}\delta_{kl} = \mathbb{D}_{ijkl}. \tag{A-25}$$

For *a hypoelastic model based on the Green–Naghdi rate of the Kirchhoff stress*, the constitutive equation is

$$\boldsymbol{\tau}^{\Delta} = \dot{\boldsymbol{\tau}} + \boldsymbol{\tau\Omega} - \boldsymbol{\Omega\tau} = \mathbb{C}^{\tau^{\Delta}} : \boldsymbol{d}. \tag{A-26}$$

Using Eq. (2-14), Eq. (2-21), and Eq. (A-2), we obtain

$$\mathbb{C}_{ijkl}^{\sigma^{\Delta}} = J^{-1}\mathbb{C}_{ijkl}^{\tau^{\Delta}} - \sigma_{ij}\delta_{kl}, \tag{A-27}$$

Substituting which into Eq. (A-25) yields Eq (2-59):

$$J^{-1}\mathbb{C}_{ijkl}^{\tau^{\Delta}} - \sigma_{im}B_{mjkl} + \sigma_{mj}B_{imkl} = \mathbb{D}_{ijkl}. \tag{A-28}$$

C ZERO-GRADED HYPOELASTIC CONSTITUTIVE MODEL BASED ON THE JAUMANN RATE OF THE CAUCHY STRESS

C PROPS(1) -> YOUNG'S MODULUS

C PROPS(2) -> POISSON'S RATIO

C

```
C Ee      = YOUNG'S MODULUS

C Nu      = POISSON'S RATIO

C Lambda  = LAME'S CONSTANT

C Mu      = LAME'S CONSTANT

C IDEN    = KRONECKER DELTA

C STRESS  = UMAT-SUBROUTINE STRESS ARRAY

C STRESSV = VECTOR VERSION OF "STRESS"

C STRESSM = MATRIX VERSION OF "STRESS"

C DSTRAN  = UMAT-SUBROUTINE INCREMENTAL STRAIN ARRAY

C DSTRANV = VECTOR VERSION OF "DSTRAN"

C DSTRANM = MATRIX VERSION OF "DSTRAN"

C C1      = FOURTH-ORDER ELASTICITY TENSOR

C DDSDDE  = UMAT-SUBROUTINE CONSISTENT JACOBIAN ARRAY

C C2      = FOURTH-ORDER TENSOR VERSION OF "DDSDDE"

C=============================================================
```

```
      SUBROUTINE UMAT(STRESS,STATEV,DDSDDE,SSE,SPD,SCD,
     1 RPL,DDSDDT,DRPLDE,DRPLDT,
     2 STRAN,DSTRAN,TIME,DTIME,TEMP,DTEMP,PREDEF,DPRED,CMNAME,
     3 NDI,NSHR,NTENS,NSTATV,PROPS,NPROPS,COORDS,DROT,PNEWDT,
     4 CELENT,DFGRD0,DFGRD1,NOEL,NPT,LAYER,KSPT,JSTEP,KINC)
C
      INCLUDE 'ABA_PARAM.INC'
C
      CHARACTER*80 CMNAME
      DIMENSION STRESS(NTENS),STATEV(NSTATV),
     1 DDSDDE(NTENS,NTENS),
     2 DDSDDT(NTENS),DRPLDE(NTENS),
     3 STRAN(NTENS),DSTRAN(NTENS),TIME(2),PREDEF(1),DPRED(1),
     4 PROPS(NPROPS),COORDS(3),DROT(3,3),DFGRD0(3,3),DFGRD1(3,3),
     5 JSTEP(4)
```

```
C
      INTEGER :: i,j,k,l
      REAL*8 :: Ee,Nu,Lambda,Mu
      REAL*8, DIMENSION(NTENS) :: STRESSV,DSTRANV
      REAL*8, DIMENSION(3,3) :: IDEN,STRESSM,DSTRANM
      REAL*8, DIMENSION(3,3,3,3) :: C1,C2
      PARAMETER(ZERO=0.D0,ONE=1.D0,TWO=2.D0)
C
      Ee=PROPS(1)
      Nu=PROPS(2)
      Lambda=Nu*Ee/((ONE+Nu)*(ONE-TWO*Nu))
      Mu=Ee/(TWO*(ONE+Nu))
C
      DO i=1,3
      DO j=1,3
```

```
      IF (i.EQ.j) THEN
      IDEN(i,j)=ONE
      ELSE
      IDEN(i,j)=ZERO
      ENDIF
      END DO
      END DO
C
      STRESSV=STRESS
      STRESSM(1,1)=STRESSV(1)
      STRESSM(2,2)=STRESSV(2)
      STRESSM(3,3)=STRESSV(3)
      STRESSM(1,2)=STRESSV(4)
      STRESSM(2,1)=STRESSV(4)
      STRESSM(1,3)=STRESSV(5)
```

```
      STRESSM(3,1)=STRESSV(5)

      STRESSM(2,3)=STRESSV(6)

      STRESSM(3,2)=STRESSV(6)

C

      DSTRANV=DSTRAN

      DSTRANM(1,1)=DSTRANV(1)

      DSTRANM(2,2)=DSTRANV(2)

      DSTRANM(3,3)=DSTRANV(3)

      DSTRANM(1,2)=ONE/TWO*DSTRANV(4)

      DSTRANM(2,1)=ONE/TWO*DSTRANV(4)

      DSTRANM(1,3)=ONE/TWO*DSTRANV(5)

      DSTRANM(3,1)=ONE/TWO*DSTRANV(5)

      DSTRANM(2,3)=ONE/TWO*DSTRANV(6)

      DSTRANM(3,2)=ONE/TWO*DSTRANV(6)

C
```

```
      DO i=1,3
      DO j=1,3
      DO k=1,3
      DO l=1,3
      C1(i,j,k,l)=
     1 Lambda*IDEN(i,j)*IDEN(k,l)+
     2 Mu*IDEN(i,k)*IDEN(j,l)+
     3 Mu*IDEN(i,l)*IDEN(j,k)
      END DO
      END DO
      END DO
      END DO
C
      DO i=1,3
      DO j=1,3
```

```
      DO k=1,3
      DO l=1,3
      STRESSM(i,j)=STRESSM(i,j)+C1(i,j,k,l)*DSTRANM(k,l)
      END DO
      END DO
      END DO
      END DO
C
      DO i=1,3
      DO j=1,3
      DO k=1,3
      DO l=1,3
      C2(i,j,k,l)=C1(i,j,k,l)+STRESSM(i,j)*IDEN(k,l)
      END DO
      END DO
```

```
      END DO
      END DO
C
      STRESS(1)=STRESSM(1,1)
      STRESS(2)=STRESSM(2,2)
      STRESS(3)=STRESSM(3,3)
      STRESS(4)=STRESSM(1,2)
      STRESS(5)=STRESSM(1,3)
      STRESS(6)=STRESSM(2,3)
C
      DO i=1,3
      DDSDDE(i,1)=C2(i,i,1,1)
      DDSDDE(i,2)=C2(i,i,2,2)
      DDSDDE(i,3)=C2(i,i,3,3)
      DDSDDE(i,4)=C2(i,i,1,2)
```

```
DDSDDE(i,5)=C2(i,i,1,3)

DDSDDE(i,6)=C2(i,i,2,3)

END DO

DDSDDE(4,1)=C2(1,2,1,1)

DDSDDE(4,2)=C2(1,2,2,2)

DDSDDE(4,3)=C2(1,2,3,3)

DDSDDE(4,4)=C2(1,2,1,2)

DDSDDE(4,5)=C2(1,2,1,3)

DDSDDE(4,6)=C2(1,2,2,3)

DDSDDE(5,1)=C2(1,3,1,1)

DDSDDE(5,2)=C2(1,3,2,2)

DDSDDE(5,3)=C2(1,3,3,3)

DDSDDE(5,4)=C2(1,3,1,2)

DDSDDE(5,5)=C2(1,3,1,3)

DDSDDE(5,6)=C2(1,3,2,3)
```

```
      DDSDDE(6,1)=C2(2,3,1,1)
      DDSDDE(6,2)=C2(2,3,2,2)
      DDSDDE(6,3)=C2(2,3,3,3)
      DDSDDE(6,4)=C2(2,3,1,2)
      DDSDDE(6,5)=C2(2,3,1,3)
      DDSDDE(6,6)=C2(2,3,2,3)
      RETURN
      END
C=============================================================
C ZERO-GRADED HYPOELASTIC CONSTITUTIVE MODEL BASED ON THE JAUMANN RATE OF THE KIRCHHOFF STRESS
C=============================================================
C PROPS(1) -> YOUNG'S MODULUS
C PROPS(2) -> POISSON'S RATIO
C
```

```
C Ee      = YOUNG'S MODULUS

C Nu      = POISSON'S RATIO

C Lambda  = LAME'S CONSTANT

C Mu      = LAME'S CONSTANT

C IDEN    = KRONECKER DELTA

C DFGRD1  = UMAT-SUBROUTINE DEFORMATION GRADIENT AT THE END OF
THE INCREMENT

C Ffin    = MATRIX VERSION OF "DFGRD1"

C Jfin    = DETERMINANT OF "Ffin"

C STRESS  = UMAT-SUBROUTINE STRESS ARRAY

C STRESSV = VECTOR VERSION OF "STRESS"

C STRESSM = MATRIX VERSION OF "STRESS"

C DSTRAN  = UMAT-SUBROUTINE INCREMENTAL STRAIN ARRAY

C DSTRANV = VECTOR VERSION OF "DSTRAN"

C DSTRANM = MATRIX VERSION OF "DSTRAN"
```

```
C C1      = FOURTH-ORDER ELASTICITY TENSOR
C DDSDDE  = UMAT-SUBROUTINE CONSISTENT JACOBIAN ARRAY
C C2      = FOURTH-ORDER TENSOR VERSION OF "DDSDDE"
C=============================================================
      SUBROUTINE UMAT(STRESS,STATEV,DDSDDE,SSE,SPD,SCD,
     1 RPL,DDSDDT,DRPLDE,DRPLDT,
     2 STRAN,DSTRAN,TIME,DTIME,TEMP,DTEMP,PREDEF,DPRED,CMNAME,
     3 NDI,NSHR,NTENS,NSTATV,PROPS,NPROPS,COORDS,DROT,PNEWDT,
     4 CELENT,DFGRD0,DFGRD1,NOEL,NPT,LAYER,KSPT,JSTEP,KINC)
C
      INCLUDE 'ABA_PARAM.INC'
C
      CHARACTER*80 CMNAME
      DIMENSION STRESS(NTENS),STATEV(NSTATV),
     1 DDSDDE(NTENS,NTENS),
```

```
     2 DDSDDT(NTENS),DRPLDE(NTENS),
     3 STRAN(NTENS),DSTRAN(NTENS),TIME(2),PREDEF(1),DPRED(1),
     4 PROPS(NPROPS),COORDS(3),DROT(3,3),DFGRD0(3,3),DFGRD1(3,3),
     5 JSTEP(4)
C
      INTEGER :: i,j,k,l
      REAL*8 :: Ee,Nu,Lambda,Mu,Jfin
      REAL*8, DIMENSION(NTENS) :: STRESSV,DSTRANV
      REAL*8, DIMENSION(3,3) :: IDEN,STRESSM,DSTRANM,Ffin
      REAL*8, DIMENSION(3,3,3,3) :: C1,C2
      PARAMETER(ZERO=0.D0,ONE=1.D0,TWO=2.D0)
C
      Ee=PROPS(1)
      Nu=PROPS(2)
      Lambda=Nu*Ee/((ONE+Nu)*(ONE-TWO*Nu))
```

```
      Mu=Ee/(TWO*(ONE+Nu))
C
      DO i=1,3
      DO j=1,3
      IF (i.EQ.j) THEN
      IDEN(i,j)=ONE
      ELSE
      IDEN(i,j)=ZERO
      ENDIF
      END DO
      END DO
C
      Ffin=DFGRD1
      Jfin= Ffin(1,1)*(Ffin(2,2)*Ffin(3,3)-Ffin(2,3)*Ffin(3,2))+
     1      Ffin(1,2)*(Ffin(2,3)*Ffin(3,1)-Ffin(2,1)*Ffin(3,3))+
```

```
     2      Ffin(1,3)*(Ffin(2,1)*Ffin(3,2)-Ffin(2,2)*Ffin(3,1))
C
      STRESSV=STRESS
      STRESSM(1,1)=STRESSV(1)
      STRESSM(2,2)=STRESSV(2)
      STRESSM(3,3)=STRESSV(3)
      STRESSM(1,2)=STRESSV(4)
      STRESSM(2,1)=STRESSV(4)
      STRESSM(1,3)=STRESSV(5)
      STRESSM(3,1)=STRESSV(5)
      STRESSM(2,3)=STRESSV(6)
      STRESSM(3,2)=STRESSV(6)
C
      DSTRANV=DSTRAN
      DSTRANM(1,1)=DSTRANV(1)
```

```
      DSTRANM(2,2)=DSTRANV(2)
      DSTRANM(3,3)=DSTRANV(3)
      DSTRANM(1,2)=ONE/TWO*DSTRANV(4)
      DSTRANM(2,1)=ONE/TWO*DSTRANV(4)
      DSTRANM(1,3)=ONE/TWO*DSTRANV(5)
      DSTRANM(3,1)=ONE/TWO*DSTRANV(5)
      DSTRANM(2,3)=ONE/TWO*DSTRANV(6)
      DSTRANM(3,2)=ONE/TWO*DSTRANV(6)
C
      DO i=1,3
      DO j=1,3
      DO k=1,3
      DO l=1,3
      C1(i,j,k,l)=
     1 ONE/Jfin*Lambda*IDEN(i,j)*IDEN(k,l)+
```

```
     2 ONE/Jfin*Mu*IDEN(i,k)*IDEN(j,l)+
     3 ONE/Jfin*Mu*IDEN(i,l)*IDEN(j,k)-
     4 STRESSM(i,j)*IDEN(k,l)
      END DO
      END DO
      END DO
      END DO
C
      DO i=1,3
      DO j=1,3
      DO k=1,3
      DO l=1,3
      STRESSM(i,j)=STRESSM(i,j)+C1(i,j,k,l)*DSTRANM(k,l)
      END DO
      END DO
```

```
      END DO
      END DO
C
      DO i=1,3
      DO j=1,3
      DO k=1,3
      DO l=1,3
      C2(i,j,k,l)=
     1 ONE/Jfin*Lambda*IDEN(i,j)*IDEN(k,l)+
     2 ONE/Jfin*Mu*IDEN(i,k)*IDEN(j,l)+
     3 ONE/Jfin*Mu*IDEN(i,l)*IDEN(j,k)
      END DO
      END DO
      END DO
      END DO
```

```
C
      STRESS(1)=STRESSM(1,1)
      STRESS(2)=STRESSM(2,2)
      STRESS(3)=STRESSM(3,3)
      STRESS(4)=STRESSM(1,2)
      STRESS(5)=STRESSM(1,3)
      STRESS(6)=STRESSM(2,3)
C
      DO i=1,3
      DDSDDE(i,1)=C2(i,i,1,1)
      DDSDDE(i,2)=C2(i,i,2,2)
      DDSDDE(i,3)=C2(i,i,3,3)
      DDSDDE(i,4)=C2(i,i,1,2)
      DDSDDE(i,5)=C2(i,i,1,3)
      DDSDDE(i,6)=C2(i,i,2,3)
```

```
END DO

DDSDDE(4,1)=C2(1,2,1,1)

DDSDDE(4,2)=C2(1,2,2,2)

DDSDDE(4,3)=C2(1,2,3,3)

DDSDDE(4,4)=C2(1,2,1,2)

DDSDDE(4,5)=C2(1,2,1,3)

DDSDDE(4,6)=C2(1,2,2,3)

DDSDDE(5,1)=C2(1,3,1,1)

DDSDDE(5,2)=C2(1,3,2,2)

DDSDDE(5,3)=C2(1,3,3,3)

DDSDDE(5,4)=C2(1,3,1,2)

DDSDDE(5,5)=C2(1,3,1,3)

DDSDDE(5,6)=C2(1,3,2,3)

DDSDDE(6,1)=C2(2,3,1,1)

DDSDDE(6,2)=C2(2,3,2,2)
```

```
      DDSDDE(6,3)=C2(2,3,3,3)
      DDSDDE(6,4)=C2(2,3,1,2)
      DDSDDE(6,5)=C2(2,3,1,3)
      DDSDDE(6,6)=C2(2,3,2,3)
      RETURN
      END
C=================================================================
C ZERO-GRADED HYPOELASTIC CONSTITUTIVE MODEL BASED ON THE
TRUESDELL RATE OF THE CAUCHY STRESS
C=================================================================
C PROPS(1) -> YOUNG'S MODULUS
C PROPS(2) -> POISSON'S RATIO
C
C Ee      = YOUNG'S MODULUS
C Nu      = POISSON'S RATIO
```

```
C Lambda  = LAME'S CONSTANT

C Mu      = LAME'S CONSTANT

C IDEN    = KRONECKER DELTA

C STRESS  = UMAT-SUBROUTINE STRESS ARRAY

C STRESSV = VECTOR VERSION OF "STRESS"

C STRESSM = MATRIX VERSION OF "STRESS"

C DSTRAN  = UMAT-SUBROUTINE INCREMENTAL STRAIN ARRAY

C DSTRANV = VECTOR VERSION OF "DSTRAN"

C DSTRANM = MATRIX VERSION OF "DSTRAN"

C C1      = FOURTH-ORDER ELASTICITY TENSOR

C DDSDDE  = UMAT-SUBROUTINE CONSISTENT JACOBIAN ARRAY

C C2      = FOURTH-ORDER TENSOR VERSION OF "DDSDDE"

C=============================================================

      SUBROUTINE UMAT(STRESS,STATEV,DDSDDE,SSE,SPD,SCD,

     1 RPL,DDSDDT,DRPLDE,DRPLDT,
```

```
     2 STRAN,DSTRAN,TIME,DTIME,TEMP,DTEMP,PREDEF,DPRED,CMNAME,
     3 NDI,NSHR,NTENS,NSTATV,PROPS,NPROPS,COORDS,DROT,PNEWDT,
     4 CELENT,DFGRD0,DFGRD1,NOEL,NPT,LAYER,KSPT,JSTEP,KINC)
C
      INCLUDE 'ABA_PARAM.INC'
C
      CHARACTER*80 CMNAME
      DIMENSION STRESS(NTENS),STATEV(NSTATV),
     1 DDSDDE(NTENS,NTENS),
     2 DDSDDT(NTENS),DRPLDE(NTENS),
     3 STRAN(NTENS),DSTRAN(NTENS),TIME(2),PREDEF(1),DPRED(1),
     4 PROPS(NPROPS),COORDS(3),DROT(3,3),DFGRD0(3,3),DFGRD1(3,3),
     5 JSTEP(4)
C
      INTEGER :: i,j,k,l
```

```
      REAL*8 :: Ee,Nu,Lambda,Mu
      REAL*8, DIMENSION(NTENS) :: STRESSV,DSTRANV
      REAL*8, DIMENSION(3,3) :: IDEN,STRESSM,DSTRANM
      REAL*8, DIMENSION(3,3,3,3) :: C1,C2
      PARAMETER(ZERO=0.D0,ONE=1.D0,TWO=2.D0)
C
      Ee=PROPS(1)
      Nu=PROPS(2)
      Lambda=Nu*Ee/((ONE+Nu)*(ONE-TWO*Nu))
      Mu=Ee/(TWO*(ONE+Nu))
C
      DO i=1,3
      DO j=1,3
      IF (i.EQ.j) THEN
      IDEN(i,j)=ONE
```

```
      ELSE
      IDEN(i,j)=ZERO
      ENDIF
      END DO
      END DO
C
      STRESSV=STRESS
      STRESSM(1,1)=STRESSV(1)
      STRESSM(2,2)=STRESSV(2)
      STRESSM(3,3)=STRESSV(3)
      STRESSM(1,2)=STRESSV(4)
      STRESSM(2,1)=STRESSV(4)
      STRESSM(1,3)=STRESSV(5)
      STRESSM(3,1)=STRESSV(5)
      STRESSM(2,3)=STRESSV(6)
```

```
      STRESSM(3,2)=STRESSV(6)
C
      DSTRANV=DSTRAN
      DSTRANM(1,1)=DSTRANV(1)
      DSTRANM(2,2)=DSTRANV(2)
      DSTRANM(3,3)=DSTRANV(3)
      DSTRANM(1,2)=ONE/TWO*DSTRANV(4)
      DSTRANM(2,1)=ONE/TWO*DSTRANV(4)
      DSTRANM(1,3)=ONE/TWO*DSTRANV(5)
      DSTRANM(3,1)=ONE/TWO*DSTRANV(5)
      DSTRANM(2,3)=ONE/TWO*DSTRANV(6)
      DSTRANM(3,2)=ONE/TWO*DSTRANV(6)
C
      DO i=1,3
      DO j=1,3
```

```
      DO k=1,3
      DO l=1,3
      C1(i,j,k,l)=
     1 Lambda*IDEN(i,j)*IDEN(k,l)+
     2 Mu*IDEN(i,k)*IDEN(j,l)+
     3 Mu*IDEN(i,l)*IDEN(j,k)+
     4 STRESSM(i,k)*IDEN(j,l)+
     5 STRESSM(j,l)*IDEN(i,k)-
     6 STRESSM(i,j)*IDEN(k,l)
      END DO
      END DO
      END DO
      END DO
C
      DO i=1,3
```

```
      DO j=1,3
      DO k=1,3
      DO l=1,3
      STRESSM(i,j)=STRESSM(i,j)+C1(i,j,k,l)*DSTRANM(k,l)
      END DO
      END DO
      END DO
      END DO
C
      DO i=1,3
      DO j=1,3
      DO k=1,3
      DO l=1,3
      C2(i,j,k,l)=
     1 Lambda*IDEN(i,j)*IDEN(k,l)+
```

```
     2 Mu*IDEN(i,k)*IDEN(j,l)+
     3 Mu*IDEN(i,l)*IDEN(j,k)+
     4 STRESSM(i,k)*IDEN(j,l)+
     5 STRESSM(j,l)*IDEN(i,k)
      END DO
      END DO
      END DO
      END DO
C
      STRESS(1)=STRESSM(1,1)
      STRESS(2)=STRESSM(2,2)
      STRESS(3)=STRESSM(3,3)
      STRESS(4)=STRESSM(1,2)
      STRESS(5)=STRESSM(1,3)
      STRESS(6)=STRESSM(2,3)
```

```
C

      DO i=1,3

      DDSDDE(i,1)=C2(i,i,1,1)

      DDSDDE(i,2)=C2(i,i,2,2)

      DDSDDE(i,3)=C2(i,i,3,3)

      DDSDDE(i,4)=C2(i,i,1,2)

      DDSDDE(i,5)=C2(i,i,1,3)

      DDSDDE(i,6)=C2(i,i,2,3)

      END DO

      DDSDDE(4,1)=C2(1,2,1,1)

      DDSDDE(4,2)=C2(1,2,2,2)

      DDSDDE(4,3)=C2(1,2,3,3)

      DDSDDE(4,4)=C2(1,2,1,2)

      DDSDDE(4,5)=C2(1,2,1,3)

      DDSDDE(4,6)=C2(1,2,2,3)
```

```
      DDSDDE(5,1)=C2(1,3,1,1)
      DDSDDE(5,2)=C2(1,3,2,2)
      DDSDDE(5,3)=C2(1,3,3,3)
      DDSDDE(5,4)=C2(1,3,1,2)
      DDSDDE(5,5)=C2(1,3,1,3)
      DDSDDE(5,6)=C2(1,3,2,3)
      DDSDDE(6,1)=C2(2,3,1,1)
      DDSDDE(6,2)=C2(2,3,2,2)
      DDSDDE(6,3)=C2(2,3,3,3)
      DDSDDE(6,4)=C2(2,3,1,2)
      DDSDDE(6,5)=C2(2,3,1,3)
      DDSDDE(6,6)=C2(2,3,2,3)
      RETURN
      END
C=============================================================
```

```
C ZERO-GRADED HYPOELASTIC CONSTITUTIVE MODEL BASED ON THE TRUESDELL RATE OF THE KIRCHHOFF STRESS

C=============================================================

C PROPS(1) -> YOUNG'S MODULUS

C PROPS(2) -> POISSON'S RATIO

C

C Ee      = YOUNG'S MODULUS

C Nu      = POISSON'S RATIO

C Lambda  = LAME'S CONSTANT

C Mu      = LAME'S CONSTANT

C IDEN    = KRONECKER DELTA

C DFGRD1  = UMAT-SUBROUTINE DEFORMATION GRADIENT AT THE END OF THE INCREMENT

C Ffin    = MATRIX VERSION OF "DFGRD1"

C Jfin    = DETERMINANT OF "Ffin"

C STRESS  = UMAT-SUBROUTINE STRESS ARRAY
```

```
C STRESSV = VECTOR VERSION OF "STRESS"

C STRESSM = MATRIX VERSION OF "STRESS"

C DSTRAN  = UMAT-SUBROUTINE INCREMENTAL STRAIN ARRAY

C DSTRANV = VECTOR VERSION OF "DSTRAN"

C DSTRANM = MATRIX VERSION OF "DSTRAN"

C C1      = FOURTH-ORDER ELASTICITY TENSOR

C DDSDDE  = UMAT-SUBROUTINE CONSISTENT JACOBIAN ARRAY

C C2      = FOURTH-ORDER TENSOR VERSION OF "DDSDDE"

C=============================================================

      SUBROUTINE UMAT(STRESS,STATEV,DDSDDE,SSE,SPD,SCD,

     1 RPL,DDSDDT,DRPLDE,DRPLDT,

     2 STRAN,DSTRAN,TIME,DTIME,TEMP,DTEMP,PREDEF,DPRED,CMNAME,

     3 NDI,NSHR,NTENS,NSTATV,PROPS,NPROPS,COORDS,DROT,PNEWDT,

     4 CELENT,DFGRD0,DFGRD1,NOEL,NPT,LAYER,KSPT,JSTEP,KINC)

C
```

```
      INCLUDE 'ABA_PARAM.INC'
C
      CHARACTER*80 CMNAME
      DIMENSION STRESS(NTENS),STATEV(NSTATV),
     1 DDSDDE(NTENS,NTENS),
     2 DDSDDT(NTENS),DRPLDE(NTENS),
     3 STRAN(NTENS),DSTRAN(NTENS),TIME(2),PREDEF(1),DPRED(1),
     4 PROPS(NPROPS),COORDS(3),DROT(3,3),DFGRD0(3,3),DFGRD1(3,3),
     5 JSTEP(4)
C
      INTEGER :: i,j,k,l
      REAL*8 :: Ee,Nu,Lambda,Mu,Jfin
      REAL*8, DIMENSION(NTENS) :: STRESSV,DSTRANV
      REAL*8, DIMENSION(3,3) :: IDEN,STRESSM,DSTRANM,Ffin
      REAL*8, DIMENSION(3,3,3,3) :: C1,C2
```

```
      PARAMETER(ZERO=0.D0,ONE=1.D0,TWO=2.D0)
C
      Ee=PROPS(1)
      Nu=PROPS(2)
      Lambda=Nu*Ee/((ONE+Nu)*(ONE-TWO*Nu))
      Mu=Ee/(TWO*(ONE+Nu))
C
      DO i=1,3
      DO j=1,3
      IF (i.EQ.j) THEN
      IDEN(i,j)=ONE
      ELSE
      IDEN(i,j)=ZERO
      ENDIF
      END DO
```

```
      END DO
C
      Ffin=DFGRD1
      Jfin=Ffin(1,1)*(Ffin(2,2)*Ffin(3,3)-Ffin(2,3)*Ffin(3,2))+
     1    Ffin(1,2)*(Ffin(2,3)*Ffin(3,1)-Ffin(2,1)*Ffin(3,3))+
     2    Ffin(1,3)*(Ffin(2,1)*Ffin(3,2)-Ffin(2,2)*Ffin(3,1))
C
      STRESSV=STRESS
      STRESSM(1,1)=STRESSV(1)
      STRESSM(2,2)=STRESSV(2)
      STRESSM(3,3)=STRESSV(3)
      STRESSM(1,2)=STRESSV(4)
      STRESSM(2,1)=STRESSV(4)
      STRESSM(1,3)=STRESSV(5)
      STRESSM(3,1)=STRESSV(5)
```

```
      STRESSM(2,3)=STRESSV(6)

      STRESSM(3,2)=STRESSV(6)

C

      DSTRANV=DSTRAN

      DSTRANM(1,1)=DSTRANV(1)

      DSTRANM(2,2)=DSTRANV(2)

      DSTRANM(3,3)=DSTRANV(3)

      DSTRANM(1,2)=ONE/TWO*DSTRANV(4)

      DSTRANM(2,1)=ONE/TWO*DSTRANV(4)

      DSTRANM(1,3)=ONE/TWO*DSTRANV(5)

      DSTRANM(3,1)=ONE/TWO*DSTRANV(5)

      DSTRANM(2,3)=ONE/TWO*DSTRANV(6)

      DSTRANM(3,2)=ONE/TWO*DSTRANV(6)

C

      DO i=1,3
```

```
      DO j=1,3
      DO k=1,3
      DO l=1,3
      C1(i,j,k,l)=
     1 ONE/Jfin*Lambda*IDEN(i,j)*IDEN(k,l)+
     2 ONE/Jfin*Mu*IDEN(i,k)*IDEN(j,l)+
     3 ONE/Jfin*Mu*IDEN(i,l)*IDEN(j,k)+
     4 STRESSM(i,k)*IDEN(j,l)+
     5 STRESSM(j,l)*IDEN(i,k)-
     6 STRESSM(i,j)*IDEN(k,l)
      END DO
      END DO
      END DO
      END DO
C
```

```
      DO i=1,3
      DO j=1,3
      DO k=1,3
      DO l=1,3
      STRESSM(i,j)=STRESSM(i,j)+C1(i,j,k,l)*DSTRANM(k,l)
      END DO
      END DO
      END DO
      END DO
C
      DO i=1,3
      DO j=1,3
      DO k=1,3
      DO l=1,3
      C2(i,j,k,l)=
```

```
     1 ONE/Jfin*Lambda*IDEN(i,j)*IDEN(k,l)+
     2 ONE/Jfin*Mu*IDEN(i,k)*IDEN(j,l)+
     3 ONE/Jfin*Mu*IDEN(i,l)*IDEN(j,k)+
     4 STRESSM(i,k)*IDEN(j,l)+
     5 STRESSM(j,l)*IDEN(i,k)
      END DO
      END DO
      END DO
      END DO
C
      STRESS(1)=STRESSM(1,1)
      STRESS(2)=STRESSM(2,2)
      STRESS(3)=STRESSM(3,3)
      STRESS(4)=STRESSM(1,2)
      STRESS(5)=STRESSM(1,3)
```

```
      STRESS(6)=STRESSM(2,3)
C
      DO i=1,3
      DDSDDE(i,1)=C2(i,i,1,1)
      DDSDDE(i,2)=C2(i,i,2,2)
      DDSDDE(i,3)=C2(i,i,3,3)
      DDSDDE(i,4)=C2(i,i,1,2)
      DDSDDE(i,5)=C2(i,i,1,3)
      DDSDDE(i,6)=C2(i,i,2,3)
      END DO
      DDSDDE(4,1)=C2(1,2,1,1)
      DDSDDE(4,2)=C2(1,2,2,2)
      DDSDDE(4,3)=C2(1,2,3,3)
      DDSDDE(4,4)=C2(1,2,1,2)
      DDSDDE(4,5)=C2(1,2,1,3)
```

```
DDSDDE(4,6)=C2(1,2,2,3)

DDSDDE(5,1)=C2(1,3,1,1)

DDSDDE(5,2)=C2(1,3,2,2)

DDSDDE(5,3)=C2(1,3,3,3)

DDSDDE(5,4)=C2(1,3,1,2)

DDSDDE(5,5)=C2(1,3,1,3)

DDSDDE(5,6)=C2(1,3,2,3)

DDSDDE(6,1)=C2(2,3,1,1)

DDSDDE(6,2)=C2(2,3,2,2)

DDSDDE(6,3)=C2(2,3,3,3)

DDSDDE(6,4)=C2(2,3,1,2)

DDSDDE(6,5)=C2(2,3,1,3)

DDSDDE(6,6)=C2(2,3,2,3)

RETURN

END
```

```
C=============================================================

C ZERO-GRADED HYPOELASTIC CONSTITUTIVE MODEL BASED ON THE GREEN-NAGHDI RATE OF THE CAUCHY STRESS

C=============================================================

C PROPS(1) -> YOUNG'S MODULUS

C PROPS(2) -> POISSON'S RATIO

C

C Ee              = YOUNG'S MODULUS

C Nu              = POISSON'S RATIO

C Lambda & Mu     = LAME'S CONSTANTS

C IDEN            = KRONECKER DELTA

C DFGRD1          = UMAT-SUBROUTINE DEFORMATION GRADIENT AT THE END OF THE INCREMENT

C Ffin            = MATRIX VERSION OF "DFGRD1"

C Bfin            = LEFT CAUCHY-GREEN DEFORMATION AT THE END OF THE INCREMENT
```

C LAM1, LAM2 & LAM3 = PRINCIPLE STRETCHES AT THE END OF THE INCREMENT

C B1, B2 & B3 = EIGENPROJECTIONS OF "Bfin"

C h12, h23 & h13 = SCALARS USED IN CALCULATION OF "B1", "B2" & "B3"

C B12, ..., B32 = MATRICES USED IN CALCULATION OF "B1", "B2" & "B3"

C STRESS = UMAT-SUBROUTINE STRESS ARRAY

C STRESSV = VECTOR VERSION OF "STRESS"

C STRESSM = MATRIX VERSION OF "STRESS"

C DSTRAN = UMAT-SUBROUTINE INCREMENTAL STRAIN ARRAY

C DSTRANV = VECTOR VERSION OF "DSTRAN"

C DSTRANM = MATRIX VERSION OF "DSTRAN"

C C1 = FOURTH-ORDER ELASTICITY TENSOR

C DDSDDE = UMAT-SUBROUTINE CONSISTENT JACOBIAN ARRAY

C C2 = FOURTH-ORDER TENSOR VERSION OF "DDSDDE"

C CSTAR = FOURTH-ORDER TENSOR USED IN CALCULATION OF "C1" & "C2"

```
C TERM1           = SCALAR USED IN CALCULATION OF "C1" & "C2"
C=============================================================
      SUBROUTINE UMAT(STRESS,STATEV,DDSDDE,SSE,SPD,SCD,
     1 RPL,DDSDDT,DRPLDE,DRPLDT,
     2 STRAN,DSTRAN,TIME,DTIME,TEMP,DTEMP,PREDEF,DPRED,CMNAME,
     3 NDI,NSHR,NTENS,NSTATV,PROPS,NPROPS,COORDS,DROT,PNEWDT,
     4 CELENT,DFGRD0,DFGRD1,NOEL,NPT,LAYER,KSPT,JSTEP,KINC)
C
      INCLUDE 'ABA_PARAM.INC'
C
      CHARACTER*80 CMNAME
      DIMENSION STRESS(NTENS),STATEV(NSTATV),
     1 DDSDDE(NTENS,NTENS),
     2 DDSDDT(NTENS),DRPLDE(NTENS),
     3 STRAN(NTENS),DSTRAN(NTENS),TIME(2),PREDEF(1),DPRED(1),
```

```
     4 PROPS(NPROPS),COORDS(3),DROT(3,3),DFGRD0(3,3),DFGRD1(3,3),
     5 JSTEP(4)
C
      INTEGER :: i,j,k,l,m
      REAL*8 :: Ee,Nu,Lambda,Mu,
     1 LAM1,LAM2,LAM3,TERM1,h12,h23,h13
      REAL*8, DIMENSION(3,3) :: IDEN,AN,STRESSM,DSTRANM,
     1 Ffin,Bfin,B12,B21,B13,B31,B23,B32,B1,B2,B3
      REAL*8, DIMENSION(6) :: STRESSV,DSTRANV,V
      REAL*8, DIMENSION(3) :: PS
      REAL*8, DIMENSION(3,3,3,3) :: C1,C2,CSTAR
      PARAMETER(ZERO=0.D0,ONE=1.D0,TWO=2.D0)
C
      Ee=PROPS(1)
      Nu=PROPS(2)
```

```
      Lambda=Nu*Ee/((ONE+Nu)*(ONE-TWO*Nu))
      Mu=Ee/(TWO*(ONE+Nu))
C
      DO i=1,3
      DO j=1,3
      IF (i.EQ.j) THEN
      IDEN(i,j)=ONE
      ELSE
      IDEN(i,j)=ZERO
      ENDIF
      END DO
      END DO
C
      Ffin=DFGRD1
      Bfin=MATMUL(Ffin,Transpose(Ffin))
```

```
V(1)=Bfin(1,1)

V(2)=Bfin(2,2)

V(3)=Bfin(3,3)

V(4)=Bfin(1,2)

V(5)=Bfin(1,3)

V(6)=Bfin(2,3)

CALL SPRIND(V,PS,AN,1,NDI,NSHR)

LAM1=PS(1)**(ONE/TWO)

LAM2=PS(2)**(ONE/TWO)

LAM3=PS(3)**(ONE/TWO)

IF (PS(1).EQ.PS(2)) THEN

B12=IDEN

B21=IDEN

ELSE

B12=ONE/(PS(1)-PS(2))*(Bfin-PS(2)*IDEN)
```

```
B21=ONE/(PS(2)-PS(1))*(Bfin-PS(1)*IDEN)

h12=(LAM2-LAM1)/(LAM1+LAM2)

END IF

IF (PS(2).EQ.PS(3)) THEN

B23=IDEN

B32=IDEN

ELSE

B23=ONE/(PS(2)-PS(3))*(Bfin-PS(3)*IDEN)

B32=ONE/(PS(3)-PS(2))*(Bfin-PS(2)*IDEN)

h23=(LAM3-LAM2)/(LAM2+LAM3)

END IF

IF (PS(1).EQ.PS(3)) THEN

B13=IDEN

B31=IDEN

ELSE
```

```
      B13=ONE/(PS(1)-PS(3))*(Bfin-PS(3)*IDEN)

      B31=ONE/(PS(3)-PS(1))*(Bfin-PS(1)*IDEN)

      h13=(LAM3-LAM1)/(LAM1+LAM3)

      END IF

      B1=MATMUL(B12,B13)

      B2=MATMUL(B21,B23)

      B3=MATMUL(B31,B32)

C

      DO i=1,3

      DO j=1,3

      DO k=1,3

      DO l=1,3

      CSTAR(i,j,k,l)=

     1 h12*B1(i,k)*B2(l,j)-h12*B2(i,k)*B1(l,j)+

     2 h13*B1(i,k)*B3(l,j)-h13*B3(i,k)*B1(l,j)+
```

```
     3 h23*B2(i,k)*B3(l,j)-h23*B3(i,k)*B2(l,j)
      END DO
      END DO
      END DO
      END DO
C
      STRESSV=STRESS
      STRESSM(1,1)=STRESSV(1)
      STRESSM(2,2)=STRESSV(2)
      STRESSM(3,3)=STRESSV(3)
      STRESSM(1,2)=STRESSV(4)
      STRESSM(2,1)=STRESSV(4)
      STRESSM(1,3)=STRESSV(5)
      STRESSM(3,1)=STRESSV(5)
      STRESSM(2,3)=STRESSV(6)
```

```
      STRESSM(3,2)=STRESSV(6)
C
      DSTRANV=DSTRAN
      DSTRANM(1,1)=DSTRANV(1)
      DSTRANM(2,2)=DSTRANV(2)
      DSTRANM(3,3)=DSTRANV(3)
      DSTRANM(1,2)=ONE/TWO*DSTRANV(4)
      DSTRANM(2,1)=ONE/TWO*DSTRANV(4)
      DSTRANM(1,3)=ONE/TWO*DSTRANV(5)
      DSTRANM(3,1)=ONE/TWO*DSTRANV(5)
      DSTRANM(2,3)=ONE/TWO*DSTRANV(6)
      DSTRANM(3,2)=ONE/TWO*DSTRANV(6)
C
      DO i=1,3
      DO j=1,3
```

```
 DO k=1,3
 DO l=1,3
 TERM1=ZERO
 DO m=1,3
 TERM1=
1 TERM1+
2 CSTAR(i,m,k,l)*STRESSM(m,j)-
3 STRESSM(i,m)*CSTAR(m,j,k,l)
 END DO
 C1(i,j,k,l)=
1 TERM1+
2 Lambda*IDEN(i,j)*IDEN(k,l)+
3 Mu*IDEN(i,k)*IDEN(j,l)+
4 Mu*IDEN(i,l)*IDEN(j,k)
 END DO
```

```
      END DO
      END DO
      END DO
C
      DO i=1,3
      DO j=1,3
      DO k=1,3
      DO l=1,3
      STRESSM(i,j)=STRESSM(i,j)+C1(i,j,k,l)*DSTRANM(k,l)
      END DO
      END DO
      END DO
      END DO
C
      DO i=1,3
```

```
 DO j=1,3
 DO k=1,3
 DO l=1,3
 TERM1=ZERO
 DO m=1,3
 TERM1=
1 TERM1+
2 CSTAR(i,m,k,l)*STRESSM(m,j)-
3 STRESSM(i,m)*CSTAR(m,j,k,l)
 END DO
 C2(i,j,k,l)=
1 TERM1+
2 Lambda*IDEN(i,j)*IDEN(k,l)+
3 Mu*IDEN(i,k)*IDEN(j,l)+
4 Mu*IDEN(i,l)*IDEN(j,k)+
```

```
     5 STRESSM(i,j)*IDEN(k,l)
      END DO
      END DO
      END DO
      END DO
C
      STRESS(1)=STRESSM(1,1)
      STRESS(2)=STRESSM(2,2)
      STRESS(3)=STRESSM(3,3)
      STRESS(4)=STRESSM(1,2)
      STRESS(5)=STRESSM(1,3)
      STRESS(6)=STRESSM(2,3)
C
      DO i=1,3
      DDSDDE(i,1)=C2(i,i,1,1)
```

```
DDSDDE(i,2)=C2(i,i,2,2)

DDSDDE(i,3)=C2(i,i,3,3)

DDSDDE(i,4)=C2(i,i,1,2)

DDSDDE(i,5)=C2(i,i,1,3)

DDSDDE(i,6)=C2(i,i,2,3)

END DO

DDSDDE(4,1)=C2(1,2,1,1)

DDSDDE(4,2)=C2(1,2,2,2)

DDSDDE(4,3)=C2(1,2,3,3)

DDSDDE(4,4)=C2(1,2,1,2)

DDSDDE(4,5)=C2(1,2,1,3)

DDSDDE(4,6)=C2(1,2,2,3)

DDSDDE(5,1)=C2(1,3,1,1)

DDSDDE(5,2)=C2(1,3,2,2)

DDSDDE(5,3)=C2(1,3,3,3)
```

```
      DDSDDE(5,4)=C2(1,3,1,2)
      DDSDDE(5,5)=C2(1,3,1,3)
      DDSDDE(5,6)=C2(1,3,2,3)
      DDSDDE(6,1)=C2(2,3,1,1)
      DDSDDE(6,2)=C2(2,3,2,2)
      DDSDDE(6,3)=C2(2,3,3,3)
      DDSDDE(6,4)=C2(2,3,1,2)
      DDSDDE(6,5)=C2(2,3,1,3)
      DDSDDE(6,6)=C2(2,3,2,3)
      RETURN
      END
C=============================================================
C ZERO-GRADED HYPOELASTIC CONSTITUTIVE MODEL BASED ON THE
GREEN-NAGHDI RATE OF THE KIRCHHOFF STRESS
C=============================================================
```

```
      C PROPS(1) -> YOUNG'S MODULUS
      C PROPS(2) -> POISSON'S RATIO
      C
      C Ee              = YOUNG'S MODULUS
      C Nu              = POISSON'S RATIO
      C Lambda & Mu     = LAME'S CONSTANTS
      C IDEN            = KRONECKER DELTA
      C DFGRD1          = UMAT-SUBROUTINE DEFORMATION GRADIENT AT THE END
OF THE INCREMENT
      C Ffin            = MATRIX VERSION OF "DFGRD1"
      C Jfin            = DETERMINANT OF "Ffin"
      C Bfin            = LEFT CAUCHY-GREEN DEFORMATION AT THE END OF THE
INCREMENT
      C LAM1, LAM2 & LAM3 = PRINCIPLE STRETCHES AT THE END OF THE
INCREMENT
      C B1, B2 & B3     = EIGENPROJECTIONS OF "Bfin"
```

```
C STRESS          = UMAT-SUBROUTINE STRESS ARRAY

C STRESSV         = VECTOR VERSION OF "STRESS"

C STRESSM         = MATRIX VERSION OF "STRESS"

C DSTRAN          = UMAT-SUBROUTINE INCREMENTAL STRAIN ARRAY

C DSTRANV         = VECTOR VERSION OF "DSTRAN"

C DSTRANM         = MATRIX VERSION OF "DSTRAN"

C C1              = ELASTICITY TENSOR

C DDSDDE          = UMAT-SUBROUTINE CONSISTENT JACOBIAN ARRAY

C C2              = FOURTH-ORDER TENSORORIAL VERSION OF "DDSDDE"

C=============================================================

      SUBROUTINE UMAT(STRESS,STATEV,DDSDDE,SSE,SPD,SCD,

     1 RPL,DDSDDT,DRPLDE,DRPLDT,

     2 STRAN,DSTRAN,TIME,DTIME,TEMP,DTEMP,PREDEF,DPRED,CMNAME,

     3 NDI,NSHR,NTENS,NSTATV,PROPS,NPROPS,COORDS,DROT,PNEWDT,

     4 CELENT,DFGRD0,DFGRD1,NOEL,NPT,LAYER,KSPT,JSTEP,KINC)
```

```
C
      INCLUDE 'ABA_PARAM.INC'
C
      CHARACTER*80 CMNAME
      DIMENSION STRESS(NTENS),STATEV(NSTATV),
     1 DDSDDE(NTENS,NTENS),
     2 DDSDDT(NTENS),DRPLDE(NTENS),
     3 STRAN(NTENS),DSTRAN(NTENS),TIME(2),PREDEF(1),DPRED(1),
     4 PROPS(NPROPS),COORDS(3),DROT(3,3),DFGRD0(3,3),DFGRD1(3,3),
     5 JSTEP(4)
C
      INTEGER :: i,j,k,l,m
      REAL*8 :: Ee,Nu,Lambda,Mu,Jfin,
     1 LAM1,LAM2,LAM3,TERM1,h12,h23,h13
      REAL*8, DIMENSION(3,3) :: IDEN,AN,STRESSM,DSTRANM,
```

```
     1 Ffin,Bfin,B12,B21,B13,B31,B23,B32,B1,B2,B3
      REAL*8, DIMENSION(6) :: STRESSV,DSTRANV,V
      REAL*8, DIMENSION(3) :: PS
      REAL*8, DIMENSION(3,3,3,3) :: C1,C2,CSTAR
      PARAMETER(ZERO=0.D0,ONE=1.D0,TWO=2.D0)
C
      Ee=PROPS(1)
      Nu=PROPS(2)
      Lambda=Nu*Ee/((ONE+Nu)*(ONE-TWO*Nu))
      Mu=Ee/(TWO*(ONE+Nu))
C
      DO i=1,3
      DO j=1,3
      IF (i.EQ.j) THEN
      IDEN(i,j)=ONE
```

```
      ELSE
      IDEN(i,j)=ZERO
      ENDIF
      END DO
      END DO
C
      Ffin=DFGRD1
      Jfin=Ffin(1,1)*(Ffin(2,2)*Ffin(3,3)-Ffin(2,3)*Ffin(3,2))+
     1    Ffin(1,2)*(Ffin(2,3)*Ffin(3,1)-Ffin(2,1)*Ffin(3,3))+
     2    Ffin(1,3)*(Ffin(2,1)*Ffin(3,2)-Ffin(2,2)*Ffin(3,1))
      Bfin=MATMUL(Ffin,Transpose(Ffin))
      V(1)=Bfin(1,1)
      V(2)=Bfin(2,2)
      V(3)=Bfin(3,3)
      V(4)=Bfin(1,2)
```

```
V(5)=Bfin(1,3)

V(6)=Bfin(2,3)

CALL SPRIND(V,PS,AN,1,NDI,NSHR)

LAM1=PS(1)**(ONE/TWO)

LAM2=PS(2)**(ONE/TWO)

LAM3=PS(3)**(ONE/TWO)

IF (PS(1).EQ.PS(2)) THEN

B12=IDEN

B21=IDEN

ELSE

B12=ONE/(PS(1)-PS(2))*(Bfin-PS(2)*IDEN)

B21=ONE/(PS(2)-PS(1))*(Bfin-PS(1)*IDEN)

h12=(LAM2-LAM1)/(LAM1+LAM2)

END IF

IF (PS(2).EQ.PS(3)) THEN
```

```
B23=IDEN

B32=IDEN

ELSE

B23=ONE/(PS(2)-PS(3))*(Bfin-PS(3)*IDEN)

B32=ONE/(PS(3)-PS(2))*(Bfin-PS(2)*IDEN)

h23=(LAM3-LAM2)/(LAM2+LAM3)

END IF

IF (PS(1).EQ.PS(3)) THEN

B13=IDEN

B31=IDEN

ELSE

B13=ONE/(PS(1)-PS(3))*(Bfin-PS(3)*IDEN)

B31=ONE/(PS(3)-PS(1))*(Bfin-PS(1)*IDEN)

h13=(LAM3-LAM1)/(LAM1+LAM3)

END IF
```

```
      B1=MATMUL(B12,B13)

      B2=MATMUL(B21,B23)

      B3=MATMUL(B31,B32)

C

      DO i=1,3

      DO j=1,3

      DO k=1,3

      DO l=1,3

      CSTAR(i,j,k,l)=

     1 h12*B1(i,k)*B2(l,j)-h12*B2(i,k)*B1(l,j)+

     2 h13*B1(i,k)*B3(l,j)-h13*B3(i,k)*B1(l,j)+

     3 h23*B2(i,k)*B3(l,j)-h23*B3(i,k)*B2(l,j)

      END DO

      END DO

      END DO
```

```
      END DO
C
      STRESSV=STRESS
      STRESSM(1,1)=STRESSV(1)
      STRESSM(2,2)=STRESSV(2)
      STRESSM(3,3)=STRESSV(3)
      STRESSM(1,2)=STRESSV(4)
      STRESSM(2,1)=STRESSV(4)
      STRESSM(1,3)=STRESSV(5)
      STRESSM(3,1)=STRESSV(5)
      STRESSM(2,3)=STRESSV(6)
      STRESSM(3,2)=STRESSV(6)
C
      DSTRANV=DSTRAN
      DSTRANM(1,1)=DSTRANV(1)
```

```
      DSTRANM(2,2)=DSTRANV(2)
      DSTRANM(3,3)=DSTRANV(3)
      DSTRANM(1,2)=ONE/TWO*DSTRANV(4)
      DSTRANM(2,1)=ONE/TWO*DSTRANV(4)
      DSTRANM(1,3)=ONE/TWO*DSTRANV(5)
      DSTRANM(3,1)=ONE/TWO*DSTRANV(5)
      DSTRANM(2,3)=ONE/TWO*DSTRANV(6)
      DSTRANM(3,2)=ONE/TWO*DSTRANV(6)
C
      DO i=1,3
      DO j=1,3
      DO k=1,3
      DO l=1,3
      TERM1=ZERO
      DO m=1,3
```

```
 TERM1=
1 TERM1+
2 CSTAR(i,m,k,l)*STRESSM(m,j)-
3 STRESSM(i,m)*CSTAR(m,j,k,l)
 END DO
 C1(i,j,k,l)=
1 TERM1+
2 ONE/Jfin*Lambda*IDEN(i,j)*IDEN(k,l)+
3 ONE/Jfin*Mu*IDEN(i,k)*IDEN(j,l)+
4 ONE/Jfin*Mu*IDEN(i,l)*IDEN(j,k)-
5 STRESSM(i,j)*IDEN(k,l)
 END DO
 END DO
 END DO
 END DO
```

```
C
      DO i=1,3
      DO j=1,3
      DO k=1,3
      DO l=1,3
      STRESSM(i,j)=STRESSM(i,j)+C1(i,j,k,l)*DSTRANM(k,l)
      END DO
      END DO
      END DO
      END DO
C
      DO i=1,3
      DO j=1,3
      DO k=1,3
      DO l=1,3
```

```
 TERM1=ZERO
 DO m=1,3
 TERM1=
1 TERM1+
2 CSTAR(i,m,k,l)*STRESSM(m,j)-
3 STRESSM(i,m)*CSTAR(m,j,k,l)
 END DO
 C2(i,j,k,l)=
1 TERM1+
2 ONE/Jfin*Lambda*IDEN(i,j)*IDEN(k,l)+
3 ONE/Jfin*Mu*IDEN(i,k)*IDEN(j,l)+
4 ONE/Jfin*Mu*IDEN(i,l)*IDEN(j,k)
 END DO
 END DO
 END DO
```

```
      END DO
C
      STRESS(1)=STRESSM(1,1)
      STRESS(2)=STRESSM(2,2)
      STRESS(3)=STRESSM(3,3)
      STRESS(4)=STRESSM(1,2)
      STRESS(5)=STRESSM(1,3)
      STRESS(6)=STRESSM(2,3)
C
      DO i=1,3
      DDSDDE(i,1)=C2(i,i,1,1)
      DDSDDE(i,2)=C2(i,i,2,2)
      DDSDDE(i,3)=C2(i,i,3,3)
      DDSDDE(i,4)=C2(i,i,1,2)
      DDSDDE(i,5)=C2(i,i,1,3)
```

```
DDSDDE(i,6)=C2(i,i,2,3)

END DO

DDSDDE(4,1)=C2(1,2,1,1)

DDSDDE(4,2)=C2(1,2,2,2)

DDSDDE(4,3)=C2(1,2,3,3)

DDSDDE(4,4)=C2(1,2,1,2)

DDSDDE(4,5)=C2(1,2,1,3)

DDSDDE(4,6)=C2(1,2,2,3)

DDSDDE(5,1)=C2(1,3,1,1)

DDSDDE(5,2)=C2(1,3,2,2)

DDSDDE(5,3)=C2(1,3,3,3)

DDSDDE(5,4)=C2(1,3,1,2)

DDSDDE(5,5)=C2(1,3,1,3)

DDSDDE(5,6)=C2(1,3,2,3)

DDSDDE(6,1)=C2(2,3,1,1)
```

```
DDSDDE(6,2)=C2(2,3,2,2)

DDSDDE(6,3)=C2(2,3,3,3)

DDSDDE(6,4)=C2(2,3,1,2)

DDSDDE(6,5)=C2(2,3,1,3)

DDSDDE(6,6)=C2(2,3,2,3)

RETURN

END
```

APPENDIX B: SIGNIFICANCE OF LOCAL ANATOMICAL MEASURES AND LOCAL ASYMMETRY

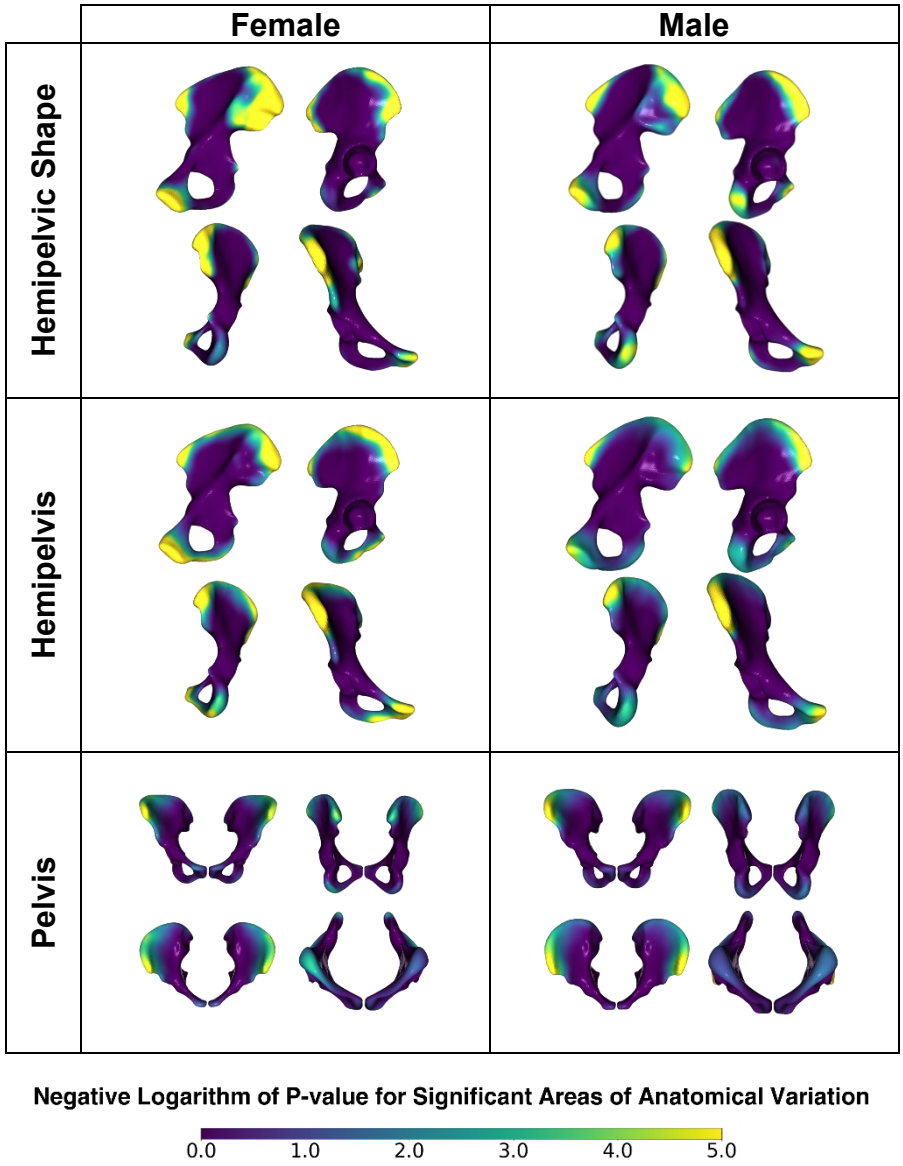

Figure B-0-1: Color map plots for the statistical test on the significance of local anatomical variation. The color mapping represents the negative logarithm of the p-values. The hemipelvis is visualized from lateral (top-left), medial (top-right), posterior (bottom-left) and anterior views (bottom-right). The views of the pelvis include anterior (top-left), posterior (top-right), inlet (bottom-left) and outlet (bottom-right).

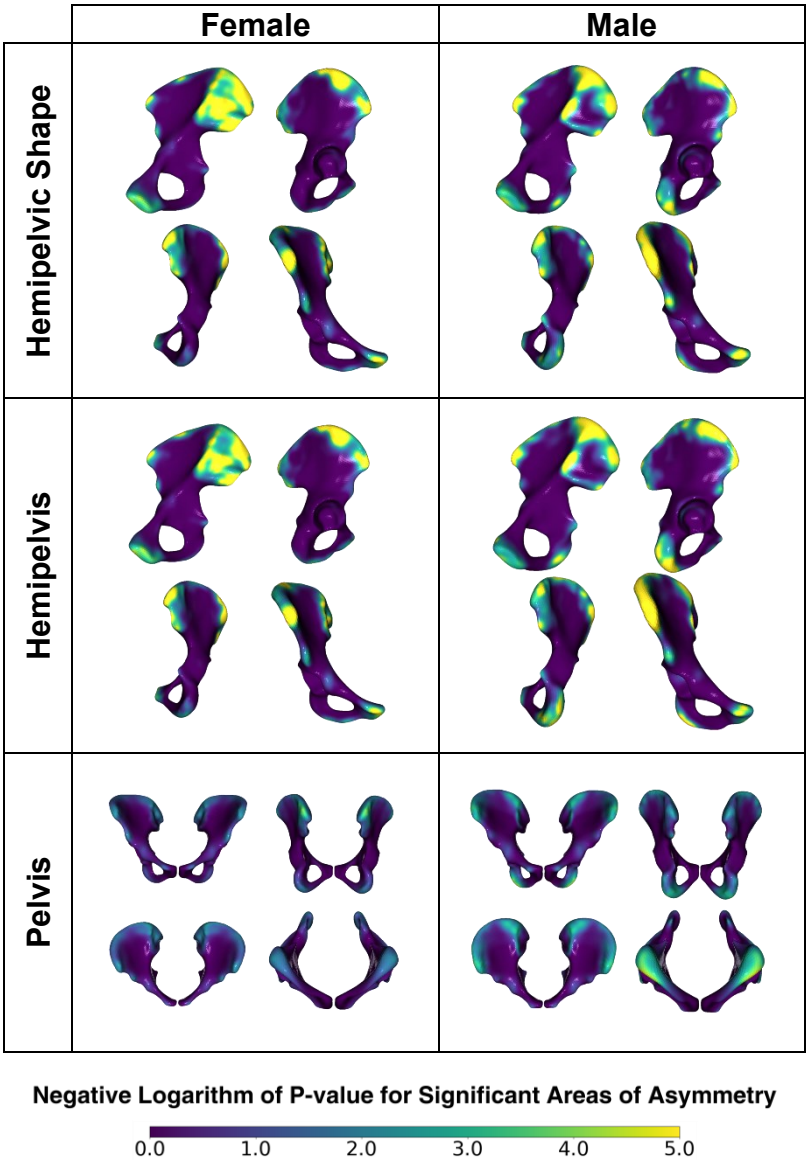

Figure B-0-2: Color map plots for the statistical significance of local asymmetry. The color mapping represents the negative logarithm of the p-values. The hemipelvis is visualized from lateral (top-left), medial (top-right), posterior (bottom-left) and anterior views (bottom-right). The views of the pelvis include anterior (top-left), posterior (top-right), inlet (bottom-left) and outlet (bottom-right).

APPENDIX C: NON-RIGID COHERENT POINT DRIFT METHOD

The CPD method approaches the point-set registration problem as a probability estimation problem with regularization. In the CPD method, one point set represents the centroids of an isotropic Gaussian Mixture Model (GMM) and the other point set is considered as the data points, observed from the GMM. The first point set is referred to as the *source* point set and the second point set is called the *target* point set. In addition to the GMM components, a uniform distribution is added to the mixture to handle noise and outliers. Denoting the source point set by $\boldsymbol{Y} = \{\boldsymbol{y}_1, \dots, \boldsymbol{y}_M\}$ and the target point set by $\boldsymbol{X} = \{\boldsymbol{x}_1, \dots, \boldsymbol{x}_N\}$, the mixture model in the CPD method takes the form:

$$p(\boldsymbol{x}) = \sum_{m=1}^{M+1} P(m)p(\boldsymbol{x}|m) = \frac{\omega}{N} + \frac{1-\omega}{M}\sum_{m=1}^{M} p(\boldsymbol{x}|m), \tag{C-1}$$

$$p(\boldsymbol{x}|m) = \frac{1}{(2\pi\sigma^2)^{D/2}} \exp\left\{-\frac{\|\boldsymbol{x} - T(\boldsymbol{y}_m, \theta)\|^2}{2\sigma^2}\right\} \text{ for } m = 1, \dots, M \tag{C-2}$$

Here, ω is a weight parameter between 0 and 1 to handle outliers and noise; all of the GMM components share the same width σ and the same membership $P(m)$; and, the centroids of the GMM components, denoted by $T(\boldsymbol{y}_m, \theta)$, are parameterized by a set of transformation parameters θ. An important quantity in the CPD method is the *posterior* or *assignment* probability of a GMM component to a data point, which is computed based on Baye's theorem:

$$p(m|\boldsymbol{x}_n) = \frac{p(\boldsymbol{x}_n|m)P(m)}{p(\boldsymbol{x}_n)}. \tag{C-3}$$

The method minimizes the expectation of the mixture model for all of the data points:

$$\mathcal{L}(\sigma, \theta) = \prod_{n=1}^{N} p(\boldsymbol{x}_n), \tag{C-4}$$

or equivalently, minimize the negative log-likelihood of the mixture:

$$E(\sigma, \theta) = -\ln \mathcal{L}(\sigma, \theta) = -\sum_{n=1}^{N} \ln p(\boldsymbol{x}_n). \tag{C-5}$$

However, taking the derivative of the negative log-likelihood function E w.r.t. its parameters leads to a set of highly nonlinear coupled expressions. To overcome this, an *expectation-maximization* (EM) algorithm is employed to optimize the function $E(\sigma, \theta)$. The EM algorithm initializes the parameters σ and θ, and iteratively updates them to decrease E. The parameters at the start of each iteration are called *old* parameters and the updated parameters are referred to as the *new* parameters. Using the posterior probability for the old parameters and Jensen's inequality, the EM algorithm minimizes the following function at each iteration:

$$Q(\theta, \sigma^2) = -\sum_{n=1}^{N} \sum_{m=1}^{M+1} P^{old}(m|\boldsymbol{x}_n) \ln\left(P^{new}(m) p^{new}(\boldsymbol{x}_n|m)\right). \tag{C-6}$$

This function is an upper bound for $E^{new} = E(\sigma^{new}, \theta^{new})$ (after dropping the terms which only depend on the old parameters) and its minimization in terms of the new parameters will necessarily decrease the negative log-likelihood function.

The non-rigid motion in the CPD method takes the form $T(\boldsymbol{y}, v) = \boldsymbol{y} + v(\boldsymbol{y})$, where v represents the *velocity* (or displacement) of each point on the source point set. The smoothness of the velocity function v is measured using the high-frequency energy of the motion as follows:

$$\phi(v) = \int_{\mathbb{R}^D} \frac{|\tilde{v}(s)|}{\tilde{G}(s)} ds, \tag{C-7}$$

in which, $\tilde{v}$ is the Fourier transform of the velocity function, $\tilde{G}$ is selected as a Gaussian kernel function with the width β (acting as a high-pass filter), and s is a frequency domain variable. The smoothness measure of the velocity function, i.e. $\phi(v)$, is incorporated as a *prior* probability into the likelihood function:

$$\bar{\mathcal{L}}(\sigma, v) = \mathcal{L}(\sigma, v) \times \exp\left(-\frac{\lambda}{2}\phi(v)\right), \tag{C-8}$$

in which, λ is a trade-off parameter that highlights the importance of smoothness relative to alignment. Similar to the derivation of Eq. (C-6), an upper-bound function is defined for the likelihood function (with prior knowledge of the smoothness):

$$\bar{Q}(\sigma, v) = Q(\sigma, v) + \frac{\lambda}{2}\phi(v). \tag{C-9}$$

Computing the *functional derivative* of $\bar{Q}$ w.r.t. v, the velocity function takes the form:

$$v(\boldsymbol{y}) = \sum_{m=1}^{M} \boldsymbol{w}_m G(\boldsymbol{y}, \boldsymbol{y}_m), \tag{C-10}$$

$$G(\boldsymbol{y}, \boldsymbol{y}_m) = \exp\left(-\frac{\|\boldsymbol{y} - \boldsymbol{y}_m\|^2}{2\beta^2}\right), \tag{C-11}$$

which is a set of isotropic Gaussian basis functions with equal width β, located on the source point set. Computing the Fourier transform of the velocity function, the high-frequency energy is measured as follows:

$$\phi(v) = \sum_{i,j=1}^{M} G\left(\boldsymbol{y}_i, \boldsymbol{y}_j\right) \boldsymbol{w}_i . \boldsymbol{w}_j \tag{C-12}$$

Lastly, taking the derivatives of $\bar{Q}$ w.r.t. the parameters σ and $\theta = \{\boldsymbol{w}_1, \dots, \boldsymbol{w}_M\}$, a set of decoupled equations is obtained for updating the unknown parameters. In each iteration, the posterior probability is computed based on the old parameters (called the expectation step or E-step), and then the parameters are updated based on the decoupled equations (called the maximization step or M-step).